The Integration and Miniaturisation of the Patch-clamp Technique into Planar Silicon-based Microstructures for the Electrophysiological Study of Network Behaviour

Bradley Jay Dworak

Doctor of Philosophy

The University of Edinburgh

2005

Abstract

This study investigates the hypothesis that the important aspects of the patch-clamp technique for detailed electrophysiological studies of neurons can be miniaturised and scaled down to micron-size silicon-based microstructures. The work strives to emulate the important characteristics that this electrophysiological method offers for the study of network behaviour of in-vitro cell cultures to improve upon the current limitations of multi-electrode-array (MEA) design.

The first part of the study focused on the preparation and assessment of healthy and viable cell cultures of primary rat cortical neurons for the study of network behaviour. Cultures were grown on silicon surfaces of varying composition and roughness to test the feasibility of integrating these cultures on silicon-based electronic devices. Also, the health and viability of neurons growing on non-transparent silicon substrates have been assessed by detailed histological analysis and cell counting using standard immunofluorescence techniques. Neurons extracted from various ganglia of the pond snail *Lymnaea stagnalis* have been prepared for patch-clamping using established dissection, isolation and enzymatic digestion protocols.

The second part of the project concentrated on formulating a theory of gigaseal formation during patch-clamping by a critical review of the literature. The critical factors for highly resistive seal formation were identified and realised on prototype devices, including the patch aperture length and physical nature of the aperture surface. The physical natures of SiO_2 and Si_3N_4 (and modifications by boron deposition) were investigated by wettability experimentation. A relationship between interactive molecular surface energy and the wetting angle was obtained from an established theoretical wetting model.

The third part of this study focused on the geometric properties of microfabricated apertures. Apertures were modified by deposition techniques to increase the radius of curvature of the edge profile, thereby mimicking a rounded glass pipette opening. An image analysis algorithm was developed to quantify the radius of curvature of the cross-section profile from atomic force microscopy (AFM) data. A second algorithm was developed to quantify the circularity error of the aperture top-view by analysis of the profile texture. The profile was exacted after the application of contrast enhancement and edge-detection filters from scanning electron microscopy (SEM) image data.

Lastly, patch-clamp electrodes have been successfully integrated into planar silicon-based devices. This work presents the first patch-clamp microstructure capable of being scaled to a 100-μm inter-nodal spacing for construction of MEA designs. The electrical performances have been tested and found to be comparable to that of conventional borosilicate patch pipettes of similar aperture diameter. A base unit to contain the silicon devices and provide suction has been designed and produced.

At the time of writing, electrophysiological recordings from *Lymnaea stagnalis* neurons have not been achieved. Seal resistances $\leq$600 MΩ have been recorded, but it remains unclear whether patch-clamp recordings from neurons can be achieved using silicon-based microfabricated apertures.

Declaration

I, Bradley Jay Dworak, hereby declare that:

a) The entirety of this thesis was composed by me;

b) I have contributed to a substantial portion of the work contained in this thesis, and work contributable by somebody within my research group is clearly shown;

c) This work has not been submitted for any other degree or professional qualification.

Bradley Jay Dworak

Acknowledgements

I wish to offer my thanks to the guidance and support of Prof. Alan Murray to carry out this work over the last four years. I wish to thank Dr. Nikki MacLeod for her guidance, support, and providing me with a home in George Square to conduct my research. I wish to offer my thanks to Dr. Mike Hunter for helping me to integrate into this interdisciplinary project.

Furthermore, I wish to thank my parents, Ken and Barb Dworak, for their unending support and acceptance for myself living overseas and taking on a new life here in Europe.

I would like to thank Dr. John Curtis for his knowledge, guidance and help with this project. I would like to thank Keith Baldwin for his help on all technical aspects of the microfabrication and imaging. I would like to thank Bobby Hogg for his help with the shop-work, including Bill Parks and Alan Ross at the SMC. I would also like to thank Raphael Mollaret and Frederic Mandini for their help with the wettability experiments.

I wish to thank Fr. Garry Cappleman OP for his spiritual guidance throughout my life. Also, I wish to thank Rev. Di Williams for her guidance and support for my growth. I wish to thank Fr. Tom Kearns OP, Fr. Simon Gaine OP and Fr. Peter OP for their advice and listening abilities when the work was not going very well!

Finally, I wish to thank Hélène Puech-Samson, Andy Loughe, Takeshi Koike, Steve Feltbower and all my friends at the CSU for all of their prayers and support. It has been a joy for me meeting so many lovely people in Edinburgh!

Table of Contents

ABSTRACT I

DECLARATION III

ACKNOWLEDGEMENTS V

TABLE OF CONTENTS VII

TABLE OF FIGURES XIII

ABBREVIATIONS XIX

General Abbreviations xix

Material Abbreviations xx

1 INTRODUCTION 1

2 THEORY AND BACKGROUND OF PATCH CLAMPING AND SEAL FORMATION 7

2.1 Introduction to Patch Clamping 7

2.1.1 History and Background 7

2.1.2 Electrical Circuitry of Patched Cell 9

2.2 Review of Modern Patch Clamping Methods with Planar Devices 11

2.3 Critical Assessment of Patch Formation Theory 13

2.3.1 Theory of Seal Formation in Patching 13

2.3.2 Application of gigaseal formation theory to microstructures 15

2.3.3 Electrochemical and Biophysical Model of Seal 16

2.3.4 Atomic distance considerations for patch formation theory 21

2.4 Physical and Chemical Properties of Patch Materials 21

2.4.1 The Composition and Structure of Glass 22

2.4.2 Electrostatic bond considerations in patch formation 24

2.4.3 Surface chemistry of cell membranes 24

2.5 Conclusion 25

3 NEURON PREPARATION, PATCH-CLAMPING AND IMMUNOHISTOLOGY OF CELL CULTURE 27

3.1 Introduction 27

3.2 Primary neuronal cultures 27

3.2.1 Background on glial problems in culture 27

3.2.2 Materials and Methods 28

3.3 Immunofluorescence Staining and Confocal Microscopy 31

3.3.1 Introduction 31

3.3.2 Materials and Methods 32

3.3.3 Accessing neuronal health and viability 33

3.3.4 Effects of using Ara-C on culture to reduce glial count 33

3.4 Snail Neuron Preparation and Viability 33

3.4.1 Introduction 33

3.4.2 Materials and Methods 33

3.5 Results 34

3.5.1 Cell Culturing 34

3.5.2 Patch-clamping snail neurons 38

3.6 Discussion 42

3.6.1 Cell Culturing 42

3.6.2 Patch-clamping snail neurons 42

3.7 Conclusion 42

4 SURFACE ENERGY, ROUGHNESS AND *IN-VITRO* CELL CULTURE ANALYSIS 43

4.1 Introduction 43

4.2 Surface characterisation by wettability measurement 44

4.2.1 Introduction 44

4.2.2 Theory of Wettability 45

4.3 Wettability Experimentation 48

4.3.1 Introduction 48

4.3.2 Sample preparation 49

4.3.4 Experimental setup and methodology 51

4.4 Results from Wettability Experiment A 52
4.5 Results from Wettability Experiment B 56
4.6 Results of Surface Roughness Analysis 59
4.7 Cell Culture Growth Analysis 64
4.7.1 Materials and Methods 64
4.7.2 Results 65
4.8 Discussion 68
4.8.1 Experiment A 68
4.8.2 Experiment B 70
4.8.3 Surface Roughness 72
4.8.4 Cell Culturing 72
4.9 Conclusion 74
4.10 Additional Figures 75

5 CIRCULARITY ERROR MEASUREMENT BY TEXTURE ANALYSIS 81

5.1 Introduction 81
5.2 Materials and Methods 81
5.3 Development of Pre-Processing Algorithm 83
5.3.1 Introduction 83
5.3.2 Methods 83
5.3.3 Results of Pre-Processing Algorithm 85
5.4 Texture Analysis Algorithm 86
5.4.1 Background to Circularity Measurement 86
5.4.2 Introduction to Development 87
5.4.3 Methods 88
5.5 Results 94
5.6 Discussion 104
5.6.1 Focus-Exposure-Matrix (FEM) 104
5.6.2 Patch Apertures 105
5.7 Conclusion 105

6 MODIFICATION AND ANALYSIS OF THE APERTURE CURVATURE. 107

6.1 Introduction 107

6.2 Materials and Methods 107
6.2.1 MEMS Processing 107
6.2.2 Defocusing 110
6.3 Curvature Profiling of Parametric Data Sets of Extrinsic Curves 112
6.3.1 Introduction 112
6.3.2 The Algorithm 113
6.4 Results 118
6.4.1 AFM profiling 118
6.4.2 Curvature Analysis 122
6.5 Discussion 123
6.5.1 MEMS Processing 123
6.5.2 De-focusing 125
6.5.3 Curvature Calculation from the Algorithm 125
6.6 Conclusion 125
6.7 Additional Figures 127

7 MICROSTRUCTURE DESIGN, FABRICATION AND ASSESSMENT 133

7.1 Introduction 133
7.2 Patch Device I 134
7.2.1 Introduction 134
7.2.2 Electrical theory and design 135
7.2.3 Materials and methods 138
7.2.4 Platform design and construction 141
7.2.5 Results 143
7.2.6 Discussion 146
7.3 Patch Device II 147
7.3.1 Introduction 147
7.3.2 Electrical theory and design 147
7.3.3 Materials and Methods 150
7.3.4 Platform II design and construction 159
7.3.5 Cross-sectional analysis 161
7.3.6 Electrical Performance Measures 162
7.3.7 Surface roughness measurements 167

7.3.8 Discussion – device II 167

7.4 Towards Highly Resistive Neuronal Recordings 169

7.4.1 Establishing the Neuron-electrode Junction 169

7.4.2 Discussion 171

7.5 Conclusion 172

8 CONCLUSION 173

BIBLIOGRAPHY 175

APPENDIX 183

Table of Figures

Figure Number and Description	Page
Figure 2.1.1: Patch-clamp configurations and electrical circuit diagrams.	8
Figure 2.1.2: Electrical model and schematic diagram of a patched neuron in the whole-cell configuration with pictorial detail of each component location.	10
Figure 2.3.2: Cross section of patched cell membrane inside pipette inner wall.	17
Figure 2.3.3: Theoretical value of patched membrane length vs. seal resistance	20
Table 3.2.2: Neurobasal-A Growth Medium.	31
Figure 3.5.1a: Healthy neuronal culture (red) with glial (green) feeder layer	35
Figure 3.5.1b: Unhealthy neuronal culture (red) showing disintegration and abnormal morphology around a glial cell (green).	36
Figure 3.5.1c: Histogram of Neurons per Observation.	36
Figure 3.5.1d: Hippocampal cell culture after 8 days without Ara-C added	37
Figure 3.5.1e: Hippocampal cell culture after 8 days with 10 μM Ara-C added	37
Figure 3.5.2a: Neurons from fluorescing with Cell Tracker Green™.	38
Table 3.5.2a: The extracellular medium used for snail patching.	39
Table 3.5.2b: Intracellular solution for snail patching	39
Figure 3.5.2b: Image of a glass pipette patch-clamped on a snail neuron.	40
Figure 3.5.2c: Intracellular voltage spike train from the snail neuron	40
Figures 3.5.2d and 3.5.2e: A dual patch-clamp recording of a snail neuron	41
Figure 4.2.1: Cross section of a typical liquid droplet on a solid surface material.	45
Figure 4.2.2: Interactive molecular surface energy vs. contact angle for water.	47
Figure 4.3.1: A 3-μL droplet of NaCl solution on thermal oxide.	48
Table 4.3.2: Table of Materials used in experiments A and B.	49
Figure 4.3.4: Wettability experiments diagram.	51
Figures 4.4.1 and 4.4.2: Contact angles of sessile water drops (Milli-Q™ water) on a hydrophobic and hydrophilic surface.	53
Table 4.4.1: Contact angle and surface energy statistical summary	54
Figures 4.4.3 and 4.4.4: Box-plot graphs of contact angle and surface energy	55
Figure 4.5.1: Contact angle vs. time graph of NaCl solution on (Gr).	56

Table 4.5.1: Contact angle and interactive molecular surface energy statistical summary for droplets of NaCl solution for different materials.	57
Figure 4.5.11: Box-plot graph depicting the range and variability and standard deviation of contact angles of droplets of NaCl solution vs. material group.	58
Figures 4.6a and 4.6b: AFM scan results for a borosilicate glass coverslip (Gr).	59
Figures 4.6c-h: AFM scans for surfaces: (c, d) TO, (e, f) TO+B and (g, h) P.	60
Figures 4.6i-n: AFM scans for surfaces: (i, j) N, (k, l) N+B and (m, n) P+B.	61
Figures 4.6o-t: AFM scans for surfaces: (o, p) NO, (q, r) NO+B and (s, t) P+A.	62
Table 4.6: Surface roughness results expressed as Ra.	63
Figures 4.7a-f: (a,b) Histogram traces of the stained neuronal cultures.	66
Figure 4.7g: Grouped bar graph of the normalised cumulative frequency data.	67
Figure 4.10.2: Contact angle of vs. time graph of NaCl solution on (P+A).	75
Figure 4.10.3: Contact angle vs. time graph of NaCl solution on (P).	75
Figure 4.10.4: Contact angle vs. time graph of NaCl solution (P+B).	76
Figure 4.10.5: Contact angle vs. time graph of of NaCl solution on (TO).	76
Figure 4.10.6: Contact angle vs. time graph of NaCl solution on (TO+B).	77
Figure 4.10.7: Contact angle vs. time graph of NaCl solution on (N).	77
Figure 4.10.8: Contact angle vs. time graph of NaCl solution (N+B).	78
Figure 4.10.9: Contact angle vs. time graph of NaCl solution on (NO).	78
Figure 4.10.10: Contact angle vs. time graph of NaCl solution on (NO+B).	79
Figures 5.2.1a through 5.2.1e: Reticule layout for aperture printing	82
Figure 5.2.2: A 21x10 Focus-Exposure-Matrix (FEM) of the 2-μm feature.	82
Figure 5.3.2a: Curve adjustment graph for SEM images for the algorithm.	84
Table 5.3.2: Chronological list of pre-processing algorithm steps and associated SEM images for apertures I7 (high contrast) and G10 (low contrast).	85
Figure 5.4.3a: Graph of the radial distance (in pixels) from the centroid to the outline from 0 to 360° of a circular aperture (from Fig. 5.5.1h).	90
Figure 5.4.3b: Graph of the radial distance (in pixels) from the centroid to the outline from 0 to 360° of a square aperture (from Fig. 5.5.1d).	90
Figure 5.4.3c: Graph of the smoothed and original XY data set of a circular aperture	91
Figure 5.4.3d: Graph of the smoothed and original XY data set of a square aperture	91

Figure 5.4.3e: Graph of dr/dt vs. theta of a circular aperture	92
Figure 5.4.3f: Graph of dr/dt vs. theta of a square aperture	92
Figure 5.4.3g: Graph of d2r/dt2 vs. theta of a circular aperture (from Fig. 5.5.1h).	93
Figure 5.4.3h: Graph of d2r/dt2 vs. theta of a square aperture (from Fig. 5.5.1d).	93
Table 5.5.1: Acquired apertures from the 3-μm FEM of test wafers no. 1, 2 and 3.	95
Table 5.5.2: Acquired apertures from the 2-μm FEM of test wafers no. 1, 2 and 3.	95
Table 5.5.3: Acquired apertures from the 3-μm FEM of test wafers no. 1, 2 and 3.	96
Table 5.5.4: Acquired apertures from the 2-μm FEM of test wafers no. 1, 2 and 3.	96
Figure 5.5.13: Circularity error type-I vs. focus offset.	97
Figure 5.5.14: Circularity error type-I vs. exposure time.	97
Figure 5.5.15: Circularity error type-II vs. focus offset.	98
Figure 5.5.16: Circularity error type-II vs. exposure time.	98
Figure 5.5.17: Aperture diameter vs. focus offset.	99
Figure 5.5.18: Aperture diameter vs. exposure time.	99
Figure 5.5.19: Elongation vs. focus offset.	100
Figure 5.5.20: Elongation vs. exposure time.	100
Table 5.5a: Post-processed aperture SEM images, sorted in ascending order by circularity error type-II (CE-2) from 0.1481 to 0.2177.	101
Table 5.5b: Post-processed aperture SEM images, sorted in ascending order by circularity error type-II (CE-2) from 0.2203 to 0.3221.	102
Table 5.5c: Post-processed aperture SEM images, sorted in ascending order by circularity error type-II (CE-2) from 0.3244 to 0.8154.	103
Figure 5.5.22: Histogram of circularity error type-II (CE-2).	103
Figures 6.2.1: Aperture Evolution Block Diagram	109
Figures 6.2.2a through 6.2.2e – SEM images of cross sections of apertures	111
Figure 6.3.2a: 2nd degree bisquare fit to pixel coordinates for G7 left curve.	115
Figure 6.3.2b: 2nd degree bisquare fit to pixel coordinates for G7 right curve.	115
Figure 6.3.2c: 3rd degree bisquare fit to dx/dt and dy/dt for the G7 left curve.	116
Figure 6.3.2d: 3rd degree bisquare fit to dx/dt and dy/dt for the G7 right curve.	116
Figure 6.3.2e: Radius of curvature vs. Δt for the left black trace of aperture G7.	117
Figure 6.3.2f: Radius of curvature vs. Δt for the right black trace of aperture G7.	117
Figures 6.4.1a and 6.4.1b: Section analysis and surface profile for aperture B2.	119

Figures 6.4.1c and 6.4.1d: Section analysis and surface profile for aperture B3.	119
Figures 6.4.1e and 6.4.1f: Section analysis and surface profile for aperture B10.	119
Figures 6.4.1g and 6.4.1h: Section analysis and surface profile for aperture E7.	120
Figures 6.4.1i and 6.4.1j: Section analysis and surface profile for aperture F6.	120
Figures 6.4.1k and 6.4.1l: Section analysis and surface profile for aperture F11.	120
Figures 6.4.1m and 6.4.1n: Section analysis and surface profile for aperture G5.	121
Figures 6.4.1o and 6.4.1p: Section analysis and surface profile for aperture G7.	121
Figures 6.4.1q and 6.4.1r: Section analysis and surface profile for aperture J2.	121
Figures 6.4.1s and 6.4.1t: Section analysis and surface profile for aperture J10.	122
Figure 6.4.2a: Data profile and curvature analysis for the G7 right curve.	122
Table 6.4.2: Curvature analysis data summary.	123
Figure 6.7a: Data profile and curvature analysis (left curve of aperture G7).	127
Figure 6.7b: Data profile and curvature analysis (right curve of aperture B3).	127
Figure 6.7c: Data profile and curvature analysis (right curve of aperture B2).	128
Figure 6.7d: Data profile and curvature analysis (right curve of aperture B10).	128
Figure 6.7e: Data profile and curvature analysis (right curve of aperture E7).	129
Figure 6.7f: Data profile and curvature analysis (right curve of aperture F6).	129
Figure 6.7g: Data profile and curvature analysis (right curve of aperture F11).	130
Figure 6.7h: Data profile and curvature analysis (right curve of aperture G5).	130
Figure 6.7i: Data profile and curvature analysis (right curve of aperture J2).	131
Figure 6.7j: Data profile and curvature analysis (right curve of aperture J10).	131
Figure 7.2.2a: Electrical circuit diagram of patch device I.	135
Figure 7.2.2b: Theoretical capacitance of the bottom insulator CU vs. oxide thickness and the diameter of the area in contact with patch solution.	138
Figure 7.2.3: Cross-section of the process steps for device I.	140
Figure 7.2.4: Cross-section of device platform version I.	142
Table 7.2.5a: Intracellular patch solution for device testing.	143
Table 7.2.5b: Extracellular solution for device testing.	143
Table 7.2.5c: The electrical performance measures	144
Figure 7.2.5a: Current step and voltage traces for device A.	145
Figure 7.2.5b: I-V plots for device A, device B and the glass pipette.	145

Figure 7.2.5c: The voltage relaxation responses of device I.	146
Figure 7.3.2a: Electrical circuit diagram of patch device II.	148
Figure 7.3.2b: Theoretical access resistance RA vs. patch aperture length and diameter for device II.	149
Figure 7.3.3a: A 21x21 Focus-Exposure-Matrix (FEM) of apertures	151
Figure 7.3.3b: SEM image at 45° of a street cross-section sidewall	152
Figure 7.3.3c: Light microscopy image of aperture and backside cavity.	154
Figure 7.3.3d: Backside cavity with surrounding PDMS after curing.	156
Figure 7.3.3e: Cross-section representation of the process steps for device II.	158
Figure 7.3.3f: Patch-clamp II mask layout on 4" wafer (7-mm square devices).	159
Figure 7.3.4: Cross-section of device platform version I.	160
Figure 7.3.5: An embedded planar patch-clamp electrode in silicon (device B10).	161
Table 7.3.6: Electrical parameters for device II and pipettes.	163
Figure 7.3.6a: Current-step response for device H6.	164
Figure 7.3.6b: I-V plots for devices G8, H6 and I10.	164
Figure 7.3.6c: Relaxation responses for patch chip version II	165
Fig 7.3.6d: Box-plot graph showing the range and distribution of time responses from three glass pipettes and six ver. II patch devices.	165
Figure 7.3.6e: Bode-plot of the amplitude attenuation in dB for device II	166
Figure 7.3.6f: Bode-plot of the phase offset for device II	166
Table 7.3.7: Mean roughness Ra and std. dev. for 10 ver II devices.	167
Table 7.3.8: Microfabrication yield statistics for device II.	168
Figure 7.4a and 7.4b: Seal-resistance recordings.	170
Figure 7.4c: The visualisation of patch-clamping on a snail neuron with device II.	171
Table A.2.1: Processing steps and SEM images for aperture Athermal.	189
Table A.2.2: Processing steps and SEM images for aperture Apecvd.	190
Table A.2.3: Processing steps and SEM images for aperture Bthermal.	191
Table A.2.4: Processing steps and SEM images for aperture Bpecvd.	192
Table A.2.5: Processing steps and SEM images for aperture C1,thermal.	193
Table A.2.6: Processing steps and SEM images for aperture C2,thermal.	194
Table A.2.7: Processing steps and SEM images for aperture C1,pecvd.	195
Table A.2.8: Processing steps and SEM images for aperture C2,pecvd.	196

Table A.2.9: Processing steps and SEM images for aperture D1,thermal.	197
Table A.2.10: Processing steps and SEM images for aperture D2,thermal.	198
Table A.2.11: Processing steps and SEM images for aperture D1,pecvd.	199
Table A.2.12: Processing steps and SEM images for aperture D2,pecvd.	200
Table A.2.13a: Processing steps and SEM images for aperture E1,thermal.	201
Table A.2.13b: Processing steps and SEM images for aperture E1,thermal.	202
Table A.2.14a: Processing steps and SEM images for aperture E2,thermal.	203
Table A.2.14b: Processing steps and SEM images for aperture E2,thermal.	204
Table A.2.15: Processing steps and SEM images for aperture E1,pecvd.	205
Table A.2.16 Processing steps and SEM images for aperture E2,pecvd.	206
Table A.3.1: Thermal oxidation parameters	207
Table A.3.2: Photoresist parameters for thin coating (1.18 μm)	207
Table A.3.3: Photoresist parameters for medium coating (1.4 μm)	207
Table A.3.4: Photoresist parameters for thick coating (3.2 μm)	207
Table A.3.5: Ashing parameters	208
Table A.3.6: Si3N4 deposition parameters	208
Table A.3.7: Development parameters	208
Table A.3.8: Reactive ion etching parameters	208
Table A.3.9: SiO2 deposition parameters	209
Table A.3.10: Boron deposition parameters	209
Table A.3.11: Deep Silicon Etch Parameters for ICP Configuration.	209

Abbreviations

General Abbreviations

HVEM -- High-Voltage Electron Microscopy

PECVD – Plasma Enhanced Chemical Vapour Deposition

LPCVD – Low Pressure Chemical Vapour Deposition

MEMS – Micro-Electro-Mechanical-Systems

PDL – poly-D-lysine

SF_6 – sulphur hexafluoride

LF – (Dielectric) Loss Factor

LSV – liquid-solid-vapour

ECM – extracellular matrix

SNR – Signal to Noise Ratio

HMDS – hexamethyldisilazane

FEM – focus-exposure matrix

ICP – inductively coupled plasma

IPA – isopropyl alcohol

FIB – focused ion beam

BESOI – bonded and etched back silicon on insulator

PDMS – polydimethylsiloxane

CE-1 – circularity error type-I

CE-2 – circularity error type-II

POD – PECVD oxide deposition

ThOx – wet thermal oxidation

Material Abbreviations

TO – thermal oxide

TO+B – thermal oxide with boron deposition

N – silicon nitride

N+B – silicon nitride with boron deposition

P – PECVD oxide

P+B – PECVD oxide with boron deposition

P+A – PECVD with annealing at 1100°C.

NO – oxidized silicon nitride

NO+B – oxidized silicon nitride with boron deposition

Gr – borosilicate glass w/rinse

G – borosilicate glass

G+PLrd – borosilicate glass w/rinse and PDL (in dish)

G+PLd – borosilicate glass w/o rinse and PDL (in dish)

G+PLrt – borosilicate glass w/rinse and PDL (in centrifuge tube)

G+PLt – borosilicate glass w/o rinse and PDL (in centrifuge tube)

1 Introduction

The expansion of research in neuroscience in the last 20 years has extended current understanding of consciousness, perception, and decision making processes in the brain [1]. The central nervous system carries out these complex processes using continuous synaptic activity and spiking events between millions of neurons. Neuronal networks facilitate distinct and important behavioural patterns and rhythms of the organism [2]. However, the current understanding of how these neuronal networks in the brain facilitate the mental and physiological attributes of the organism is incomplete. There are many ongoing investigations into the underlying molecular and sub-cellular mechanisms that affect neuronal computation. Bio-physical models and simulations of these neuronal networks (and neuronal properties) have been researched extensively [3]. Cellular mechanisms may affect firing thresholds and patterns of neurons and moderate network activity [4]. However, electrophysiological recordings have not yet identified the information processing and computation of sub-threshold activity that constitute a living neuronal network that these biophysical models suggest. Neurological studies are limited by the resolution at which neuronal activity can be detected for a given location and epoch. To date, only synaptic activity of pairs of neurons in living neuronal networks has been achieved [5].

The investigation into the information processing, synaptic activity and neuronal computation of *in-vitro* living neuronal networks may give support to a biophysical model of computational neuroscience. This can only be achieved if single synaptic events can be mapped to many individual neurons of known morphology. The location of active synapses and the observation of cellular morphology are possible from neuronal cultures. The principles of network behaviour and models of these systems from vertebrate and invertebrate neurons might mimic conditions found in the brain. It

is likely that the synaptic connections of two-dimensional structures will be found to be similar to the neural connections with the organism.

Thus, the study of dissociated neuronal cultures *in-vitro* promises an advancement of understanding of network behaviour. Specifically, the principles of neuronal computation performed in a network can be investigated. Also, certain neuropathogenic disorders such as Alzheimer's disease, epileptogenesis [6] and schizophrenia may be modelled in an *in-vitro* neuronal network. Also, the real-time computation of neurons and its influence in a network could be compared to current models like Hebbian and Antisymmetric Hebbian learning [7;8]. Synaptic and network formation during development may be studied by control of the environmental conditions. Also, the study of these functional networks may help determine to what extent the brain is "hard-wired". Current research and intuition suggests that the nervous system has inherently "plastic" structures in which the continuous monitoring of the use and disuse determines which connections will be the weakest and the strongest, a process loosely called synaptic "learning" [9].

Bio-electronic devices are routinely utilised in the study of neuroscience. There are two fundamental ways of investigating neuronal properties using microelectronics: (a) hardware implementation and software modelling of neuronal behaviour and theory (i.e. artificial neural networks) and (b) coupling of living neurons/tissue to electronic circuitry (i.e. patch-clamping and multi-electrode array (MEA) devices). To allow bidirectional communication between an electrical circuit and a living cell, it is necessary to establish a coupling of neuronal activity to an electrical signal. Hence, neuronal activity would produce a change to the electrical signal, and electrical voltages and currents would produce synaptic and action potentials. How this coupling is achieved is vitally important for increased signal-to-noise ratio, probability of coupling, minimisation of leakage current and overall response of the system.

Studies of ionic conduction of nerve cells, particularly the pioneering work of Hodgkin, Huxley and Katz, have greatly advanced the understanding of the ionic nature of neuronal function [10-13]. Many studies of neuronal activity and network behaviour use conductive electrodes to detect individual electrical signals. Advances in cell culturing

and multi-electrode device fabrication have provided an additional pathway to the detailed study of living neuronal networks [14-16]. To date, many attempts to investigate *in-vitro* network activity involve multiple planar surface electrodes to link electrical connections to nerve cells, coupled resistively or capacitively to the neuron for extracellular measurements [17].

For example, multi-electrode-array (MEA) devices made with up to 60 channels (electrodes) or more offer a significant bandwidth of data extraction to distinguish network behaviour (e.g. circadian rhythms and differentiating firing patterns in dissociated cell cultures of hippocampal neurons) [18;19]. Also, long-term neurological studies can be conducted for periods up to months. However, using these devices, it is difficult to map and isolate single synaptic events to individual cells and synapses. Typically, only spiking events are measured. Other evidence suggests this approach has problems regarding cell/substrate adhesion and the proximity between the nerve cell and electrode [20]. Furthermore, it has been suggested that neurons do not form ion channels well along the contact surface, decreasing the quality of electrode recordings [21].

At the time of writing, there is new academic and commercial interest in integrating MEA and patch-clamp technology into a single planar-clamp device, featuring a novel hybrid neuro-electronic coupling [22]. Such a device would retain the advantages of high bandwidth extraction and precision patching measurements: including high seal resistance (1-10 GΩ), simultaneous recordings from a dense region of interest, single-channel resolution and direct observations/mapping of neuronal circuits. This configuration would allow, for example, studies of network behaviour and computation produced by synaptic activity or noise injection only theorized by mathematical models [23]. Also, this hybrid device would have the advantage of being operated by technical personnel other than a trained specialist in the field of patch-clamping.

Patch-clamping presents some problems and disadvantages compared to MEA recordings that need to be addressed. For example, the duration of a patch-clamp recording is limited due to the dialysis of intracellular medium. Typically, recording times up to six or more hours can be expected, and perforated patch-clamping may

extend this time limitation only slightly. Therefore, it would not be feasible to use integrated patch array recordings for extended recording times currently offered by MEA devices. Generally, examining the neuronal activity of one, two or three patched neurons is not an easy task. Positioning patch pipettes is difficult because the positioning devices are bulky and are sensitive to vibration from the surrounding environment. To date, up to three neurons have been recorded simultaneously using conventional sharp or patch micropipette recordings to study synaptic transmission [24].

To fabricate planar patch-clamp microstructures in silicon-based platforms, the use of semiconductor processing techniques with the incorporation of MEMS technology (Micro-Electro-Mechanical-Systems) is a logical choice. These technologies are capable of fabricating a multitude of geometric configurations in the bulk substrate, including: aperture openings, membranes and micro-channels. The mass production of patch electrodes embedded into silicon devices has advantages over traditional glass pipette blowing and making. For example, high-throughput useable devices would allow patch-clamping of many cells in a short period of time.

Today, single patch-clamp microstructures are being produced in industry primarily for pharmacological studies. The high throughput is extremely desirable in drug screening and pharmacology, because many cells with specific receptor expression need to be pooled. Also, a qualified and trained scientist is not needed with these devices, where a technician can easily run a robotic machine that performs patch-clamping of cells automatically. The major companies specialising in patch clamping technology at the time of print include: Cytocentrics© (http://www.cytocentrics.com); Axon Instruments© (now a subsidiary of Molecular Devices Corp.); Aviva Biosciences© (http://www.avivabio.com); MultiChannelSystems© (http://www.multichannelsystems); Sophion Biosciences© (http://www.sophion.dk) and Nanion Technologies© (http://www.nanion.de). Today, commercial machines include the: PatchExpress™, Q-Patch™ [25] and Roboocyte™ [26]. These platforms are offered from: Axon Instruments©, Sophion© and Multi-Channel-Systems© respectively. Currently, Nanion Technologies© is using glass substrates as opposed to silicon, in the hope that improved electrode performance can be achieved.

This study investigates the hypothesis that the important aspects of the patch-clamp technique can be miniaturised and scaled down to micron-size silicon-based microstructures. The work will strive to emulate the important characteristics that this electrophysiological method offers to extend the study of network behaviour of *in-vitro* cell cultures. The study focuses on the investigation and experimentation of a single integrated patch-clamp electrode to simplify the testing and modifications of the design prototype. The answer to this hypothesis may depend upon the type of cell used and the physical characteristics (aperture diameter) of the microstructure. This study concentrates on the use of snail neurons from *Lymnaea stagnalis* for patch-clamping and rat cortical neurons for cell culturing. Whole-cell patch-clamp recordings of these neurons have been achieved and published [24;27-30]. The silicon microstructure characteristics sought were based upon those of standard borosilicate patch pipettes for use in patch-clamp recordings.

The outline for this thesis is highlighted by chapter in the points below:

- Chapter 1 – This chapter discusses the background and motivation to the study of neuronal function. It introduces the types of study currently undertaken, advantages and limitations thereof, including the use of *in-vitro* neuronal cultures and MEA devices. The possibility of fabricating an array of patch-clamp microstructures is introduced.

- Chapter 2 – This chapter discusses the background and theory of patch-clamping. The relevant electrical diagrams are given, including a critical assessment and literature search of patch-formation theory. The critical factors of patch-formation are identified.

- Chapter 3 – This chapter outlines the essential techniques for cell culturing and snail preparations. The techniques include: immunohistology, dissociated culture preparation and assessment techniques for culture health and vitality. The patch-clamp recordings were taken by Dr. John Curtis as part of the team project.

- Chapter 4 – This chapter focuses on surface analysis measurements, including surface energy by wettability experimentation, surface roughness by atomic force microscopy, and tests on cell adhesion in culture. The concept of wettability is introduced, and theories are explained to correlate preferential cell growth to various surface types. The cell culture preparation and analysis was performed by Dr. John Curtis as part of the team project.

- Chapter 5 – This chapter introduces the development of a new algorithm to quantify the circularity of an object. The chapter includes results on the algorithm tested on fabricated apertures in Chapter 7. Two types of circularity are assessed.

- Chapter 6 – This chapter focuses on the curvature profiling of the aperture. It includes the developed algorithm to find the locate and quantify of curvature from an AFM dataset. It explains how de-focused lithographic exposure and process parameters alter the curvature characteristic of the microstructure.

- Chapter 7 – This chapter discusses the microfabrication and assessment of two versions of the patch-clamp microstructure. The fabrication steps and platform developments and given. The electrical characteristics are given for both devices and compared to standard borosilicate glass pipettes.

- Chapter 8 – This chapter highlights the overall conclusions formed from this work.

- Appendix – The scripts used in Chapter 6 are given in A.1, along with the SEM images of the apertures in A.2. The process parameters are located in Appendix A.3.

2 Theory and Background of Patch Clamping and Seal Formation

2.1 Introduction to Patch Clamping

2.1.1 History and Background

To undertake a design of a microstructure to facilitate "gigaseal" formation successfully at the neuron-silicon junction, the most logical approach is to investigate how these seals are formed with glass microelectrodes using the patch clamp method introduced by Sackmann and Neher in 1976 [31]. Once a theoretical understanding is established, an attempt can be made to create microstructures with properties supporting theoretical claims in forming seals to obtain highly resistive ($\geq$1 GΩ) electrophysiological recordings from neurons using silicon devices. If such devices are realisable, it is conceivable that many recording sites could be integrated on a single planar-patch chip for multi-channel recording.

The patch clamp method using glass microelectrodes has been practiced extensively since its invention. The technique is straightforward and very well documented [32-34]. As originally developed in 1976, the patch clamp method enabled the first recordings to be made of pico-amp resolution of ion conduction of individual ion channels [31]. Patch electrodes have tip diameters small enough (typically 1-5μm) to measure ion conduction of single cells. An electrode is positioned appropriately by pressing the pipette tip against a cell, typically called "on-cell", or "loose-cell" patching. Henceforth, this configuration will be referred to "loose-cell" in this work (see Figure 2.1.1a). This process introduces a resistive seal of approximately 50 MΩ between electrode and the cell bath. Current traces feature deflections of 5-10 pA over periods of approximately 10-50 ms. The deflections were interpreted as single-channel events opening and closing. The difficulty in interpreting data in this patch configuration was limited by the background noise level of the measured ion conduction. Furthermore, the quality of

these recordings is dependent on many factors throughout the patch clamp electrical circuit (including the headstage circuitry, amplifier equipment, and quality of the electrode). Assuming all component circuitry to be of sufficient quality, the leakage current between cell and electrode is a primary source of low signal input (this applies to many types of electrophysiological recordings in general).

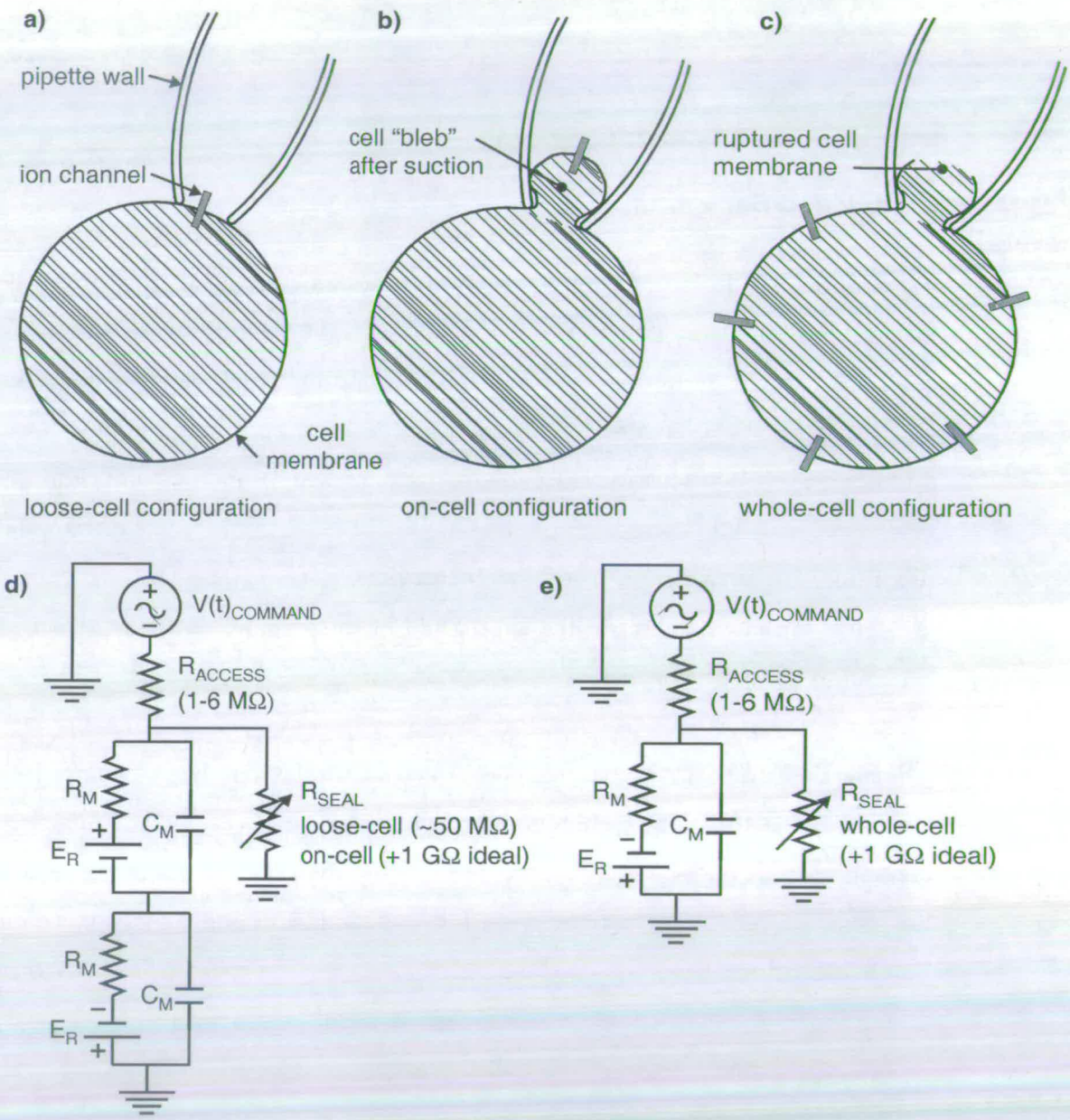

Figure 2.1.1: Patch-clamp configurations and corresponding electrical circuit diagrams. Three configurations of the patch-clamp method–loose-cell, on-cell and whole-cell–are depicted in figures (a), (b) and (c) respectively. Electrical circuit diagrams for 1) loose-cell or on-cell and 2) whole-cell configurations are given in figures (d) and (e) respectively. Electrical components included in the circuits are: membrane resistance (R_M), resting potential (E_R), membrane capacitance (C_M), seal resistance (R_{SEAL}) and pipette access resistance (R_{ACCESS}). The membrane is modelled as an RC parallel circuit.

In 1980, the patch clamp method was improved by establishing a closer and more stable contact between pipette and cell by applying slight negative pressure (0.02-0.03 atm) inside the pipette [35]. The pressure gradient is able to suck a portion of the cell, or "bleb", into the pipette tip [36]. (This configuration is called "on-cell," see Figure 2.1.1b). The tighter contact reduces the leakage current between the electrode and cell-bath, thereby decreasing the background noise significantly. The seal resistance can be any value up to 100 GΩ, and thus termed a "gigaseal." This discovery has led to higher resolution recordings of ionic current (especially useful in single-channel recording), and the ability to measure the total ionic conduction by controlling the intracellular voltage potential by means of voltage clamping in the whole-cell configuration [35] (see Figure 2.1.1c).

2.1.2 Electrical Circuitry of Patched Cell

A patch configuration takes the form of an RC electrical circuit. The tip of the glass pipette is positioned in the cell bath, normally set to ground voltage potential. A small capacitance $C_{pipette}$, is introduced between the patch and extracellular solutions from the pipette wall, typically around 5-10 pF. (The thickness and properties of the glass and/or the application of Sylgard™ will change this capacitive value. A capacitance compensation circuit can be utilised to reduce the circuit capacitance to a minimum [32].) A voltage $V(t)_{command}$ is applied to inject current inside the cell (provided that a proper whole-cell configuration is achieved and the seal resistance R_{seal} is large). The acceptable cell membrane capacitance is estimated at 1 $\mu F/cm^2$, published as 0.81 $\mu F/cm^2$ in [37].

A membrane potential is established from the ionic concentration and electrical gradients between the interior and exterior of the cell. The primary ions that influence the membrane potential at any time are K^+, Cl^- and Na^+. The membrane potential for individual ions can be quantified by the Nernst equation below [38].

Equation 2.1.2a

$$E_{ion} = \frac{R \cdot T}{Z \cdot F} \ln \frac{[ion_concentration]_{exterior}}{[ion_concentration]_{interior}}$$

where R is the universal constant (8.314 Joules/(mole x K)), T is the absolute temperature in degrees Kelvin, Z is the charge number of the ion, and F is the Faraday constant (96,500 C° / mole).

The resting potential is typically around -60 mV, but can range from -40 to -75 mV. The membrane voltage potential is constantly changing owing to the opening and closing of selective ion channels embedded in the lipid-bilayer. These mechanisms account for action potentials, excitatory and inhibitory post-synaptic responses. Patch clamping allows the observation of these events, and also of single ion-channel events. The Goldman-Hodgkin-Katz equation can be used to quantify the membrane voltage of a neuron. The equation quantifies the membrane voltage potential by combining the Nerst equation from all primary ions in signal transduction, given below [38]:

Equation 2.1.2b

$$V_m = \frac{R \cdot T}{F} \ln \frac{P_K[K^+]_{ext} + P_{Na}[Na^+]_{ext} + P_K[Cl^-]_{ext}}{P_K[K^+]_{int} + P_{Na}[Na^+]_{int} + P_{Cl}[Cl^-]_{int}}$$

where P_K, P_{Na} and P_K are permeability values for the respective ions at any given time.

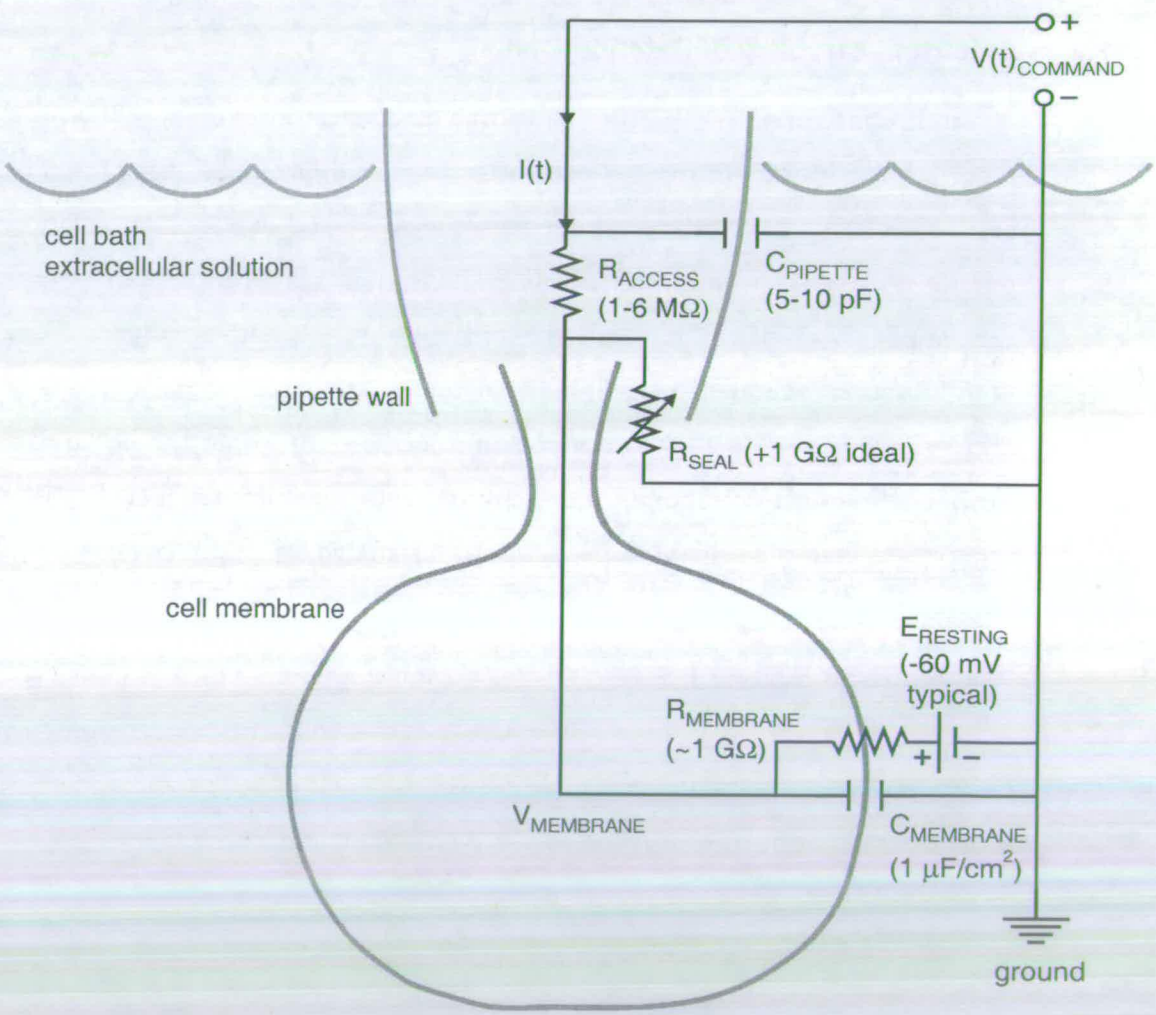

Figure 2.1.2: Electrical model and schematic diagram of a patched neuron in the whole-cell configuration with pictorial detail of each component location.

2.2 Review of Modern Patch Clamping Methods with Planar Devices

Patch-clamping has evolved with modern advances in microfabrication technology. For example, modern implementations of glass pipettes have been fabricated in MEMS microstructures since the year 2000. These recent advancements have been critically reviewed and analysed. Many discrepancies were noted, including: (a) the type of cell or vesicle used; (b) the value of seal resistance obtained; and (3) the type of surface used. To date, no patch recordings from a living neuron from microstructures have been achieved.

In the year 2000, N. Fertig, J. C. Behrends *et al.* published a paper detailing a microstructure used to stabilise a rat striatum cell for electrophysiological recording purposes [39]. The structure consisted of a backside silicon etched cavity and a free-standing suspended 0.12-μm thick Si_3N_4 membrane (see Fig. 7.2.2a for a pictorial example). No detailed recordings were given in the study, suggesting that a gigaohm seal is not achievable with a thin layer membrane and/or the use of rat striatum cells used in the experiment. We speculate that the thin silicon nitride layer does not support gigaseal formation from the critical analysis of patch theory in Section 2.3.3.

The same year, a study was peformed on a similar microstructure with giant lipid vesicles by C. Schmidt, M. Mayer and H. Vogel [40]. Here, the surface was modified chemically with the addition of poly-L-lysine or 4-aminobutyldimethylmethoxysilane, creating an excess of positive charge on the surface. It was hypothesised that positive charges resulted in formation of electrostatic bonds with the net negatively charged lipid vesicle. Highly resistive seals up to 200 GΩ were obtained. This was the first publication to report successful measurement single ion-channel recordings from biological tissue on a planar microfabricated device. It is particularly noted that no living cells or neurons were tested, only lipid vesicles.

The electrical performance and microstructure of the planar device was improved in the year 2002 by N. Fertig, Ch. Meyer *et al.* with the use of glass material [41]. Glass properties, discussed in Section 2.4.1, include a smaller dielectric constant, $\varepsilon_Q = 3.9$, compared to silicon $\varepsilon_Q = 10$. The patch aperture length was extended to approximately 80 μm by thinning the glass by HF etching. A single gold atom from a linear accelerator

was used to form a cylindrical aperture. The capacitance of the device was measured at ~1 pF, smaller and therefore superior to the capacitance values of the silicon microstructure discussed above. Stable gigaohm seals up to 100 GΩ and single ion-channel events were observed when patching with lipid vesicles.

The first whole-cell recordings from a planar device were obtained from this glass microstructure discussed in the preceding paragraph by a study conducted by N. Fertig, R. Blick and J. Behrends [42]. CHO cells [43] were tested and seals (not gigaseals necessarily) were obtained (the value of the seal resistance was not given). In this experiment, whole-cell configuration patch recordings were achievable by positioning and sucking the cell into the glass aperture made by the gold ion beam. Ionic current was recorded from Ca^{2+} -activated K^{+}-channels. Also, it was possible to block the current by application of charybdotoxin to the extracellular medium. This experiment gives support for the ability to conduct pharmacological studies.

From refinements of the same technique discussed above, a more detailed study was published detailing on-cell patch recordings with CHO cells [44]. Single-ion channel events were recorded from BK-type potassium channels. Seal resistances were typically found to be between 2-5 GΩ, and occasionally up to 25 GΩ. It is speculated that whole-cell recordings, as opposed to on-cell recordings, may be more difficult to achieve using these microstructures.

In the year 2002, K. Klemic and F. Sigworth were able to form gigaseals with micro moulded planar electrodes made from a silicone elastomer polydimethylsiloxane (PDMS) [45]. To form the patch aperture, a conventional glass patch pipette was pulled using standard pulling techniques and used as a master mould. Next, PDMS was poured around the pipette and cured. After curing, the glass pipette was removed, and the PDMS mould was sliced perpendicularly at 200-μm steps. A slice revealing the opening of the aperture was selected and positioned on a solid glass substrate with a hole punch. The hole allowed the filling of the bottom cavity with patch solution and forms an electrical circuit. Gigaseals ≥1 GΩ were obtained in the "on-cell" configuration with *Xenopus* oocytes 0.7-1 mm in diameter. To achieve gigaseal formation, PDMS surfaces were subjected to an oxygen plasma for a duration up to 60 min @ 100 watts. This treatment increased the hydrophilicity of the surface (to be

discussed in Chapter 3). The change in hydrophilicity was found to be only temporary. However, it has been reported that permanent hydrophilic PDMS surfaces can be obtained [46]. Seven of the 13 devices tested and subjected to oxygen plasma achieved gigaseals; and zero out of four devices not subjected to oxygen plasma did not achieve gigaseal formation.

A review of progress in planar patching with microstructures was published in 2002 by F. Sigworth and K. Klemic [47]. They speculated that difficulties in patching onto cells with free-standing Si_3N_4 membranes exist because of the sharp sidewalls and insufficient contact area for proper seal formation. It was hypothesised that sub-gigaseal seal resistances is due from surface roughening after HF etching the amorphous quartz substrate. We speculate that roughening increases the ability for ions to "tunnel" more easily between the cell membrane and aperture wall (discussed in more detail in Section 2.3.4).

Finally, a modified version of a silicon based planar patch electrode was produced by B. Matthews and J. W. Judy and reported in 2003 [48]. Here, the thin silicon nitride layer was replaced by a 30-μm thick bulk silicon layer. This was achieved by chemical wet-etching a V-shaped groove from the backside of the wafer and terminating the etch process at a precise time, thereby leaving a portion of the silicon bulk unetched at the topside. A 3-μm diameter patch aperture was formed by deep silicon etching from the topside. The study did not report on any attempts at electrophysiological recording. This lengthened patch aperture resembles device version II that was fabricated in this project (see Section 7.3).

2.3 Critical Assessment of Patch Formation Theory

2.3.1 Theory of Seal Formation in Patching

For engineering purposes, it is important to understand what causes a high-seal resistance between glass and pipette. Unfortunately at the time of writing, the exact nature of gigaseal formation is not entirely understood, although various theories have been put forward to explain it [36;49-52]. These theories do not all agree about the exact nature of the sealable region. Since the knowledge of the phenomenon of gigaseal

formation is incomplete, a critical review of the possible theories associated with it is necessary.

Knowledge of the separation distance between cell membrane and glass pipette can contribute to a theory for gigaseal formation [53]. In 1983, Corey and Stevens developed a mathematical model to solve for the separation distance between cell membrane and glass (discussed in further detail in Section 2.3.3. This separation distance was calculated to be $H \leq 10$ Å, and approximated down to 1 Å (atomic dimensions) for seal resistances ≥ 10 GΩ [49]. From this atomic scale distance, it was suggested that chemical bonding between the glass surface and lipid bilayer accounts for this close surface apposition. [49].

However, in 1984, Sachs performed a series of measurements on patches using experimental techniques for seal resistance, noise characteristics and ion conduction of channel events [51]. A new model was presented that accounted for these observations. According to this model, small ionic pathways are present between glass and the lipid bilayer. Sachs theorised that no chemical bond occurs between membrane and glass, unlike Corey and Steven's postulation [49]. However, it must be stressed that this theory does not rule out the possibility of chemical bonding present elsewhere in the sealable area. The absence of chemical bonding seems unlikely due to the high mechanical and electrical stability offered by the patch method.

During 1990, Sokabe and Sachs studied the detailed structure of patches using light microscopy [36]. They discovered that the portion of the cell sucked into the pipette is not just membrane, but also contains cytoplasm, organelles and vesicles. Once a seal is formed, positive pressure can decrease the length of the patch significantly without the loss of a seal. They suggested that the high-seal resistance is distributed throughout the length of the patch and that the seal resistance per unit length is very high.

In 1991, a technique to study the structure of the patch in greater detail was made possible by freeze fixating a patch cell inside a glass pipette and then performing a high-voltage electron microscopy (HVEM) analysis on the specimen [52]. Despite the enhanced detail that HVEM offered and advances in freezing techniques, a measurement on the separation distance between glass and membrane was

unachievable. The same year, Sokabe, Sachs and Jing performed an analysis of time-lapse photography of the patching process using light-microscopy [50]. This information supported a theory that, during gigaseal formation, the lipid bilayer moves up the glass pipette while a separate sealable region remains stationary. It was suggested that membrane proteins attach to the glass, or "denature", and anchor and support the lipid to move up the pipette [50]. However, because highly resistive ($\geq$1 GΩ) patch-clamping onto phospholipids is possible, this data cannot be taken to imply that membrane proteins are necessary for highly resistive seal formation. It may be possible that chemical bonding to either membrane protein or the lipid bilayer can form and maintain gigaseals. Alternatively, a wholly new explanation may be required to model the patching process.

2.3.2 Application of gigaseal formation theory to microstructures

All the theories of gigaseal formation mentioned above indicate the use of a material of high surface energy (such as glass, to be discussed in Chapter 4), even though the phenomenon is not entirely understood. However, one study in 1989 by P. Coleman and R. Miller indicated that hydrophobic pipette surfaces (produced by dipping in hexamethyldisilizane solution) were able to form gigaseals, without the use of fire-polishing the tip [54]. Chemical bonding (including any denaturing of proteins) may play a significant role in seal formation. If this is true, the surface chemistry will greatly influence what types of interactions and forces occur. It was shown that the addition of a high concentration (10 mM) of Ca^{+} to the extracellular solution improves the probability of patch formation [55]. Therefore, high-energy surfaces may promote salt-bridge formation between cell membrane and glass (see Section 2.4.2). Furthermore, high-energy surfaces, despite the formation of highly resistive seals, may contribute to the great mechanical and electrical stability involved in tightly patched cells. It is plausible that low-energy surfaces such as PDMS [56] (γ=21 dynes/cm; cited in [57] p.2672) will decrease the probability of seal formation in the desirable >1 GΩ range [45].

The following paragraphs present a critical review of a biophysical model of seal formation for the application of engineering patch microstructures on silicon planar devices. Here, it is critical to examine the physical characteristics of the patch electrode

in conjunction with the different biophysical models of gigaseal formation already outlined. For engineering applications using MEMS, it is critically important to estimate a sufficient tip length L to facilitate gigaseal formation.

2.3.3 Electrochemical and Biophysical Model of Seal

The input (access) resistance of a glass microelectrode is determined by the tip shape and diameter. Usual values are between 1-4 MΩ [58]. In practice, however, the access resistance can be any value up to 10 MΩ. Close proximity between the cell membrane and an appropriate amount of glass surface reduces the leakage ion conduction between the pipette patch solution and bath solution (this leakage value is also dependent on ion concentration gradients of bath solution and pipette). This resistive pathway can be modelled as a conductor inside the glass microelectrode. Generally, the resistance R of a fluid of conductivity ρ through a known area $A_{conduction}$ (a width W multiplied by a height H) and length L is given by the following equation:

Equation 2.3.3a

$$R = \frac{\rho \cdot L}{A_{conduction}}$$

Thus, the resistivity of the seal is proportional to the resistivity of the patch solution and length of the conductor (tip shape), and inversely proportional to the cross-sectional area of ionic flow. A typical 150 mM saline patch solution, for example potassium chloride (KCl) solution, has a resistivity of ρ = 51 Ohm · cm at room temperature [53]. For the application of patching, a schematic diagram is given outlining the physical geometry of the seal, shown in Figure 2.3.2.

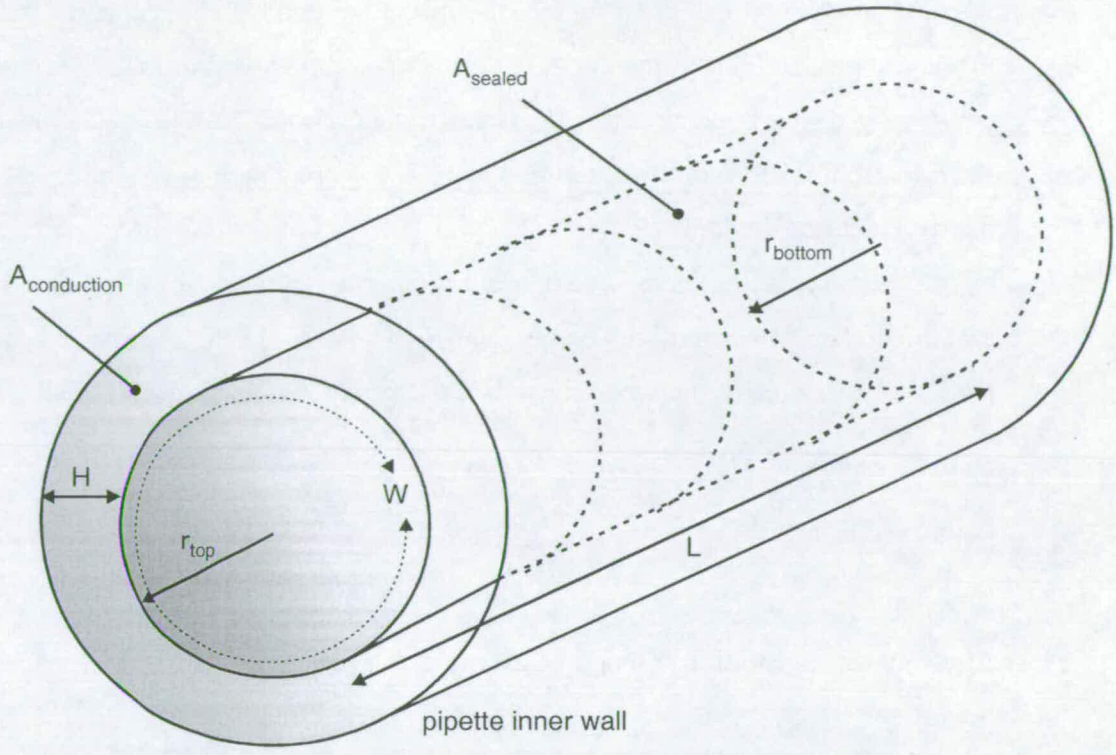

Figure 2.3.2: Cross section of patched cell membrane inside pipette inner wall. The key is as follows: *L* is the length of the patched membrane, *W* is the circumference of the patched membrane, *H* is the separation distance between the membrane and inner wall, $A_{conduction}$ is the area of the ionic pathway, A_{sealed} is the area of the patched membrane, r_{top} and r_{bottom} are the radii of the membrane at the tip of the pipette and point extruded into the pipette.

If the cylindrical sealed area A_{sealed} is uniformly distributed around the axis of the pipette, knowledge of the separation distance H (distance between membrane and glass) can be useful in approximating a sufficient patch aperture length L. A_{sealed} is governed by the equality L (the length of isolated lipid-bilayer) times W (the average circumferential width of the pipette tip). The width W is equal to $2 \cdot \pi \cdot r_{ave}$. Thus, a useful substitution can be made and Equation 2.3.3a can be modified to produce Equation 2.3.3b:

Equation 2.3.3b

$$R_{seal} = \frac{\rho \cdot L}{W \cdot H} = \frac{\rho \cdot L^2}{A_{sealed} \cdot H}$$

Previous studies have approximated the sealed area of patched cells. For example, it is possible to form a 2 GΩ patch seal by isolating a section of spherical rat muscle cell [53]. It is assumed that the properties of these cells (for purposes of patching, i.e. membrane properties) are similar to neuronal cells. For one experiment, the patch length was 3.75 μm as measured from the top hemisphere of the membrane to the tip

opening (the actual length of membrane in contact with glass is approximately 3 μm) inside the pipette [53]. Equation 2.3.3b can be modified to find the separation distance between glass and membrane. The method described here (outlined elsewhere) is rewritten to introduce an engineering perspective on patching in general (glass and novel microstructures) [49]. Taking into account the geometry of this pipette (a general geometry for patch pipettes), we can model the volume of the isolated cell as a sectioned cone with two slices perpendicular to its axis. Using this model, the equation for the surface area of the lipid-bilayer in close proximity with the glass walls (A_{sealed}) is:

Equation 2.3.3c

$$A_{sealed} = 2\pi \cdot (\frac{r_{top} + r_{bottom}}{2}) \cdot L$$

Applying this equation to the above example, the sealed area of the bleb is calculated to be:

$$A_{sealed} = 2\pi \cdot (\frac{(1.25\mu m + 0.5\mu m)}{2}) \cdot (3\mu m) = 16.49\mu m^2$$

The seal resistance in this example was approximately 2 GΩ. Therefore, the equation can be solved for the surface separation H for the given patch resistance. Solving for H, the equation becomes:

Equation 2.3.3d

$$H = \frac{\rho \cdot L^2}{A_{sealed} \cdot R_{seal}} = \frac{(510 \times 10^3 \Omega \cdot \mu m) \cdot (3\mu m)^2}{(16.49\mu m) \cdot (2 \times 10^9 \Omega)} = 1.39 \times 10^{-4} \mu m = 1.39 Å$$

The surface-to-surface separation distance of this patched cell in a glass micropipette was calculated to be H = 1.39 Å. This example patch measurement was part of a larger study. After patching a total of seven spherical rat muscle cells with identical pipettes, the average value of A_{sealed} = 14 ± 5 μm^2 [53]. Assuming a seal resistance of 2 GΩ, the value of L is governed by the inequality in Equation 2.3.3e.

Equation 2.3.3e $$L \geq \frac{A_{sealed}}{(2\pi)\cdot(\frac{r_{top}+r_{bottom}}{2})} = \frac{(14\pm 5\mu m^2)}{(2\pi)\cdot(0.875\mu m)}$$

i.e. $$L \geq 2.55 \pm 0.91\mu m$$

A boundary can be set on H by inserting the calculated range of L into Equation 2.3.3d. Assuming the same pipette shape throughout the experiment with r_{ave} = 0.875 and seal resistance of 2 GΩ, the calculation is as follows:

$$H = \frac{\rho \cdot L}{W \cdot R_{seal}} = \frac{\rho \cdot L}{2\pi \cdot r_{ave} \cdot R_{seal}} = \frac{(510\times 10^3 \Omega \cdot \mu m)\cdot(2.55\mu m \pm 0.91\mu m)}{(5.50\mu m)\cdot(2\times 10^9 \Omega)}$$

i.e. $$H = 1.18\text{Å} \pm 0.42\text{Å}$$

Generally, the average separation distance of two hydrophilic surfaces (e.g. lipid and glass) under no external forces in saline solution is measured to be between 20-50 Å [59]. However, this separation distance is made considerably smaller in the patching process by applying negative pressure. Here, the bleb can be sucked into the pipette with the cell surface in much closer proximity to the interior walls. The separation distance (~1 Å) is of atomic-scale, as the above model suggests.

Thus, the dependence of newly formed electrostatic chemical bonds to form and maintain gigaseals, over the entire length of the patch, is supported by this small separation distance. To facilitate gigaseals in the range of (2-100 GΩ), the sealable area is made considerably greater (and therefore the length L of the patched membrane increases along the pipette), or the average separation distance is much less than H calculated in the previous example; or in theory it could be a combination of both phenomena. Figure 2.3.3 is a graph relating the length of isolated membrane as a function of seal resistance, assuming that H falls within the value of 1.18 Å ± 0.42 Å.

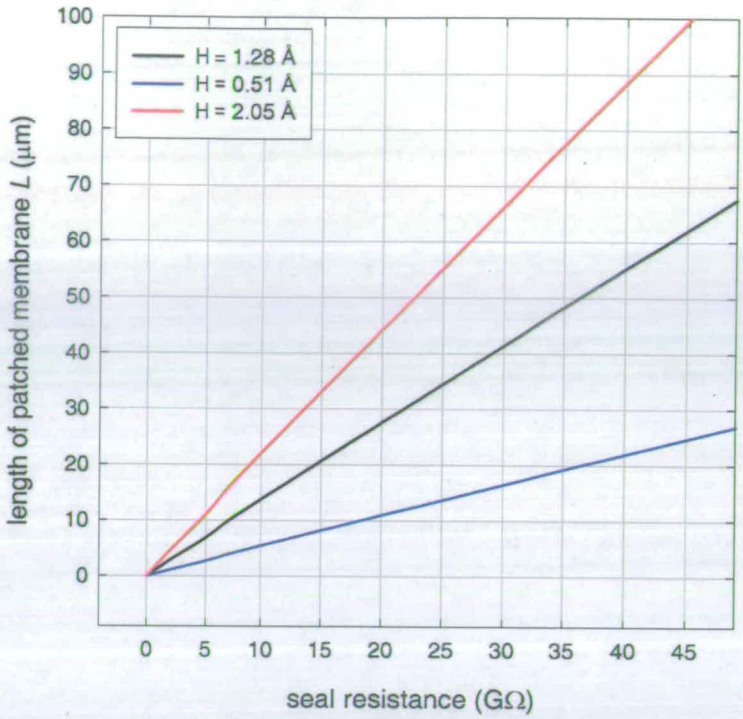

Figure 2.3.3: Theoretical value of patched membrane length vs. seal resistance (under bounded separation distance *H*). The red and blue dotted lines represent upper and lower bounds (2.05 Å < H < 0.51 Å) of the expected patch length for any given seal resistance. For many gigaohm seals, the length of isolated membrane can be any value up to 20 or 30 μm.

2.3.4 Atomic distance considerations for patch formation theory

The juxtaposition of cell membrane and the interior of the glass wall dictates the likelihood and degree of leakage current. If leakage current is present, ions are moving bi-directionally inside the sealable region to some extent. Again, the separation distance between cell membrane and glass wall was calculated to be $H = 1.18$ Å $\pm$ 0.42 Å, on the scale of atomic distance. Sodium, chloride and potassium ions will not move easily through the sealable area unless the separation distance is greater or approximately equal to the covalent radius of these individual ions. The covalent radii of ions used in channels expressed on the cell membrane are approximately: Na^+ = 1.54 Å, K^+ = 2.03 Å and Cl^- = 0.99 Å. With the presence of hydration shells (electrostatic bonding of water molecules), water molecules orient themselves around these ions with typical radii of up to approximately 2-10 Å [60]. Hence, it is speculated that the separation distance over local atomic distances varies, assuming some non-uniformity of cell membrane composition and protein distribution. Thus, ions may be able to "tunnel" through the formation of channels within the sealable region, as evidenced from Sachs' model [51]. Without the tunnelling effect, it is unlikely that voltage gated responses could be measured from ion channels residing in the sealable region.

This juxtaposition of membrane and wall, along with the small separation distance, also dictates the likelihood and types of interactions and electrostatic forces within the sealable region. For example, hydrogen bonds typically have bond lengths of ~2.5 Å. If hydrogen bonding is the only contributor to gigaseal formation, then a separation distance of ~1 Å is implausible. Thus, other types of bonding must be present. It is speculated that the presence of dispersion forces along the glass surface is also an important contributor to small leakage currents.

2.4 Physical and Chemical Properties of Patch Materials

As discussed above, gigaseal formation is dependent on the close proximity of two surfaces: glass and the exterior cell lipid-bilayer or membrane. From this perspective, producing gigaohm seals in planar silicon patch devices will require using materials with surfaces feasible for supporting and maintaining a separation distance of atomic scale. To facilitate the phenomenon of sealing in MEMS devices, suitable candidate materials

should have some properties similar to glass to support chemical bonding. Thus, a reasonable first step toward material fabrication is to study the physical structure and composition of the glass used in manufacturing glass capillary tubes for pipette pulling (and any changes of structure thereafter). If the physical and chemical nature of glass is understood, devices can be tailored to feature similar properties of glass to form gigaseals similar to or better than those found in glass microelectrodes.

2.4.1 The Composition and Structure of Glass

Silica (silicon dioxide) is the primary substance used to make glass. The physical state of glass contains some properties of solids (crystals in this case) and liquids. The physical structure of glass is very irregular and disorganised on a large-scale distance. On a small-scale distance, glass forms regular and organised tetrahedral structures. Unlike the crystalline structure in quartz, there exists no general (long-term) ordering of atomic structure in glass, but chains or ordered structures exist locally. Glass consists of a random distribution of silica and possibly other impurities (such as boron or sodium), needed for specific applications. Glass is made by melting these constituents together and immediately supercooling the mixture to prevent the molecules forming an ordered lattice structure and crystallising. By supercooling the mixture, the molecules are randomly bonded together without any general ordering or orientation. This process of supercooling produces the unique properties of glass. [61]

To make patch pipettes from glass capillaries of an appropriate tip shape and size, glass (in the initial form of a capillary tube) is heated beyond its melting point in the middle of the tube and simultaneously pulled apart with equilateral velocity. After some maximum velocity setting, the pulling stops momentarily as the glass is supercooled below the melting point. Supercooling the glass prevents the glass from forming a more ordered crystal lattice structure. The process is repeated until a particular shape and diameter hole is formed after the glass is pulled, thereby forming two identical halves. After pulling, a patch pipette is also a highly disorganised arrangement of SiO_2 molecules with no long-range lattice pattern.

Generally, glass capillary tubes used for patching are fabricated with different constituents: (silicon dioxide - SiO_2, boric oxide - B_2O_3, potassium oxide - K_2O,

aluminium oxide - Al_2O_3, lithium oxide - Li_2O, sodium oxide - Na_2O, lead oxide – PbO and others). The first two, SiO_2 and B_2O_3 are able to form glass due to their low bond strength; they are called glass formers. Potassium oxide, aluminium oxide, lithium oxide, sodium oxide and lead oxide are glass modifiers. These impurities do not form glass due to their high bond strength, and therefore they weaken the structure and decrease the material melting point. The desired glass composition for patching will depend on how these impurities modify its properties, including electrical and thermal [62]. Electrical properties contribute to the noise and capacitance characteristics of the glass electrode. Thermal properties are important for the proper pulling of glass capillaries to form geometrically favourable patch tip openings (this geometry is studied at a later section). Many different types of glass are commercially available for patching, with varying percentages of impurity types. A common electrical performance measure for glass is the dielectric loss factor (LF) or loss index multiplied by the dielectric constant. This is often an indicator of how much capacitance and noise may be introduced into the circuit. Pipettes with smaller values of this measure will tend to exhibit lower RMS noise values at a given frequency.

The atomic arrangement of the glass constituents is worth investigation to address the issue of seal formation. The chemical structure of a glass surface consists of approximately one oxygen atom per square nanometre, bridged or un-bridged. The number of un-bridged oxygen atoms not single-bonded to a Si atom is also dependent on the proportion of impurities of non-glass forming atoms in its composition. For pure crystal, this number is theoretically zero. For glass with impurities (glass modifiers), this number increases proportionally to the quantity of additional oxygen atoms introduced from the impurities not needed to form the tetrahedral structure of SiO_2. For example, surface charge density (not total surface energy) increases from $0.0/nm^2$ for pure crystal to $0.2/nm^2$ with the addition of 20% PbO. Specifically, these oxygen atoms will have a negative charge from a free electron, or otherwise will be single-bonded to a hydrogen atom to form an OH^- hydroxyl group. Negatively charged oxygen atoms establish an overall net negative surface charge on glass. Both configurations of un-bridged oxygen atoms have the ability to attract other charged or polarised molecules, such as H_2O or positively charged alcohol head groups of phospholipids on the surface or membrane proteins of cell membranes (to be addressed in the next section).

2.4.2 Electrostatic bond considerations in patch formation

If chemical bonding between glass and lipid can facilitate gigaseal formation, then at least four different types of electrostatic forces between the surface of glass and the cell membrane may contribute to the highly resistive seal formed in patching. If the average distance between glass and membrane is around the value of 1 Å, then the possible electrostatic forces are: (1) electrovalent bonding between negatively charged O^- atoms present on the surface and positive charges (NH_3^+ and $N^+(CH_3)_3$) on the alcohol head group of phospholipids; (2) hydrogen bonding due to attraction of hydrogen atoms to highly electronegative oxygen atoms on the surface and the hydrogen from the hydroxyl groups on glass and the nitrogen or hydrogen atoms in the phospholipids; (3) other electrostatic forces involving ionic atoms in saline solution, such as Na^+ and Ca^{2+} forming salt bridges between charged molecules between surface and membrane; and (4) dispersion forces and dipole-dipole interactions if the distance between atoms is sufficiently small. Electrostatic forces, although crucial for molecular configurations and processes, are relatively weak compared to covalent bonding. In theory, a multitude of these weak forces would be required for gigaohm formation, regardless of whether membrane proteins "denature" from molecular re-arrangement or direct bonding to lipid exists. If the density of un-bridged oxygen atoms can be controlled in a fabrication process, an experiment could be performed to test the hypothesis that a minimum surface energy is required for gigaseal formation.

2.4.3 Surface chemistry of cell membranes

The surface chemistry of cell membranes is highly complex, including the addition of many ECM proteins irregularly positioned on the membrane. The phospholipid bilayer is composed mainly of three types of phospholipids: phosphatidylethanolamine, phosphatidylcholine and phosphatidylserine. The phosphate group of all these molecules is negatively charged. The ethanolamine and choline groups are positively charged, thereby forming net neutrally charged molecules. However, serine groups have a negative and positive charge, therefore the net charge for this molecule is negative. Therefore, the net charge on most cell membranes is negative mainly because phosphatidylserine is negatively charged. Moreover, on the atomic scale of a distance of 5-10 Å, negative and positive charges exist regularly on the cell surface.

2.5 Conclusion

From the current literature, there are strong indications of the ability to make electrophysiological recordings with microstructures using the patch-clamp technique. However, at the time of writing, no patch recordings from living neurons with planar microstructures have been published. This may, in part, be due to the overwhelming interest in high throughput patching of non-neuronal cells for ion-channel screening in the pharmaceutical industry.

Large electrostatic forces in the sealable area require high-energy surfaces for molecular bonding, decomposition or reconfiguration. If high-energy surfaces are required to facilitate high total bonding energy from many small electrostatic forces between molecules, then a method to measure the quantity of surface energy of different materials is desirable. Moreover, current studies of patch-clamping with microstructures suggest that high-energy surfaces increase the overall probability of patch formation, and perhaps necessary for any sealing to occur [45].

Therefore, it was decided to study surface energy of patch materials in greater detail in Chapter 3. This shift in focus led to the study of surface energy of various materials. It was therefore hoped that a theoretical model could be formed that gives support for the requirement of the use of high-energy surfaces in patch-clamping. This could be achieved by future experimentation with microstructures with variable surface energies.

3 Neuron Preparation, Patch-Clamping and Immunohistology of Cell Culture

3.1 Introduction

The recording of network activity is not achievable unless *in-vitro* neuronal cultures can be maintained. Specifically, the culture must be capable of performing synaptic transmission and spiking events between cells. Hence, protocols were established to grow healthy cultures of cortical neurons from post-natal rats. Also, the quality of the patch-clamp microstructures can be reliably assessed only after successfully demonstrating that patch-clamping on neurons with a glass pipette can be achieved. Thus, neurons from the pond snail *Lymnaea stagnalis* were prepared for electrophysiological study and then used for whole-cell patch-clamp recordings.

3.2 Primary neuronal cultures

3.2.1 Background on glial problems in culture

It is widely understood that glial cells in culture provide neurons with support mechanisms and growth factors and to sustain their health and vitality. Planar *in-vitro* cortical cultures develop a carpet of proliferated glial cells primarily underneath the neurons within 48 hours after plating. In order for recordings to be possible with the planar patch-clamp technique the neuron must be in direct contact with the aperture opining. However, most glial cells would be resting on a hole and render the device incapable of patching on individual neurons grown *ad libitum*.

In an attempt to decrease the likelihood of a glial cell covering an aperture, an enriched neuronal fraction of cell suspension was obtained in a gradient isolation process. To prevent glial proliferation and sustain a high neuron/glial ratio, the drug Ara-C was added into culture 24 hours after initial plating to prevent mitosis.

3.2.2 Materials and Methods

Glass coverslips (purchased from R.A.Lamb Ltd.) were cleaned in ethanol for 48 hours, rinsed in distilled water, and autoclaved. Next, the coverslips were soaked in poly-D-lysine solution (50 μg/mL conc.) at 37°C for at least 2 hours, rinsed with distilled water, and allowed to dry for 30 min. Also, five Pasteur pipettes to be used in the trituration were autoclaved. All culture preparation was performed under a sterile fume hood. All solutions were sterilised before use. The protocol below is a modification of the gradient cell isolation and washing protocols outlined in previous literature [63;64]:

1. Between 3-10 post-natal Sprague-Dawley rats aged 3-7 days were anaesthetised with halothane and decapitated;
2. The scalp was cut with micro-scissors and removed to expose the cortex;
3. The tissue was quickly removed by one of the following methods:
    a. hippocampus
        i. the cortex gently split down the middle with forceps to loosen left and right hemisphere;
        ii. one side of the cortex was pulled away to expose the hippocampus;
        iii. using tweezers, the hippocampus was obtained and immediately placed in EBSS (Earle's Balanced Salt Solution) solution at 4°C;
        iv. the hippocampus was obtained from the opposite hemisphere;
    b. cortex
        i. using tweezers, both cortical hemispheres were gently removed;
4. The carcass was discarded;
5. Once all cortices were collected, the hippocampi or cortices were placed in line (perpendicular to its major axis) on the McIlwain™ tissue chopper and sliced in 500-μm steps at a speed of approximately two slices per second.[1]
6. The tissue chopping board was rotated 90° and chopping was repeated to slice tissue in both orthogonal directions;
7. For enzymatic treatment, the tissue was transferred to a 15-mL tube containing a 6.25-mL solution of: 100 units of papain; 500 units of D-Nase I; and 0.5 mM EDTA, purchased from Sigma©. The solution was pre-heated to 37°C in an incubator with a loose lid for CO_2 gas to diffuse into the solution from the ambient 5% CO_2 gas mixture.

[1] This rate was adjusted from (1.5-2.5 Hz) depending on the mass of tissue dissected from the litter.

8. The tube was shaken by hand to loosen large unchopped sections of tissue, then immediately placed in an incubator at 37°C for 30-45 minutes depending on the amount of tissue present. Tissue was re-shaken approximately once every 15 minutes and placed back into the incubator.

9. Four Pasteur pipettes were fire polished to obtain a wide-bore (~1.5 mm), medium-bore, small-bore and very-small bore pipette (0.7 to 0.9 mm).

10. The solution was triturated with the wide-bore pipette 10 times, allowed to settle, and then the top 2 mL of supernatant containing mostly single cells was transferred to a new tube. This process was repeated two more times using a subsequent small pipette opening for a total of 6 mL of triturated solution;

11. The cell suspension was centrifuged at 300 g for 5 minutes;

12. The supernatant was aspirated and re-suspended in a 3.15 mL solution of: 3 mg bovine serum albumin (BSA; 3 mg ovomucoid; and 300 units of D-Nase I);

13. A cell fractionation gradient was prepared by the following method:
    a. In a 15-mL centrifuge tube, four gradient layers were created by gently placing 1 mL of gradient solution in the order of decreasing density: 35%, 25%, 20%, and 15% (v/v) Nycoprep™ 1.077A diluted in a solution of 10 mg/ml BSA and 10 mg/ml ovomucoid.[2]

14. The suspension was gently placed on the top of gradient step and centrifuged at 800 g for 15 minutes (no brake was applied).

15. Fractions F1, F2, F3, and F4 were collected from the fractionation layers with a 5-mL plastic pipette and diluted into individual 15-mL tubes containing 5 mL of Neurobasal-A/B-27 growth medium at 37°C (see Table 3.2.2).[3]

16. The fractions were centrifuged for 2 minutes at 300 g and the supernatant was removed.

17. The fractions were re-suspended in 1-3 mL of Neurobasal-A.

18. Fraction F3 was re-triturated five times with the very-small bore pipette to further break down any remaining visible chunks of tissue.

19. Three to four dry coverslips were placed in each culture well, ensuring separation from themselves and the well walls.

20. The fraction was agitated with a 100-µL Gilson pipette to create an evenly distributed cell suspension.

---

[2] Periodically, 1-10 µL of $NaHCO_3$ was added to each gradient to adjust the alkaline solution to the correct pH level.

[3] Fraction F1 is abundant in oligodendrocytes, F2 is the densest band of fragments and cells, F3 is enriched with neurons, and F4 is enriched with microglia [64].

21. Immediately after, a cell suspension density and viability assessment was performed by the following method:
    a. 15 μL of suspension was placed in an empty Eppendorf;
    b. The suspension was diluted with 15 μL Trypan blue solution;
    c. The suspension was placed in a haemocytometer and placed under a transmission light microscope.
    d. Viable cells remained unstained and looked transparent, and nonviable cells with defects were stained black.
    e. A cell count per mm^2 was obtained of viable and non-viable cells.

22. The suspension was diluted (or re-centrifuged at 300 g and re-diluted) to the desired plating density of 100-500 cells/mm^2.

23. The cell suspension was plated at 50 μm per glass/silicon coverslip covering approximately a 5 to 10-mm diameter area.

24. Cultures were placed in an incubator for 1 hour, allowing the cells to settle and adhere to the surface.

25. Cells were washed in EBSS at 37°C to remove any non-stuck cells, debris and chunks.

26. Finally, 2 mL of Neurbasal-A solution (supplemented with a β-FGF growth factor at 5 ng/mL concentration, see Table 3.2.2) was added to each well.[4]

27. After 3 days of growth, 1 mL of solution was aspirated from each culture well and replace with growth medium supplemented with β-FGF at 10 ng/mL concentration.

28. After every 3-5 days in culture, 1-mL of the glial conditioned medium was replaced with fresh medium.[5]

---

[4] The growth medium was optionally supplemented with the anti-mitotic drug Ara-C, as an experimental condition.

[5] The glial conditioned medium from a past experiment can be used as the initial growth medium after plating on consecutive experiments. It is speculated that the use of glial conditioned medium improves the health and viability of the fresh dissociated neurons (see Section 3.6).

	Final Concentration
Neurobasal™-A (Gibco)	(solvent)
L-glutamine (100x)	0.5 mM
B-27 supplement (50x)	1 mL/50 mL
Penicillin-streptomycin	125 units pen/mL
Ara-C (optional)	10 µM
β-FGF (low conc.)	5 ng/mL
β-FGF (high conc.)	10 ng/mL

Table 3.2.2: Neurobasal-A Growth Medium.

3.3 Immunofluorescence Staining and Confocal Microscopy

3.3.1 Introduction

Growing healthy neurons requires a reliable method to assess the health conditions of each cell and culture as a whole. Good health conditions of neurons include the following:

- expected cell morphology (including a tapered axon and no fasciculation of dendrites);
- no disintegration of cell body and processes;
- no vacuolisation of soma;
- relative brightness of staining;
- no neural clumping.

Each neuron culture was assessed using immunofluorescence in combination with confocal microscopy. Immunofluorescence is a histological method where anti-bodies conjugated with fluorescent markers attach to specific proteins expressed on certain types/areas of cells. Detailed discussions to the principles of the technique are found in the current literature [65]. Confocal microscopy has advantages over standard optical microscopy in that the depth of field can be precisely controlled.

3.3.2 Materials and Methods

The antibodies used in these experiments included: (1) Mouse anti-β-tubulin at 1:100 dilution for neuron expression; (2) Goat anti-GFAP at 1:50 dilution used for astrocyte (glial) expression; (3) Donkey anti-Mouse 594 Alexa Fluor™ at 1:100 dilution (red marker); (4) and Donkey anti-Goat 488 Alexa Fluor™ at 1:50 dilution (green marker), purchased from Molecular Probes.© The following protocol was used:

1. Cultures were placed in new culture wells and washed in PBS three times for 5 minutes each; (All washing steps were performed with the aide of a table shaker.)
2. Fixation was performed for 30 minutes in 4% formaldehyde solution [66];
3. A fresh phosphate buffered saline (PBS) solution was prepared [66];
4. Coverslips were washed in PBS for 5 minutes each;
5. The cell membranes were permeated by washing for 15 minutes with a 0.2% (v/v) Triton-X100/PBS solution;
6. A 5% (v/v) donkey serum/(0.2%Tx/PBS solution) was prepared;
7. Cultures were blocked against non-specific binding for 1 hr.
8. Petri-dishes were filled with Whatman filter paper and soaked with PBS. Two strips of paraffin were placed in each Petri dish on top of the filter paper.[6]
9. The primary antibodies were applied (diluted to 1:25 together in blocking solution from step 6) to the cultures for at least 1 hr (2hr at room temperature is preferred or overnight at 4°C).[7] Typically, 50 µl of solution was applied per 10-mm coverslip ;
10. Cultures were washed twice in 0.2% Triton-X100/PBS for 5-15 minutes each;
11. The secondary antibodies were applied (diluted to 1:50 together in blocking solution) for 1 hr. Coverslips were kept in darkness to avoid any bleaching from the ambient light;
12. Coverslips were washed three times in regular PBS for 5-15 minutes each;
13. Coverslips were mounted upside-down on standard glass slides using a polyvinyl alcohol (aqueous base) mounting agent [66]. While mounting, a slight force was applied to centre of the coverslip to keep the coverslip level with the glass.
14. Preparations were stored at 4°C and wrapped in aluminium foil.

Several important advantages are gained using this technique. With reflection microscopy, cultures could be measured growing on transparent glass or opaque silicon substrates. This allowed easy monitoring of two cultures under each experimental

[6] With the lid on, these dishes create a humid atmosphere so the primary antibody solutions do not evaporate and the dilution ratio stays constant.

[7] As a control, only blocking solution was applied to some coverslips to check for non-specific binding of the secondary antibody.

condition (placed in the same culture well), one growing on a glass substrate (easily viewable under a light microscope) and the other a silicon substrate.

3.3.3 Accessing neuronal health and viability

An optimal viewing area of 250 μm^2 was adapted for cell counting and assessing neuron health. Since cultures showed significant variance of neuronal density per field of observation, six consecutive random fields were captured as a TIFF file and later measured. Neuron health was measured on an ordered nominal scale from 0-4, 4=Excellent health, 3=Good, 2=Fair, 1=Poor, 0=Very Poor. Each field measurement was calculated by observation under each of the five health conditions which were subsequently pooled together.

3.3.4 Effects of using Ara-C on culture to reduce glial count

As mentioned earlier in this paper, growth of primary hippocampal cultures with standard growth medium form a bottom bed, or carpet of glial cells within a period of 48 hours. As a way to circumvent glial proliferation, a 10-μM concentration of Ara-C was added as an experimental condition to study its effects on the culture. The hypothesis is that an anti-mitotic drug would stop glial from proliferating and forming a carpet, thus keeping the original neuron/glia ratio obtained in the enriched neuron fraction. The effect of the usage of an anti-mitotic drug on neuronal health and density was investigated.

3.4 Snail Neuron Preparation and Viability

3.4.1 Introduction

3.4.2 Materials and Methods

Pond snails *(Lymnaea stagnalis)* were purchased from Blades Biological [Kent].© Snails were maintained and bred in an aquarium with a solution ecologically tested to sustain life [67]. Snails were fed *ad libitum* with lettuce. The following protocol was used to extract single dissociated viable neurons:

1. The snail was removed from the shell;
2. The body was pinned down dorsal side up in a Agar Petri dish and opened with standard dissecting instruments (including Vanner micro-scissors);

3. Snail extracellular solution at 4°C (see Table 3.4.3a) was poured into the dish[8];
4. The central ring of ganglia was exposed and the connecting axons were cut;
5. The ganglia were removed and carefully pinned to the bottom of another Agar Petri dish with the same extracellular solution;
6. Using micro-dissection instruments, the outer sheath was removed from the ganglia;
7. Various ganglia were incubated for 15-30 min in a 1% (w/w) trypsin/extracellular solution;
8. The trypsin solution is washed out with 10 exchanges of medium;
9. The preparation was incubated in a 1% ovomucoid/extracellular solution for 10 min to stop the enzymatic process;
10. The ovomucoid solution was rinsed out with five exchanges of medium;
11. The inner membrane was carefully removed from each ganglion, revealing clean neuronal cell membranes;
12. Each individual ganglion was removed from the ring structure;
13. Larger ganglia were quartered with micro-scissors;
14. All the ganglia were collected in a 100-µL Gilson pipette and added to an Eppendorf with 200 mL of fresh extracellular solution;
15. The tissue was triturated using 50-µL Gilson pipette (the cycle was repeated 20-40 times).
16. To check for neuron viability, 20 mL of a 10-mM stock solution of Cell Tracker™ from Molecular Probes© was added to 300 mL of dissociated neurons. The solution was left for 1 hr for the tracker to take affect;
17. The suspension was centrifuged at 10,000 rcf for 1 sec (ramping speed was 12 sec and total spin time was 25 sec);
18. For purposes of recording, approximately 25 mL of cell suspension was added to either a 35-mm Petri dish or the device.
19. The neurons were allowed to settle for 5-10 min.
20. After settling, 100 µL of additional extracellular solution was added to the cell-bath of the device platform.

3.5 Results

3.5.1 Cell Culturing

Qualitatively, neurons could be differentiated from non-neuronal (glial) cells. Preliminary tests confirmed that a dissociated neuron culture will form a layer of glial cells mostly underneath the living neurons, highly decreasing the probability of getting a neuron positioned over a hole. Statistics on cultures were obtained by capturing each field by confocal microscopy and performing a post-analysis using cell counting methods and health measurements defined on a nominal ordered scale.

[8] The snails were thought to be partially anesthetised by this process.

Figure 3.5.1a is an example field showing a culture of healthy hippocampal neurons (stained red) growing on a glial feeder layer (stained green). These cells exhibit good cell morphology, they show no signs of disintegration and stained very brightly (indicating the protein neuronal marker is expressed abundantly). Figure 3.5.1b is an example of an unhealthy neuronal culture. Here, the neurons exhibit abnormal morphology and show signs of disintegration, especially near the right side of the image where the dendrites are broken lines.

After 5-7 days of culturing, the number of neurons varies for each field/observation (see Figure 3.5.1c). The two experimental conditions tested were: (1) the effect of adding 10-μm Ara-C to cultures with glial conditioned medium, and (2) the effect of removing non-conditioned medium to cultures with 10-μm Ara-C. These conditions were assessed by the health and neuron/glial ratio per observation. Five observations were made for each culture condition. The statistical analysis and discussion can be found in Section 3.6.

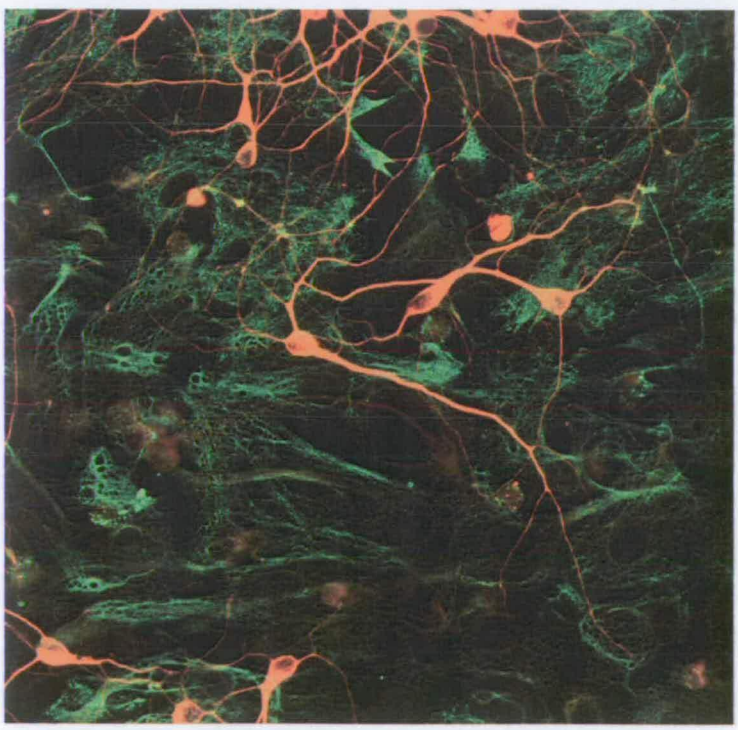

Figure 3.5.1a: Healthy neuronal culture (red) with glial (green) feeder layer (250-μm square). The culture condition was ranked as 4 stars.

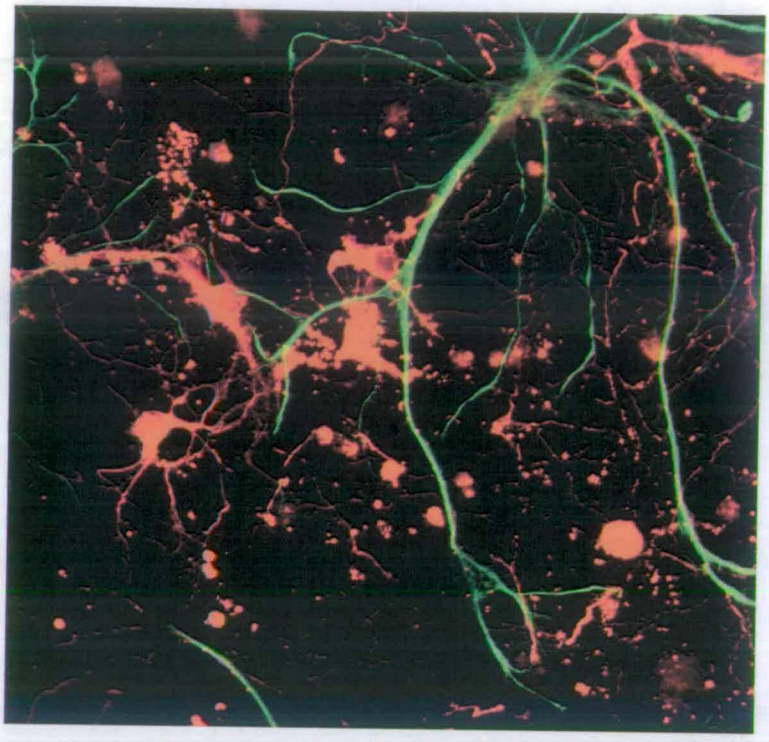

Figure 3.5.1b: Unhealthy neuronal culture (red) showing disintegration and abnormal morphology around a glial cell (green). This culture condition was ranked as 1 star (250-µm square).

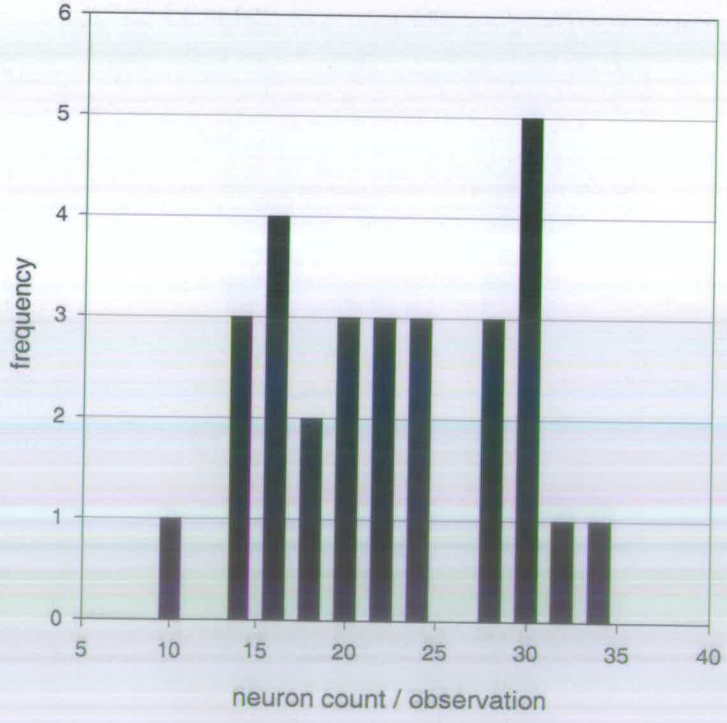

Figure 3.5.1c: Histogram of Neurons per Observation.

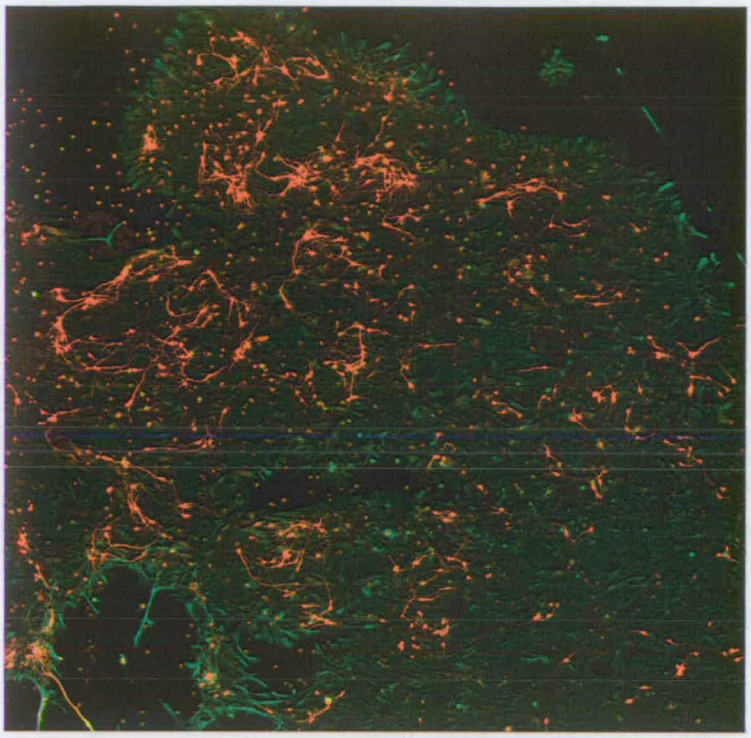

Figure 3.5.1d: Hippocampal cell culture after 8 days without Ara-C added to the glial conditioned medium, (2-mm square).

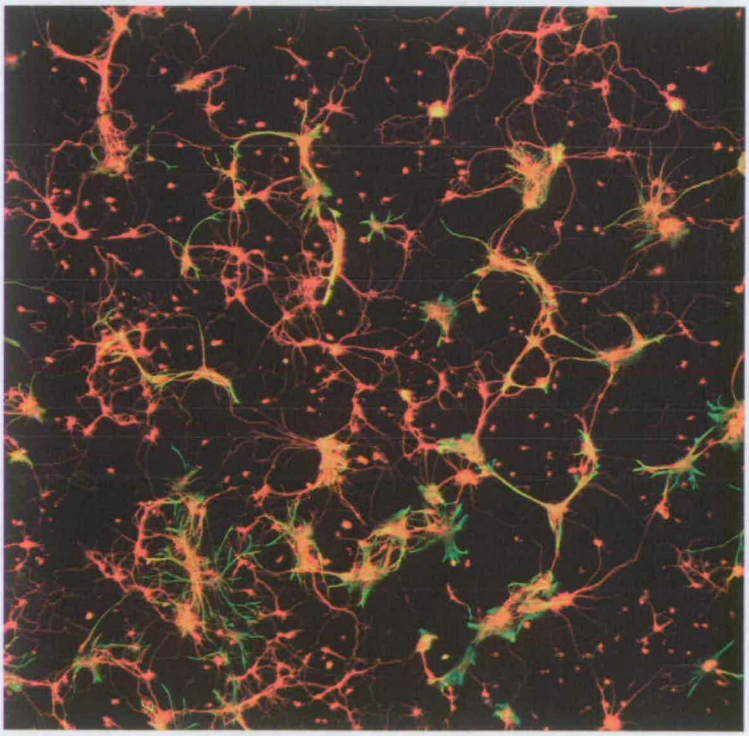

Figure 3.5.1e: Hippocampal cell culture after 8 days with 10-µM Ara-C added to the glial conditioned medium (2-mm square).

3.5.2 Patch-clamping snail neurons

Whole-cell recordings in bridge mode were performed using an AxoClamp-2B amplifier operating in bridge mode with an appropriate headstage (H=0.1), used in conjunction with a Digidata 1320A ADC/DAC converter running at a sampling rate at 100 kHz/channel. The equipment was controlled by a computer running the software package p-Clamp ver. 9.0. Software and instrumentation were purchased from Axon Instruments©. Conventional glass pipettes were pulled from Clark GC-150 glass capillaries using a Sutter-P-87™ puller. Pipette access resistances were typically around 4.5 MΩ after filling with intracellular medium (see Table 3.5.2b). The maximum seal resistance (explained in Chapter 2) of the recordings was approximately 1.5 GΩ. Also, to test the feasibility of patching with a microstructure and a pipette concurrently, dual patch-clamping was performed on the same neuron with two pipettes (see Figures 3.5.2d and 3.5.2e).[9]

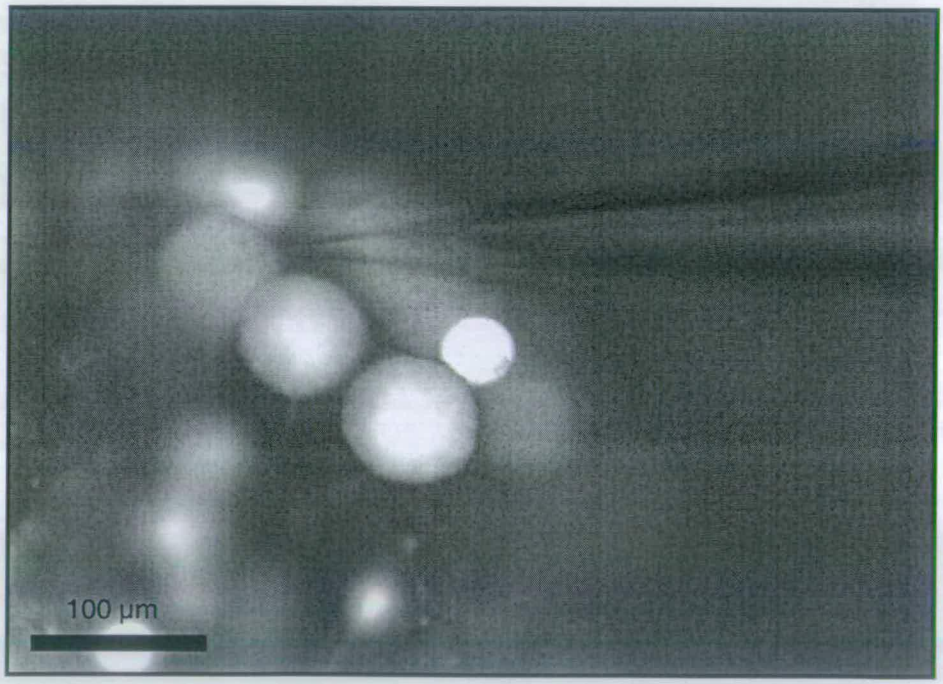

Figure 3.5.2a: Neurons from a snail ganglion fluorescing with Cell Tracker Green™. The bright glow indicates that the cells are alive. The staining method does not hinder patch-clamping on these neurons.

[9] This was performed to check whether the quality of the microstructure could be assessed using this method.

Chemical	Conc. (mM)
NaCl	30
KCl	1.7
$CaCl_2$	4
$MgCl_2$	1.5
$NaCH_3SO_4$	10
$NaHCO_3$	5
HEPES	10

Table 3.5.2a: The extracellular medium used for snail patching (Soest and kits [68]).

Chemical	Conc. (mM)
NaCl	2.0
KCl	64
$CaCl_2$	2.3
EGTA	11
Mg-ATP	2
GTP	0.1
HEPES	10

Table 3.5.2b: Intracellular solution for snail patching (Soest and kits [68]).

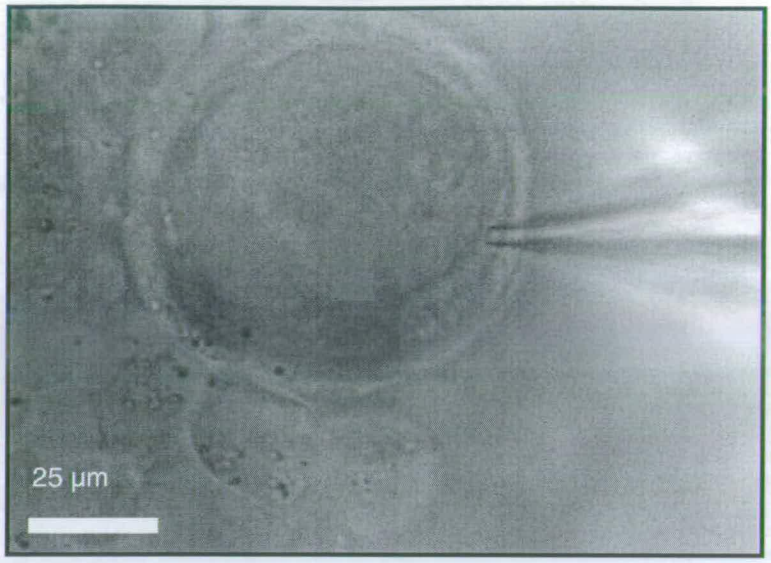

Figure 3.5.2b: Image of a glass pipette patch-clamped on a snail neuron.

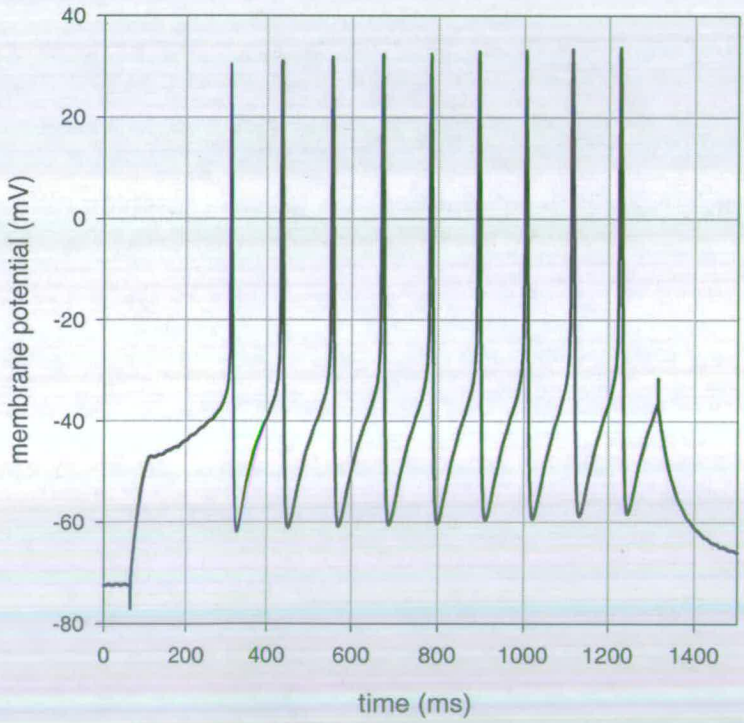

Figure 3.5.2c: Intracellular voltage spike train from the snail neuron from Figure 3.4.3b following a depolarising (inward) current step.

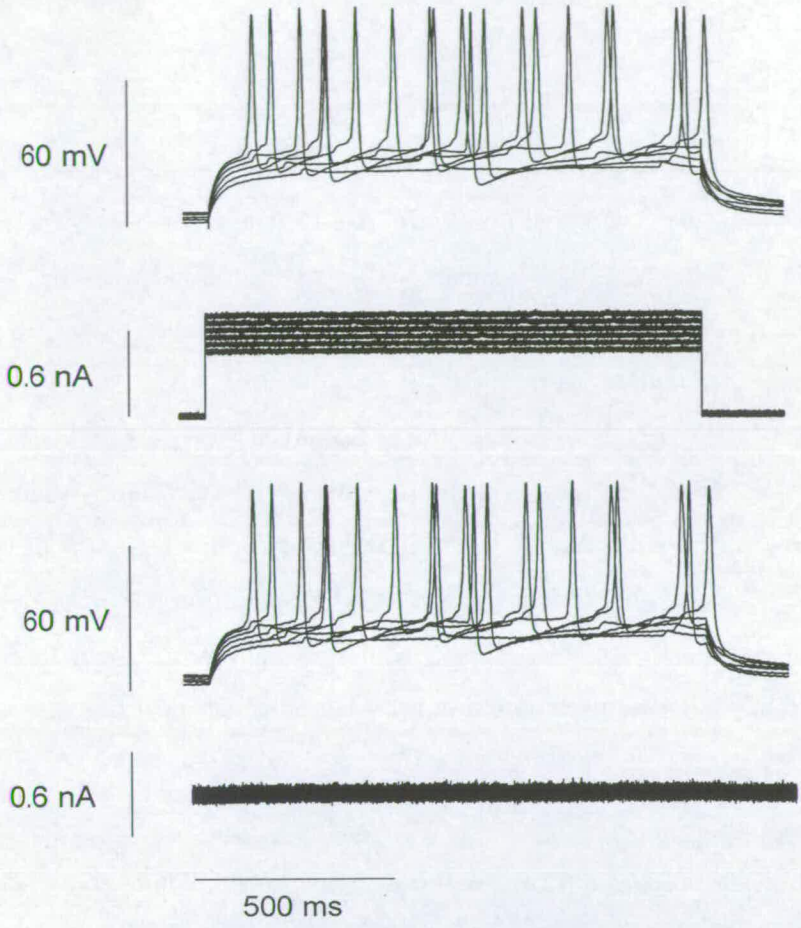

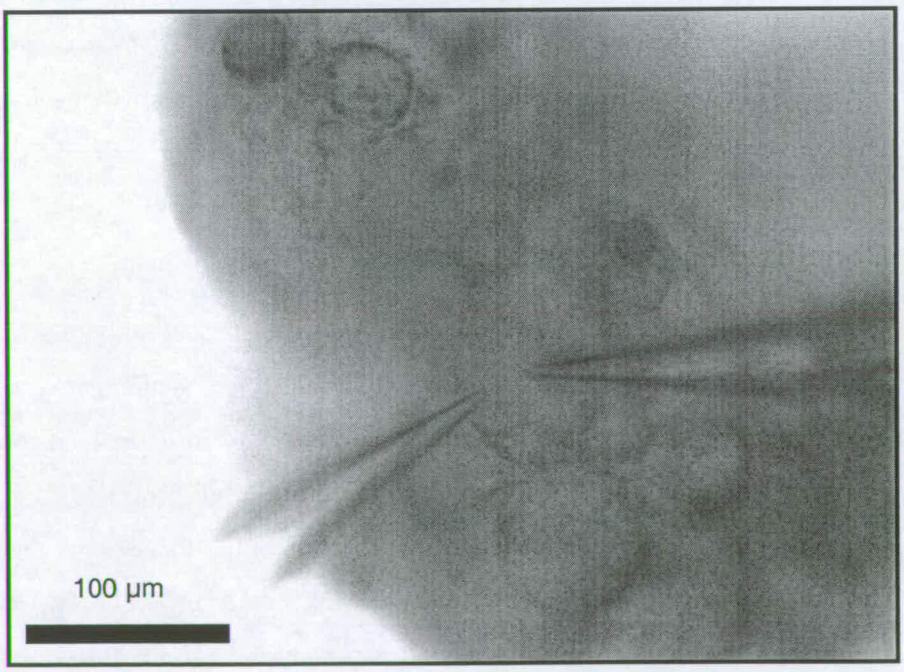

Figures 3.5.2d and 3.5.2e: A dual patch-clamp recording of a snail neuron using two simultaneous patched electrodes. The top voltage traces show a train of spiking events from the depolarisation of the neuron following the current injection of the other electrode.

3.6 Discussion

3.6.1 Cell Culturing

There is a statistical difference on the health of the neurons when non-conditioned medium was used with cultures with Ara-C (t-test; p=0.004; mean with conditioned medium = 3.2; s.d. = 0.837; mean without conditioned medium = 1.4; s.d. = 0.548). There is no statistical significance on health when adding Ara-C to cultures with glial-conditioned medium (t-test; p=0.740; mean without Ara-C = 3.00; s.d. = 1.00; mean with Ara-C = 3.2; s.d. = 0.837). As expected, there is a statistical significance for the neuron/glia ratio for cultures with and without Ara-C (Mann-Whitney Rank Sum Test; p=0.008; mean with Ara-C = 2.56; mean without Ara-C = 0.30). This was also expected because neuron survivability is dependent on glial-derived growth factors. Thus, if Ara-C is used to increase the neuron/glia ratio, then the neurons need to be cultured in glial-conditioned medium to maintain their health.

3.6.2 Patch-clamping snail neurons

The whole-cell recordings obtained were compared to these results taken from previous studies by Soest and Kits [68]. The resultant action potential waveforms were comparable. Thus, the results gave an expected performance using conventional glass pipettes. The waveforms should be identical to any recordings taken using a silicon-based microstructure.

3.7 Conclusion

It remains the task to patch-clamp and record electrical activity reliably on dissociated snail neurons, as opposed to neurons still attached to the ganglion. Cell cultures can be grown healthy on various insulating materials. At the time of writing, the synaptic activity of these cultures needs to be verified and established. To properly position the neuron over the electrode, other means to control the location of the neurons in culture should be explored, such as patterning techniques by protein stamping. Immunohistology is a useful tool for post-analysis of the cultures, especially on opaque substrates where light-microscopy cannot be used. Finally, the use of glial-conditioned medium is essential to maintain healthy cultures of neurons when an anti-mitotic drug is used to stop proliferation of glial cells.

4 Surface Energy, Roughness and *In-Vitro* Cell Culture Analysis

4.1 Introduction

A logical approach to form high-seal resistances in planar patch devices is to fabricate a smooth patch aperture with high surface energy. From the established engineering perspective, the material surface chemistry should resemble glass (in particular, borosilicate glass), a known material that is capable of forming gigaseals. Theoretically, the surface energy of the patch aperture may alter the resistive properties of a patched seal.

Patching with materials of varying surface energy may provide an indication of the dependency of high surface energy on seal formation. In this chapter, it is shown that suitable materials used in the microfabrication of planar devices can be made to exhibit considerable differences in surface energy. Although the absolute surface energy of solid surfaces cannot be directly measured by observation, the interactive molecular (IM) surface energy can be measured by wettability (see subsection 4.2.1). The IM surface energy is a strong indicator of the absolute surface energy of a material.

An attempt to replicate the hydrophilic nature of borosilicate glass has been investigated on various planar patch devices. To begin the process of finding a suitable material to fabricate the aperture, some candidates, generally used in semiconductor fabrication, are Si_3N_4 and SiO_2. These surfaces, including thermally oxidised silicon nitride materials, were among those selected for study. Furthermore, as an attempt to create a borosilicate surface, these materials were subjected to boron deposition from a solid source at annealing temperature of 1000°C. In this process, boron oxide molecules modify and interact with the surface composition [69].

Silicon dioxide can be particularly useful in this application. Again, it is the main constituent in glass and has excellent dielectric properties for insulation. A SiO_2 thin-film layer can typically be thermally grown or deposited on silicon (as in a PECVD or LPCVD process). When thermally grown, silicon dioxide, is associated with a low dielectric constant of 3.9 relative to silicon [70].

The surface roughness and cell culture growth was tested on various material types. From Chapter 2, the surface roughness will directly impact seal formation during patch-clamping. Thus, atomic force microscopy was used to investigate the roughness on different material surfaces. Also, neurons must be capable of adhering to a semiconductor substrate if cells are to be cultured and recorded from the device. Thus, cell cultures were analysed on many materials for test for proper growth and adhesion.

4.2 Surface characterisation by wettability measurement

4.2.1 Introduction

An indirect and theoretical method of approximating surface energy on biomaterial surfaces is to measure the interplay of water molecules at the solid/liquid interface [71]. By calculating the wettability of a known fluid (free from impurity) on a surface, for example, by contact angle measurement, the surface tension of these materials attributable to molecular interactions can be measured. The wettability of a surface is typically defined as the contact angle of a sessile drop of liquid resting on a solid surface [72]. Water, for example, is an especially useful liquid because the cohesive tension is well established, $\gamma_{l/v}$ = 72.8 dynes/cm [71]. To investigate material surface energies greater than the cohesive tension of water, other liquids can be used. These liquids will exhibit cohesive tensions greater than water, such as highly concentrated salt solutions used in this study.

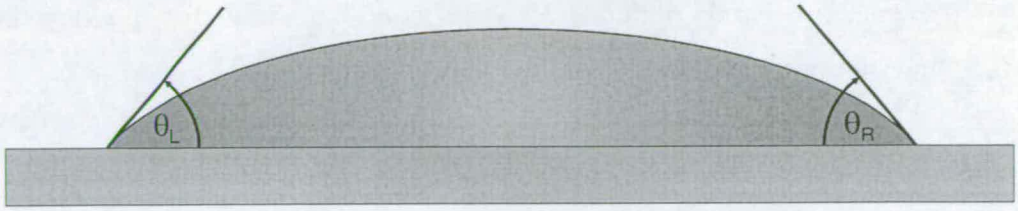

Figure 4.2.1: Cross section diagram of a typical liquid droplet on a solid surface material. The angles of interest, θ_L and θ_R, vary as a function of time and are not necessarily equal. The FTA software incorporates a spherical fitting procedure to calculate a single contact angle for the drop.

4.2.2 Theory of Wettability

The interplay of liquid molecules by the application of various adhesive forces $\pi_{s/l}$, and cohesive forces $\gamma_{l/v}$, are attributable to a specific wetting angle for a given liquid type [72]. The definitions of boundary terminology are as follows: s = solid, l = liquid, v = vapour, o = vacuum. Cohesive forces (for example, self-association by hydrogen bonding in water) act to keep the drop of liquid in a spherical shape, minimising the exposed surface area. Adhesive forces (due to dispersion forces, hydrogen bonding and other electrostatic forces at the surface) act to spread the liquid over the surface [73]. Differences in surface chemistry account for these adhesive forces, including: atomic composition, lattice structure and roughness. The ratio of these two opposing forces is defined as the cosine of the wetting angle, listed in Equation 4.2.1.

Equation 4.2.1 $$\cos\theta = \frac{\pi_{s/l} - \pi_{s/v}}{\gamma_{l/v}}$$

Assuming $\pi_{s/v} = 0$ for relatively low-energy surfaces such as glass and materials studied here, this equation can be reduced to:

Equation 4.2.2 $$\cos\theta = \frac{\pi_{s/l}}{\gamma_{l/v}}$$

Young's Equation was modified by Girifalco and Good [74] to model for a system that only accounts for dispersion forces acting on molecules at the interface between solid and liquid, much like in dissimilar molecules in the gas phase [72]. For molecular

interactions that do not cross the solid/liquid boundary, they introduced a parameter Φ at a later point and developed the following equation:

Equation 4.2.3 $$\gamma_{s/l} = \gamma_{s/o} + \gamma_{l/v} - 2\Phi\sqrt{\gamma_{s/o} \cdot \gamma_{l/v}}$$

Finally, Fowkes [75;76] introduced a subtle modification of Equation 4.2.3 (excluding the Φ parameter) to account for only the additive properties of independent interactions (such as hydrogen bonding or dispersion forces) that occurred across the solid/liquid interface, attributable to wetting. Although this was a slight modification to the original equation, it introduced a way to express wettability as an effect of molecular interactions, as opposed to tensions [72]. Thus, assuming $\gamma_{l/v}$ is the component of $\gamma^{d}_{l/v}$ (cohesive tension due to molecular interactions), combining Equation 4.2.2 with Equation 4.2.3 yields:

Equation 4.2.4 $$\gamma^{d}_{s/o} = \frac{\gamma_{l/v}(1+\cos\theta)^2}{4}$$

This equation can be used to calculate $\gamma^{d}_{s/o}$, the interaction surface energy attributable to wetting (not the total surface energy $\gamma_{s/o}$, provided $\gamma_{l/v}$ is known). Although other models exist for calculating surface energy (tension), this model requires the use of only one known liquid/vapour interface tension and wetting angle. There are limitations of the use of the Girifalco-Good-Fowkes-Young (GGFY) model. For instance, the calculation is only attributable from the total energy of many independent molecular interactions, like hydrogen-bonding and dispersive forces. Unfortunately, these forces cannot be independently calculated without the use of other models and experimentation with more than one liquid type.

A graph depicting the relationship between interactive molecular surface energy vs. contact angle for distilled water and a 25.92% (w/w) NaCl solution is given in Figure 4.2.2.

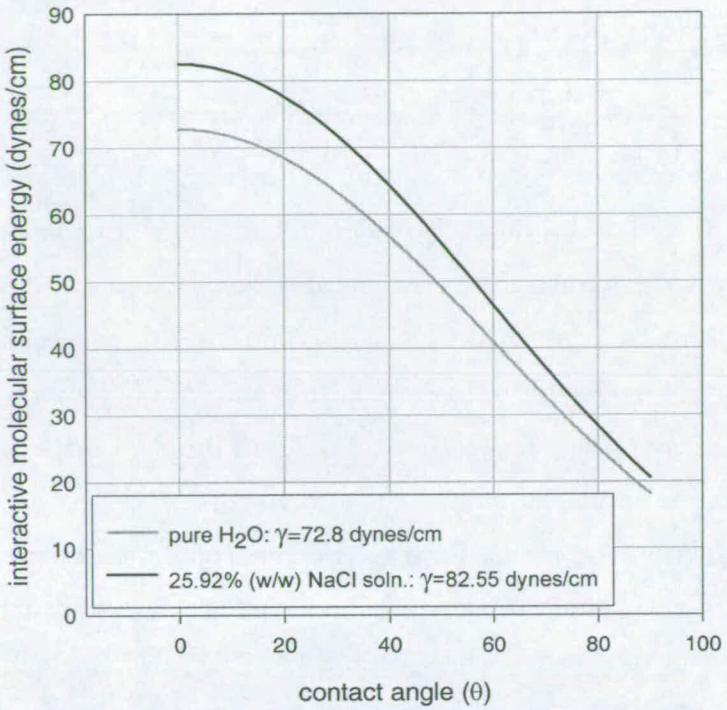

Figure 4.2.2: Interactive molecular surface energy vs. contact angle for water. The interactive molecular surface energy, $\gamma^{d}_{s/o}$, was plotted for a range of contact angles from 0 to 90° for pure water ($\gamma_{l/v}$ = 72.8 dynes/cm) and a 25.92% (w/w) NaCl solution ($\gamma_{l/v}$ = 82.55 dynes/cm [77]). The plots are calculated from the Girifalco-Good-Fowkes-Young model found in Equation 4.2.4.

The hydrophilicity of a surface is specifically a measure of the wettability of a liquid, proportional to the wetting angle. Generally, no approximate angle (or range of angles) divides the usage of the terms "hydrophobic" or "hydrophilic." In this section, the usage of this terminology will be relative, not absolute. As the wetting angle of water approaches zero degrees, the surface is more hydrophilic and less hydrophobic. High surface tension (and therefore hydrophilicity) can be attributable to hydrogen bond formation by the attraction of polar water molecules at the surface [78]. These forces are so great that the competing forces of self-association of water cannot prevent the spreading of water on the surface to form more hydrogen bonds [71]. In general, the availability of a percentage (this being dependent on the amount of glass impurities) of negatively charged oxygen atoms on glass surfaces have a great propensity to induce electrostatic forces with other molecules by means of electrovalent or hydrogen bonding. Thus, the high density of non-bridged oxygen atoms at the surface of glass is attributable to hydrophilicity.

4.3 Wettability Experimentation

4.3.1 Introduction

The experimental method consisted of accurately measuring the contact angle of successive water drops on a control and other patch materials. Borosilicate glass was used as the control surface. To begin, the experiment requires the use of a pure liquid of known surface tension. Two reliable liquids were selected, water (Milli-Q™ de-ionised) and a 25.92% (w/w) NaCl solution. Also, a reliable wettability experiment dictates that the sample of interest is clean and void of impurity. Generally, the contact angle varies by some degree from droplet to droplet on the same surface. The study attempted to produce results to an accuracy of ±3%. Second, the surface may exhibit certain dynamic properties for a given liquid-solid interaction. Thus, the contact angle will change as a function of time and rapid changes can occur following the initial contact with the surface (see section 4.4). Overall, sufficient numbers of trails are required to gain some statistical significance from material groups of varying surface energy. An example of an observation of a liquid drop at an instance in time is given in the picture frame in Figure4.3.1.

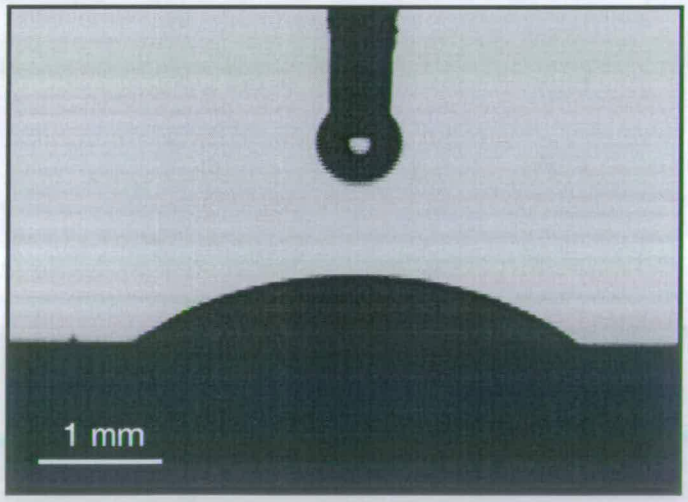

Figure 4.3.1: A 3-µL droplet of NaCl solution on thermal oxide. The contact angle is 35.36°. The base length of the droplet is 3.62 mm.

4.3.2 Sample preparation

Two separate experiments, denoted by A and B, were conducted with two different groups of surfaces. Sample materials that were tested for each experiment are listed in Table 4.3.2. All process materials were grown or deposited on standard silicon 3" <100> wafers.

Abrev.	Process Materials	A: thickness	B: thickness
TO	thermal oxide	5500 Å	2200 Å
TO+B	thermal oxide with boron (B^+) deposition		
N	silicon nitride	2350 Å	2200 Å
N+B	silicon nitride with B^+ deposition	not tested	
P	PECVD deposited silicon dioxide	5000 Å	2200 Å
P+B	PECVD deposited silicon dioxide with B^+ dep.	not tested	
P+A	PECVD with anneal	not tested	
NO	oxidized silicon nitride	2350 Å	2200 Å
NO+B	oxidized silicon nitride with B^+ deposition		
	Glass Materials and Modifications		
Gr	borosilicate glass w/rinse	0.13-0.16 mm	0.13-0.16 mm
G	borosilicate glass w/o rinse		not tested
G+PLrd	borosilicate glass w/rinse and PDL (in dish)		
G+PLd	borosilicate glass w/o rinse and PDL (in dish)		
G+PLrt	borosilicate glass w/rinse and PDL (in tube)		
G+PLt	borosilicate glass w/o rinse and PDL (in tube)		

Table 4.3.2: Table of Materials used in experiments A and B. The material thickness is given for each experiment.

For experiment A, the materials tested included six process materials and six surface modifications of borosilicate glass. As a control, 12-mm round no. 1 standard borosilicate coverglass (manufactured by Schott Displayglas©, Germany) were sterilised in ethanol in a centrifuge tube for over 48 hours, rinsed in distilled water for 10 min and finally autoclaved at 18 lbs./in^2 (121°C) for 1.5 hours. The percentage composition of the glass is as follows: 64.1% SiO_2, 8.4% B_2O_3, 4.2% Al_2O_3, 6.4% Na_2O, 6.9% K_2O, 5.9% ZnO, 4.0% TiO_2, 0.1% Sb_2O_3. The coverglass was coated with poly-D-lysine at varying concentration of solution to test for effects of PDL binding on concentration. Also, one group of coverglass was left unrinsed after the sterilisation step, the other group was rinsed with distilled water for 10 min immediately after sterilisation. These conditions for converglass were introduced in the experimental design to test for neuronal adhesion in culture. Material surfaces included various grown or deposited materials on standard silicon substrates in a semiconductor grade cleanroom. The

materials for experiment A were not cleaned prior to testing. The process parameters for these materials can be found in Section A.3. Boron deposition was performed for 30 min at 1000°C.[10] Oxidation of silicon nitride was performed in the same conditions as thermal oxide growth. Coverglasses were stored in dust free 6-well culture-grade plastic well containers during shipping and opened immediately upon use. The materials were stored in a wafer handling shipping container once taken from the cleanroom.

For experiment B, a total of 10 materials were tested from Table 4.3.2, including all nine process materials and borosilicate glass. As a control measure, materials were deposited or grown to a thickness of 2200 Å. Some materials underwent boron deposition for 30 min at 1000°C. Annealing the PECVD oxide was performed at 1000°C. Again, the control material consisted of the same borosilicate coverglass and conditions as in experiment A. However, in experiment B, all materials were cleaned in rigorous and carefully controlled conditions (outlined below). It is important to note that this cleaning method is bound to roughen the surface by a small degree. It was assumed that significant etching of the material in these conditions to affect the contact angle is limited and can be ignored. However, surface roughness alters the contact angle of a surface and has been carefully studied [79;80].

Four glass crystallising dishes (also cleaned with a 2M HCl solution for 1 hr and rinsed in Milli-Q water) were used for the cleaning process, and Milli-Q water (stored in a complete filled clean glass container) was used throughout. The cleaning solution was acidic piranha, or Caro's Acid, consisting of 15 mL of 98% H_2SO_4 (sulphuric acid) added to 25 mL of 30% H_2O_2 (hydrogen peroxide) for a total of 40 mL of solution. The solution was left to cool down for 2 to 5 min to a temperature of approximately 80-85°C before cleaning. The materials were then placed in the dish and allowed to clean for 10 min. Gentle agitation to the dish was applied in the cleaning stage. After cleaning, each material underwent three rinsing steps in three separate dishes of water: (1) a bulk rinse dip for 5 sec, (2) a 30 min rinse with gentle agitation and (3) a final dip in fresh Milli-Q water for 5 sec. Nitrogen air was then blown over the surface to remove

[10] The quantity of boron deposited is unknown without the use of analysis tools such as secondary ion mass spectroscopy (SIMS). However, some studies have been conducted for boron implantation into Si and SiO_2 [17].

and evaporate the water. Then, the surface inspected for any water blemishes. If any blemishes were observed, the material was re-rinsed in the same rinse cycle and re-inspected. Finally, the materials were placed in dust free containers.

4.3.4 Experimental setup and methodology

The experimental apparatus consisted of a CCD camera mounted horizontally at a distance of approximately 30 cm from a movable sample stage facing upward. In this configuration, the image consists of a field of view across the sample surface. Illumination of the sample was provided by a rear light source (of variable luminosity) positioned behind the stage shining towards the camera. Samples were positioned near the front edge of an adjustable stage to minimise any off-focus or stage artefacts on the camera display. A high-precision Hammilton™ syringe was mounted just above the sample to introduce a single uniform sessile drop of 1.0, 2.0, 3.0 or 5.0 µl on each surface (the amount depending on the experiment and material type). A diagram of the setup is shown in Figure 4.3.4.

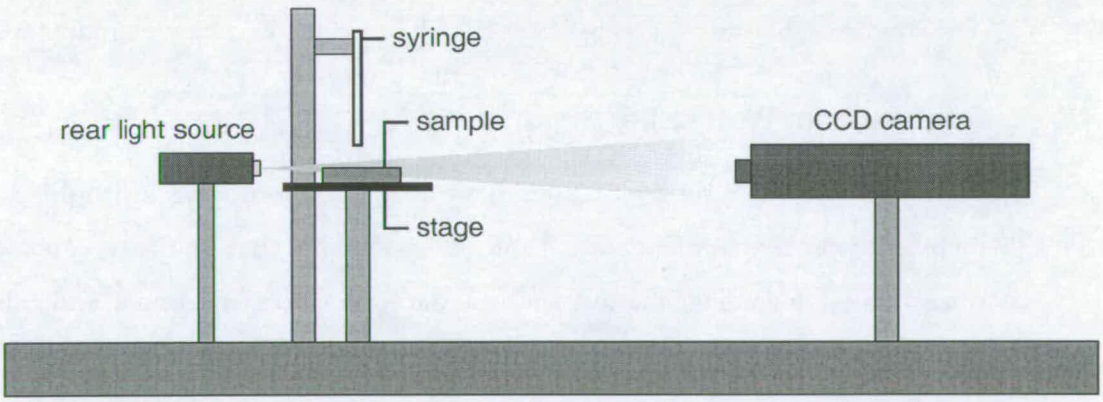

Figure 4.3.4: Wettability experiments diagram depicting relative component locations.

The camera output was connected to a computer with a frame-grabber card and running a contact angle software program called FTA™ (First-Ten-Angstroms). Samples were removed from the dust-free container prior to being placed on the movable stage using tweezers and minimal contact. Immediately after a sessile drop was formed, a series of time-lapsed images (the image period varying from 0.0333 sec to 1 sec) were captured and stored on the computer for a total run-time of 5 to 75 sec (depending on the

dynamic time-response) to ensure the drop was completely settled on the surface with a constant change in contact angle associated only with evaporation. The image data was loaded into the software, and a pattern recognition algorithm identified the contour of the droplet from the silhouette formed by the back light and shadow of the liquid. The angle measurement was calculated by a best-fit algorithm to the left and right contact angles formed by the droplet outline and horizon (sample stage) to a curve (assuming the water drop is mostly uniform). Different material samples under the same experimental condition were tested multiple times for repeatability purposes and statistical significance.

For experiment A, droplet sizes of 5 μl of Milli-Q™ water (12.4 MΩ/cm) were used, and a total of four droplets were measured per surface. Standard room conditions of pressure, temperature and humidity were not recorded. For experiment B, droplet sizes of 1 or 3 μl were used consisting of a 25.92% w/w NaCl solution, using Milli-Q™ as the solvent. This solution was made to increase the surface tension from 72.8 dynes/cm (for water) to 82.55 dynes/cm to obtain a measurable contact angle for all the surfaces (see Discussion). Between five and eight droplets were analysed per surface. The room conditions were as follows: 1014.9 mbar, 63% relative humidity at 24° C.

4.4 Results from Wettability Experiment A

First, two individual runs representative of a hydrophobic and hydrophilic surface are included from experiment A. Table 4.4.1 outlines the statistical outcome of the observations, including: the average, standard deviation, maximum and minimum for the contact angle and inferred intermolecular surface energy. As a graphical representation of the statistical measures, two box-plot graphs in Figures 4.4.3 and 4.4.4 detail the distribution of contact angles and inferred interactive molecular surface energy for each material group.

Figure 4.4.1

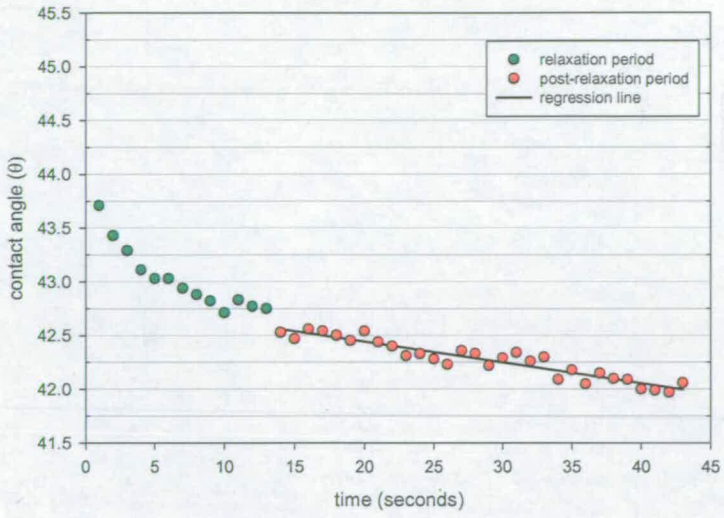

Figure 4.4.2

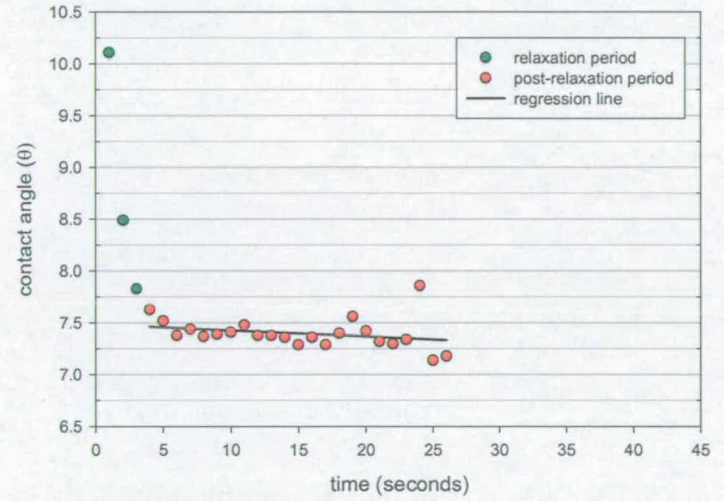

Figures 4.4.1 and 4.4.2: Contact angles of sessile water drops (Milli-Q™ water) on a hydrophobic and hydrophilic surface. The data in each graph was divided between two periods, a relaxation period (in green dots) followed by the post-relaxation period (in red dots). Relaxation period time intervals varied from different surfaces and drops. Generally, for hydrophilic surfaces water wets the surface more rapidly than hydrophobic surfaces. The post-relaxation period is a linear drop in contact angle in time due to evaporation (the experiment was done in standard room conditions). The post-relaxation period was fitted to a first-order regression line to find a single value for the contact angle for each drop, and to account for the error in observation from the resolution of the CCD camera. The slopes for the evaporation lines of the hydrophobic and hydrophilic graphs are -0.02°/sec and -0.006°/sec, respectfully. The different slope values are attributable to measuring the affect of evaporation on the cosine of the contact angle, even though the evaporation rate (µl/sec) is constant. A single value for the contact angle was calculated using the value of the regression line at the first time interval of the post-relaxation period. Figure 4.4.1 is a typical response curve on a hydrophobic thermal oxide surface (TO). The single value for a contact angle was calculated to be 42.8°, with a relaxation period was 13 seconds. Figure 4.4.2 is a typical response curve on a hydrophilic coverglass surface with poly-D-lysine (G+PLrt). The contact angle for was calculated to be 7.49°, with a shorter relaxation period of 3sec compared to 12 sec in Figure 4.4.1.

		Contact angle (θ)				IF Surface energy (dynes/cm)			
Abv.	Description	Mean	Std.Dev.	Max	Min	Mean	Std.Dev.	Max	Min
TO+ B	thermal oxide; B^+ deposition	(1)	(0)	(1)	(1)	> 72.8	—	—	—
P	PECVD oxide	(3)	(0)	(3)	(3)	> 72.8	—	—	—
N	silicon nitride	(3)	(0)	(3)	(3)	> 72.8	—	—	—
G+ PL	coverglass; rinse; PDL (in dish)	(3)	(0)	(3)	(3)	> 72.8	—	—	—
G	coverglass; rinse	(3)	(0)	(3)	(3)	> 72.8	—	—	—
G+ PLrt	coverglass; rinse; PDL (in tube)	9.25	2.55	12.22	6.80	71.16	0.53	72.29	71.16
NO+ B	silicon nitride; oxidation; B^+ dep.	19.19	0.80	18.41	20.13	68.81	0.32	69.12	68.42
G+ PLd	coverglass; no rinse; PDL (in dish)	26.99	2.98	30.88	24.39	65.04	1.65	66.45	62.85
G	coverglass; no rinse	27.62	6.93	37.96	23.48	64.47	4.19	66.9	58.21
G+ PLt	coverglass; no rinse; PDL (in tube)	35.68	5.04	42.25	29.98	59.66	3.41	63.39	55.12
NO	oxidation of silicon nitride	40.04	1.74	42.63	38.95	56.73	1.27	57.52	54.83
TO	thermal oxide	46.21	7.23	56.68	40.47	51.99	5.71	56.42	43.69

Table 4.4.1: Contact angle and interactive molecular surface energy statistical summary. Values given are the mean, standard deviation, maximum and minimum for twelve different samples.

Figure 4.4.3

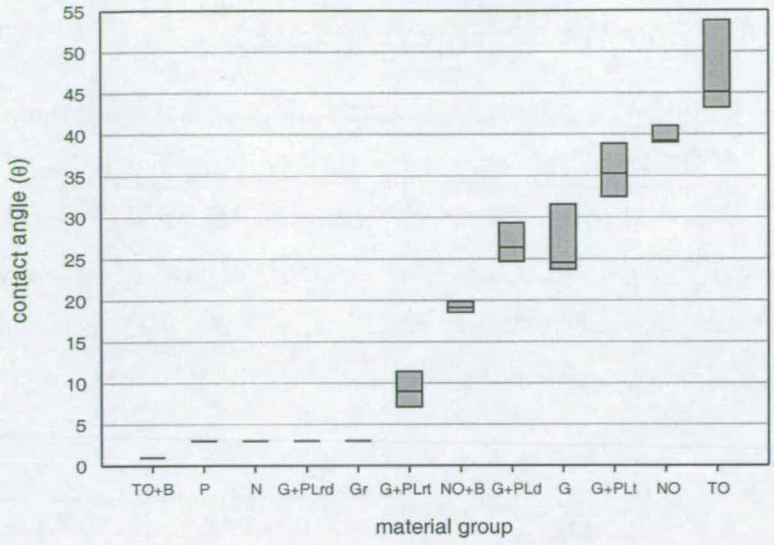

Figure 4.4.4

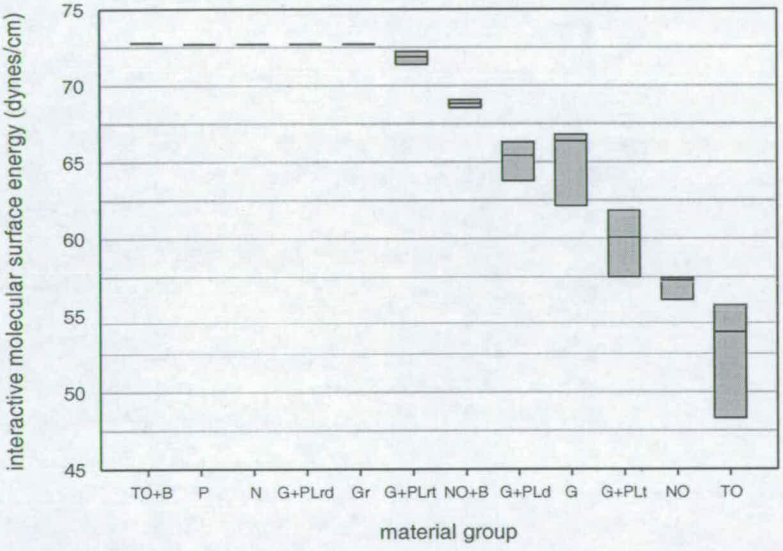

Figures 4.4.3 and 4.4.4: Box-plot graphs depicting range and variability of contact angle and interactive molecular surface energy vs. material group. Each box plot is representative of upper and lower quartiles and median value of four sessile water drops per surface (N=4). Key: material and modifications: (TO+B) thermal oxide with boron deposition; (G+PLrd) coverglass; modifications – a. ethanol cleaning, b. rinsed twice in distilled water, c. placed in centrifuge tube and autoclaved, d. placed in culture tray and soaked overnight in a 50 µg/mL concentration of PDL, e. rinsed in distilled water, f. dried; (Gr) coverglass; modifications – a. ethanol cleaning, b. rinsed twice in distilled water, c. placed in centrifuge tube and autoclaved, d. rinsed in distilled water, e. dried in air; (N) silicon nitride layer; (P) PECVD oxide; (G+PLrt) coverglass; modifications – a. ethanol cleaning, b. rinsed twice in distilled water, c. placed in centrifuge tube and autoclaved, d. placed in centrifuge tube and soaked overnight in a 50 µg/mL concentration of PDL, e. rinsed in water, f. dried; (NO+B) silicon nitride layer; modifications – a. thermal oxidation of nitride, b. boron deposition; (G+PLd) coverglass; modifications – a. ethanol cleaning, b. ethanol aspirated and same tube autoclaved, c. coverglass placed in culture wells and soaked overnight in a 50 µg/mL concentration of PDL, d. rinsed in water, e. dried; (G) coverglass; modifications – a. ethanol cleaning, b. ethanol aspirated and same tube autoclaved; (G+PLt) coverglass; modifications – a. ethanol cleaning, b. ethanol aspirated and same tube autoclaved, c. glass in same tube soaked overnight in a 50 µg/mL concentration of PDL, d. rinsed once with distilled water, e. dried; (NO) silicon nitride; modifications – a. thermal oxidation of nitride; (TO) thermal oxide.

4.5 Results from Wettability Experiment B

First, a time-lapse graph of the drop contact angle for each material is included is included from experiment B (see Figure 4.5.1 and Figures 4.10.2 through 4.10.10). For these graphs, time zero (0 msec) represents the initial contact time of the drop wetting the surface. Second, Table 4.5.1 outlines the statistical outcome of the observations from each material group, as done in the results section for experiment A. Finally, a graphical representation of the data was produced by a box-plot graph in Figure 4.5.11.

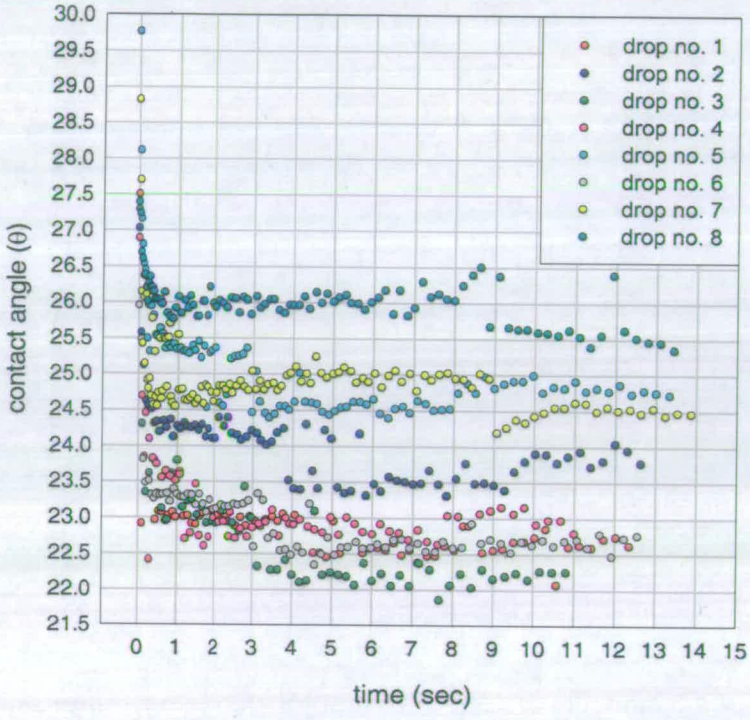

Figure 4.5.1: Contact angle vs. time graph of (8) 1 µl sessile drops of NaCl solution on borosilicate coverglass (Gr).

		Contact angle (θ)				IF Surface energy (dynes/cm)			
Abv.	Description	Mean	Std.Dev.	Max	Min	Mean	Std.Dev.	Max	Min
P	PECVD oxide	9.00	0.50	9.72	8.31	81.53	0.11	81.69	81.37
P+B	PECVD oxide + B^+ dep.	20.75	1.05	22.49	19.55	77.27	0.53	77.86	76.39
TO+B	thermal oxide + B^+ dep.	21.04	0.33	21.41	20.66	77.14	0.17	77.33	76.95
N+B	silicon nitride + B^+ dep.	19.30	1.04	20.59	18.17	77.97	0.48	78.49	77.36
NO+B	oxidation of silicon nitride + B^+	19.70	1.44	21.80	17.82	77.77	0.68	78.64	76.75
Gr	borosilicate glass	24.31	1.17	26.09	23.06	75.38	0.66	76.09	74.35
N	silicon nitride	25.24	1.87	27.27	22.90	74.83	1.09	76.17	73.63
P+A	annealed PECVD oxide	28.97	0.95	30.39	27.78	72.53	0.62	73.31	71.60
TO	thermal oxide	36.39	1.11 *	37.67	35.14	67.23	0.85	68.19	66.24
NO	oxidised silicon nitride	39.09	1.95 *	42.21	36.94	65.08	1.59	66.81	62.53

Table 4.5.1: Contact angle and interactive molecular surface energy statistical summary for droplets of NaCl solution for different materials. Values given are the mean, standard deviation, maximum and minimum for 10 different samples. * This indicates that the standard deviation was calculated from all droplet data. If the last two drops were excluded from the calculation, the standard deviation would be 0.42 for thermal oxide and 0.75 for oxidised silicon nitride. (At the time of study, it was speculated that contamination from the ambient air increased the contact angle over time. The values of the contact angle of last two drops are significantly greater than the previous.)

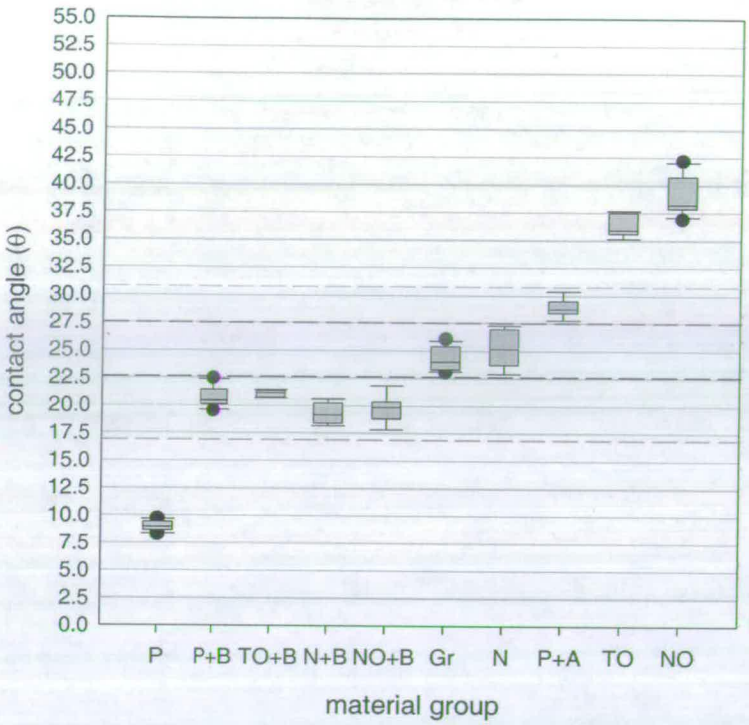

Figure 4.5.11: Box-plot graph depicting the range and variability and standard deviation of contact angles of droplets of NaCl solution vs. material group. Each box plot is representative of upper and lower quartiles and median value of five to eight sessile water drops per surface. Key: material and systematic modifications: (P) – PECVD oxide, (P+B) – PECVD and B+ dep., (P+A) – PECVD oxide and anneal, (TO+B) – thermal oxide and B+ dep., (N+B) – silicon nitride and B+ dep., (NO+B) – oxidation of nitride and B+ dep., (Gr) – borosilicate cover glass, (N) – silicon nitride, (TO) – thermal oxide and (NO) – oxidised silicon nitride.

4.6 Results of Surface Roughness Analysis

AFM scans were performed inside a 500x500 nm^2 area using standard AFM tips. The scan rate was typically around 1 Hz. Each scan line is composed of 512 sample points. All surface plots were adjusted to display a limited height range between 0 and 8 nm (values outside this range were displayed as 0 or 8). A range bar is included (red represents 0 nm and purple represents 8 nm). The median value of the height was adjusted to 4 nm and displayed as green. A grain size analysis was performed that gives a histogram plot of the height and distribution of the pixel dataset. Either two or three runs were conducted for each material. The results are given in Figures 4.6a through 4.6t. A tabulated summary of the data is given in Table 4.6.

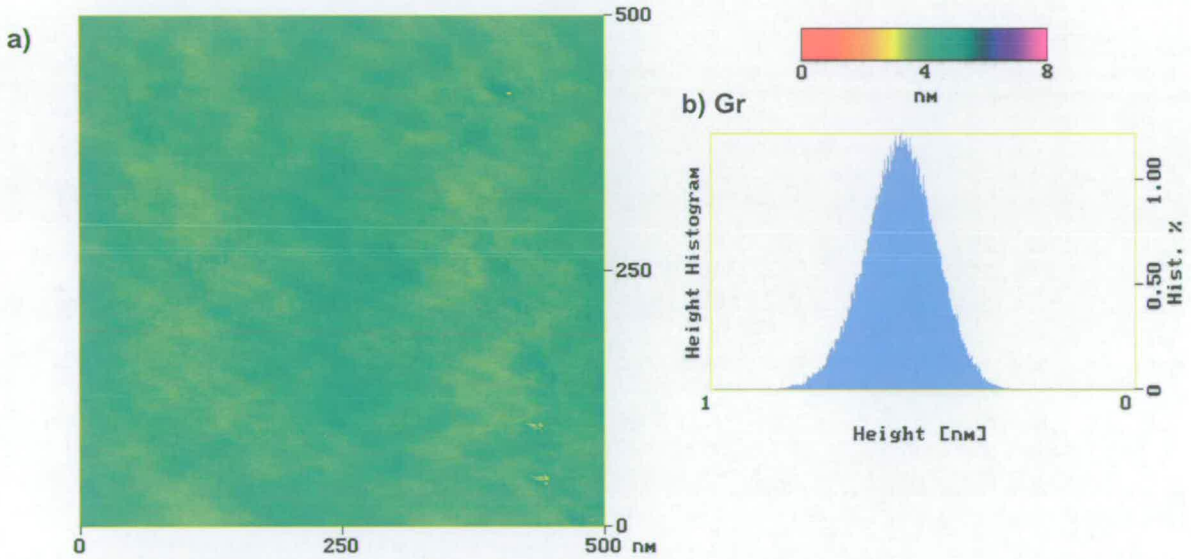

Figures 4.6a and 4.6b: AFM scan results for a borosilicate glass coverslip (Gr).

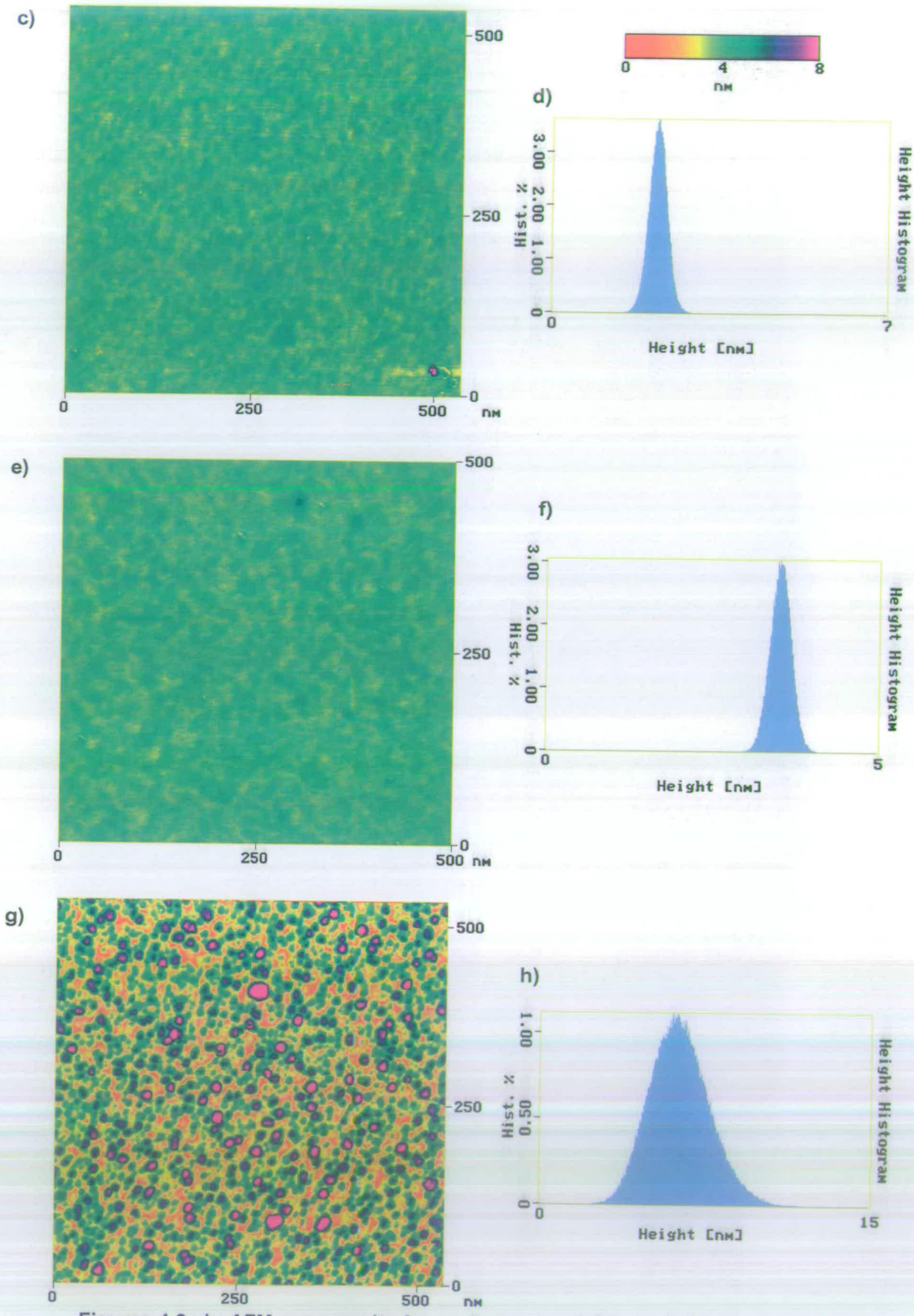

Figures 4.6c-h: AFM scan results for surfaces: (c, d) TO, (e, f) TO+B and (g, h) P.

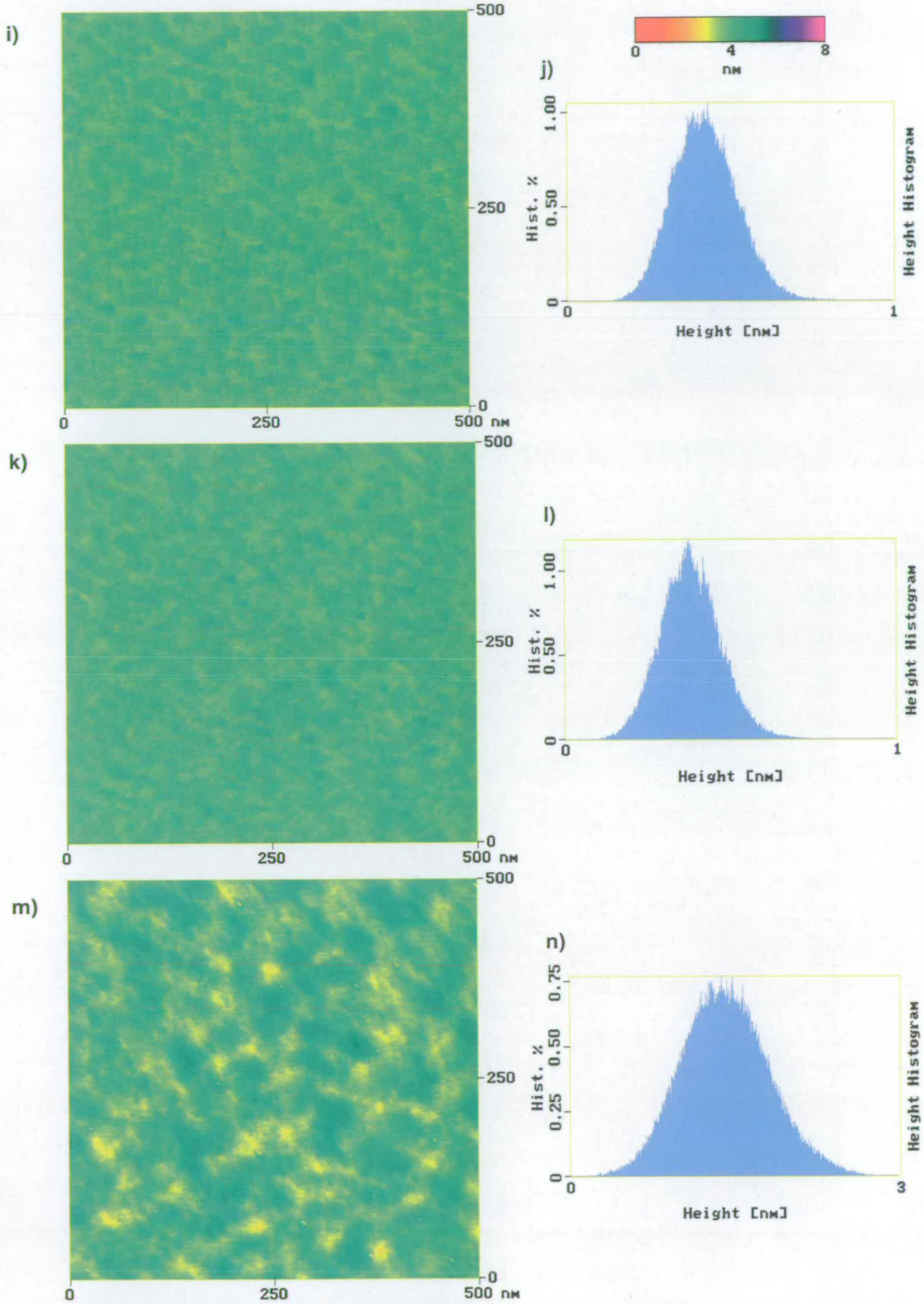

Figures 4.6i-n: AFM scan results for surfaces: (i, j) N, (k, l) N+B and (m, n) P+B.

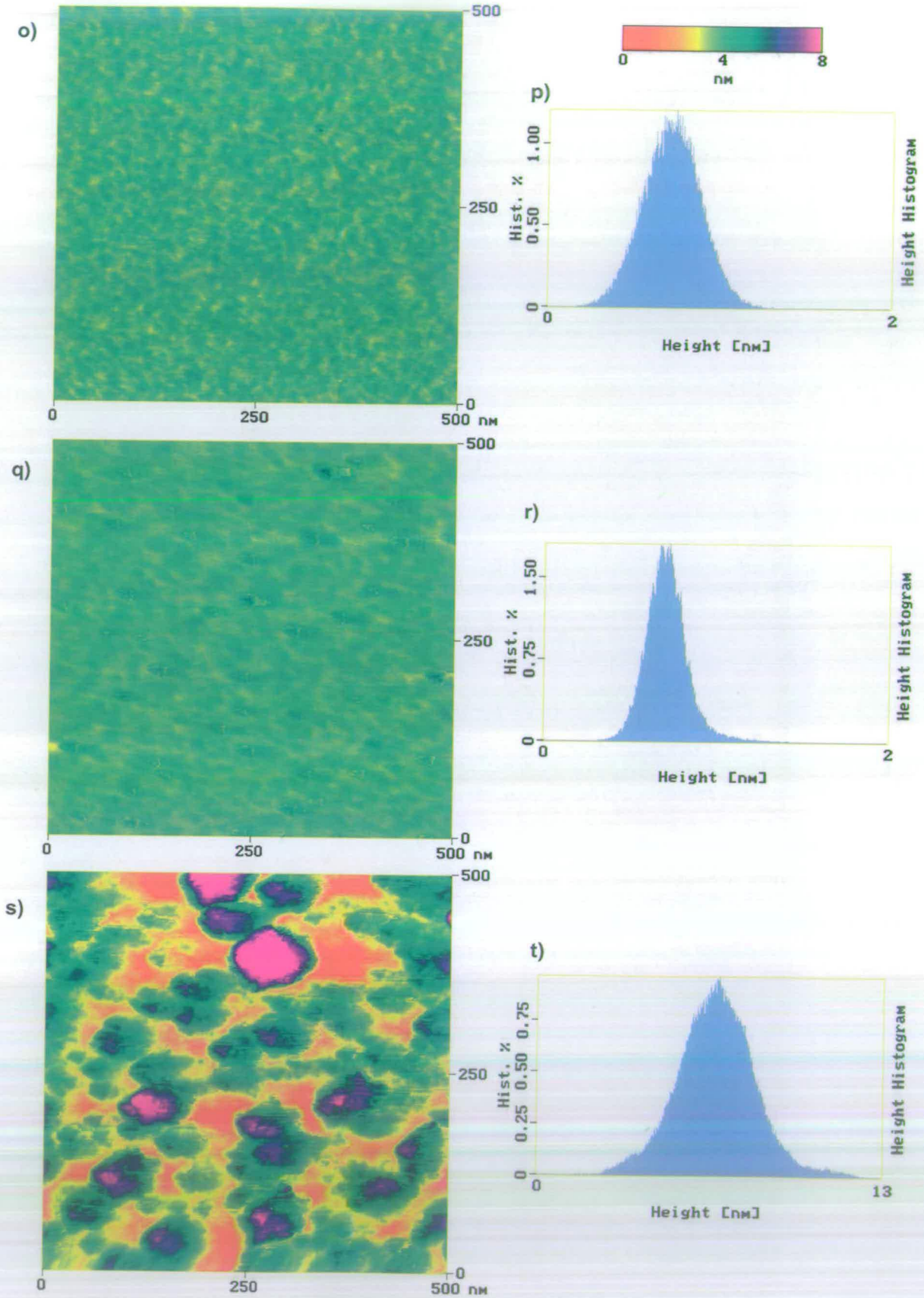

Figures 4.6o-t: AFM scan results for surfaces: (o, p) NO, (q, r) NO+B and (s, t) P+A.

Abbrev.	Material	Modification	R_a (nm)
Gr	Glass 1	none	0.124
Gr	Glass 2	none	0.145
N	Si_3N_4 1	none	0.130
N	Si_3N_4 2	none	0.122
NO	Si_3N_4 1b	oxidation	0.182
NO	Si_3N_4 2b	oxidation	0.169
N+B	Si_3N_4 1c	1000°C B^+	0.109
N+B	Si_3N_4 2c	1000°C B^+	0.107
NO+B	Si_3N_4 1d	1000°C anneal; 1000°C B^+	0.122
NO+B	Si_3N_4 1e	1000°C anneal; 1000°C B^+	0.147
TO	SiO_2 1a	none	0.162
TO	SiO_2 2a	none	0.169
TO+B	SiO_2 1b	1000°C B^+	0.199
TO+B	SiO_2 2b	1000°C B^+	0.150
P	PECVD SiO_2 1a	none	1.131
P	PECVD SiO_2 2a	none	1.113
P	PECVD SiO_2 3a	none	1.142
P+B	PECVD SiO_2 1b	1000°C B^+	0.319
P+B	PECVD SiO_2 2b	1000°C B^+	0.338
P+A	PECVD SiO_2 1c	1000°C anneal	1.227
P+A	PECVD SiO_2 2c	1000°C anneal	1.108

Table 4.6: Surface roughness results expressed as R_a.

4.7 Cell Culture Growth Analysis

4.7.1 Materials and Methods

Neurons were grown for 5 days in culture and stained for immunohistological study using the techniques outlined in Chapter 3. A run consisted of a group of cultures grown on the varying surfaces from the same cell preparation. A total of three runs were performed in the experiment. After staining, a 2-mm square area was captured as an image from the centre of the coverslip using confocal microscopy. Three images of separate cultures were captured for each surface type.

It is generally known that neurons grow and evenly distribute themselves across adhesive surfaces (i.e. PDL coated glass) [81]. When neurons poorly adhere to the surface, clumping and fasciculation occurs. Hence, it was decided to assess the cell culture in a way that best describes this characteristic of the behaviour of culture growth.

Cell cultures growth was quantified by measuring the amount of surface area with no neuronal growth, or "dead-space". During confocal microscopy, the red-level gain of the photomultiplier tube was kept constant for all surfaces of each run. From a PDL surface, the offset of the photomultiplier tube was set so regions of no culture growth (no brightness) gave an intensity value of 0. The gain was adjusted so that the centre of neuronal clumps became saturated at a brightness level of 255.

The TIFF files of the images were collected and analysed. A histogram of the pixel intensity was evaluated for all surfaces (see Figure 4.7a). Next, the input pixel intensity was mapped to different ranges of the output intensity of the PDL and thermal oxide surfaces.[11] The resulting images were qualitatively analysed to determine the best representative threshold intensity at which "dead-space" and neuron growth are differentiated.

[11] From the results section, these surfaces were found to exhibit the greatest differences in culture growth.

4.7.2 Results

From the methods section, a threshold intensity value of 20/255 gave the best differentiation between dead-space and cell culture. Therefore, only pixel intensities up to 20/255 brightness were included in the histogram analysis (see Figure 4.7b). The frequency of pixel intensities of values 0 through 20 were summed and tabulated. (This method has the same effect as measuring the area under the curve.) This value represented the area of no cell growth and compared to the control surface PDL for each run. Due to the variable conditions between experiments (original plating density, general health, staining brightness, etc.), each run was normalised to the best PDL surface (least dead-space) by tabulating the percentage difference between surface areas for each culture. After normalising, the data from all three runs was pooled together.

As a statistical analysis, a two-way ANOVA was performed on all three runs on all surfaces excluding annealed PECVD and glass (only 1 run contained these surfaces). A representative culture of TO, TO+B, PDL, and N is given in Figures 4.7c through 4.7f. A cumulative frequency bar-graph is given in Figure 4.7g.

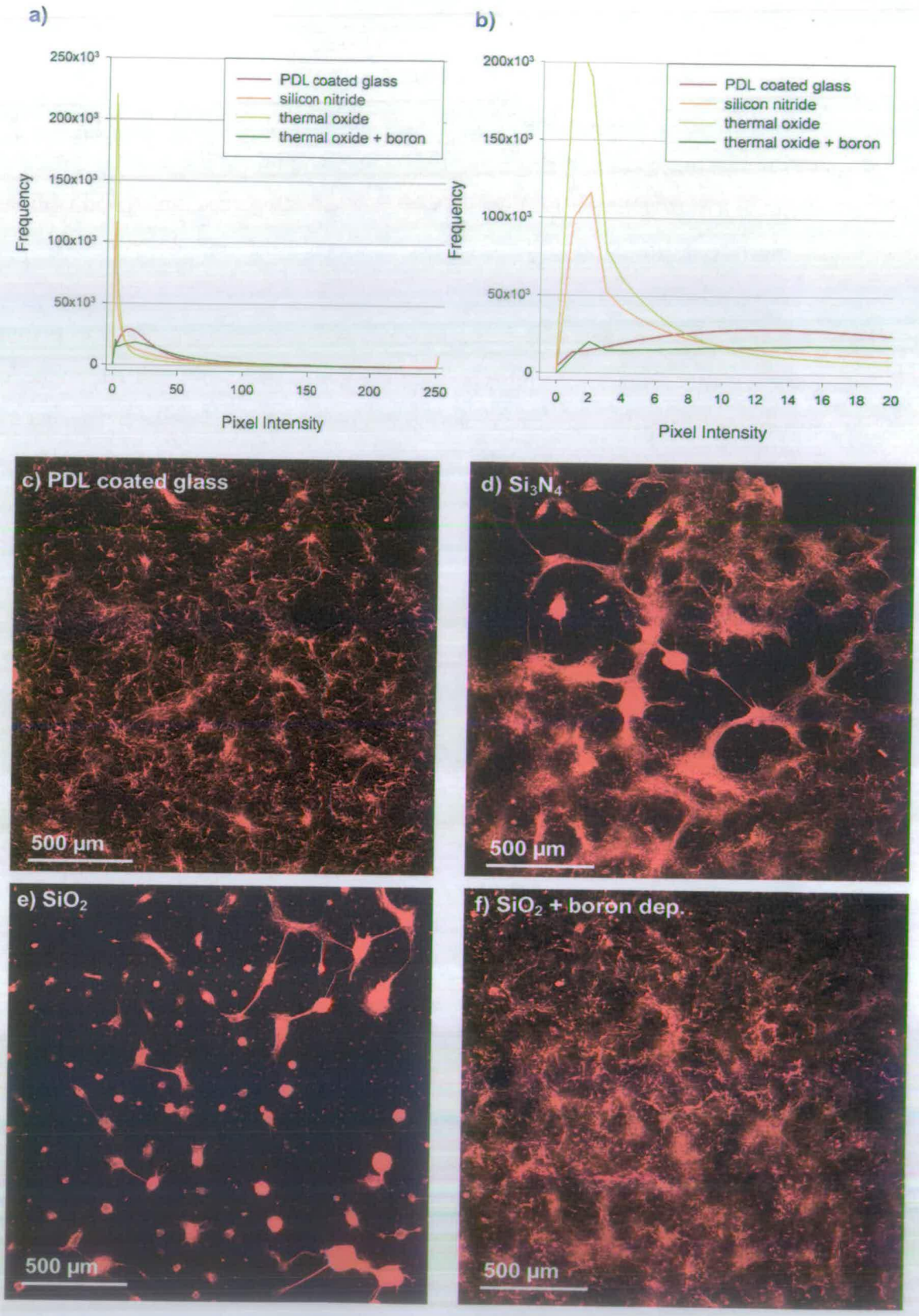

Figures 4.7a-f: (a,b) Histogram traces of pixel intensity of the representative stained neuronal cultures grown on (c) PDL coated glass, (d) Si_3N_4, (e) thermal oxide and (f) thermal oxide with boron deposition.

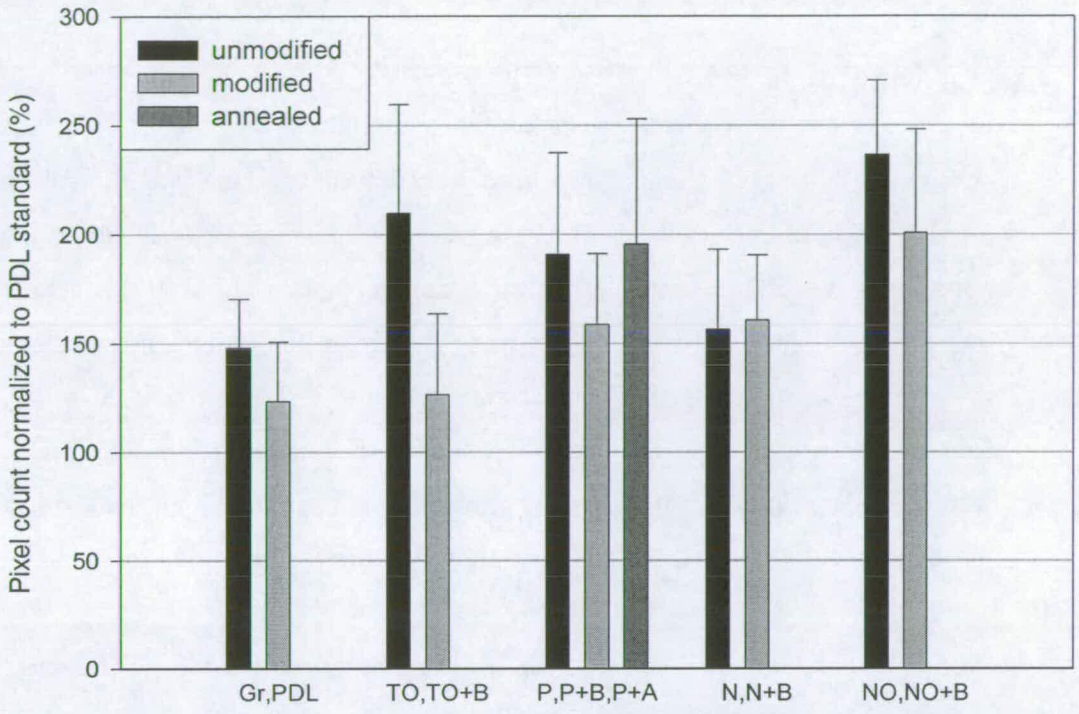

Figure 4.7g: Grouped bar graph of the normalised cumulative frequency data. The mean value is shown with an error bar representing the standard deviation of the value from three experiments (the data for Gr and P+A surfaces are only from run 1). A two-way ANOVA was performed (Tukey Test; again excluding the Gr and P+A data). Statistical significance ($p<0.05$) was found for the following groups: NO vs. N ($p<0.001$), NO vs. NO+B ($p=0.023$), and TO vs. TO+B ($p<0.001$). Only a trend can be found between P and P+B (two-way ANOVA gives $p=0.11$; and a t-test on the pooled data gives $p=0.058$). There is no significant difference between P vs. P+A (t-test gives $p=0.845$) and N vs. N+B (result: do not test). There is no statistical difference between TO+B vs. PDL (result: do not test). The data was normalised to the PDL control surface exhibiting the smallest cumulative frequency in pixel value from 0 to 20 pixel brightness (all values are above 100). The percentage difference was tabulated between different surfaces.

4.8 Discussion

4.8.1 Experiment A

Experiment A revealed significant differences in surface energy for the materials of interest. First, the contact angles of five materials (TO+B, P, N, G+PLrd and Gr) could not be experimentally measured because the surface was critically wetting to water. These critically wetting surfaces had non-measurable contact angles approximately $\leq 3°$. Critically wetting angles (approaching 0°), occur where the interfacial and surface tensions are approximately in equilibrium [82]. For purposes of interpretation, one material (TO+B) contact angle was approximated to 1°, the other four surfaces to 3° (from qualitative video data, thermal oxide was observed to be most wetting). As a logical way of interpreting the data, thermally grown oxide and silicon nitride surfaces (and thermal oxidation thereof) will be discussed first.

From the experimental results, the thermally grown oxide (TO) was the most hydrophobic of the group study (see Table 4.4.3). This hydrophobicity (and therefore low surface energy) is explained from the process of thermal growth of the layer. The thermal oxide process temperature was 1100°C. As the oxide grows, this heat provides nucleation sites with enough energy to form a more organised lattice structure of SiO_2 (as compared to glass), thereby decreasing the number of un-bridged oxygen atoms at the surface. The decrease in non-bridged oxygen atoms is directly related to the decrease in surface energy.

The silicon nitride surface (N) deposited by thermal chemical vapour deposition at 805°C was critically hydrophilic (the wetting angle was estimated at 3°). The atomic structure is speculated to be amorphous, densely packed and under stress [83]. A material with a densely packed amorphous structure will not have a long-term range ordered lattice structure. If the atomic structure of LPCVD nitride is disorganised and dense, many electronegative nitrogen atoms can potentially hydrogen bonded to water molecules by the many positive amine sites ($Si\text{-}NH_2$) and silanol groups (Si-OH) [84] expressed on the surface.

As a modification of silicon nitride, thermally oxidized silicon nitride (NO) was second highest in hydrophobicity. In this oxidation process, silicon nitride is only partly converted to silicon oxide (SiO_x) and silicon oxynitride (SiO_xN_y) at a ratio of 1.64/3.00 [85] by thermal chemical vapour deposition at 1100°C. Originally, the silicon nitride surface (no. 3) was critically hydrophilic, but after conversion, the contact angle increased nearer the value of thermal oxide. The contact angle data between silicon nitride and thermally oxidized silicon nitride is very highly significant (t-test $p \leq 0.001$). Because the process of conversion is only partial, surface energy is between the range of values of Si_3N_4 and SiO_2.

A direct result from experiment A is that boron implantation directly affects wettability. For example, the thermally grown oxide (TO) was strongly hydrophobic, but after boron deposition (TO+B), the surface was the most hydrophilic material tested (with critical wetting angles estimated at 1° from a qualitative video data analysis). The contact angle data between these two groups is very highly significant (t-test; $p \leq 0.001$). Thus, the boron deposition is interacting with the thermally oxidised surface, thereby increasing the surface energy. It is speculated that the boron atoms are being doped into the material and creating Si-B_x sites, thereby creating an electron deficiency. This positive surface charge increases the adhesion to the negatively charged cells.

Moreover, thermally oxidised silicon nitride (NO), undergoing boron deposition (NO+B), increased in hydrophilicity from an average contact angle of approximately 40.04° to around 19.19°. The data for these two groups are also very highly significant (t-test; $p \leq 0.001$. Noticeably, the wetting angle does not jump into the immeasurable range, like boron deposition of thermal oxide.

To explain this observation, it was speculated from experiment A that oxidised silicon nitride, after partial conversion to a SiO_x/SiO_xN_y type material, remains partially impervious to the effects of boron deposition where silicon nitride is still expressed on the surface. However, this is in sharp contrast to the results from experiment B, indicating that all materials after boron deposition exhibit roughly the same wetting angle (see subsection 4.6.2). It is believed that the surface energy of NO+B is best represented in the contact angle results from experiment A (s.d. = 0.80). Thus, the

decrease in contact angle measured from NO and the NO+B material is best explained from the affect of boron deposition at places where Si_3N_4 has been converted to SiO_x by wet thermal oxidation. Boron deposition increases the localised surface energy in places where SiO_x has been formed.

The borosilicate coverglass control surface (Gr) was critically hydrophilic, exhibiting contact angles ≤3°. Conversely, coverglass not rinsed in distilled water (G) after soaking in ethanol exhibited larger contact angles ranging from 23-38°. Borosilicate glass rinsed after ethanol cleaning and properly placed in evenly distributed culture wells placed in a 50 μg/mL solution of poly-D-lysine (G+PLrd) were critically hydrophilic. This is an expected result because poly-D-lysine is a charged molecule, capable of forming hydrogen bonds with water. It must be noted that, from these experiments alone, it cannot be deduced that PDL adhered to the surface, as both control and PDL treated glass have the same contact angle. A possible way to verify this is to use PDL conjugated to a fluorescent marker, such as FITC, available from Sigma©. Interestingly, glass treated with PDL solution exhibited an increase in hydrophobicity when placed in centrifuge tubes instead of culture wells (no. 6 and 10). For example, the contact angle increased from around 3° to 7-12° for rinsed glass (Gr and G+PLrt), and consequently increased from 23-38° to 30-42° for non-rinsed glass (G and G+PLt). It is speculated that when glass surfaces are not fully exposed to the PDL solution (i.e. semi-stacked in centrifuge tubes), the ability of PDL to adhere uniformly and sufficiently is affected. It was speculated that complete surface exposure is critical to proper adhesion of PDL to the surface.[12]

4.8.2 Experiment B

Results from experiment B have differences from and similarities to the first experiment. Firstly, the standard deviation of the data was reduced from a range of [0.8 to 7.23] to [0.33 to 1.95]. This improvement was made possible by cleaning the surfaces in piranha solution immediately prior to measurement. Other improvements in

[12] It was deduced that glass soaked in ethanol for over 48 hours without subsequent rinsing with distilled water decreased neuronal health. Cells were typically clumped and were not encouraged to adhere directly to the glass.

experiment B included: an improved lens quality, the use of an air table and computerised precision in drop formation.

Regarding the thermally oxidised materials, the outcome is similar to Experiment A in that TO and NO have the greatest wetting angles of the group, averaging 36.39° and 39.09° respectively. However, following the discussion from Experiment A, the wetting angle NO was expected to be slightly less than TO. It is speculated that liquids with high ionic concentration may be affecting the wetting angle for materials with differences in localised surface energy. In addition to this, from Table 4.5.1, the median value of the data set for these materials is closer to the minimum value than the mean. It is speculated that oxidised surfaces are more susceptible to contamination compared to other surfaces. Furthermore, it is assumed that the value of the surface energy of oxidised silicon nitride is closer to thermal oxide than measured. It was noted that oxidised silicon nitride was measured 30 min after thermal oxide, during which time the material is subjected to contamination from air. Other experiments can be performed to prove this conclusion by measuring both surfaces at equal times after cleaning.

The data also indicates that borosilicate coverglass and silicon nitride exhibited similar wetting angles, 24.31° and 25.24° respectfully. This data follows the similar observation of surface energy as in experiment A, with borosilicate glass considered as a control measure. However, because a higher surface tension liquid was used in experiment B, a measurable contact angle was observed for these and other materials.

Finally, PECVD deposited oxide exhibited the smallest wetting angle of the group, an average of 9.00°. Interestingly, the angle was significantly smaller than borosilicate glass. From this observation, it is speculated that the number of un-bridge oxygen atoms is significantly greater compared to borosilicate glass control surface. Silicon dioxide material deposited in a plasma system contains hydrogen and is has a significantly smaller lattice energy compared to other deposited configurations, shown by the increased HF etch rate from 30 Å/min to 400 Å/min [83]. However, boron deposition increased the contact angle of the surface and decreased the surface roughness (see Figure 4.5.11 and Table 4.6). An explanation is given in Section 4.8.3.

4.8.3 Surface Roughness

The average roughness values R_a for all surfaces ranged from 0.11 to 1.2 nm. PECVD oxide was the only surface to show differences in roughness after boron deposition. Annealing the surface did not smooth the surface as expected. Qualitatively, the effect of annealing changed the surface roughness contour, yet no differences were expressed for the value of R_a. Thus, it was deduced that the average roughness does not reflect changes in the true surface roughness for all circumstances. Boron deposition was shown to smooth the PECVD oxide surface (the roughness value decreased from 1.1 to 0.3 nm). It is speculated that boron deposition is interacting with the surface differently from the other material types. It is speculated that the effect of boron deposition is mostly creating a "glassy" surface. Boron is a glass former. Since the lattice energy is small for PECVD oxide, many oxygen atoms from the amorphous structure at high annealing temperatures become available to form a surface material resembling borosilicate glass.

4.8.4 Cell Culturing

There is a detectable contrast in surface area between PDL glass (used as a control) and some semiconductor surfaces exhibiting poor adherence. The general observation of these cell cultures is that neurons tended to distribute themselves across adhesive surfaces, and clump for poorly adhesive surfaces. The amount of positive charge expressed on the surface best explains this observation. The cell membrane surface expresses a net negative charge and therefore is attracted to the positive charges on the surface. PDL coated glass is positively charged. Hence, cultures adhere to and grow well on these surfaces. Thermal grown oxide surfaces exhibit lower wetting angles and smaller surface energy. Furthermore, thermal oxide is negatively charged from the presence of oxygen atoms. The net electrostatic attraction has decreased, and neurons do not adhere very well to the surface. The same case can be partially applied to oxidised nitride surfaces. These surfaces also exhibit low-energy, and therefore, cells do not adhere very well. This data shows some correspondence with other studies showing that neurons adhere easily to hydrophilic surfaces, and do not adhere well to hydrophobic surfaces [86;87]. However, this work is also in strong contradiction to these studies. Cell cultures were poor when grown on PECVD oxide deposited surfaces

(see Fig. 4.7g). This gives support to our theory that cells are mainly attracted to surfaces with positive charge, and not necessarily total charge. It is therefore erroneous to assume that cells would adhere to hydrophilic surfaces only expressing an abundance of negative charge.

In this thesis, it was shown that the quantity of positive charge can be increased by boron deposition of the surface from solid source. For example, after boron deposition of thermal oxide surfaces, no statistical significance between PDL glass and TO+B was expressed. It is speculated that the boron species interaction with the thermal oxide surface creates a positive charge, which is sensed from the neurons. Also, boron deposition of oxidised nitride surfaces showed an increased in culture health (two-way ANOVA, $p=0.023$). However, cultures grown on the NO+B surface was significantly poorer than cultures grown on the TO+B surfaces ($p<0.001$). Thus, it is speculated that the boron deposition has a different interaction than the thermal oxide surface. This can be explained by the fact that the conversion from Si_3N_4 to SiO_x is only partial (1.64/3.00) [85]. Therefore, the interaction of the boron will not necessarily be the same for this surface, as the surface composition is different. Cultures show no statistical difference between unmodified and modified Si_3N_4. This suggests that either: (1) the silicon nitride is impervious to the boron deposition process, or (2) the interaction of the boron deposition with the nitride simply has no effect on the neuron adhesion affinity. Wettability experiment A revealed that NO+B was statistically different in surface energy than TO+B, suggesting that the surface is different. However, wettability experiment B shows that the effects of surface energy after boron deposition all fall within similar values (see Table 4.5.11). It is possible that the high concentration of Na^+ and Cl^- used in the wetting solution in experiment B affect the contact angle measurement of boron deposited surfaces in a unique way. Also, the exposure of the materials to air in experiment A may also have modified those surfaces.

There exists only a trend for a difference in culture growth from the interaction of boron deposition on PECVD oxide (two-way AVONA: 158% to 190% ($p=0.11$), simple t-test of the pooled data gives $p=0.058$). It is speculated that the amount of positive charge has increased from an accumulation of boric oxide formation on the surface, perhaps hinted by the decrease in roughness (as different from annealed

PECVD oxide). The affect of annealing has no statistical significance on cell culture growth compared to PECVD oxide. The high-energy negatively charged surface was shown to decrease substantially after annealing. However, it is speculated that the amount positive charge does not change during annealing.

4.9 Conclusion

Overall, increasing the surface tension of the liquid made possible the measurement of all material surfaces, especially the control. In experiment A, five surfaces were critically wetting and immeasurable because the interactive molecular surface energy was greater or equal to 72.8 dynes/cm, the surface tension of water. This result shows that a 25.92% (w/w) solution of NaCl can be used to measure the wetting angle on many surfaces used routinely in MEMS devices.

Interestingly, boron deposition can be used on normally hydrophobic materials, such as thermal oxide, to create a more hydrophilic surface with greater surface energy. This can be advantageous where hydrophilic materials, such as PEVCD oxide, cannot readily be applied or formed. It was shown that the same quantitative amount of surface energy (to the combination of dispersion forces and hydrogen bonding) of glass routinely used in patch clamping is obtainable by use of these materials in MEMS processing techniques.

The results also provide useful insight into the surface energy that fabricated planar patch devices will exhibit. It can be useful to relate surface energy values from process materials to a borosilicate glass control material if; for example, high surface energy is proportional to high resistive seal formation. Thus, it is suggested that boron deposited materials or PECVD oxide may be superior surfaces to glass. Rigorous testing of many planar devices of different process materials may prove or disprove this theory.

4.10 Additional Figures

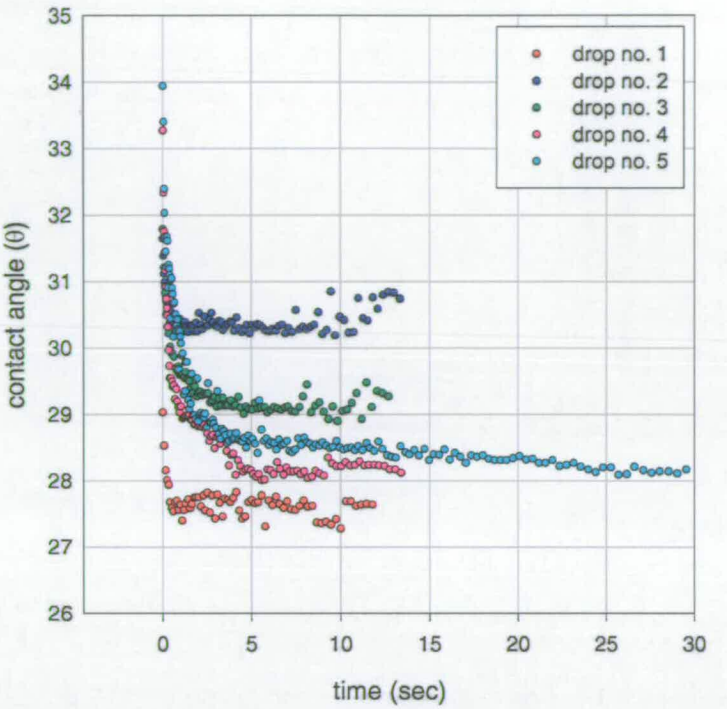

Figure 4.10.2: Contact angle of vs. time graph of (5) 1-µl sessile drops of NaCl solution on annealed PECVD at 1000°C (P+A).

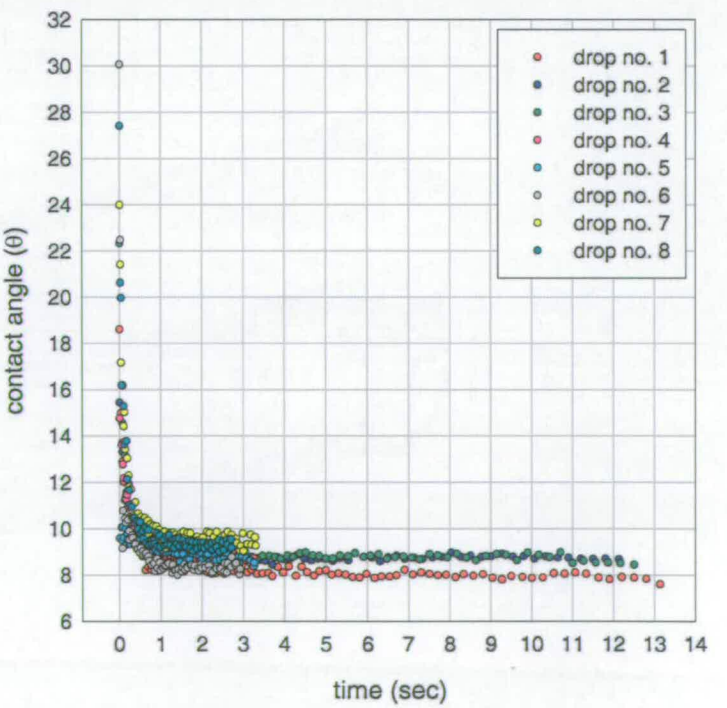

Figure 4.10.3: Contact angle vs. time graph of (8) 1-µl sessile drops of NaCl solution on PECVD oxide (P).

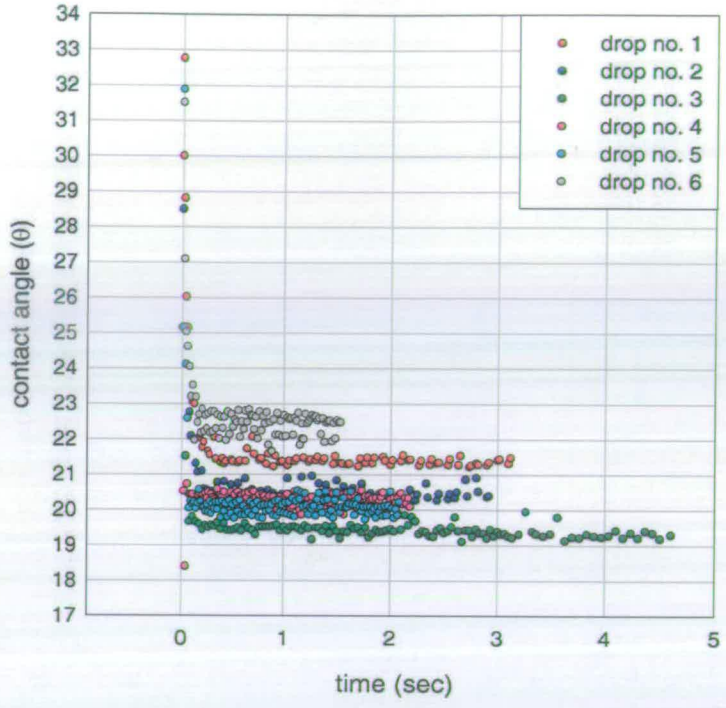

Figure 4.10.4: Contact angle vs. time graph of (6) 3-µl sessile drops of NaCl solution on PECVD oxide with boron deposition (P+B).

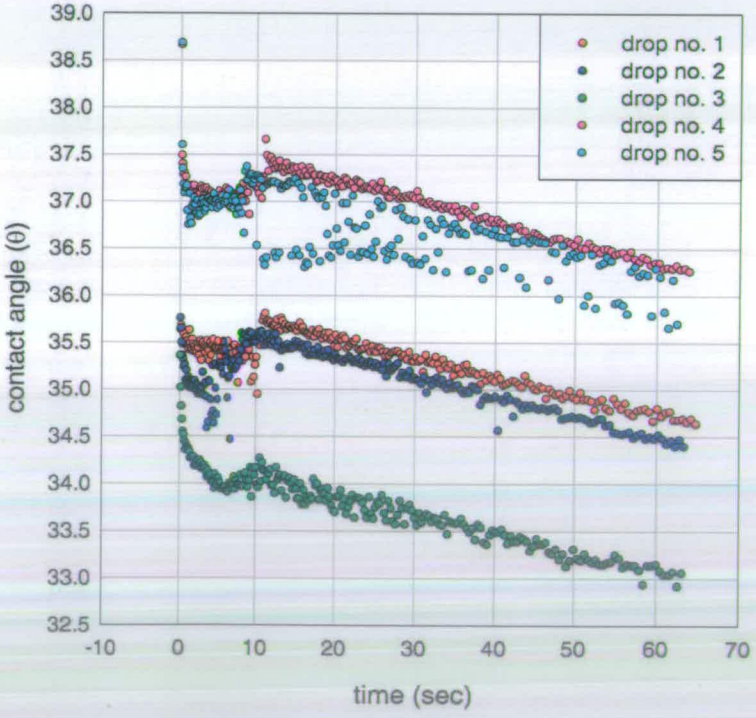

Figure 4.10.5: Contact angle vs. time graph of (5) 3-µl sessile drops of NaCl solution on thermal oxide (TO). It is speculated that the last two drops exhibit an increased contact angle because of contamination. The average time between droplets is 150 sec.

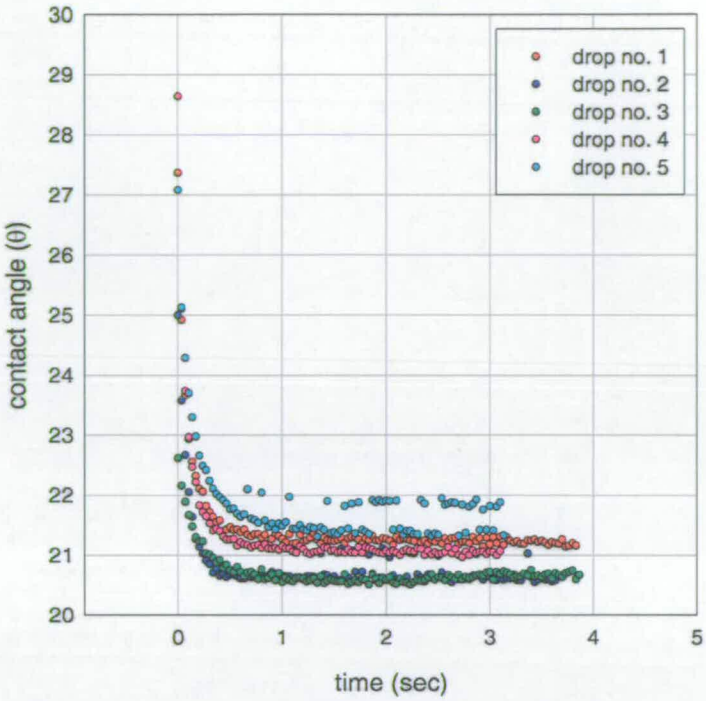

Figure 4.10.6: Contact angle vs. time graph of (5) 3-µl sessile drops of NaCl solution on thermal oxide and boron deposition (TO+B).

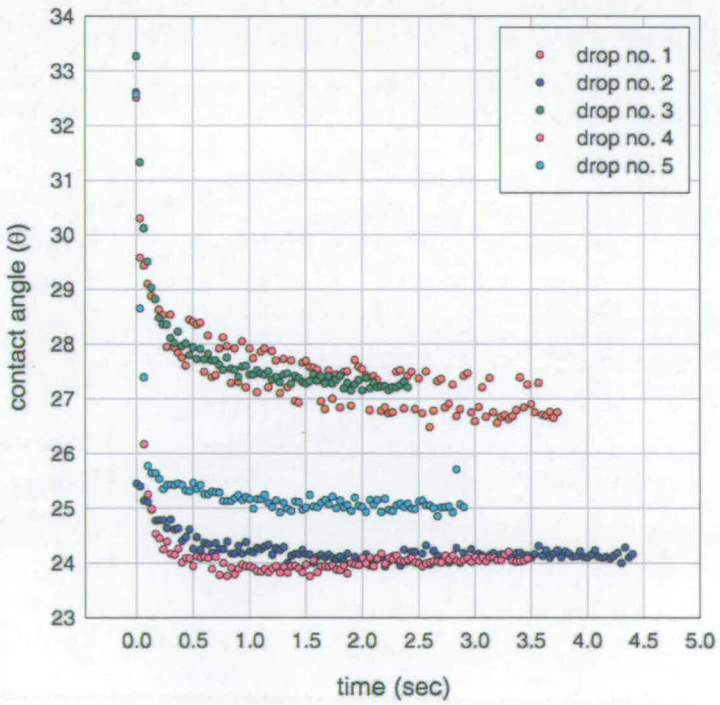

Figure 4.10.7: Contact angle vs. time graph of (5) 1-µl sessile drops of NaCl solution on LPCVD silicon nitride (N).

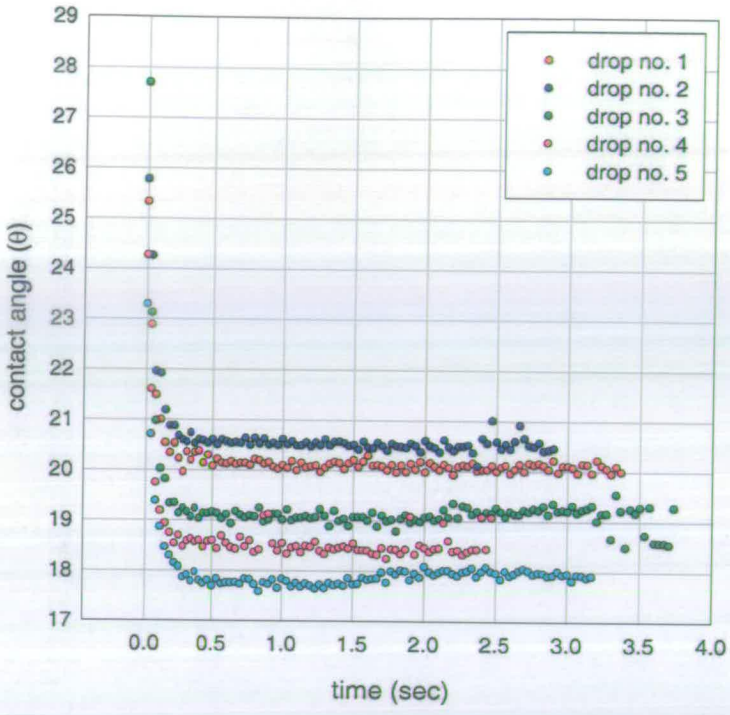

Figure 4.10.8: Contact angle vs. time graph of (5) 1-µl sessile drops of NaCl solution on LPCVD silicon nitride with boron deposition (N+B).

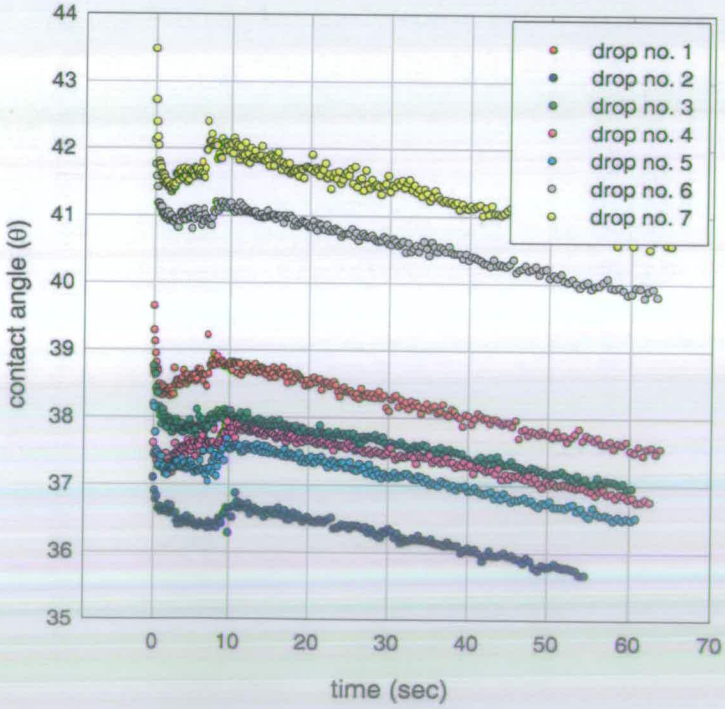

Figure 4.10.9: Contact angle vs. time graph of (7) 3-µl sessile drops of NaCl solution on oxidised silicon nitride (NO). It is speculated that the last two drops exhibit an increased contact angle because of contamination. The average time between droplets is 150 sec.

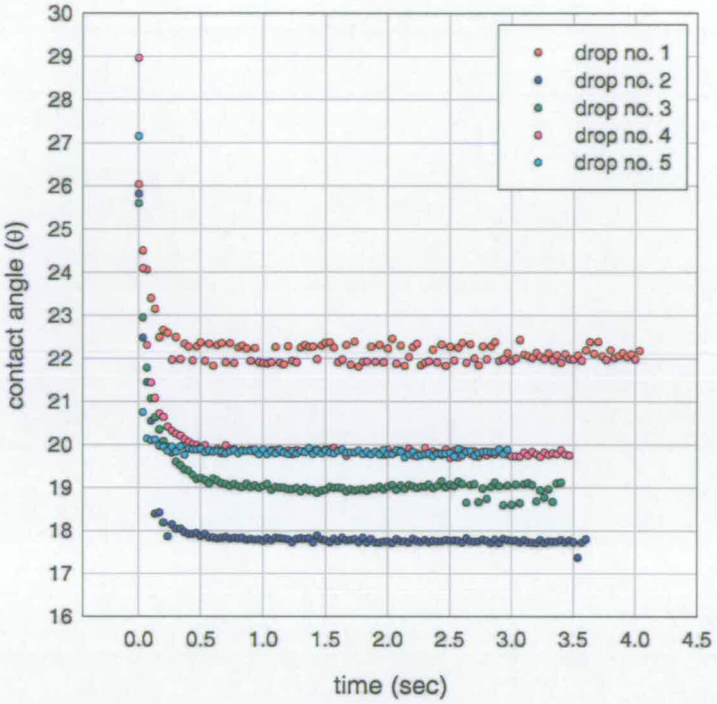

Figure 4.10.10: Contact angle vs. time graph of (5) 1-µl sessile drops of NaCl solution on oxidised silicon nitride with boron deposition (NO+B).

5 Circularity Error Measurement by Texture Analysis

5.1 Introduction

The circular shape of the pipette aperture is thought to be critical to seal formation during patch-clamping. Any non-circularity of the aperture may increase the leakage current during patch-clamping and reduce the signal-to-noise ratio of the recording. The use of a particularly square aperture may render any attempt at patch-clamping futile. Therefore, the quantification of the "sharpness" of the aperture outline was investigated. It is hypothesised that sharp corners will have the greatest impact on patch-clamp performance. This section concentrates on the attempt to fabricate reliable and highly circular apertures during microfabrication and quantify two types of circularity error, "out-of-roundness" and "sharpness".

5.2 Materials and Methods

Circular apertures were etched from the process steps listed below:

1. A single feature was printed on a mask reticule at 0.5-μm resolution for use with a lithographic process. The mask was comprised of a set of five similar features of varying size to modify the aperture diameter (see Fig. 5.2.1). To minimise production costs, the mask reticule contained no complex curving shapes, only 90° corners. Therefore, non-conventional fabrication methods were required to produce some degree of circularity from rectangular shaped objects;

2. To fabricate the feature set, a 315-nm Si_3N_4 layer was grown on a standard silicon 3" wafer. Then, a 1.18-μm layer of photoresist was spun on the topside;

3. To study the effects of de-focusing and exposure time simultaneously and interactively, a set of five focus-exposure-matrices (FEMs) was created from each of the five features on the mask (see Figure 5.2.2). Therefore, each of the five features was repeatedly exposed across the surface at a 10-μm pitch with a 5x reduction Optimetrix™ stepper[13].

[13] At extreme de-focusing the machine had difficulty sensing the wafer plane.

4. The exposure was de-focused along each column at a range of offsets of ±10 µm of 1-µm increments. To finely adjust the aperture diameter, the exposure was varied along each row from a range of 1.0 to 2.8 sec in 200-msec increments. This process formed a 21-row by 10-column matrix.

5. The set of five FEMs was repeated on three separate wafers to test for feasibility, robustness and repeatability.

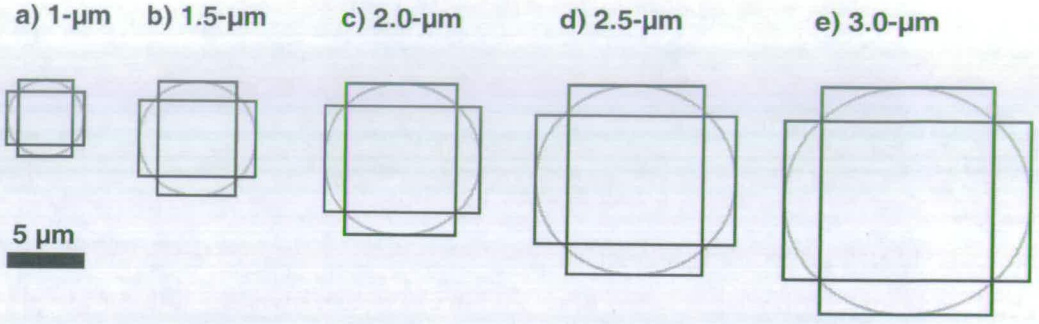

Figures 5.2.1a through 5.2.1e: Reticule layout for aperture printing of the Optimetrix™ x5 stepper. Five apertures of increasing size (final size listed after x5 reduction) of diameters of 1, 1.5, 2, 2.5 and 3 µm were utilised. The greyed circle is a representation of the printed feature (the maximum resolution does is approximately 0.5 µm). The figure is drawn to scale at x5000.

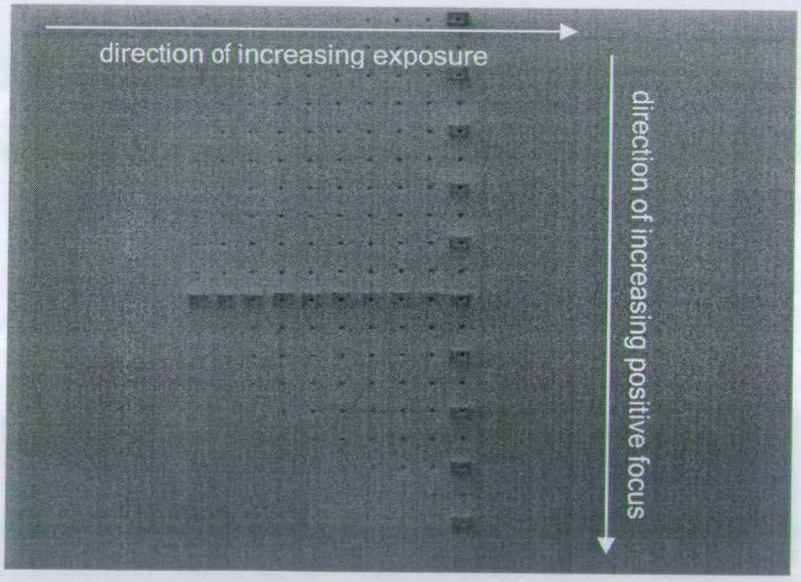

Figure 5.2.2: A 21x10 Focus-Exposure-Matrix (FEM) of the 2-µm printed feature (wafer B) etched in a 310-nm Si_3N_4 layer. Exposure is varied horizontally left to right from 1.0 sec to 2.8 sec in increments of 200 msec. Focus is varied vertically top to bottom from -10 µm to +10 µm in increments of 1 µm (0 µm is in focus). The absence of features in the top and bottom-right corners is due to insufficient light exposure of the positive photoresist from the synergistic effect of high defocusing and small exposure times. Darkened squares around apertures are interpreted as charge accumulation from high magnification SEM imaging over individual apertures.

5.3 Development of Pre-Processing Algorithm

5.3.1 Introduction

To analyse the plan-view geometry of apertures in the form of SEM images, it was necessary to pre-process each image to highlight the aperture outline. Therefore, a contrast mask was developed using standard image processing tools using Adobe© Photoshop 7. Each image was placed on a white background with a single black centred feature. To analyse the circularity and size of the feature, the outline pixel data was extracted using ImageTool™ 3 with the embedded scripting language.

5.3.2 Methods

Due to variations in focusing, contrast, and brightness of the SEM images, two separate algorithms were developed. First, images were manually grouped into high and low contrast profiles. Most often, the aperture appears as a dark-pixel feature; and the material surface appears as a random distribution of grey-pixel shades (see Figs. 5.3.2b and 5.3.2c). During development, many algorithms were tested to achieve the desired pre-processed image and a robust algorithm was developed that requires only initial image sorting. The algorithm is outlined below and the process can be viewed step-by-step in Table 5.3.2.

1. SEM images were loaded into Adobe© Photoshop ver 7.0 and cropped to a square so that the aperture radius and background border were approximately of equal distance. A 180-pixel square were used on device apertures fabricated in Section 7.3.2, and a 330-pixel square was used for all apertures in the FEM;

2. A +50 contrast adjustment was performed on each image to increase the sensitivity of the mid-tone greyscale image to highlight the outline of the aperture;

3. To increase the highlight of the outline, the image curves scale was adjusted separately for high and low-contrast images. For high-contrast images, 75% of the input was linearly mapped across 100% of the output spectrum. For low-contrast images, 50% of the input was linearly mapped across 100% of the output spectrum (see Figure 5.3.2a).[14]

4. Once a reasonable outline was established, a "glowing edges" filter was applied to the image, with settings of: 1-pixel thickness; 15/20 brightness; and 15/15

[14] Input values outside this range were mapped to absolute darkness.

smoothness[15]. The filter places white pixels where neighbouring pixels exhibit large brightness changes above a certain threshold. Likewise, the filter places dark pixels where changes in brightness do not reach threshold.

5. A "magic wand" selection was performed at the centre of the image (always located inside the aperture) at a threshold of 0 pixels;

6. Finally, an inverse selection was made to create a distinct background from the centre feature;

7. A white-pixel paint bucket was performed.

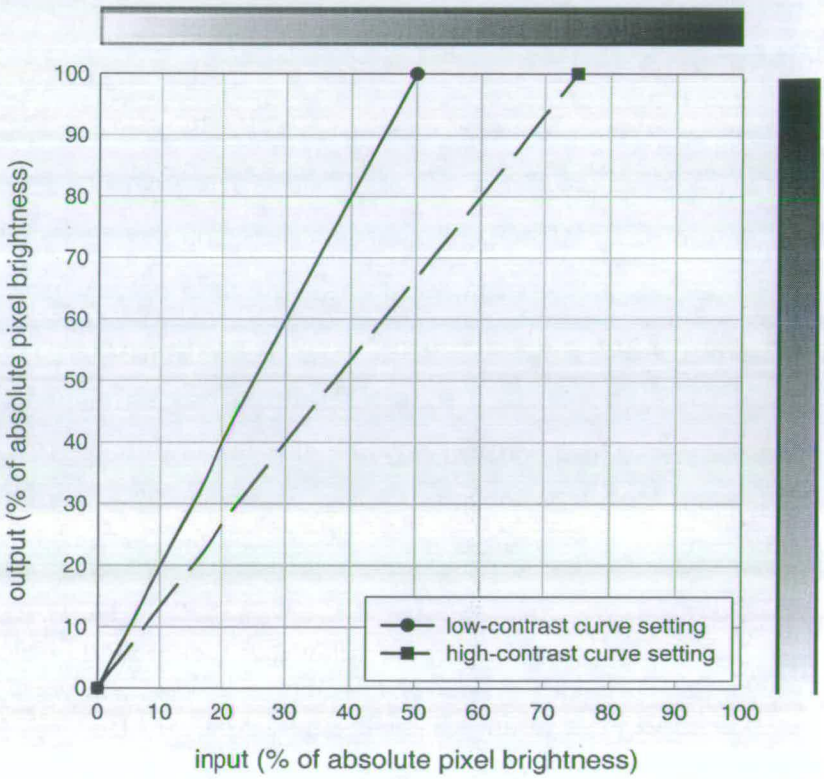

Figure 5.3.2a: Curve adjustment graph for low and high-contrast SEM images for the pre-processing algorithm.

[15] The filter smoothness setting decreases the sharpness and "softens" the white outline. The filter settings were selected to give an optimum result.

No.	Pre-Processing Algorithm Step	SEM images of device I7 and G10
		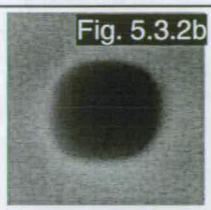 Fig. 5.3.2b 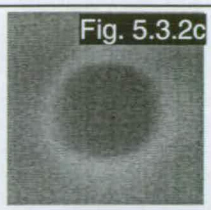 Fig. 5.3.2c
1.	crop to a 330-pixel square ROI	
		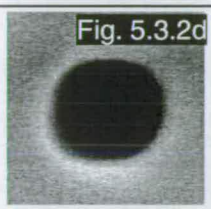 Fig. 5.3.2d 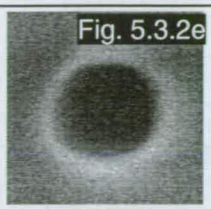 Fig. 5.3.2e
2.	contrast enhancement of +50	
		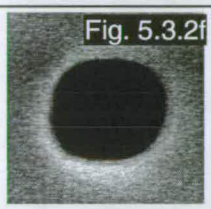 Fig. 5.3.2f 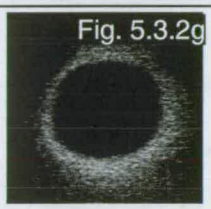 Fig. 5.3.2g
3.	curves at 75% (high-contrast I7) or	
3.	curves at 50% (low-contrast G10)	
		Fig. 5.3.2h Fig. 5.3.2i
4.	glowing edges filter applied	
		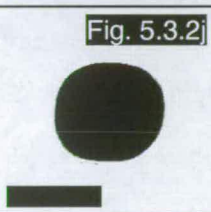 Fig. 5.3.2j Fig. 5.3.2k
5.	magic wand aperture selection	
6.	inverse selection	
7.	white colour paint bucket applied	

Table 5.3.2: Chronological list of pre-processing algorithm steps and associated SEM images for apertures I7 (high contrast) and G10 (low contrast). The scale bars are 2 μm in length.

5.3.3 Results of Pre-Processing Algorithm

Generally, the algorithm was successful in modifying each greyscale image to create a simple black and white image for post-processing analysis. By comparing the original and final images qualitatively, it was decided that the aperture profile was preserved. From a total of 107 device images, 95 images were correctly modified. Therefore, the algorithm yield was 89% (95/107), leaving a defect percentage of 11.2%. Next, the images were post-processed from an algorithm developed to analyse the profile texture in the next section.

5.4 Texture Analysis Algorithm

5.4.1 Background to Circularity Measurement

Many machine products must be inspected for quality control, and circular objects are commonplace and important in industry. Computer-aided pattern recognition machines and vision systems, called coordinate measurement machines (CMMs), have the capability to map a set of pixels outlining the object of interest. A standard control measurement for circular objects is the "circularity error", or "out-of-roundness." Here, mathematical algorithms are used to fit a circle to a set of pixel coordinates. Next, an optimisation method is used to compute the size, centre point, and the associated fitting error of the circle. Four common measurement algorithms are available that define the roundness of circular objects [88;89]. The most common types of measurement of circularity are: (1) minimum radius circumscribing circle (MCC), (2) maximum radius circumscribing circle (MIC), (3) least squares circles (LSC) and (4) the minimum radial zone circles (MZC). The MZC measurement is the only recognised algorithm that complies with current ANSI and ISO standards. [90] The MZC measurement finds two concentric circles that circumscribe and enclose the data set. [91] For methods (1), (2) and (4), these techniques involve non-linear optimisation methods to find the best-fit circle. The least-squares method is the most computationally simplistic of the group and can be calculated in closed-form. However, the least squares method is limited in accuracy and the result may be greater than 20% of the actual roundness error [89].

During patch-clamping, a high degree of aperture circularity is believed to be an important criterion for patch formation. However, the out-of-roundness aperture assessment is not the most logical measurement for this application. For example, a slightly elliptical aperture, with a relatively high index of circularity error in an MZC measurement, may perform as well as a well-defined circular aperture. However, an aperture with sharp edges may seriously increase current leakage and decrease seal probability during patch-clamping. Thus, it was decided to develop an algorithm based on texture analysis two distinct forms of circularity error: "out-of-roundness" and "sharpness."[16]

[16] Finding the best-fit circle to the data was not necessarily for this application.

5.4.2 Introduction to Development

The first task to creating an algorithm is to define the term "circularity error" in the context of texture analysis. Consider that we have a perfect smooth circle and the location of the centre point in a polar coordinate system. At any point on the circle, the radius is invariable over the entire range of θ. Now, if we apply a deformation to the circle while keeping the perimeter constant, the object decreases in circularity. If we allow the deformation to occur, the distance from the outline to the centre will not remain constant at one or more points along Δθ. Therefore, the "circularity error" of an object was defined as a measure of the deviation of the radial distance of a closed curve to the centre point, measured over the entire range of θ (360°).

Using this definition of circularity error, the next task was to quantify a measurement of deviation of the radial distance *r(t)* of the object. Two types of circularity error can be studied, denoted by type-I (CE-1) and type-II (CE-2). A single value for the out-of-roundness (CE-1) can be obtained by calculating of the root-mean-square (RMS) value of (dr/dt) along the curve. Using this approach, the value of CE-1 will be zero for a perfect circle, and will increase as the object deviates from a circular shape.

Using the same methodology as above, CE-2 can be quantified by measuring the deviation of (dr/dt). This is achieved by calculating the RMS value of (d^2r/dt^2). This measurement is particularly useful because it is sensitive to abrupt deformities of the object (i.e. sharp edges). For example, a slightly elliptical shape and a square both have CE-1 indexes above zero. However, the value of (d^2r/dt^2) for the square will be greater due to the sharp corners of the square as opposed to the smooth curves of an ellipse.

The algorithm requires re-sampling the data set at equally spaced intervals of θ to ensure all values of *r(t)* have equal weighting. Each set will have a different number of pixels depending on the shape and size of the outline. Therefore, it is not possible to re-sample the data simply by extracting points at a regular integral interval, because the total number of pixels in all data sets is not a multiple of a single common denominator[17]. Thus, a bisquare fitting algorithm of 4th degree and 0.2 sampling

[17] For example, to achieve 100 sampling intervals, only pixel sets having multiples of 100 could be re-sampled without means of interpolation.

proportion was performed on all data sets to extract 100 uniformly spaced sampling intervals along the outline. For the analysis to be independent of size, it is necessary to normalise all data sets. This was achieved by scaling $r(t)$ to $r_{max}(t)$ so that $r_{max}(t)$ was the same value for all data sets.

5.4.3 Methods

The developed algorithm to measure the circularity error is listed below. For illustrative purposes, a set of 2 figures are given to compare two apertures with a large difference in CE-1 and CE-2; one aperture is a near circle, the other has sharp corners that resembles a rounded-edge square (see Figs 5.5.1d and 5.5.1h). The algorithm uses an embedded scripting language made in ImageTool ver. 3.0.

1. The pre-processed image (see Table 5.3.2) was loaded into the software package ImageTool ver 3.0;

2. The image outline was extracted as a list of pixel coordinates in the Results Window (see script in Appendix A.1.2);

3. Since the algorithm does not require fitting a circle to the data set, the centre point was estimated to be the centroid of the object. To estimate the centroid, the area of the feature (considered a polygon of many vertices) was initially calculated from the general equation below:

$$A = 0.5 \cdot \sum_{i=0}^{N-1} (x_i \cdot y_{i+1} - x_{i+1} \cdot y_i)$$

4. The centroid of the feature was calculated from the equations below:

$$X_{centre} = \frac{1}{6 \cdot A} \sum_{i=0}^{N-1} (x_i + x_{i+1}) \cdot (x_i \cdot y_{i+1} - x_{i+1} \cdot y_i)$$

$$Y_{centre} = \frac{1}{6 \cdot A} \sum_{i=0}^{N-1} (y_i + y_{i+1}) \cdot (x_i \cdot y_{i+1} - x_{i+1} \cdot y_i)$$

5. A Cartesian to polar coordinate transformation was applied to the data with the centroid as the origin, and displayed in the Results Window;

6. The pixel data was selected from the Results Window and pasted into SigmaPlot 2000©. To correct a bug in the ImageTool, the curve was flipped across the X-axis by applying the function $\theta_{adj} = 360° - \theta$, and the polar to Cartesian coordinate transformation was re-applied;

7. A smoothing algorithm was applied to the polar data using θ as the independent variable. The smoothing algorithm incorporated the use of a bisquare weight function at 0.2 sampling proportion to a 4th order polynomial. Specifically, the bi-square weight function is $(1-\mu^2)^2$, where μ is the normalised distance of each data point to the smoothed curve. The data set was re-sampled and parameterised at 100 intervals of Δt along the full range of θ. Figures 5.4.3a through 5.4.3d contain graphs of the extracted pixel data and the bisquare fitted curve.[18]

8. The maximum value r_{max} of all apertures was calculated. Then, the extracted data from every aperture was normalised to r_{max}.

9. To quantify the circularity error, the 1st derivative of r (dr/dt) was calculated at each parameterised sampling interval by use of a difference function on two consecutive values of r inside the data range.[19] Graphs of the 1st derivative for both shapes can be found in Figures 5.4.3e and 5.4.3f;

10. The RMS value of the 1st derivative was calculated by the general equation below:

$$\sqrt{\frac{1}{N-1}\int_{i=0}^{N-1}[f(t)]^2 dt}$$

11. The 2nd derivative of r (d^2r/dt^2) was calculated by a difference function on (dr/dt) at each parameterized sampling interval as in step 9. Graphs of the 2nd derivative for both shapes can be found in Figures 5.4.3g and 5.4.3h;

12. The RMS value of the 2nd derivative was calculated by the general equation in step 10, substituting (N-2) for (N-1).

[18] Figures 5.5.1a through 5.5.1k were used to test and finalise the polynomial order and sampling proportion parameters for the smoothing algorithm.

[19] The derivative was undefined at the last value and excluded in the following step.

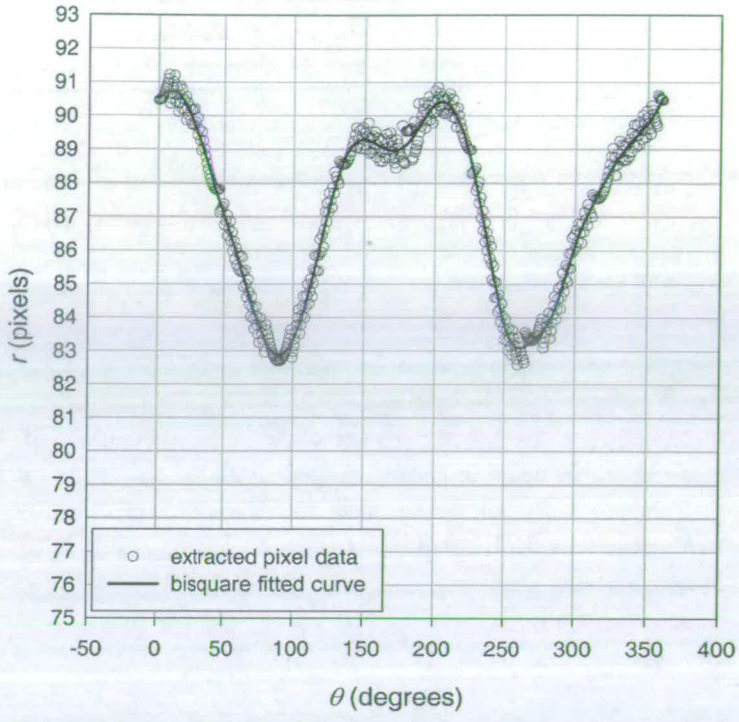

Figure 5.4.3a: Graph of the radial distance (in pixels) from the centroid to the outline from 0 to 360° of a circular aperture (from Fig. 5.5.1h). The circle symbol diameter represents a length of 0.32 pixels.

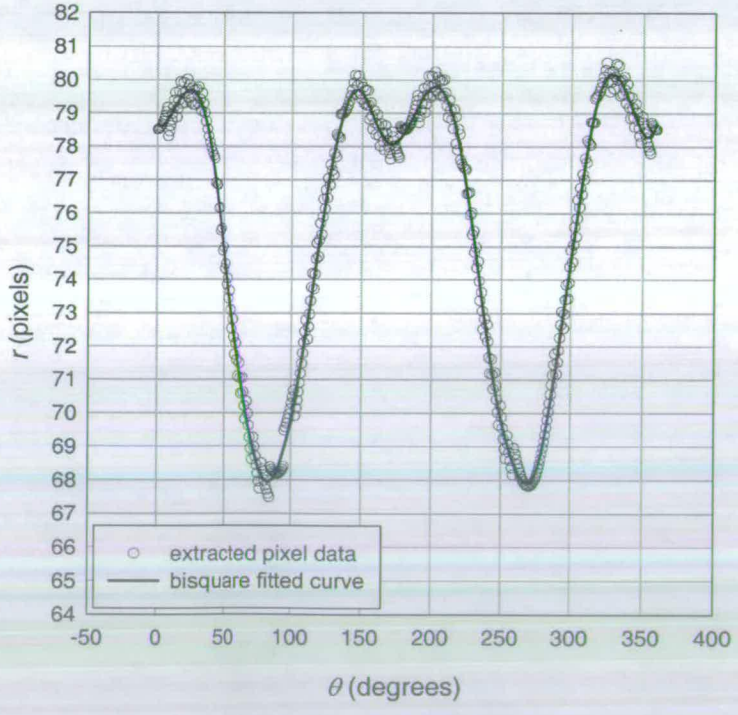

Figure 5.4.3b: Graph of the radial distance (in pixels) from the centroid to the outline from 0 to 360° of a square aperture (from Fig. 5.5.1d). The circle symbol diameter represents a length of 0.32 pixels.

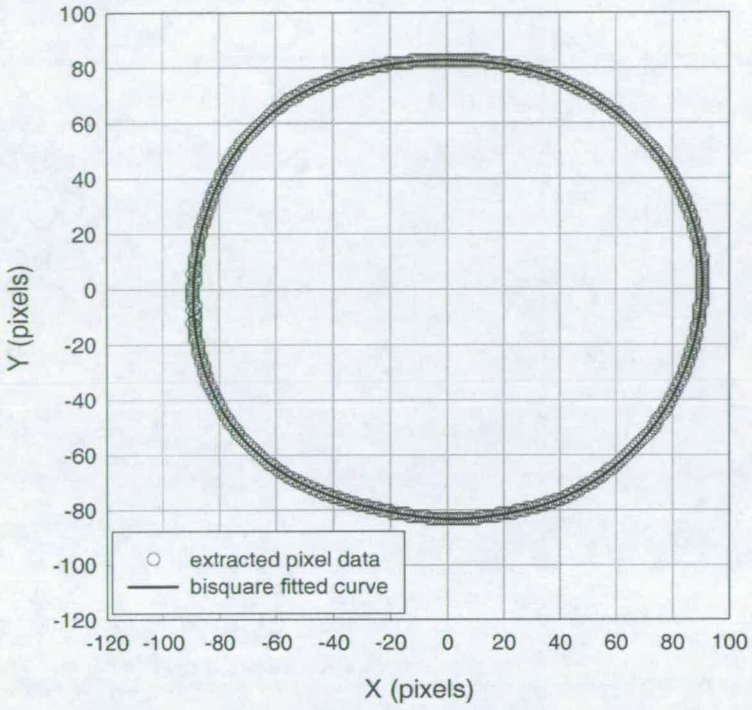

Figure 5.4.3c: Graph of the smoothed and original XY data set of a circular aperture (from Fig. 5.5.1h). The circle symbol diameter represents a length of 4 pixels.

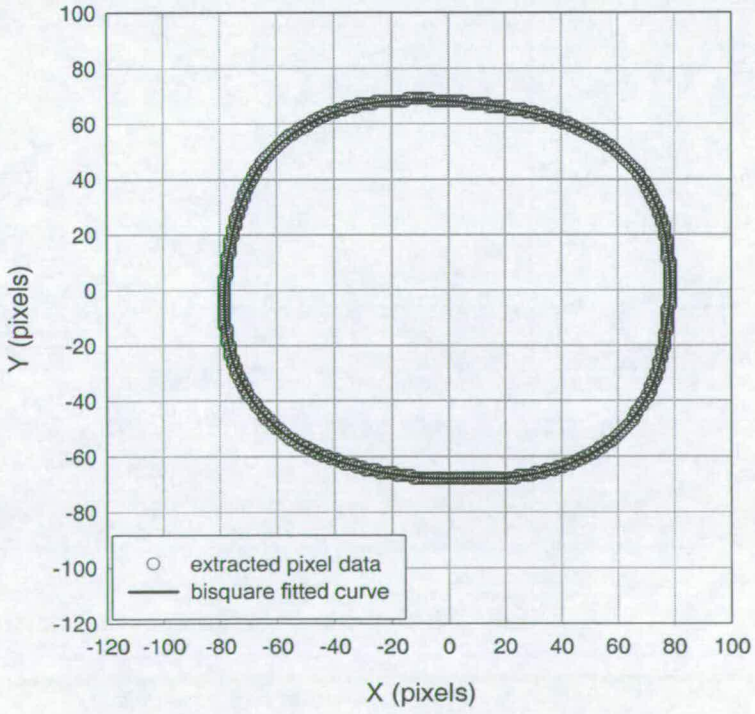

Figure 5.4.3d: Graph of the smoothed and original XY data set of a square aperture (from Fig. 5.5.1d). The circle symbol diameter represents a length of 4 pixels.

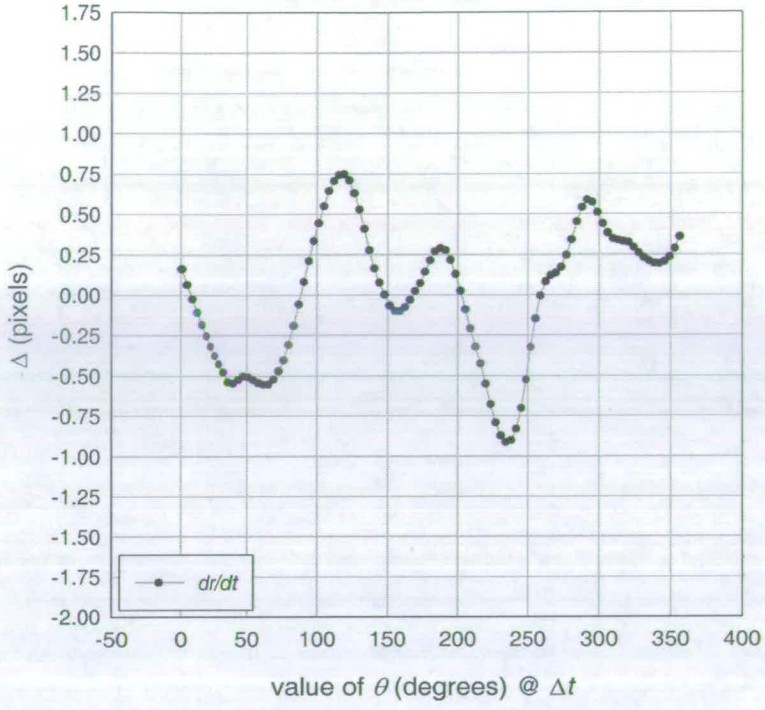

Figure 5.4.3e: Graph of *dr/dt* vs. θ of a circular aperture (from Fig. 5.5.1h).

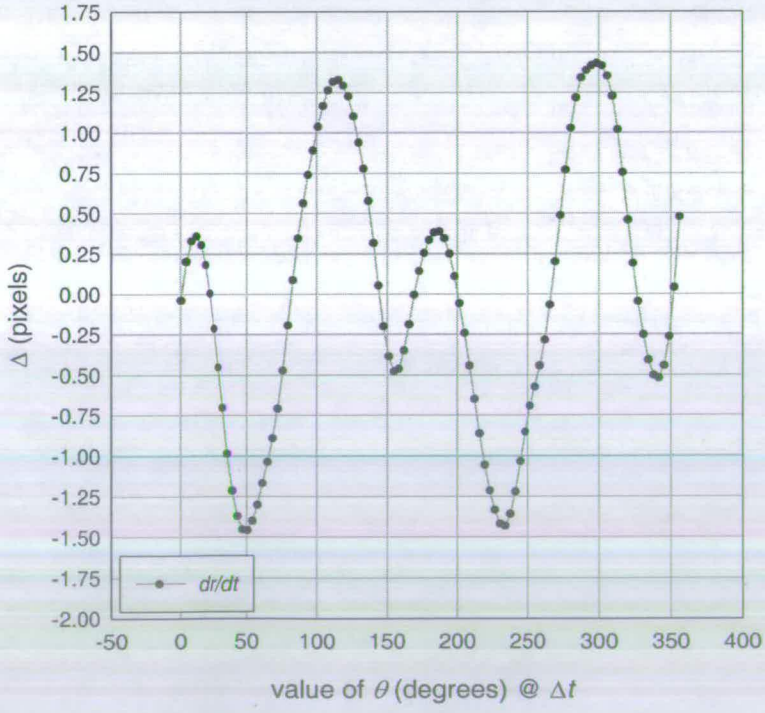

Figure 5.4.3f: Graph of *dr/dt* vs. θ of a square aperture (from Fig. 5.5.1d).

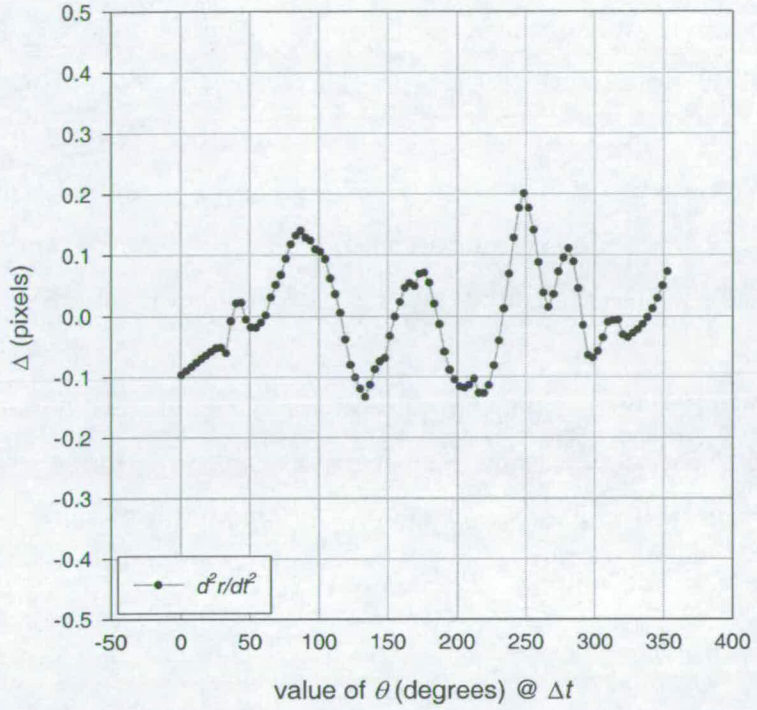

Figure 5.4.3g: Graph of d^2r/dt^2 vs. θ of a circular aperture (from Fig. 5.5.1h).

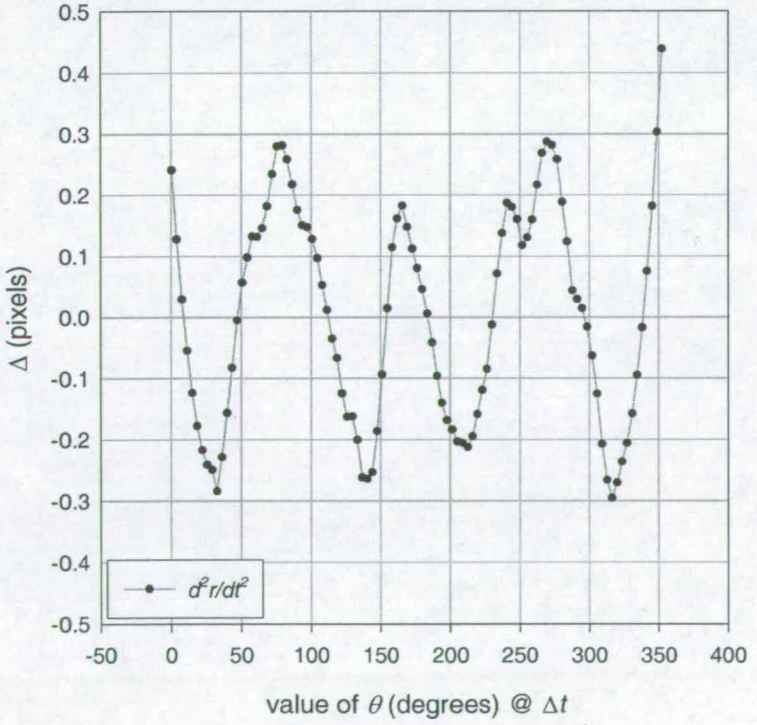

Figure 5.4.3h: Graph of d^2r/dt^2 vs. θ of a square aperture (from Fig. 5.5.1d).

5.5 Results

All apertures were pre-processed from the 2 and 3-μm size FEMs from all three wafers (see Tables 5.5.1 through 5.5.4).[20] The sets were analysed to study the following: the type-I and type-II circularity error; the diameter (the length of the major axis); and the elongation (ratio of major axis to minor axis). To study the effect of focus offset and exposure time, the exposure was kept constant at 2.8 sec and focus offset at +10 μm respectively. Graphs of the results can be found in Figures 5.5.7 through 5.5.14.

The majority of the apertures fabricated in Chapter 7 were processed and analysed (see Tables 5.5a through 5.5c). The apertures were sorted in ascending order of circularity error type-II (CE-2). A histogram of CE-2 from the apertures is given in Figure 5.5.22.

[20] Two of the images were defective and were not included.

-10 µm	-8 µm	-6 µm	-4 µm	-2 µm	0 µm	+2 µm	+4 µm	+6 µm	+8 µm	+10 µm
										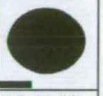
5.5.1a	5.5.1b	5.5.1c	5.5.1d	5.5.1e	5.5.1f	5.5.1g	5.5.1h	5.5.1i	5.5.1j	5.5.1k

-10 µm	-8 µm	-6 µm	-4 µm	-2 µm	0 µm	+2 µm	+4 µm	+6 µm	+8 µm	+10 µm
5.5.2a	5.5.2b	5.5.2c	5.5.2d	5.5.2e	5.5.2f	5.5.2g	5.5.2h	5.5.2i	5.5.2j	5.5.2k

-10 µm	-8 µm	-6 µm	-4 µm	-2 µm	0 µm	+2 µm	+4 µm	+6 µm	+8 µm	+10 µm
5.5.3a	5.5.3b	5.5.3c	5.5.3d	5.5.3e	5.5.3f	5.5.3g	5.5.3h	5.5.3i	5.5.3j	5.5.3k

Table 5.5.1: Acquired apertures from the 3-µm FEM of test wafers no. 1, 2 and 3. The table includes Figures 5.5.1a through 5.5.1k (wafer no. 1), 5.5.2a through 5.5.2k (wafer no. 2) and 5.5.3a through 5.5.3k (wafer no. 3). The focus offset was varied from -10 to +10 µm focus in increments of 2 µm. The exposure time is 2.8 sec. The scale bar length is 2 µm.

-10 µm	-8 µm	-6 µm	-4 µm	-3 µm	0 µm	+2 µm	+4 µm	+5 µm	+7 µm
	image defect								
5.5.4a		5.5.4b	5.5.4c	5.5.4d	5.5.4e	5.5.4f	5.5.4g	5.5.4h	5.5.4i

-8 µm	-6 µm	-4 µm	-2 µm	0 µm	+2 µm	+4 µm	+6 µm
5.5.5a	5.5.5b	5.5.5c	5.5.5d	5.5.5e	5.5.5f	5.5.5g	5.5.5h

-10 µm	-8 µm	-6 µm	-4 µm	-2 µm	0 µm	+2 µm	+4 µm	+6 µm	+8 µm
	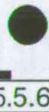							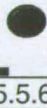	
5.5.6a	5.5.6b	5.5.6c	5.5.6d	5.5.6e	5.5.6f	5.5.6g	5.5.6h	5.5.6i	5.5.6j

Table 5.5.2: Acquired apertures from the 2-µm FEM of test wafers no. 1, 2 and 3. The table includes Figures 5.5.4a through 5.5.4i (wafer no. 1), 5.5.5a through 5.5.5h (wafer no. 2) and 5.5.6a through 5.5.6j (wafer no. 3). The focus offset was varied from -10 to +10 µm focus in increments of 2 µm. The exposure time is 2.8 sec. The scale bar length is 2 µm.

1.2 sec	1.4 sec	1.6 sec	1.8 sec	2.0 sec	2.2 sec	2.4 sec	2.6 sec	2.8 sec
5.5.7a	5.5.7b	5.5.7c	5.5.7d	5.5.7e	5.5.7f	5.5.7g	5.5.7h	5.5.7i

1.2 sec	1.4 sec	1.6 sec	1.8 sec	2.0 sec	2.2 sec	2.4 sec	2.6 sec	2.8 sec
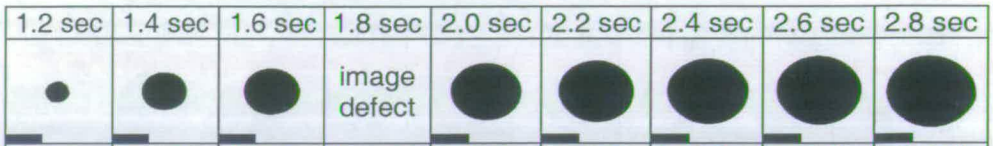			image defect					
5.5.8a	5.5.8b	5.5.8c	5.5.8d	5.5.8e	5.5.8f	5.5.8g	5.5.8h	5.5.8i

1.0 sec	1.2 sec	1.4 sec	1.6 sec	1.8 sec	2.0 sec	2.2 sec	2.4 sec	2.6 sec	2.8 sec
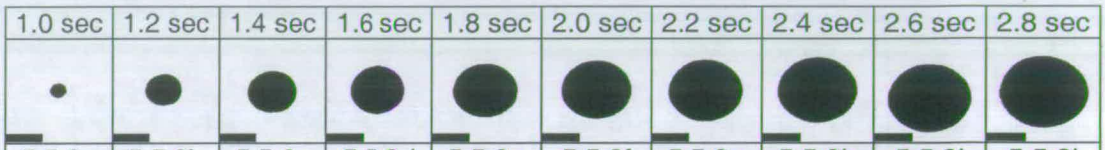									
5.5.9a	5.5.9b	5.5.9c	5.5.9d	5.5.9e	5.5.9f	5.5.9g	5.5.9h	5.5.9i	5.5.9j

Table 5.5.3: Acquired apertures from the 3-µm FEM of test wafers no. 1, 2 and 3. The table includes Figures 5.5.7a through 5.5.7i (wafer no. 1), 5.5.8a through 5.5.8i (wafer no. 2) and 5.5.9a through 5.5.9j (wafer no. 3). The exposure was varied from 1.2 sec to 2.8 sec, in increments of 200 msec (focus held constant at +10 µm). The scale bar length is 2 µm.

1.0 sec	1.2 sec	1.4 sec	1.6 sec	1.8 sec	2.0 sec	2.2 sec	2.4 sec	2.6 sec	2.8 sec
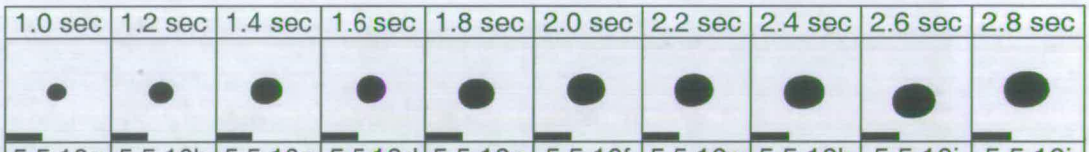									
5.5.10a	5.5.10b	5.5.10c	5.5.10d	5.5.10e	5.5.10f	5.5.10g	5.5.10h	5.5.10i	5.5.10j

1.2 sec	1.4 sec	1.6 sec	1.8 sec	2.0 sec	2.2 sec	2.4 sec	2.6 sec	2.8 sec
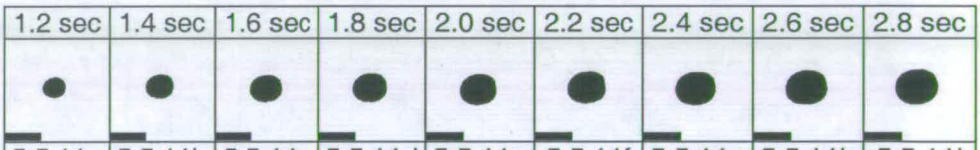								
5.5.11a	5.5.11b	5.5.11c	5.5.11d	5.5.11e	5.5.11f	5.5.11g	5.5.11h	5.5.11i

1.2 sec	1.4 sec	1.6 sec	1.8 sec	2.0 sec	2.2 sec	2.4 sec	2.6 sec	2.8 sec
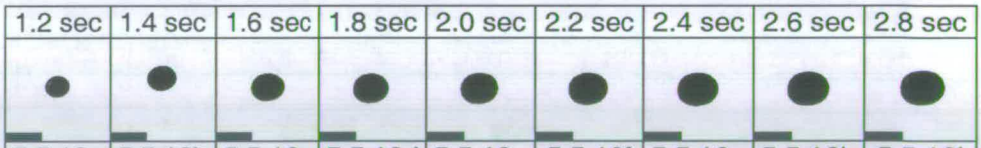								
5.5.12a	5.5.12b	5.5.12c	5.5.12d	5.5.12e	5.5.12f	5.5.12g	5.5.12h	5.5.12i

Table 5.5.4: Acquired apertures from the 2-µm FEM of test wafers no. 1, 2 and 3. The table includes Figures 5.5.10a through 5.5.10j (wafer no. 1), 5.5.11a through 5.5.11i (wafer no. 2) and 5.5.12a through 5.5.12i (wafer no. 3). The exposure was varied from 1.2 sec to 2.8 sec, in increments of 200 msec (focus held constant at +10 µm). The scale bar length is 2 µm.

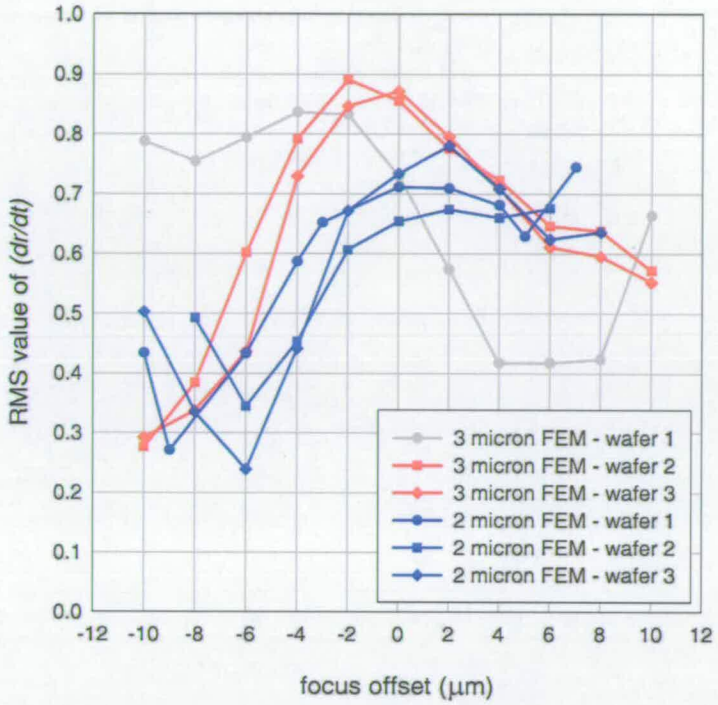

Figure 5.5.13: Circularity error type-I vs. focus offset.

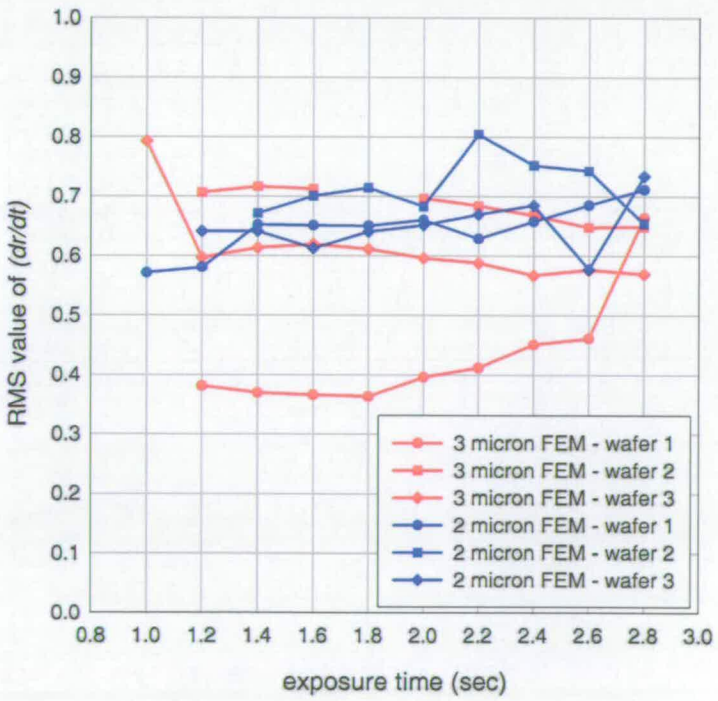

Figure 5.5.14: Circularity error type-I vs. exposure time.

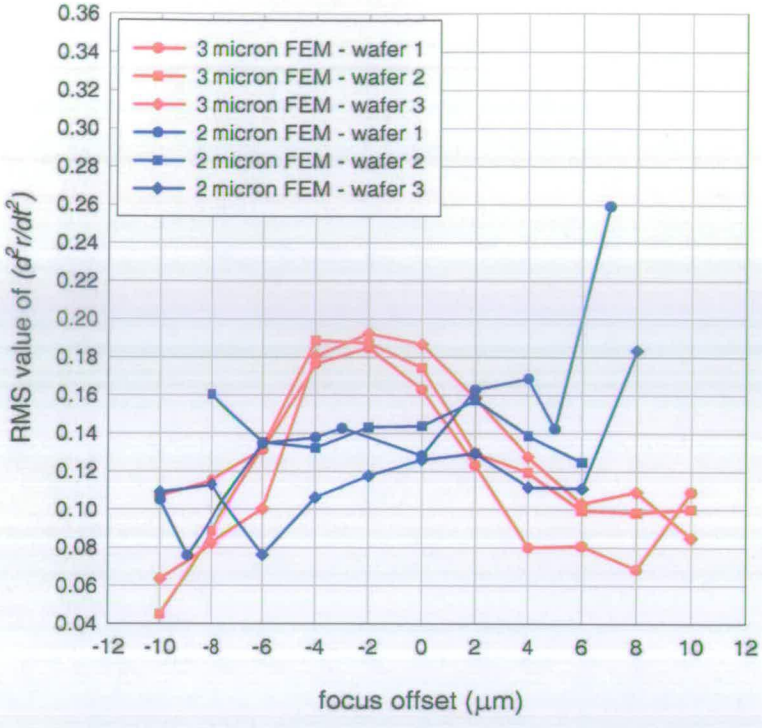

Figure 5.5.15: Circularity error type-II vs. focus offset.

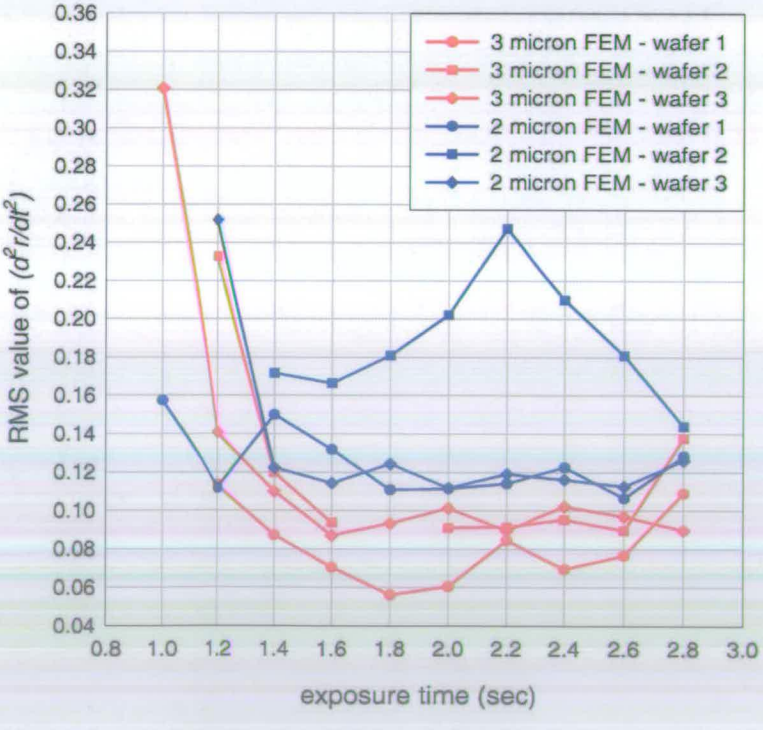

Figure 5.5.16: Circularity error type-II vs. exposure time.

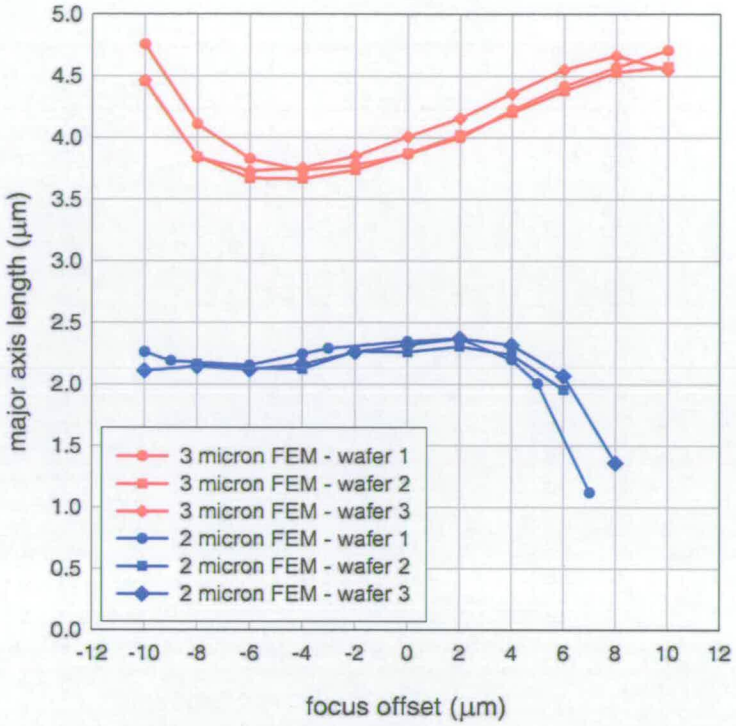

Figure 5.5.17: Aperture diameter vs. focus offset.

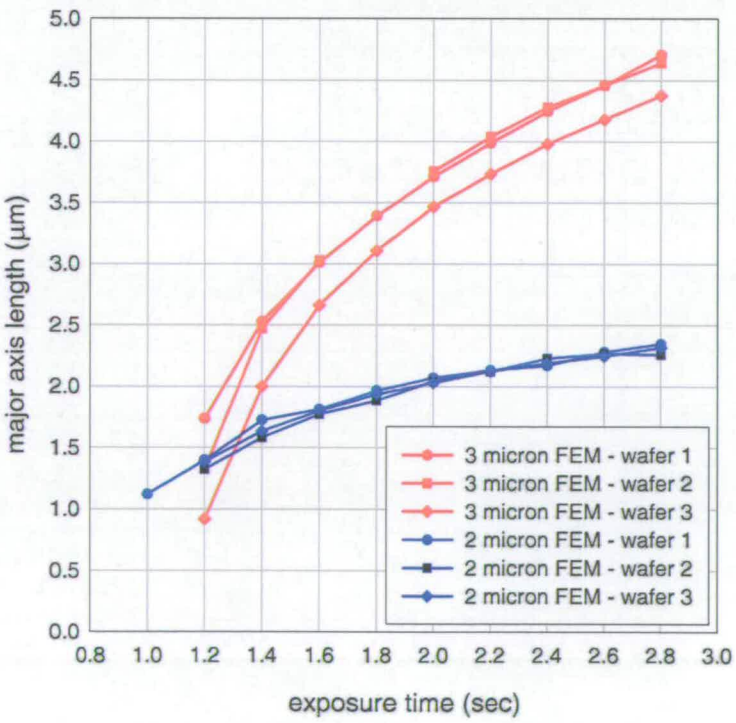

Figure 5.5.18: Aperture diameter vs. exposure time.

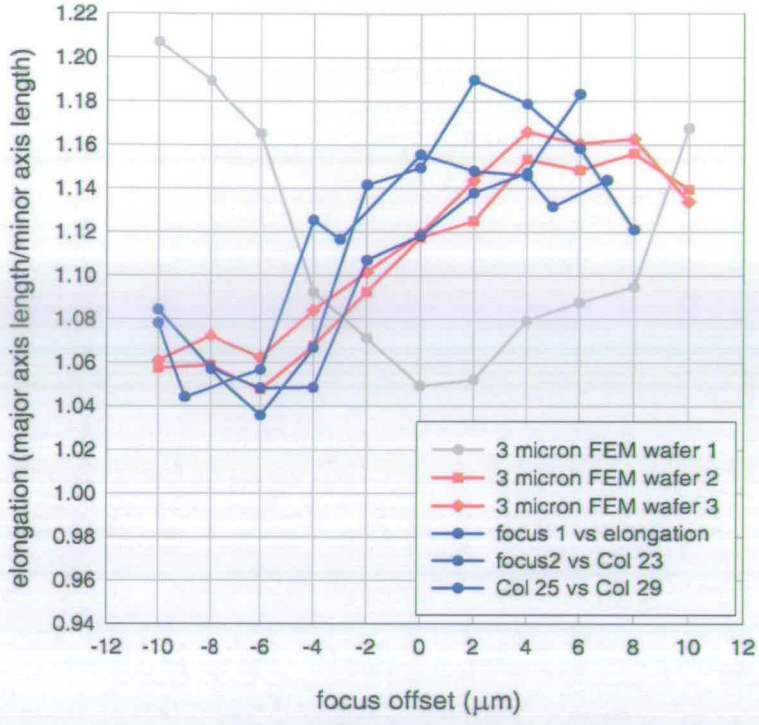

Figure 5.5.19: Elongation vs. focus offset.

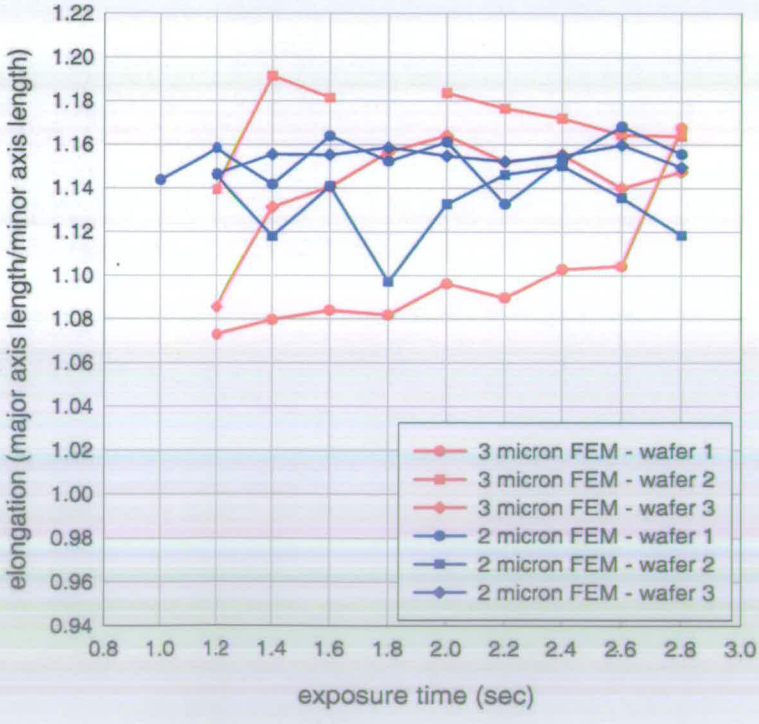

Figure 5.5.20: Elongation vs. exposure time.

Aperture	G8	I6	I7	H9	D7	C9	I5
Image	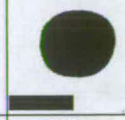						
CE-1	0.6028	0.6569	0.6414	0.6257	0.6604	0.6117	0.6870
CE-2	0.1481	0.1518	0.1530	0.1538	0.1576	0.1577	0.1609
Figure	5.5.21.g8	5.5.21.i6	5.5.21.i7	5.5.21.h9	5.5.21.d7	5.5.21.c9	5.5.21.i5
Aperture	D8	H5	H4	E7	H8	G3	C7
Image	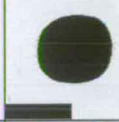	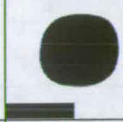	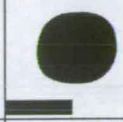	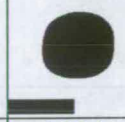	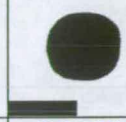		
CE-1	0.6354	0.6497	0.6839	0.6646	0.6304	0.6674	0.6641
CE-2	0.1648	0.1655	0.1656	0.1671	0.1672	0.1690	0.1707
Figure	5.5.21.d8	5.5.21.h5	5.5.21.h4	5.5.21.e7	5.5.21.h8	5.5.21.g3	5.5.21.c7
Aperture	G9	C6	G4	G10	G11	F7	F10
Image	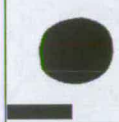		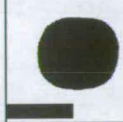	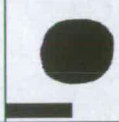		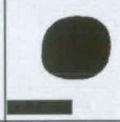	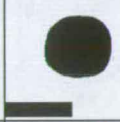
CE-1	0.5858	0.9047	0.7165	0.7454	0.8240	0.6836	0.5745
CE-2	0.1725	0.1735	0.1773	0.1789	0.1818	0.1832	0.1843
Figure	5.5.21.g9	5.5.21.c6	5.5.21.g4	5.5.21.g10	5.5.21.g11	5.5.21.f7	5.5.21.f10
Aperture	B7	I9	E10	H7	E9	E6	C4
Image	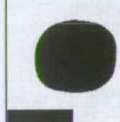		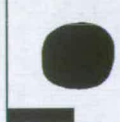	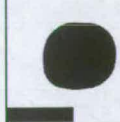			
CE-1	0.7408	0.7855	0.7055	0.6876	0.6665	0.8786	0.8810
CE-2	0.1852	0.1869	0.1881	0.1882	0.1884	0.1941	0.1957
Figure	5.5.21.b7	5.5.21.i9	5.5.21.e10	5.5.21.h7	5.5.21.e9	5.5.21.e6	5.5.21.c4
Aperture	F8	E8	J6	E3	F4 *	B6	G2
Image							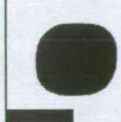
CE-1	0.5740	0.6991	0.7488	0.9536	0.9889	0.9660	0.8630
CE-2	0.1973	0.1979	0.1995	0.2001	0.2005	0.2049	0.2064
Figure	5.5.21.f8	5.5.21.e8	5.5.21.j6	5.5.21.e3	5.5.21.f4	5.5.21.b6	5.5.21.g2
Aperture	I4	B10	G7	D10	J5	G5	F2
Image	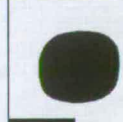		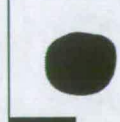	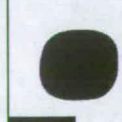		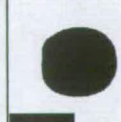	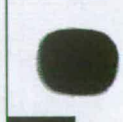
CE-1	0.8093	0.9323	0.7884	0.8606	0.8488	0.7184	1.0306
CE-2	0.2066	0.2084	0.2109	0.2112	0.2142	0.2170	0.2177
Figure	5.5.21.i4	5.5.21.b10	5.5.21.g7	5.5.21.d10	5.5.21.j5	5.5.21.g5	5.5.21.f2

Table 5.5a: Post-processed aperture SEM images, sorted in ascending order by circularity error type-II (CE-2) from 0.1481 to 0.2177.

Aperture	E2	I8	G6	F9	K3	K4	E4
Image							
CE-1	1.0181	0.8465	0.8892	0.6303	0.8924	0.9803	0.8035
CE-2	0.2203	0.2217	0.2260	0.2265	0.2288	0.2362	0.2386
Figure	5.5.21.e2	5.5.21.i8	5.5.21.g6	5.5.21.f9	5.5.21.k3	5.5.21.k4	5.5.21.e4
Aperture	D4	D1	C3	I11	H10	J10	D3
Image	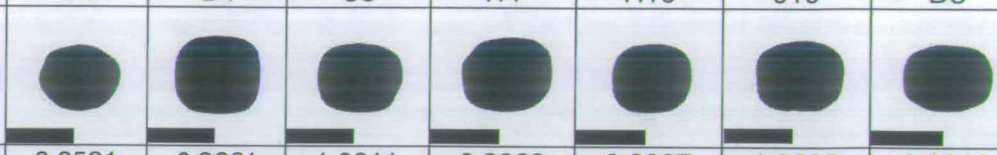						
CE-1	0.8531	0.9621	1.0211	0.9263	0.8327	1.0285	1.0312
CE-2	0.2400	0.2418	0.2477	0.2480	0.2482	0.2494	0.2504
Figure	5.5.21.d4	5.5.21.d1	5.5.21.c3	5.5.21.i11	5.5.21.h10	5.5.21.j10	5.5.21.d3
Aperture	J7	B8 *	H6	J9	E5 *	B5	B9
Image							
CE-1	1.0057	1.0314	0.8405	1.0909	0.9733	1.0515	1.0352
CE-2	0.2576	0.2588	0.2657	0.2695	0.2700	0.2703	0.2726
Figure	5.5.21.j7	5.5.21.b8	5.5.21.h6	5.5.21.j9	5.5.21.e5	5.5.21.b5	5.5.21.b9
Aperture	I1	K8	A9	B2	D2	A6	K7
Image							
CE-1	1.0439	1.0628	1.0203	1.0223	1.1283	1.0577	1.0736
CE-2	0.2740	0.2744	0.2753	0.2757	0.2760	0.2820	0.2844
Figure	5.5.21.i1	5.5.21.k8	5.5.21.a9	5.5.21.b2	5.5.21.d2	5.5.21.a6	5.5.21.k7
Aperture	B4	J8	K6	H11	A8	A7	F3 *
Image	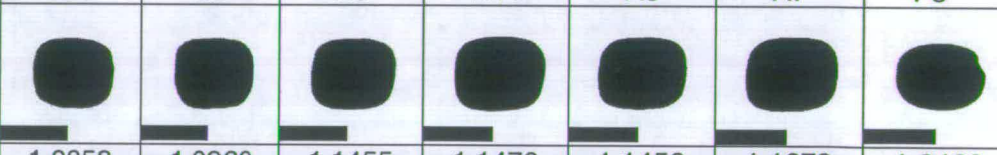						
CE-1	1.0358	1.0969	1.1455	1.1476	1.1456	1.1679	1.0468
CE-2	0.2850	0.2859	0.2866	0.2878	0.2914	0.2969	0.2974
Figure	5.5.21.b4	5.5.21.j8	5.5.21.k6	5.5.21.h11	5.5.21.a8	5.5.21.a7	5.5.21.f3
Aperture	J4	I2	J3	J3	H1	K5	G1
Image							
CE-1	1.1495	1.1156	1.1799	1.1934	1.1924	1.1729	1.1745
CE-2	0.3018	0.3022	0.3033	0.3048	0.3164	0.3175	0.3221
Figure	5.5.21.j4	5.5.21.i2	5.5.21.j3	5.5.21.j2	5.5.21.h1	5.5.21.k5	5.5.21.g1

Table 5.5b: Post-processed aperture SEM images, sorted in ascending order by circularity error type-II (CE-2) from 0.2203 to 0.3221.

Aperture	F1	C10	B3 *	E1	F5 *	H3	D6 *
Image	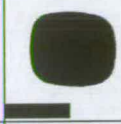	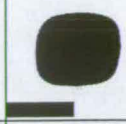		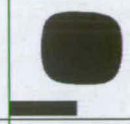			
CE-1	1.1460	1.1462	1.2264	1.1602	1.4389	1.0246	1.2165
CE-2	0.3244	0.3244	0.3247	0.3288	0.3850	0.3895	0.4042
Figure	5.5.21.f1	5.5.21.c10	5.5.21.b3	5.5.21.e1	5.5.21.f5	5.5.21.h3	5.5.21.d6

Aperture	C8 *	D5 *
Image	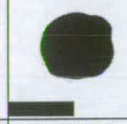	
CE-1	1.0592	2.0734
CE-2	0.4089	0.8154
Figure	5.5.21.c8	5.5.21.d5

Table 5.5c: Post-processed aperture SEM images, sorted in ascending order by circularity error type-II (CE-2) from 0.3244 to 0.8154.

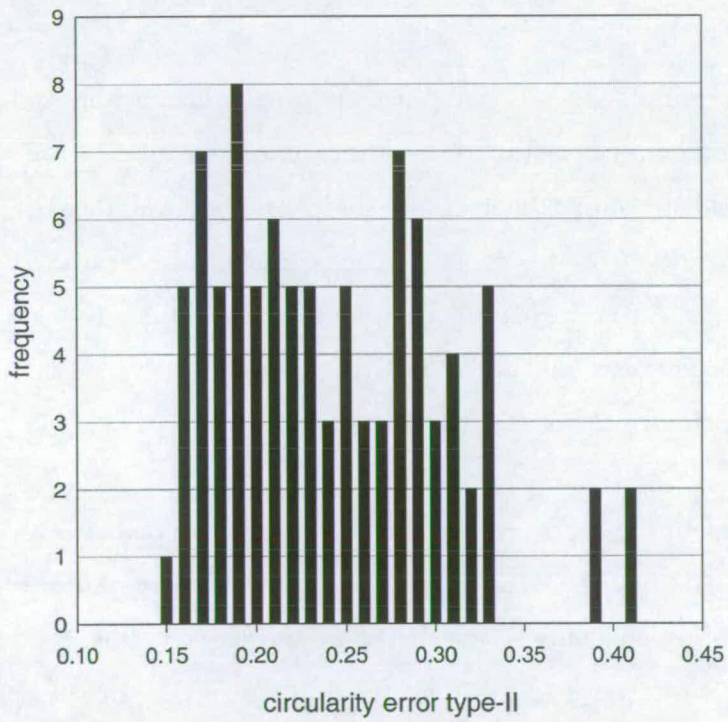

Figure 5.5.22: Histogram of circularity error type-II (CE-2).

5.6 Discussion

5.6.1 Focus-Exposure-Matrix (FEM)

Qualitatively, the apertures become "more round" as the exposure was de-focused. The value of CE-1 and CE-2 decreases proportionally with this observation and indicates these are realistic measures of the actual perceived roundness error. The printed apertures exhibited the greatest non-circularity around a focus offset of -2 μm (see Figure 5.5.13). The apertures printed from the 3-μm feature display the most affect from de-focusing from the dataset (the 2-μm feature approaches the limitations in printing resolution of approximately 0.5 μm). However, the 3-μm FEM from wafer 1 exhibited a different trend due to the affect of elongation of the printing (see the grey trace in Figure 5.5.19). The exposure time has little effect on CE-1, except at extreme de-focusing when elongation becomes large or when the photoresist is insufficiently exposed at low exposure times (see Figure 5.5.14).

The sharpness (CE-2) of the 3-μm aperture is greatest around a focus offset at -2 μm and smoothens out as the focus offset is increased (see Figure 5.5.15). However, the 2-μm FEM feature exhibits little sharpness because the 0.5-μm printing resolution prevents the effect from being seen. Instead, the sharpness shows a general trend upward as offset increases, again due to the effect of elongation. Generally, the exposure time has little affect on CE-2, except at extreme de-focusing offsets and when printing abnormalities exist (see Figure 5.5.16).[21]

De-focusing the exposure also affects the aperture diameter (see Figure 5.5.17). When de-focused, the light beam spreads and exposes more photoresist, creating a wider area of exposure, and thus a larger aperture. Generally, this trend is shown for the 3-μm FEM. This trend is less evident for the 2-μm FEM, but at a +4-μm focus offset, the diameter rapidly decreases because the photoresist becomes insufficiently exposed. There is a strong relationship between exposure time and the aperture diameter for all printed features. The increase in exposure time increases the exposure area of the printed pattern (see Figure 5.5.18).

[21] For example, the 2-μm FEM from wafer 2 has a printing defect in the upper right corner (see Table 5.5.4: Figures 5.5.11b through 5.5.11h).

Generally, the elongation increases as the focus offset is adjusted positively (see Figure 5.5.19). The grey trace exhibited an abnormal elongation printing effect that influenced the results of the circularity error (see Figure 5.5.13). No correlation is evident between exposure time and elongation (see Figure 5.5.20).

5.6.2 Patch Apertures

Qualitatively, the apertures (fabricated from Ch. 7) increase in sharpness as the value of CE-2 increases and indicates that the CE-2 measurement is realistic value of the actual sharpness. For example, the apertures appear very smooth in first row of Table 5.5a but very sharp in the final two rows of Table 5.5c. Half of the apertures exhibit CE-2 values ≤ 0.23 (see Figure 5.5.22). Both types of circularity error (CE-1 and CE-2) are highly correlated.[22] This is explained by the fact that the object exhibits some shape in-between a circle and a square with rounded corners (no elliptical shapes are evident).

5.7 Conclusion

The results indicate that it is possible to fabricate features to some degree of circularity using masks with rectangular shapes. Therefore, it is not necessary to use circular masks. This tolerance is dependent on a number of factors, including: drift in the offset of the stepper focus; the degree of thermal oxide growth along the <100> plane (see Chapter 6); and defects in the aperture from etching and boron deposition at 1000°C (see Section 7.3.8).

The developed algorithm is a powerful tool in assessing object circularity error as a measure of "out-of-roundness" and "sharpness." Thus, the analytical method studied here may be used as a control engineering measure for fabrication of circular (or non-circular) features.

---

[22] Spearman Rank Order Correlation Test; correlation coefficient = 0.915; P<0.000; N=93

6 Modification and Analysis of the Aperture Curvature

6.1 Introduction

An important characteristic of the patch-clamp technique is the cross-sectional geometry of the aperture. It has been suggested that difficulties in seal formation in microstructures arise from sharp corners that damage the cell membrane [92]. Thus, two methods were studied to create a rounded edge profile: (1) different combinations of standard MEMS processes and parameters and (2) de-focused lithographic exposure. Thus, the aim was to create a rounded and smooth aperture lip with a desired opening diameter.

6.2 Materials and Methods

6.2.1 MEMS Processing

The effect of the following processes on aperture geometry were studied:

- deep silicon etching;
- SF_6 etching;
- HF etching;
- wet thermal oxidation;
- PECVD oxide deposition.

In order to experiment on different process combinations, five distinct aperture families (including two sub-groups per family) were produced, denoted by A, B, C, D and E (see Figure 6.2.1). Each family is divided into two sub-groups $X_{thermal}$ and X_{pecvd} to test the affect of thermal oxidation and PECVD oxide deposition concurrently within the same family. Aperture family A focused on the effect of SF_6 etching for a short 20 sec

duration (see Tables A.2.1 and A.2.2). Aperture family B focused on the effect of leaving oxide on the surface during SF_6 etching (see Tables A.2.3 and A.2.4). The oxide was HF etched for a short period to remove the oxide partially at the edges of the aperture lip to prevent the expansion of the aperture opening and to achieve a more pronounced rounding effect. Aperture family C concentrated on SF_6 etching for extended period of 50 sec (see Tables A.2.5 through A.2.8).[23] Aperture families D and E focused on the effects of thermal oxidation, HF stripping, and re-thermal oxidation to increase the top-view circularity of the opening (the only difference in processing between these families is the initial SF_6 etch for 8 sec in family D).

All apertures were initially formed by the following processes:

1. Four 4" silicon dummy wafers (frontside polished) were wet thermally oxidized for 2.5 hrs for an oxide growth of 1.1 μm;
2. Wafers with coated with photoresist of 1.2-μm thickness;
3. The 2.5-μm square cross feature (see Figure 5.2.1d) was repeatedly exposed across these wafers with a 7-mm pitch with a 5x reduction Optimetrix© stepper. The stepper configuration consisted of a range of exposures from 1.9 sec to 2.9 sec in increments of 100 msec, and focus ranging from -1.9 μm to +0.2 μm in increments of 0.1 μm;
4. The photoresist was developed;
5. The wafers were RIE etched to remove the oxide and then ashed, creating an oxide mask for the deep silicon etching process;
6. The silicon was deep etched (see Table A.3.11) for 8 cycles for groups A, B and C, creating an aperture length of approximately 4.6 μm;[24]

Additional processing steps in all aperture families are listed in Figure 6.2.1. After each process, many of the apertures were examined under SEM (see Tables in Appendix A.2).

---

[23] Based on the results from families A and B, it was concluded that SF_6 etching for 20 sec etches too far down into the aperture and a shorter time will be studied.

[24] The etch period was shortened to 4 cycles for groups D and E, since it was uncertain at the time whether AFM scanning is possible at a hole deeper than the tip length. After subsequent testing, it was discovered that the tip does not crash when attempting to scan a "bottomless pit!"

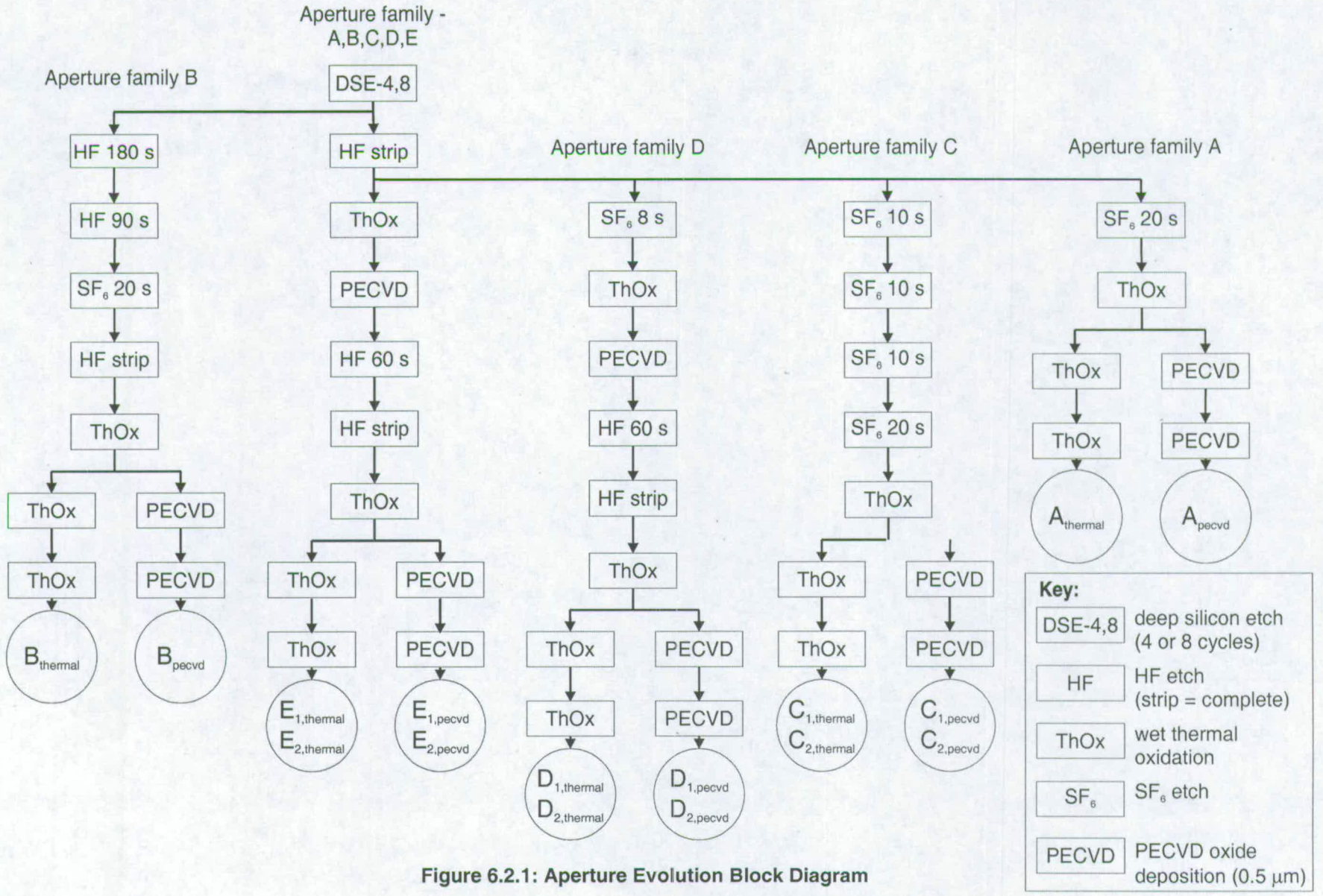

Figure 6.2.1: Aperture Evolution Block Diagram

6.2.2 Defocusing

The 3-μm FEM etched in wafer no. 1 was chosen for this study. To investigate the effect of de-focusing and exposure time, six apertures were milled in a FEI© Focused Ion Beam (FIB) 200xP system machine.[25] After milling, the side-walls of were revealed and examined in an SEM.

[25] The exposure and focus settings for the apertures were: a) 1.0 s, -10-μm; b) 1.4 s, -6-μm; c) 1.8 s, -2-μm; d) 2.0 s, +2-μm; e) 2.4 s, +6-μm; f) 2.8 s, +10-μm.

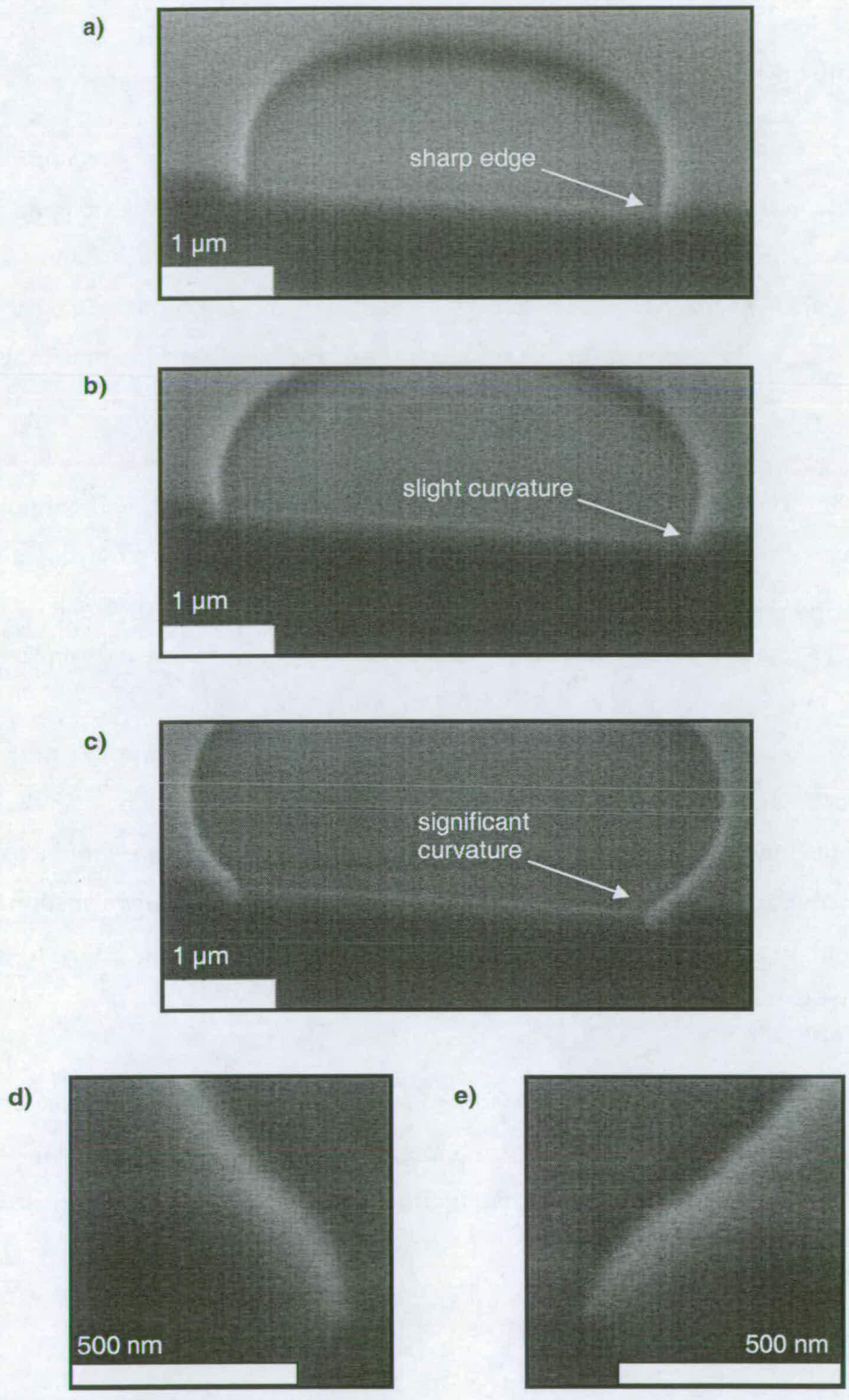

Figures 6.2.2a through 6.2.2e – SEM images of cross sections of apertures etched in Si_3N_4 layer. Images are arranged in increasing de-focus and exposure: a) 2.0 sec, focus = +2 µm; b) 2.4 sec, focus = +6 µm; and c), d) and e) 2.8 sec, focus = +10 µm. The edges are sharp in Figure 6.2.2a. In Figure 6.2.2b, the edges show some semblance of rounding. Significant curvature has occurred in Figures 6.2.2c through 6.2.2e.

6.3 Curvature Profiling of Parametric Data Sets of Extrinsic Curves

6.3.1 Introduction

No known analysis packages exist that measure the radius of curvature from a given arc of pixel data in an AFM data file. Thus, an algorithm was developed and tested to measure the radius of curvature of the profile. This algorithm, although mainly developed for AFM data, can be adapted for studies of other sets of pixel data from many coordinate measurement machines (CMMs) and profilometric tools.

The goal was to measure the minimum radius of curvature R_{min}, or circle of curvature, of the data set [93]. To represent the pixel data as a smooth and continuous curve, the straightforward approach was to represent the curve parametrically [94]. This representation allows the radius of curvature to be computed at each Δt along the curve. The minimum numerical value can be obtained from this set and tabulated as R_{min}.

Along a curve composed of pixel data, a change in direction can only take an abrupt $\pm 45°$ angle. Therefore, the data must be interpolated along the curve. Moreover, obtaining a correct value of R requires an accurate measurement of the X and Y derivatives. The derivatives (and tangent lines) can show large variation over the curve, and thus R can be largely variable. It was therefore necessary to smooth the 1st derivative of $X(t)$ and $Y(t)$ to achieve realistic R values.

The algorithm quantifies curvature independently of the length or shape of the curve, as the entire curve is analysed at each re-sampled point. This algorithm allows the freedom of independent profiling without limiting the data set to a pre-defined area.

6.3.2 The Algorithm

For illustrative purposes, two example Figures are given from data set of aperture G7 that represent the left and right black traces where appropriate. The algorithm is explained below:

1. By use of the AFM analysis software title Nanoscope© III v.442 release 8, a snapshot of the section analysis screen was exported as a TIFF file and re-opened in Adobe© Photoshop v.7.0.

2. The black trace (representing the centre vertical slice) was selected out of the image into a new image by selection of black colour. Using the Selection Tool, the region of interest (ROI) was positioned approximately where: (1) the trace begins the ascent from the bottom of the aperture; (2) the trace curves to form the lip of the aperture; (3) and the curve flattens out over the planar surface. The ROI was cropped as a square of varying size to approximately centre the curve with a 10 to 15-pixel border.[26]

3. Next, the ROI was converted to an 8-bit greyscale BMP and a subsequent 0.5-pixel Gaussian blur was performed on the image;[27]

4. The image was loaded in ImageTool. A script was executed and the ROI was selected around the curve with a threshold of 250 of 256 (see Appendix A.1.2). For the purpose of polar coordinate conversion, the upper-corner (not the lower-corner) pixel location in the image was used as the centre point;

5. The pixel data was selected from the results window and loaded into SigmaPlot 2000;

6. Next, a bisquare smoothing algorithm was applied using a 2nd order polynomial and 0.5 sampling proportion.[28] The data set was re-sampled at 100 intervals of Δt along the full range of θ. The polar pixel coordinates and the smoothing results for the left and right traces for aperture G7 are given in Figures 6.3.2a and 6.3.2b;

7. The re-sampled data was converted to Cartesian coordinates. Next, dx/dt and dy/dt were calculated by running a difference function (where the previous value is subtracted from the current) on x and y;[29]

8. Then, the dx/dt and dy/dt data sets were smoothed using another bisquare weight function at 0.5 sampling proportion using the 3rd degree polynomial,

---

[26] This was done because, firstly, the pixel data at a later point will be converted to polar coordinates. The aim was to measure the curve parametrically at an equal interval along θ for maximum curve sensitivity to R along the complete curve.

[27] The Gaussian blur was used to help extract the pixel data in ImageTool.

[28] For further details, see the algorithm development in Chapter 5.

[29] The derivative is undefined at the first re-sampled point and therefore excluded.

using the re-sampled θ as the independent variable (see Figures 6.3.2c and 6.3.2d);

9. The value of $\tan(\phi)$ (defined as dy/dx, or $(dy/dt)/(dx/dt)$) was calculated by dividing each value of dy/dt by dx/dt at each Δt;

7. Next, the value of ϕ (defined as the tangential angle at a point along the curve) was calculated by the function $\tan^{-1}((dy/dt)/(dx/dt))$;

8. The value of $d\phi/dt$ was calculated by running a difference function on ϕ. As before, the derivative was undefined at the first re-sampled point and excluded;

9. The curvature κ at each interval t along the re-sampled data was calculated using the following formulae [95]:

$$\kappa = \frac{d\phi}{ds} = \left(\frac{\frac{d\phi}{dt}}{\frac{ds}{dt}} \right) = \frac{\left(\frac{d\phi}{dt} \right)}{\sqrt{\left(\frac{dx}{dt} \right)^2 + \left(\frac{dy}{dt} \right)^2}}$$

where ϕ is the tangential angle along the curve, and s is the arc length;

10. The radius of curvature R is defined as $1/\kappa$ and computed as the inverse of κ;[30]

11. Finally, the centre of the circle of curvature at R_{min}, the following values of X_{centre} and Y_{centre} were computed by the following functions:

$$x_{centre} = x + R \cdot \cos(\tan^{-1}(\frac{-1}{\tan\phi})) \qquad y_{centre} = y + R \cdot \sin(\tan^{-1}(\frac{-1}{\tan\phi}))$$

[30] It is possible to achieve an inflection point, where dx/dt changes sign, causing $d\phi/dt$ to be negative at one instance of t and thus giving an incorrect negative value for R. This artefact was negligible, and a single negative value for the radius for curvature was rejected for four of the R data sets for apertures G5, G7 left, G7 right, J2 and J10.

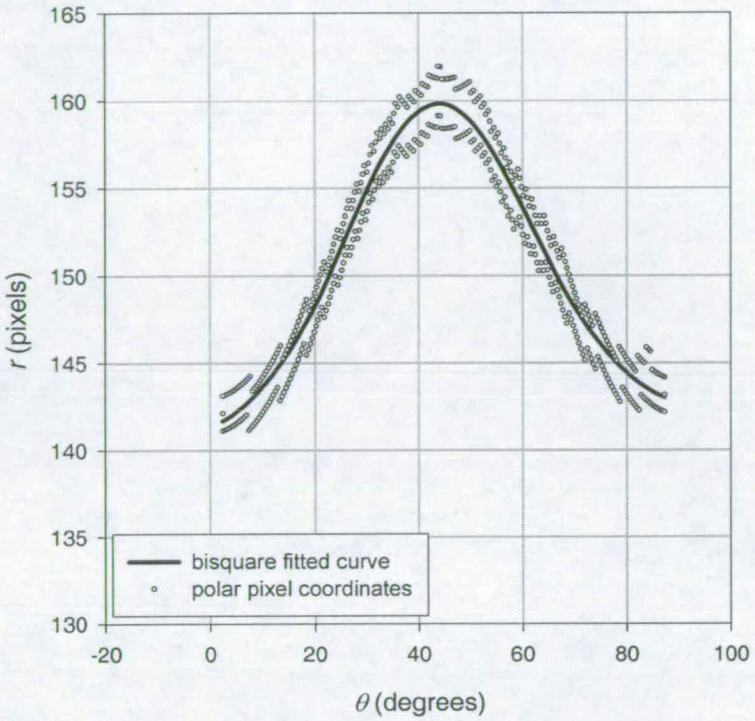

Figure 6.3.2a: 2nd degree bisquare fit to extracted pixel coordinates for G7 left curve.

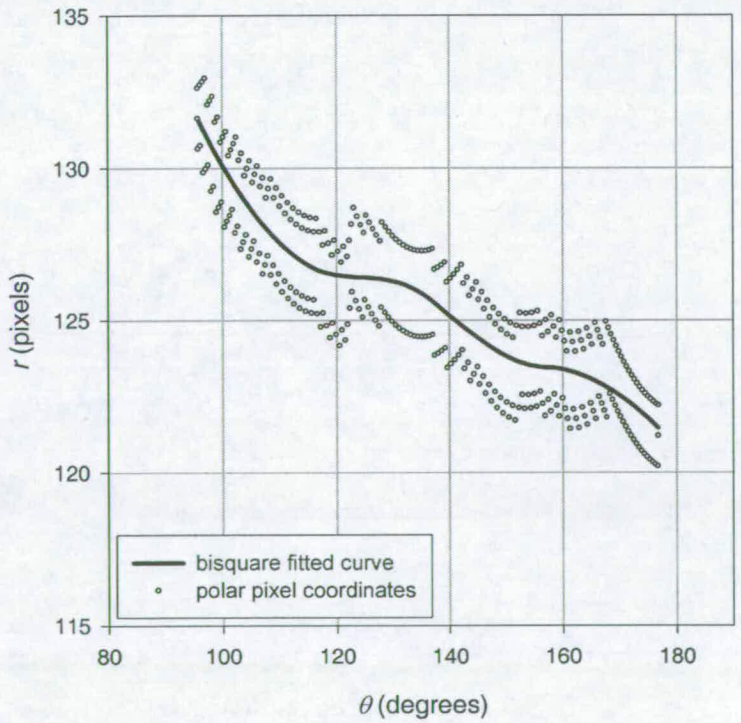

Figure 6.3.2b: 2nd degree bisquare fit to extracted pixel coordinates for G7 right curve.

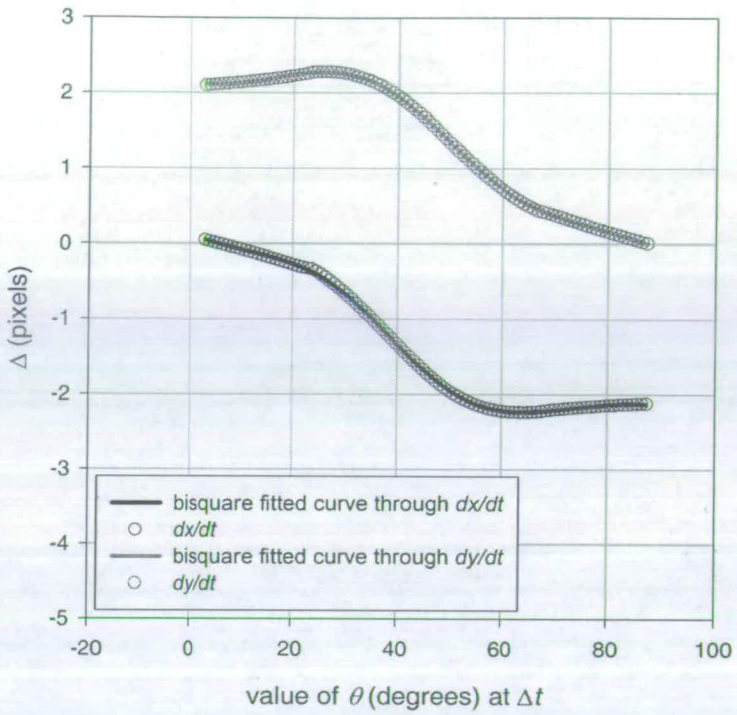

Figure 6.3.2c: 3rd degree bisquare fit through *dx/dt* and *dy/dt* for the left curve of G7.

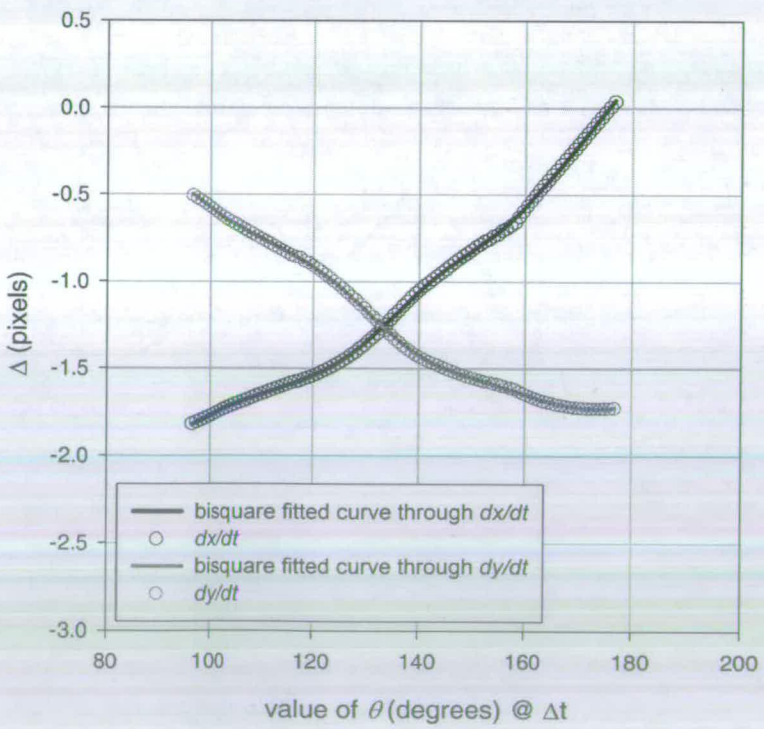

Figure 6.3.2d: 3rd degree bisquare fit through *dx/dt* and *dy/dt* for the right curve of G7.

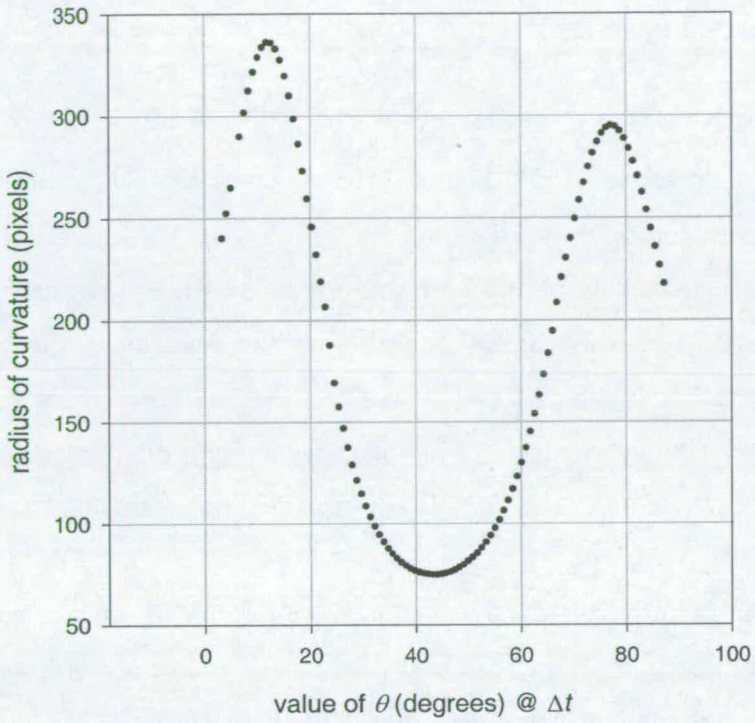

Figure 6.3.2e: Radius of curvature vs. Δt for the left black trace of aperture G7.

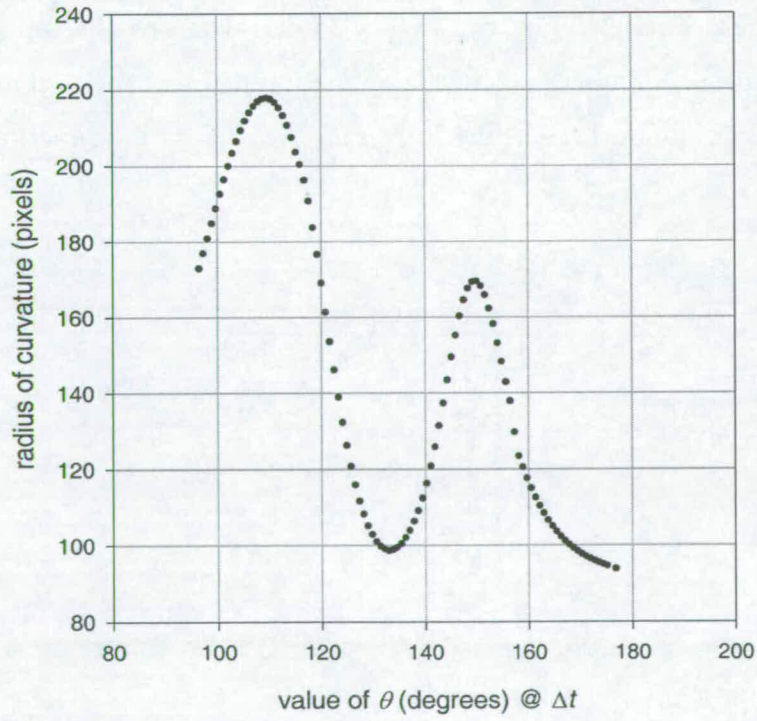

Figure 6.3.2f: Radius of curvature vs. Δt for the right black trace of aperture G7.

6.4 Results

6.4.1 AFM profiling

Ten patch-clamp version II devices (see Table 6.4.2) were profiled using an Atomic Force Microscope (AFM) Digital Instruments™ D5000 in Tapping Mode to measure the aperture cross-sectional curvature. Profiling such a feature required the utilisation of an especially narrow tip, because the sidewalls of the apertures approach 90°. Thus, a special AFM tip was chosen with an ability to trace along the steep sloping sidewalls. Specifically, a Nanosensors© high-aspect-ratio (HAR) tip was used (part no. AR5-NCHR). The tip length is > 2 μm at an aspect ratio of approximately 7:1 (the overall tip length is 10-15 μm). The tip radial diameter is approximately 10 nm.

The scan field size of each aperture was approximately 4 μm at a typical scan rate of 0.3 Hz with 256 samples across each trace. A section analysis and surface profile was plotted for each aperture (see Figures 6.4.1a through 6.4.1t).[31] To minimise any distortion created by tracing in the horizontal direction and offsets in surface flatness of the specimen, only vertical sections were plotted. Three vertical fixed sections were examined in the analysis (the left, centre and right lines are coloured black, red and green respectively). For consistency in the data analysis, only the black trace was analysed. In addition, the left side of aperture G7 was analysed to demonstrate that the curvature algorithm can be performed for both sides of the aperture.

[31] To correctly measure the curvature, the Z-range (the Y-axis on the section analysis plot) was adjusted to the same distance scale to the X-axis.

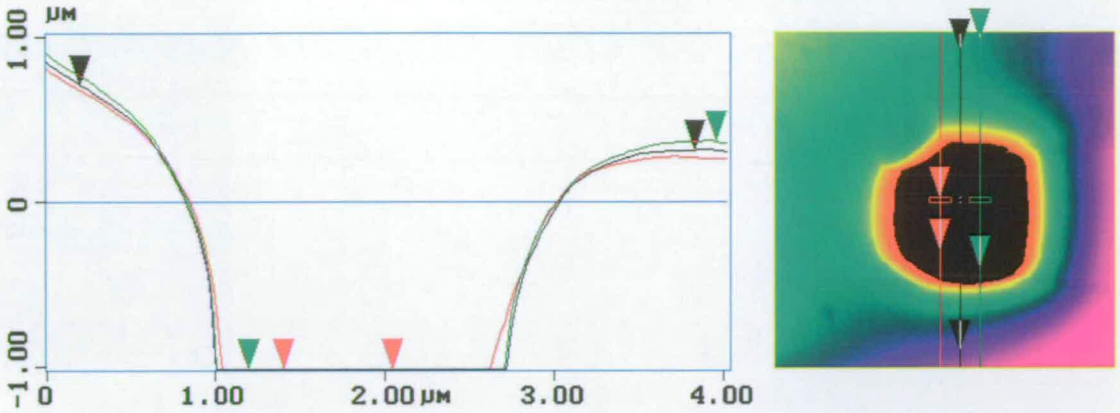

Figures 6.4.1a and 6.4.1b: Section analysis and surface profile for aperture B2.

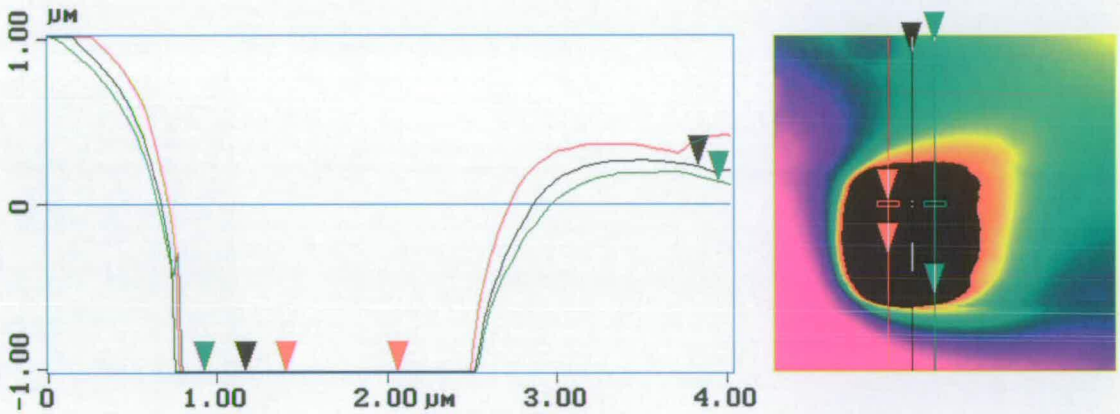

Figures 6.4.1c and 6.4.1d: Section analysis and surface profile for aperture B3.

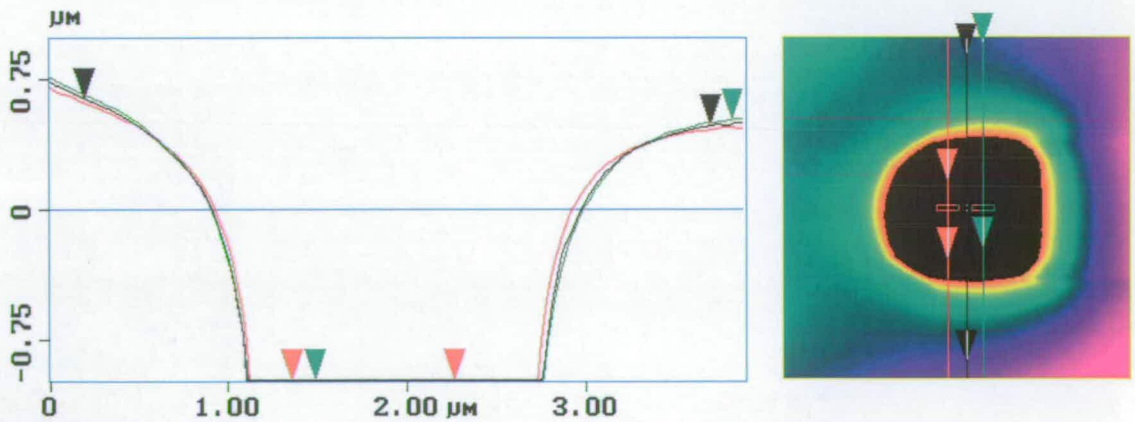

Figures 6.4.1e and 6.4.1f: Section analysis and surface profile for aperture B10.

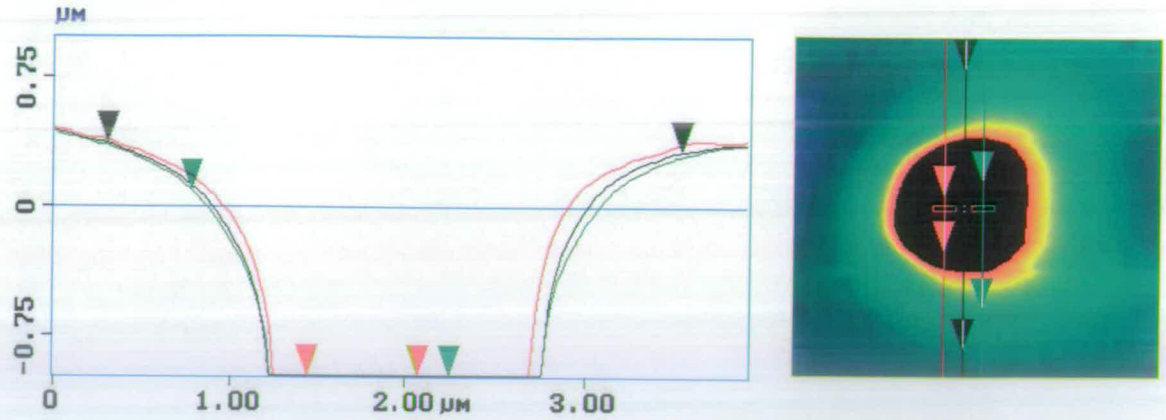

Figures 6.4.1g and 6.4.1h: Section analysis and surface profile for aperture E7.

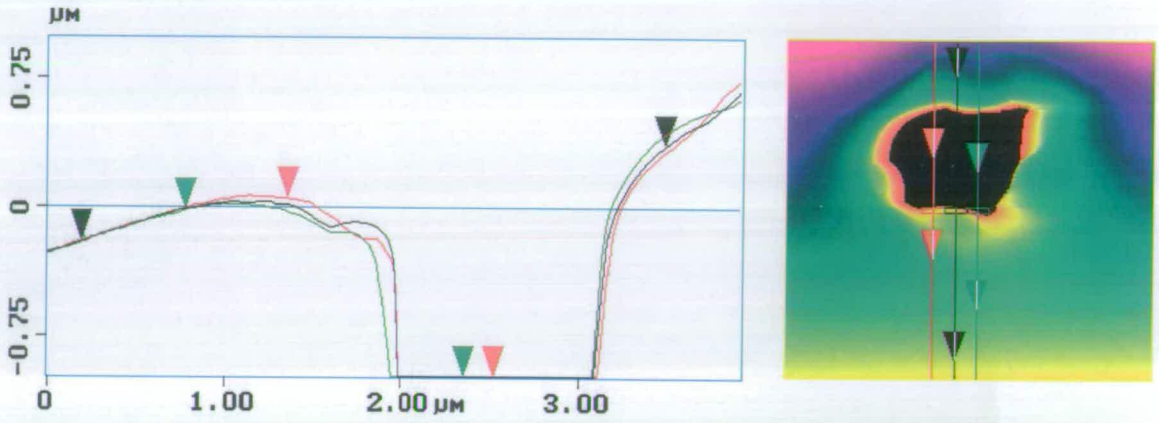

Figures 6.4.1i and 6.4.1j: Section analysis and surface profile for aperture F6.

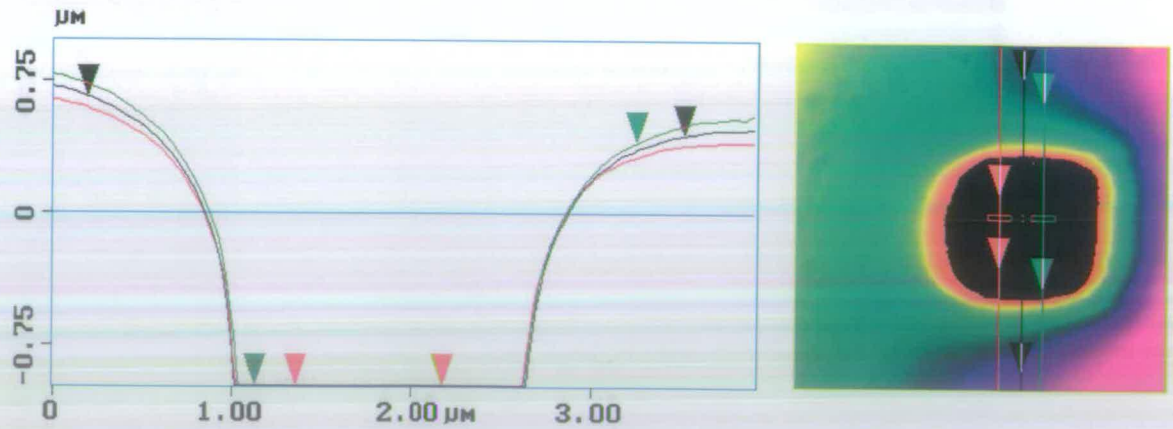

Figures 6.4.1k and 6.4.1l: Section analysis and surface profile for aperture F11.

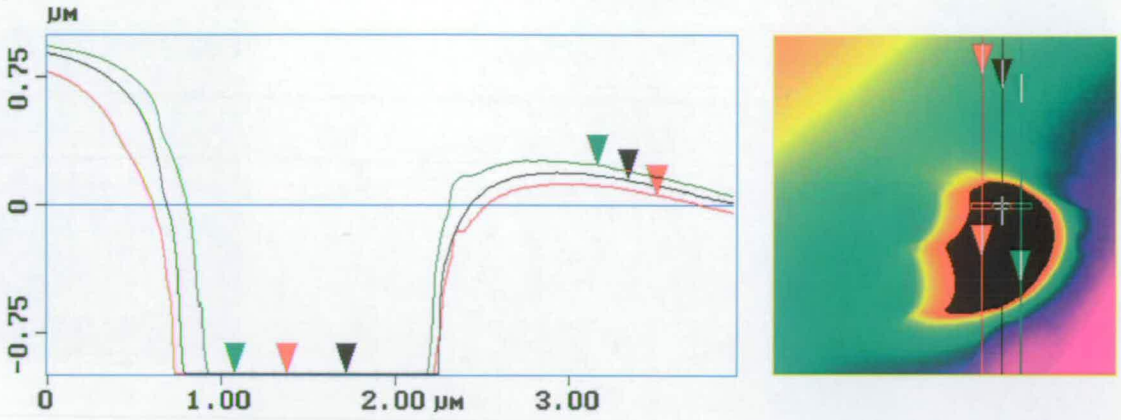

Figures 6.4.1m and 6.4.1n: Section analysis and surface profile for aperture G5.

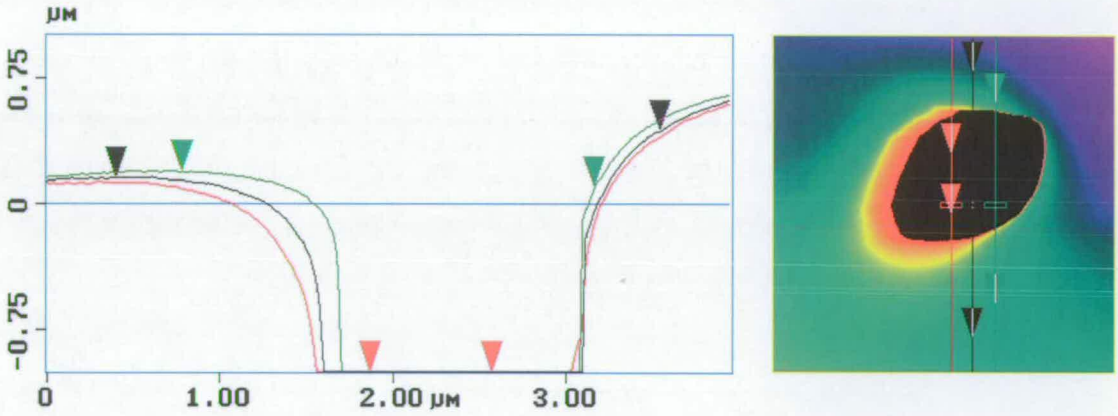

Figures 6.4.1o and 6.4.1p: Section analysis and surface profile for aperture G7.

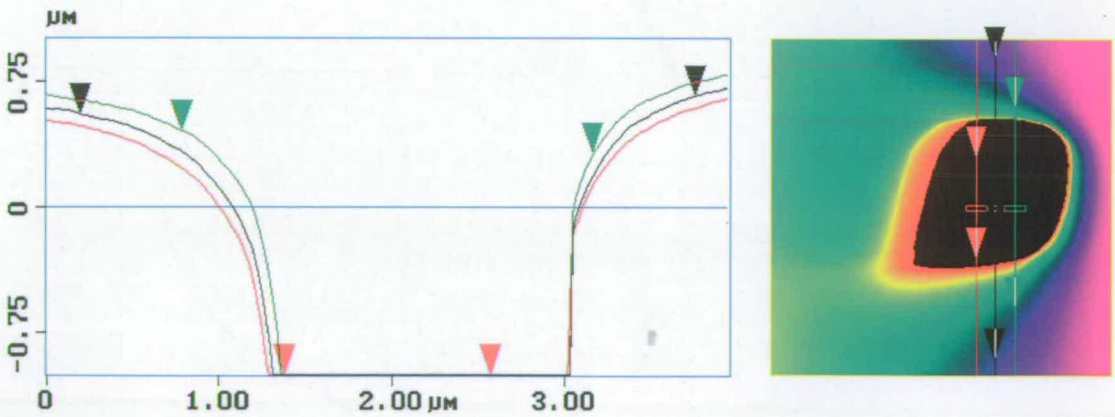

Figures 6.4.1q and 6.4.1r: Section analysis and surface profile for aperture J2.

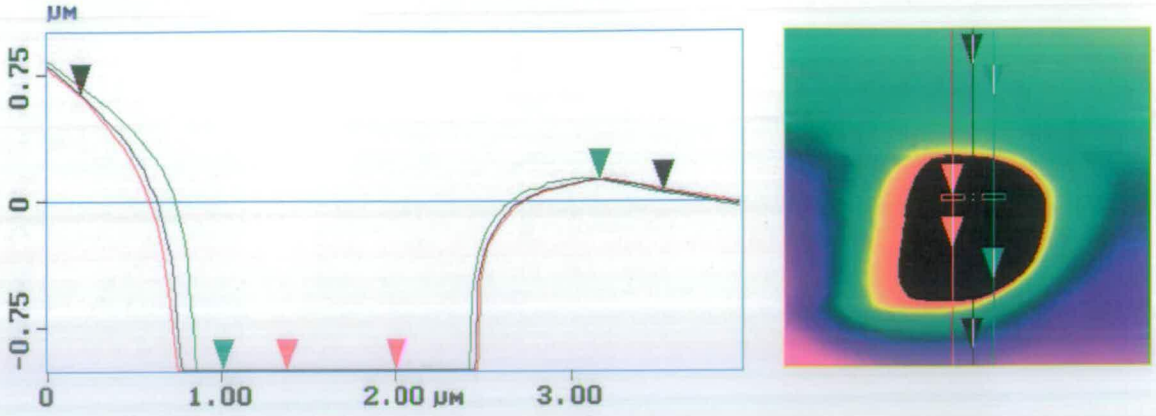

Figures 6.4.1s and 6.4.1t: Section analysis and surface profile for aperture J10.

6.4.2 Curvature Analysis

This algorithm was tested on AFM traces obtained on the ten profiled apertures from Section 6.4.1. Graphs of the extracted pixel data, the re-sampled data from the bisquare smoothing algorithm, the location of R_{min} and the circle of curvature, centre point and calibration bar are given in Figure 6.4.2a and Figures 6.7a through 6.7j. A tabulated summary of the data is given in Table 6.4.2.

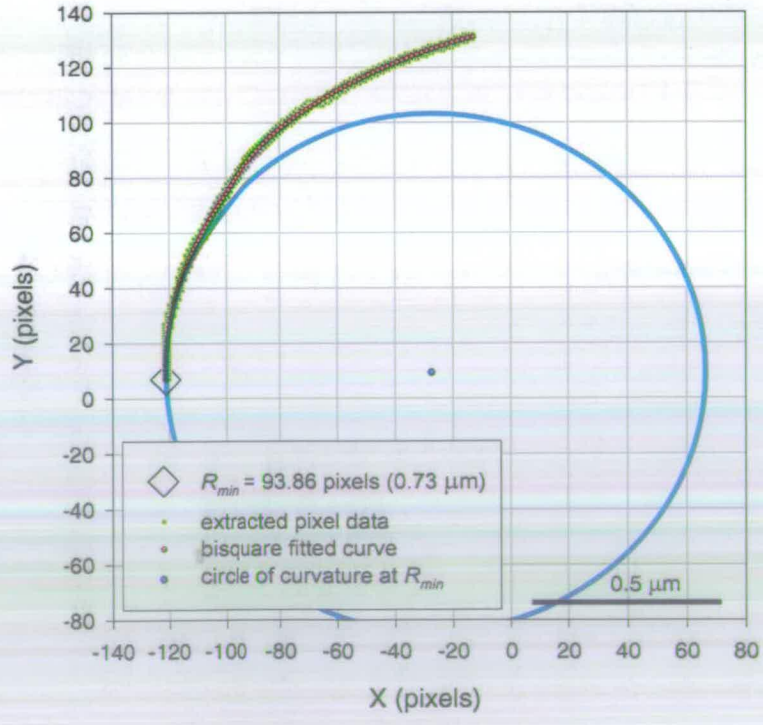

Figure 6.4.2a: Data profile and curvature analysis for the right curve of aperture G7.

Aperture	Analysed Curve	R_{min} (pixels)	Calibration (pixels/μm)	R_{min} (μm)	Group
G7	left black	74.77	129	0.58	control
G7	right black	93.86	129	0.73	control
J10	right black	62.76	129	0.49	control
G5	right black	60.09	129	0.47	800°C B^+
J2	right black	89.99	129	0.70	800°C B^+
B10	right black	82.83	131	0.63	1000°C anneal
E7	right black	92.98	131	0.71	1000°C anneal
F11	right black	95.26	131	0.73	1000°C anneal
B2	right black	81.29	126	0.65	1000°C B^+
B3	right black	68.21	126	0.54	1000°C B^+
F6 *	right black	110.85	131	0.85 *	1000°C B^+

Table 6.4.2: Curvature analysis data summary. This table gives and calculated R_{min} value in units of pixels and microns for the respective curve. The calibration scale is a function of the scan size from the section analysis exported TIFF file. (*) Aperture F6 was a grossly irregular aperture and not included in the data set statistics in the discussion section.

6.5 Discussion

6.5.1 MEMS Processing

Aperture Family A (Tables A.2.1 and A.2.2)

The effect of SF_6 etching produced significant curvature and expansion of the aperture. Thermal oxidation "squared up" the aperture significantly, due to preferential oxide growth along the plane with the normal away from the surface. The effects of POD (PECVD oxide deposition) and ThOx (thermal oxidation) decrease the tip diameter. However, POD did not continue to square up the aperture, and also created a visually smoother aperture (by the observation of less pronounced deep etch grooves; see Fig A.2.2.5b).[32]

Aperture Family B (Tables A.2.3 and A.2.4)

Undesirably, SF_6 etching removed the silicon underneath and oxide, producing an odd-looking concave lip around the aperture tip.[33] The lip remained pronounced for all

[32] It was not possible to obtain good SEM images at 0° AOI, due to the pronounced charging of the surface.

[33] The etched silicon is evident from the bright ring in Figure A.2.3 (step 5).

subsequent processing steps. Thus, leaving oxide on the surface during SF_6 etching was found to create a visually undesirable structure.

Family C (Tables A.2.5 through A.2.8)

The SF_6 etch process removed the silicon significantly into the depths of the aperture, notably after 20 sec. After 10 sec of etching, the grooves at 0° AOI are not easily observed. It was apparent that SF_6 etching preferentially squared up the aperture (although less pronounced than ThOx). As in the results for families A and B, POD smoothed the aperture significantly and decreased the aperture size back to an acceptable size for patch-clamping (≤ 2 μm).[34]

Families D and E (Tables A.2.9 through A.2.16)

After the first ThOx step, the aperture opening was rounded, but showed signs of "ripple" from oxide growth around the grooves. Immediately after, the POD process undesirably produced an abruptly angled and less rounded opening, with the ripples still present.[35] From observation, HF etching potted the surface significantly and made the surface less smooth. After performing a complete oxide strip, the aperture appeared more circular than initially etched with the deep silicon process. Subsequent POD and TOx produced similar effects as in families A, B and C.[36] Furthermore, the presence of grooves disappeared and the surface smoothened within the aperture. After the final ThOx process, the apertures squared up again without the presence of grooves. However, the aperture appeared smoother than subgroups $A_{thermal}$, $B_{thermal}$, $C_{1,thermal}$ and $C_{2,thermal}$. For subgroups $D_{1,pecvd}$ and $D_{2,pecvd}$, the POD process resulted in a very smooth and rounded aperture opening. Aperture family E was found to produce identical results from D. However, it is speculated that the initial 8-sec SF_6 etch created more edge curvature.

---

[34] From the results of group C, it was decided that any additional SF_6 etching for aperture groups D and E will not be for more than 10 sec. Also, because PECVD oxide deposition smoothed out the grooves and decreased the aperture diameter, it was decided that group D would be subjected to the POD process earlier in the processing stage.

[35] It was decided to HF etch for 60 sec to try to round-off the sharp corners of the opening.

[36] An observation was made that showed four obtrusive buds extending from each side (see step 9). It was decided that this was either real feature within the aperture (due to preferential growth of the silicon in this plane), or it was an artefact of surface charge during SEM imaging.

6.5.2 De-focusing

The results show that defocusing the lithographic beam can increase the radius of curvature. The curvature is not noticeable under SEM observation until the focus was approximately at +6 μm. The largest radius of curvature was obtained at a +10-μm focus setting, estimated to be approximately 0.5 μm. It is hypothesised that this curvature is attributable to the curved edge profile of the photoresist after development. This curvature profile is then transferred to the material during etching as the photoresist is milled away gradually from the edge, resulting in a curved edge profile in the material. The degree of replication of the edge profile depends on the photoresist thickness and permeability to the etchant.

6.5.3 Curvature Calculation from the Algorithm

For the selection of apertures from device version II, the average value of R_{min} for the data set was 0.62 μm (standard deviation = 0.10 μm; maximum = 0.73 μm; and minimum = 0.47 μm. The curvature is due to the non-conformal deposition of the oxide layer around the lip of the sharp corner of the thermal oxide layer during the PECVD process. Also, HF etching may have produced some curvature before the re-thermal oxidation step, although the radius of curvature from HF etching is bound to be limited.

Qualitatively, the curvature algorithm identified the location and value of R_{min} to a perceived accuracy. The circle of curvature at R_{min} overlapped a considerable number of re-sampled points near the vicinity of R_{min} (see Figures 6.4.2a through 6.4.2k). Thus, this suggests that a good representation of the curves was achieved parametrically by the use of re-sampled points.

6.6 Conclusion

The use of POD is a useful process to create significant rounding ($\geq$0.5) of the corners of the aperture. Thermal oxidation "squares-up" the aperture with use of a silicon wafer at <100> orientation. The use of a silicon wafer of <111> orientation may reduce this effect by creating a more or less hexagonal shape, as opposed to a square. Nonetheless,

ThOx is necessary for proper insulation from the bulk silicon, especially the aperture cavity where deposition techniques would not generally work. The developed algorithm provides a useful and accurate measurement of the cross-sectional curvature. Further developments into fabricating a convex aperture, as opposed to a generally cylindrical one, should be investigated. At the time of writing, it is unclear whether convex patch apertures increase the probability (or wholly required) for patch-clamping of neurons with planar silicon-based microstructures.

6.7 Additional Figures

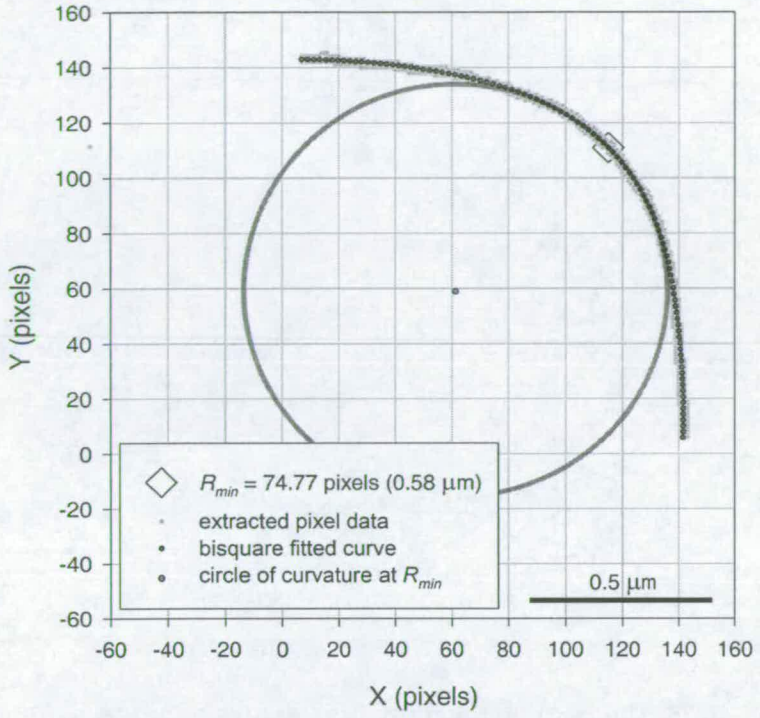

Figure 6.7a: Data profile and curvature analysis for the left curve of aperture G7.

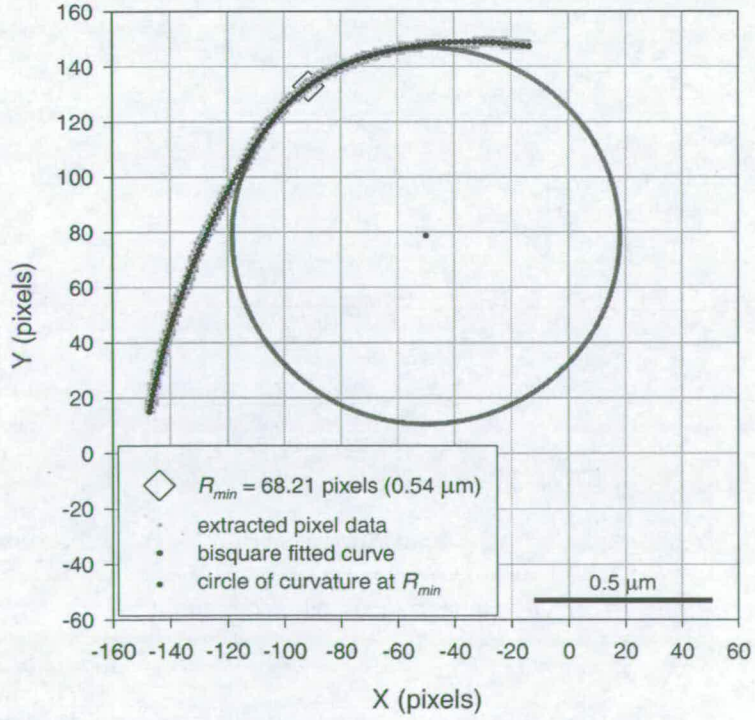

Figure 6.7b: Data profile and curvature analysis for the right curve of aperture B3.

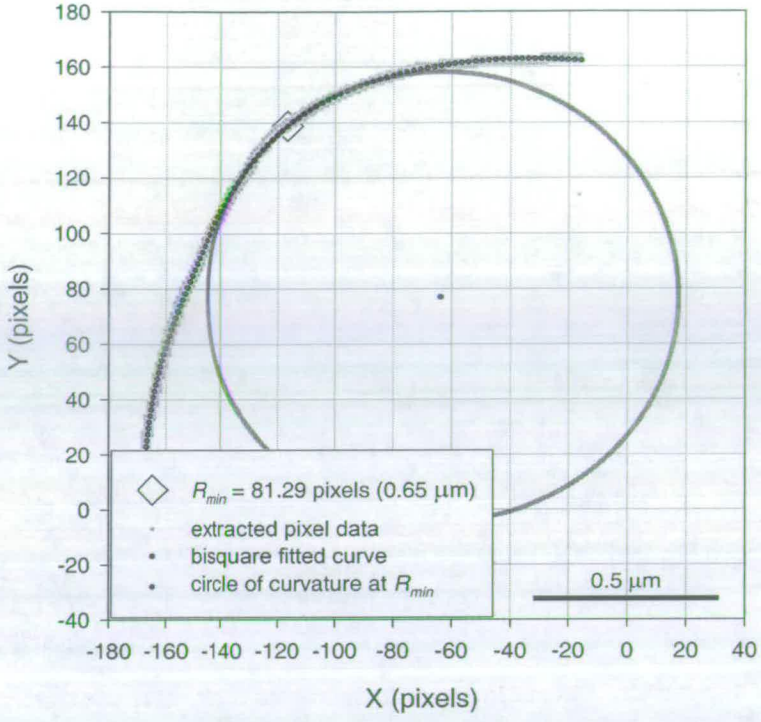

Figure 6.7c: Data profile and curvature analysis for the right curve of aperture B2.

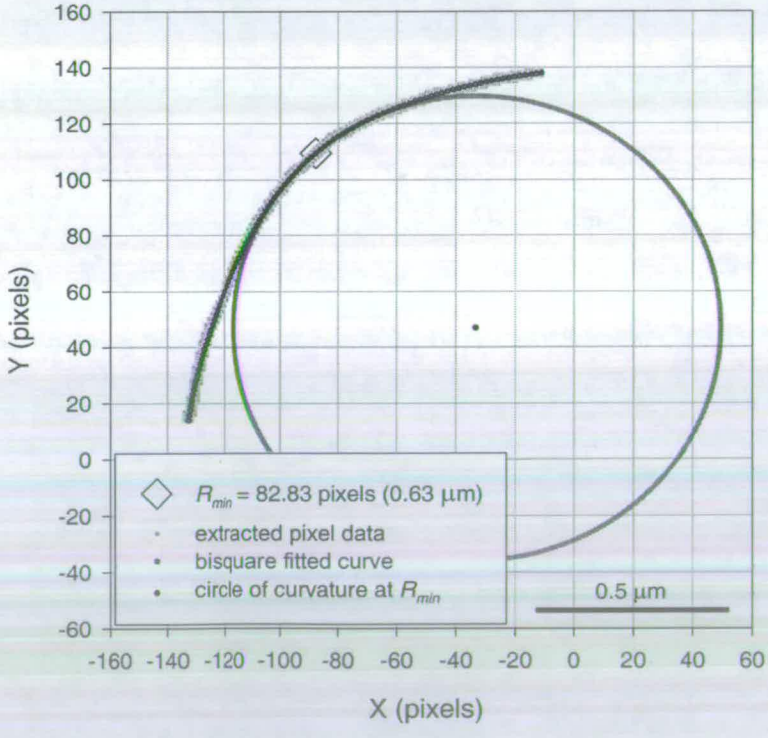

Figure 6.7d: Data profile and curvature analysis for the right curve of aperture B10.

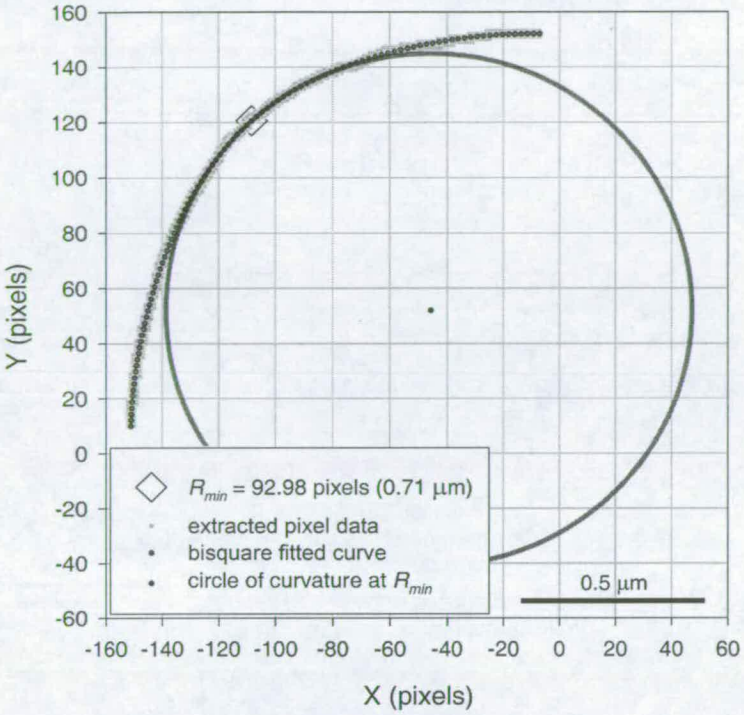

Figure 6.7e: Data profile and curvature analysis for the right curve of aperture E7.

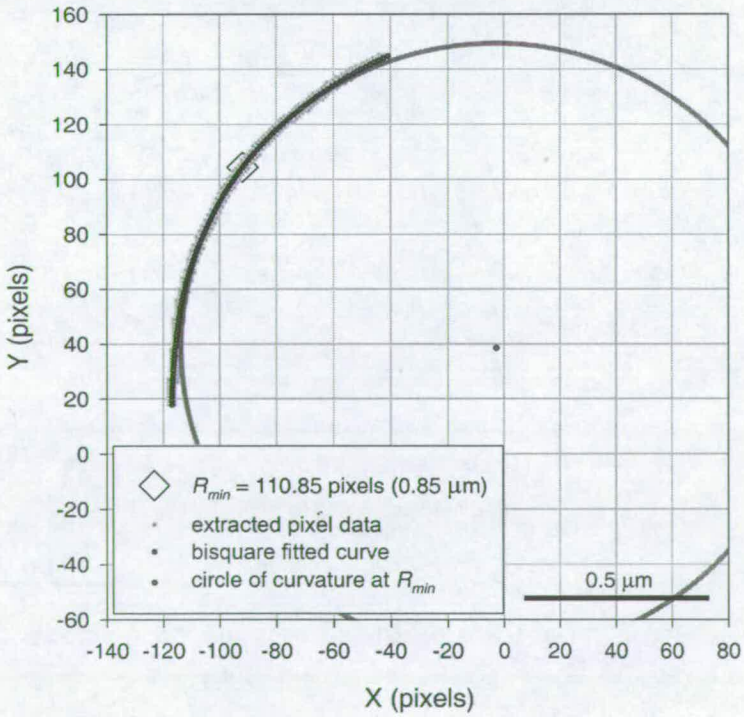

Figure 6.7f: Data profile and curvature analysis for the right curve of aperture F6.

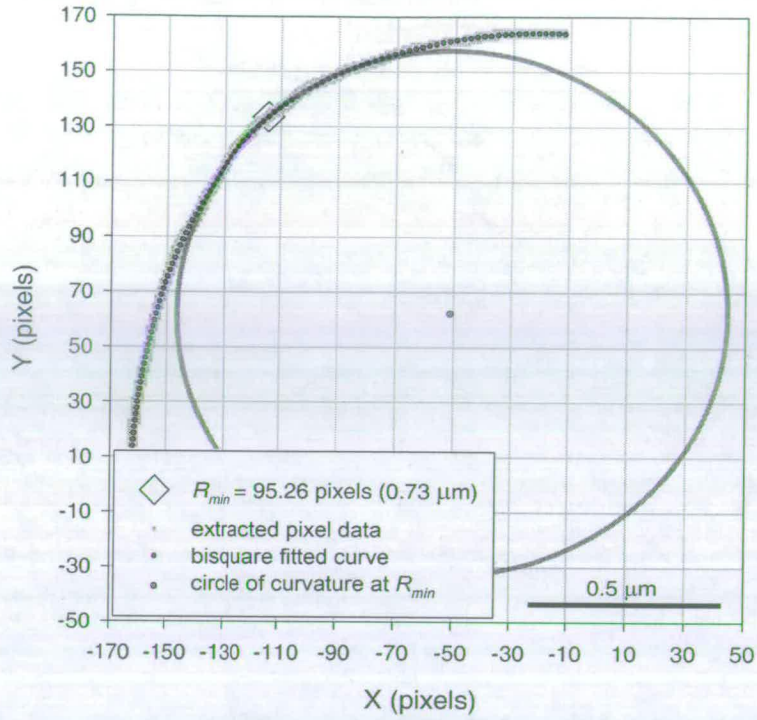

Figure 6.7g: Data profile and curvature analysis for the right curve of aperture F11.

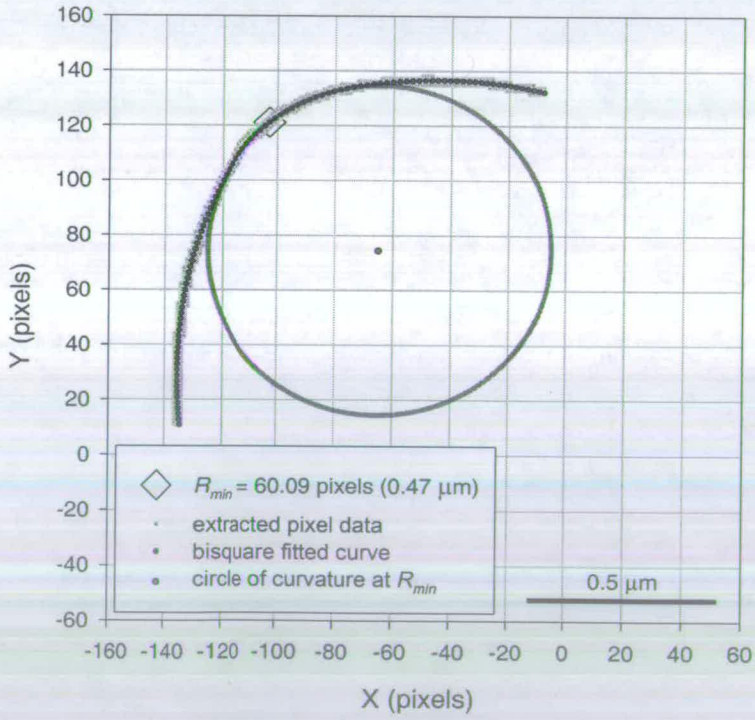

Figure 6.7h: Data profile and curvature analysis for the right curve of aperture G5.

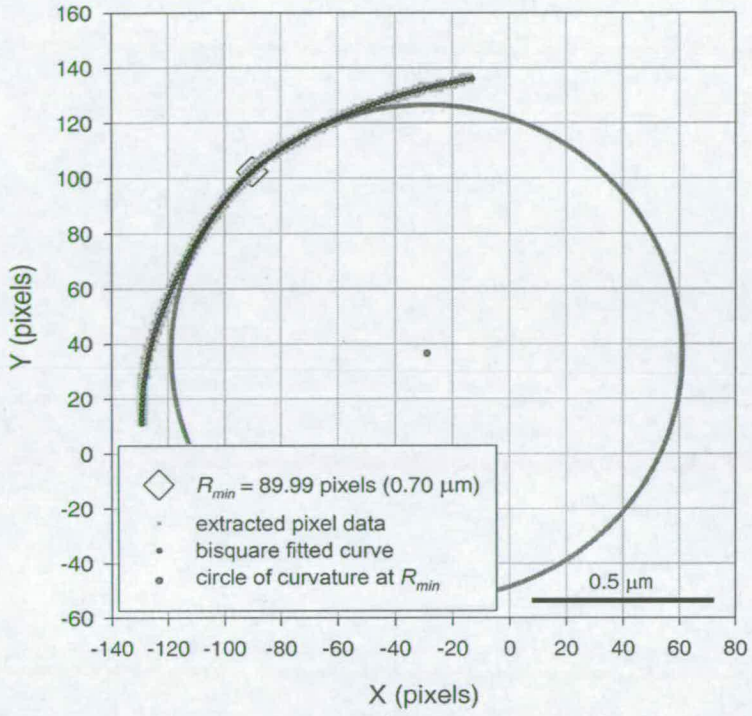

Figure 6.7i: Data profile and curvature analysis for the right curve of aperture J2.

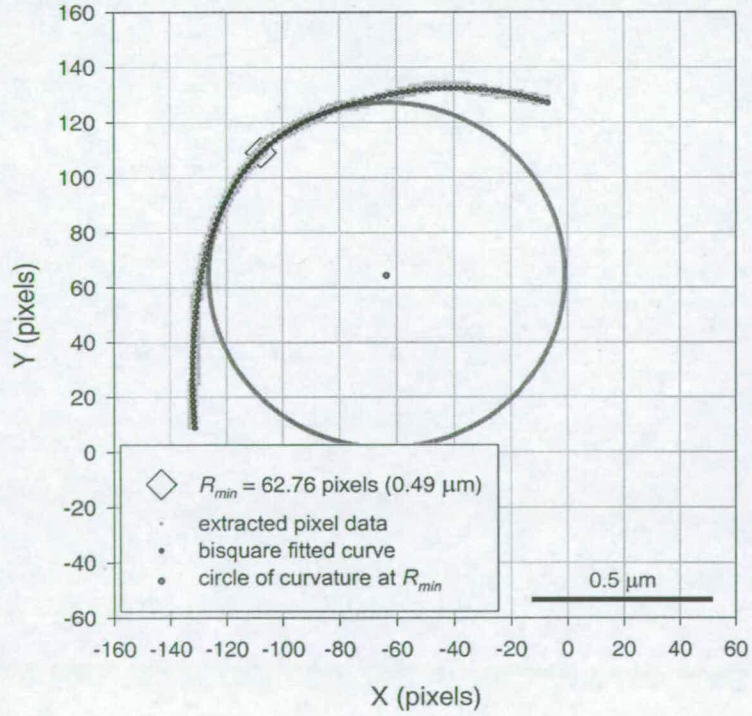

Figure 6.7j: Data profile and curvature analysis for the right curve of aperture J10.

7 Microstructure Design, Fabrication and Assessment

7.1 Introduction

Ultimately, the success of patch-clamping using microstructures depends on designing a device capable of emulating the important characteristics the electrophysiological method offers. This section focuses on the design, manufacture and assessment of a single microstructure to explore and test the feasibility of patch-clamping. The following factors are necessary to achieve for a prototype device:

- the realisation of a mechanically stable microstructure;
- the incorporation of suction;
- a tolerable electrical performance for neuronal recording;
- the use of material surfaces satisfactory for patch formation;
- some geometrical degree of aperture circularity and curvature;
- a high process yield to perform numerous testing;
- a packaged design for use under a microscope
- some degree of visualisation of the neuron and aperture

Notably, the electrical performance is most critical and therefore carefully considered in the design. Specifically, proper insulation from the bulk silicon and low capacitance are important electrical criteria, especially if multiple apertures will be fabricated on the same device for multi-channel recording.

7.2 Patch Device I

7.2.1 Introduction

Section 2.2 presented a critical review of the microstructures already studied. Here, the first prototype design had the intention to improve on the electrical performance of a free-standing Si_3N_4 membrane microstructure [96-98]. The improvement concentrated on reducing the capacitance of this device to a minimum. This device type included a small circular aperture, or hole, in a 1-μm thick free-standing membrane. The device included a backside cavity formed from anisotropic wet etching, resulting in a resistive circuit pathway for an ionic solution from backside (electrode potential) to topside (ground potential). The resistance of the electrode depends on the geometric properties of the aperture, discussed in Section 7.2.2.

Chemical etching can be used to fabricate precise geometric grooves for MEMS devices [99;100]. This process is orientation-dependent (anisotropic) and requires the use of an alkaline solution such as potassium hydroxide (KOH) or tetra-methyl-ammonium hydroxide (TMAH). The geometric formation of the anisotropic etch depends on the silicon crystal plane structure. Masking with silicon nitride or thermal oxide is possible due to the high selectivity of etch material for these chemicals. In this work, wet etching with TMAH solution with a Si_3N_4 mask can form precise V-shaped groves in the silicon bulk. The etch depth is dependent on the initial size of the exposed silicon.

Initially, the mask area must be pre-defined to form a V-shaped groove of correct geometrical dimensions. From pre-testing experiments, the etch selectivity ratio for the silicon crystal planes <100> and <110> was found to be 100:29 (the actual data was 0.42 μm/min and 0.12 μm/min respectively). Because the selectivity rate of the <111> plane is considerably higher, a precise pyramidal groove can be etched at an angle of 54.7°. However, the small selectivity of the <110> plane will expand the V-groove outward during etching. To create a free-standing Si_3N_4 membrane of 24-μm width (from a silicon bulk thickness of 388 μm), it was calculated that the final backside cavity width should be 578 μm (see Figure 7.2.2). Therefore, the initial aperture size in the design was reduced to 470 μm to compensate for this small etch selectivity.

7.2.2 Electrical theory and design

Two device versions (denoted by A and B) were constructed. Device A includes a sandwiched 1-μm SiO_2 layer between the bulk silicon and a 550-nm Si_3N_4 layer on the backside of the device. Device B only includes a single 1.7-μm SiO_2 layer (the Si_3N_4 was etched away in process step 7). The electrical circuit is given in Figure 7.2.2a. Devices A and B were modified by the application of PDMS to the device backside to try to reduce capacitance. The capacitance of the device can be calculated from equations 7.2.2a, 7.2.2b and 7.2.2c, previously outlined in a thesis by M. Maher in 2000 [101].

Equations 7.2.2a; b; c:

$$C_{device} = \frac{1}{\frac{1}{C_U + C_S} + \frac{1}{C_T}} + C_A$$

where

$$C_U = \varepsilon_o \cdot \varepsilon_{r,SiO_2} \cdot \frac{A_U}{d_{SiO_2}} \quad \text{and} \quad C_{T,A} = \varepsilon_o \cdot \varepsilon_{r,Si_3N_4} \cdot \frac{A_{U,A}}{d_{Si_3N_4}}$$

where ε_o = 8.854 pF/m; with relative permittivity values $\varepsilon_{r,SiO2}$ = 3.9 and $\varepsilon_{r,Si3N4}$ = 7.5, (referenced in G. E. Anner, *Planar Processing Primer* 1990, cited in [101], p.36).

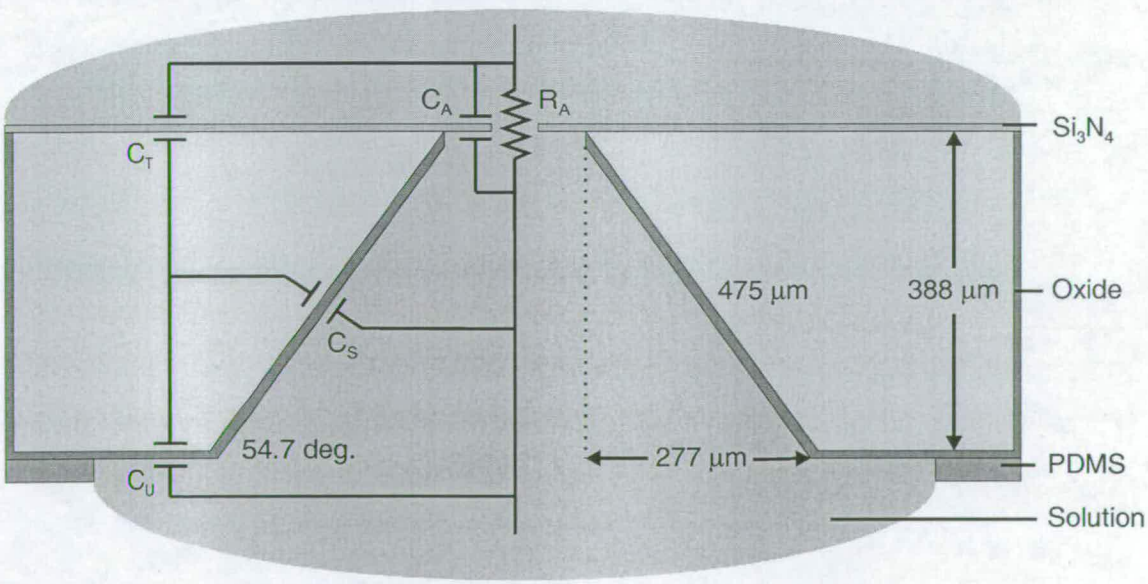

Figure 7.2.2a: Electrical circuit diagram illustrating the capacitive and resistive components of patch device I. The width of the free-standing membrane is approximately 24 μm.

The value of d_{Si3N4} (the thickness of Si_3N_4 layer) is 550×10^{-9} m. The value of A_A (the area of free-standing membrane) is 24×10^{-6} m)^2, or 5.76×10^{-10} m^2. Therefore, the capacitance of the free-standing membrane is:

$$C_A = (8.854 \times 10^{-12} F/m) \cdot (7.5) \cdot \frac{(5.76 \times 10^{-10} m^2)}{(5.5 \times 10^{-7} m)} = 6.95 \times 10^{-14} F$$

This value is negligible and can be ignored. Since the capacitive components C_U and C_T are in series, the lowest value of these will greatly influence the overall capacitance of the device. The value of A_T (the area of the cell bath) is $(8 \times 10^{-3}$ m)^2, or 6.4×10^{-5} m^2. Therefore, the capacitance of the top Si_3N_4 layer is:

$$C_T = (8.854 \times 10^{-12} F/m) \cdot (7.5) \cdot \frac{(6.4 \times 10^{-5} m^2)}{(5.5 \times 10^{-7} m)} = 7.7 \times 10^{-9} F$$

Since the value of C_T is large, it was necessary to minimise the capacitance C_U. The value of C_U is proportional to the contact area of the patch solution. Hence, a polydimethylsilosane (PDMS) coating (Do w Corning Sylgard™ 184) was applied by hand. The area was reduced to approximately a 2-mm diameter circle, slightly larger than initially planned. (Previously, Maher's thesis stated that the diameter was reduced to 1.5 mm.)

The capacitance C_S of the inner side-walls of the pyramidal etch is constant and can be obtained by calculating the area of the side-walls by the equation:

$$A_{side-walls} = (4) \cdot 0.5 \cdot h \cdot (d_a + d_b) = 2 \cdot (3.88 \times 10^{-6} m) \cdot (24 \times 10^{-6} m + 578 \times 10^{-6} m)$$

$$\text{i.e.} \qquad A_{side-walls} = 4.7 \times 10^{-7} m^2$$

Therefore, the capacitance C_S is:

$$C_S = (8.854 \times 10^{-12} F/m) \cdot (3.9) \cdot \frac{(4.7 \times 10^{-7} m^2)}{(1.4 \times 10^{-6} m)} = 1.6 \times 10^{-11} F = 16 pF$$

Finally, the area in contact with patch solution was calculated, and the capacitance of the bottom insulator C_U for each device is given by:

$$A_U = \pi \cdot r^2 - A_{cavity} = \pi \cdot (1\times10^{-3} m)^2 - (578\times10^{-6} m)^2 = 2.8\times10^{-6} m^2$$

$$\varepsilon_{r,SiO2/Si3N4} = ((7.5) \cdot (0.35) + (3.9) \cdot (0.65)) = 5.16$$

$$C_{U,devA} = (8.854\times10^{-12} F/m) \cdot (5.16) \cdot \frac{(2.8\times10^{-6} m^2)}{(550\times10^{-9} m)} = 0.83\times10^{-10} F = 83 pF$$

$$C_{U,devBnoPDMS} = (8.854\times10^{-12} F/m) \cdot (3.9) \cdot \frac{\pi \cdot (3.25\times10^{-3} m)^2}{(1.7\times10^{-6} m)} = 6.7\times10^{-10} F = 670 pF$$

$$C_{U,devBwithPDMS} = (8.854\times10^{-12} F/m) \cdot (3.9) \cdot \frac{(2.8\times10^{-6} m^2)}{(1.7\times10^{-6} m)} = 5.7\times10^{-11} F = 57 pF$$

The final theoretical values of C_{device} are listed in Table 7.2.5c.

Figure 7.2.2b shows the capacitance of the bottom insulator C_U as a function of A_U (area in contact with patch solution) and oxide thickness based Equation 7.2.2b. For example, with typical oxide thicknesses between 0.5 and 1.5 μm, the capacitance is strongly influenced by the contact area of the patch solution. However, oxide thicknesses ≥2 μm with contact area diameters of ≤1 μm can reduce the capacitance to ≤25 pF.

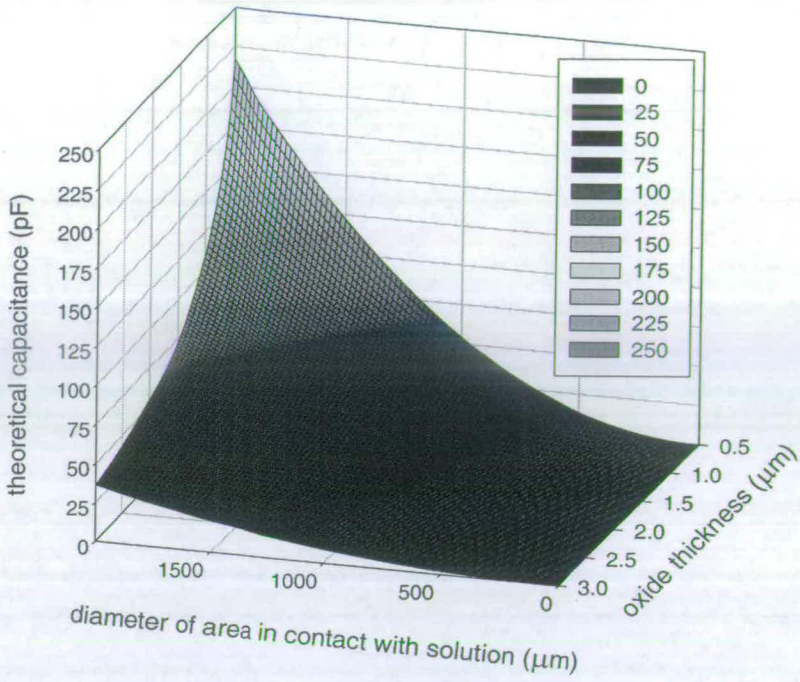

Figure 7.2.2b: Theoretical capacitance of the bottom insulator C_U vs. oxide thickness and the diameter of the area in contact with patch solution. The painted PDMS layer minimises the diameter of the area.

The theoretical resistance of the device can be calculated from Equation 2.3.3a, where L = 0.55x10^{-6} m and $A_{conduction}$ = π (1x10^{-6} m)^2.

$$R_{theoretical} = \frac{\rho \cdot L}{A_{cond.}} = \frac{(510\times10^{3}\Omega\cdot\mu m)\cdot(0.55\mu m)}{\pi\cdot(1\mu m)^{2}} = 89k\Omega$$

7.2.3 Materials and methods

Two standard 3" semiconductor-grade silicon wafers purchased from ShinEtsu© were selected for processing. The wafer characteristics are as follows: crystal orientation of <100> normal to the surface; 'p'-type silicon (boron doped); thickness of approximately 388 μm; and resistance is between 14-20 Ω-cm and polished on the frontside.

All microfabrication was performed in semiconductor class 10 cleanroom facilities. Process conditions and variables can be found in Appendix A.3. A pictorial representation of the process steps is found in Figure 7.2.3. The process steps for device B are as follows:

1. Wafers were initially thermally wet oxidized for 150 min, resulting in a 1-μm oxide thickness;

2. A 1.2-μm thick photoresist coating was applied to the wafer backside as a protective mask against HF etching;

3. The top layer of oxide was removed by dipping the wafers into a buffered HF:H_20 (4:1) solution;

4. Ashing was applied for 60 min to remove the photoresist. Next, a 550-nm Si_3N_4 layer was deposited on both sides using a low pressure chemical vapour deposition process (LPCVD). This resulted in a sandwiched thermal oxide layer between the backside of the silicon bulk and Si_3N_4. This layer will be used in step 11 to aide in the reduction of the capacitance;

5. Both sides of the wafer were coated in photoresist. The frontside photoresist was exposed using a Stepper reticule with a 1.5-μm square aperture mask (described in Chapter 5) at a +10-μm focus and 2800-msec exposure. Also, a pair of global alignment marks were printed at 60.1-mm separation for step 8;

6. The frontside was developed and the Si_3N_4 layer was RIE etched for 16 min. This process resulted in creating a 2-μm aperture diameter;

7. Ashing was applied for 60 min to remove the photoresist. The frontside was coated in photoresist and exposed to an orthogonal grid of 100-μm lines of 14-mm pitch. The mask was exposed "blindly" at 1-mm tolerance to centre each aperture to each respective square. After photoresist development, the frontside (and optionally the backside Si_3N_4 layer, as shown) was RIE etched for 16 min. Then, ashing was applied for 60 min, and the frontside and then the backside was coated;

8. The photoresist was exposed using a backside mask comprising nine 470-μm squares with double-side alignment. Then, the photoresist was developed;

9. The backside SiO_2 layer was RIE etched and subsequently ashed for 60 min;

10. Wet etching was performed with a TMAH solution at 85°C for 930 min to create the free standing Si_3N_4 layer. The final backside cavity size was 578 microns (resulting in a growth of 54 μm along the <110> plane);

11. Ashing was applied and the wafers were and thermally oxidized for 5 hours, resulting in thicknesses of 1.4-μm for the sidewall and 1.7-μm on the backside;

12. A PECVD oxide was deposited for a thickness of 300 Å;

13. The frontside was subjected to boron deposition at 1000°C for 30 minutes;

14. Devices were diamond scribed and broken manually into 14-mm squares for a total yield of nine devices.

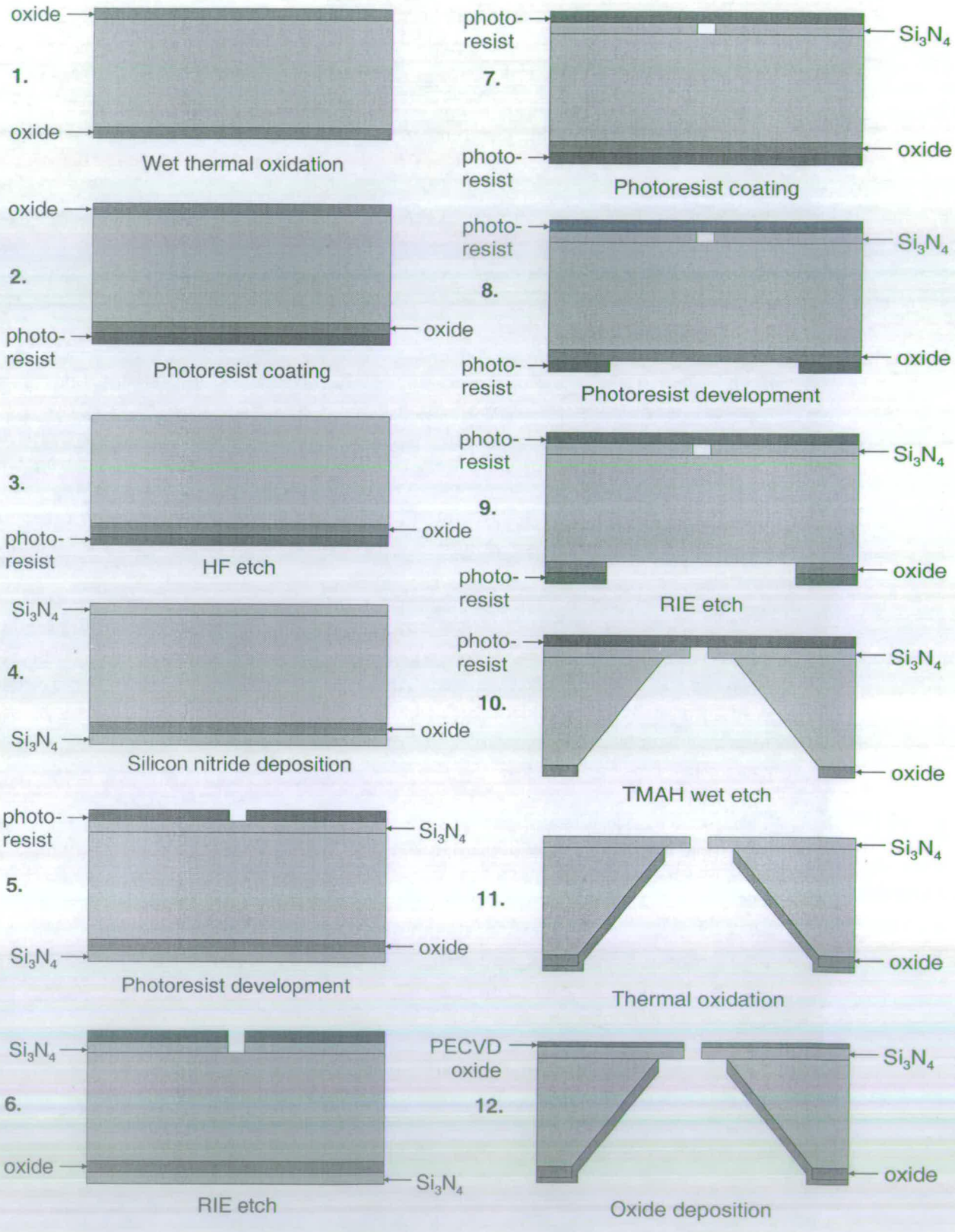

Figure 7.2.3: Cross-section pictorial representation of the process steps for device I (version B). The figure is not drawn to scale.

7.2.4 Platform design and construction

A platform was designed to meet the following requirements:

- the ability to hold each individual patch-clamp device chip during recording;
- to be re-used over and over again rapidly as different patch chips/recording devices are re-installed and tested;
- to fill the backside cavity with patch solution;
- to embed an Ag/AgCl electrode in contact with the patch solution to establish an electrode potential (microfabricated Ag/AgCl electrodes were not incorporated into the device chip);
- accommodate a topside cell-bath;
- provide suction (≤0.03 atm) from the backside of the device;

This platform also features the capability for it to be mounted to a base-plate on the microscope stage for ease of use. To provide suction, an air port was moulded in the device, allowing an external suction line to be attached as a side-port. For MEA device prototype considerations, the platform dimensions were configured to fit into a MCS© base-unit. Therefore, the platform consisted of a 51-mm square assembly with a 6.5-mm thickness.

As part of the design process, a suitable material was selected to contain the patch solution and provide sealing, so adequate suction can be maintained. It has been shown that PDMS material can be used to fabricate micro-channels for biomedical applications, micro-fluidics and MEMS devices [102-104]. PDMS is a silicon elastomer moulded from a cast. Once cured, the material retains the features of the cast to nano-scale precision. Thus, the PDMS device platform was cast from a plastic container containing non-permanent detachable parts. The mould contained:

- a patch-solution well;
- an internal suction port;
- space to insert an Ag/AgCl wire electrode.

A cross-section is shown in Figure 7.2.4 and drawn to a (4:1) scale.

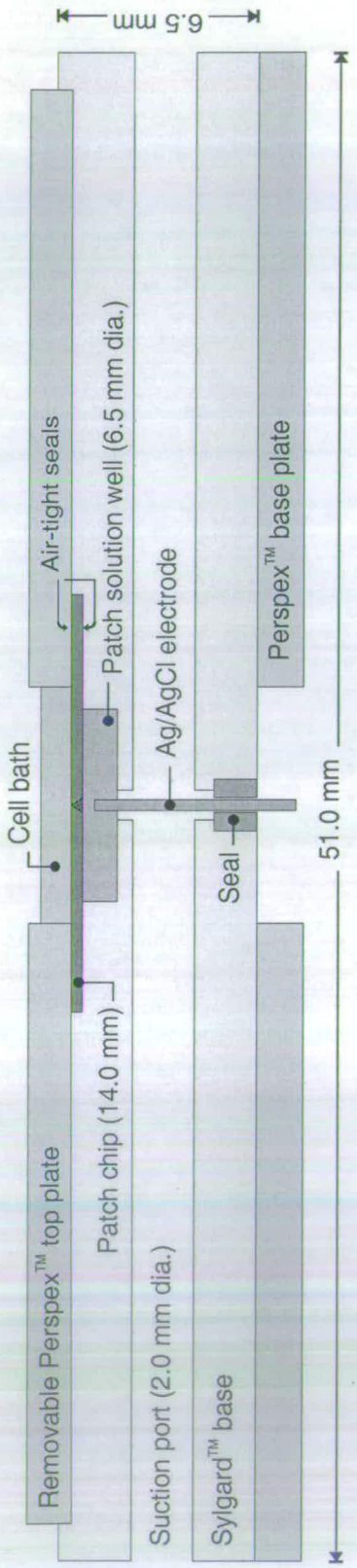

Figure 7.2.4: Cross-section diagram of device platform version I. The figure is drawn to a scale of <4:1>.

7.2.5 Results

To use the device, the platform patch solution cavity was overfilled slightly, leaving a domed meniscus to ensure that the backside of the device would be in contact with the solution. To reduce the formation of air bubbles, a 1-μL drop of the solution was placed on the underneath of the device to fill the cavity. The device was then placed on the platform and tilted slightly during the positioning to avoid trapping air pockets. Then, the removable top plate to contain the cell-bath medium was positioned on the top of the device. The unit was placed in the MCS docking unit and locked down, creating an air-tight seal.

The patch solution consisted of potassium methyl-sulphate (CH_3KSO_4) at standard ionic concentration and HEPES sodium salt ($C_8H_{17}N_2O_4SNa$) used as a pH buffer, purchased from Acros Organics© and Sigma© respectively (see Table 7.2.5a).

Chemical	Conc. (mM)
CH_3KSO_4	150
$C_8H_{17}N_2O_4SNa$	10

Table 7.2.5a: Intracellular patch solution for device testing.

The cell bath solution consisted of a basic phosphate buffered extracellular medium, listed in Table 7.2.5b.

Chemical	Conc. (mM)
NaCl	120
KCl	3.5
KH_2PO_4	0.4
TES	20
$NaHCO_3$	10
D-Glucose	5
Na_2SO_4	10

Table 7.2.5b: Extracellular solution for device testing. The medium is used for studies of cerebellar granule cell cultures [105].

All recordings were taken using the equipment setup in Section 3.5.2. The dynamic response of the electrode was measured a -7.3 nA inward current step and monitoring the voltage output. The electrode was modelled as a first-order linear measuring instrument. Therefore, the time constant *tau* (τ) was measured for the two device versions A and B (with and without PDMS), and a conventional borosilicate glass pipette with a similar 2-μm aperture diameter. The value of *tau* was approximated by fitting the relaxation response to an exponential curve:

$$y = y_o + a(1 - e^{-bx}), \text{ where } \tau = -(1/b) \text{ and } C_{actual} = \tau / R.$$

The current-voltage relationship was tested for linearity. This measurement is dependent on the ionic concentration and area of conduction of the electrode. Eleven current steps were injected from a range of -10 nA to +10 nA at Δ2 nA intervals for a duration of 500 ms (see Fig. 7.2.5a). An I-V plot was generated, and the resistance values V/I were fit to a linear equation (see Fig. 7.2.5b). A table of the measured electrical performance measures are given in Table 7.2.5c. A graph of the voltage response of the devices and pipette is shown in Figure 7.2.5c.

Device Type	R (MΩ)	$C_{theoretical}$ (pF)	C_{actual} (pF)	tau (msec)	Fit (r^2)
ver A (with PDMS)	843 kΩ	99	414	0.349	0.996
ver B (no PDMS)	313 kΩ	686	2210	0.692	0.968
ver B (with PDMS)	704 kΩ	73	192	0.135	0.135
pipette (2-μm dia.)	2.88 MΩ	(2-10)	40	0.115	0.997

Table 7.2.5c: The electrical performance measures–resistance, tau *(τ)*, and capacitance *(C)*–are given, along with the fitting performance *(r^2)* for the time response.

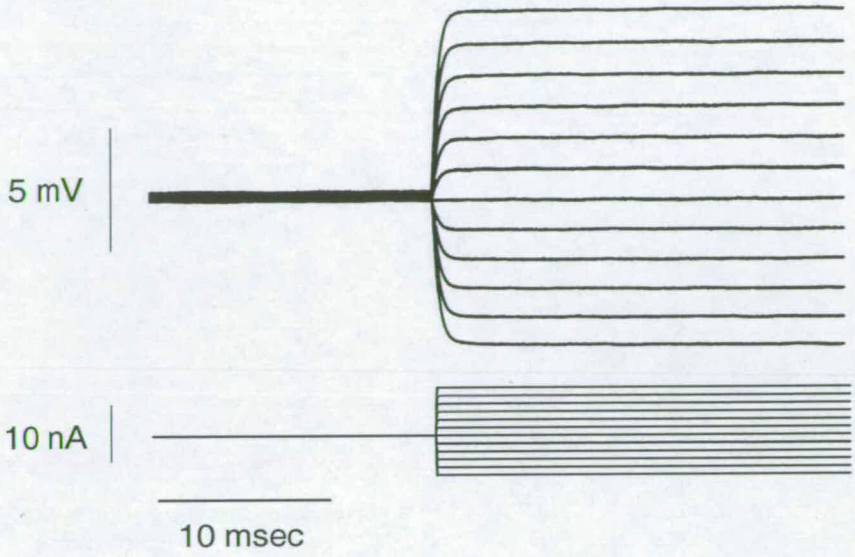

Figure 7.2.5a: Current step and voltage traces for device A.

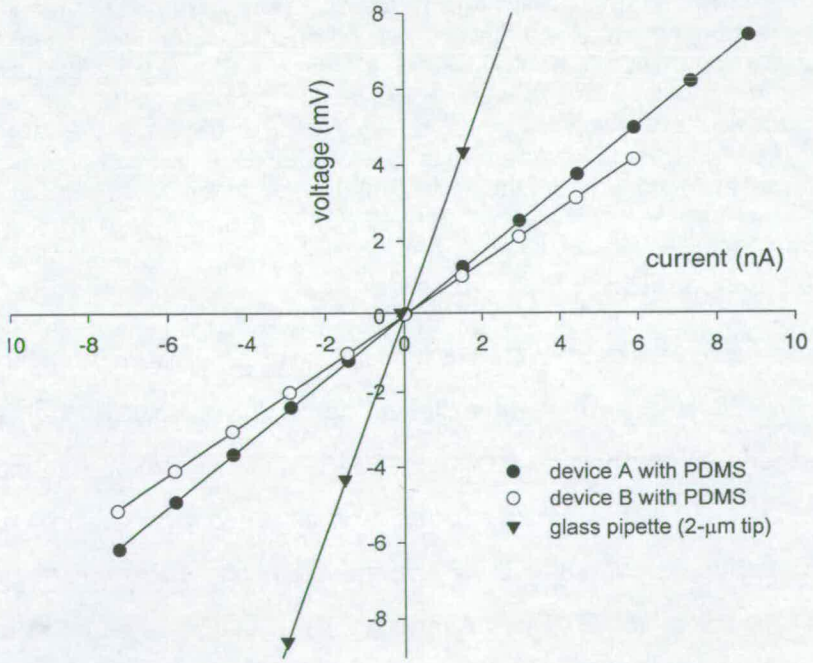

Figure 7.2.5b: I-V plots for device A, device B and the glass pipette. The fits indicate strong linear relationships.

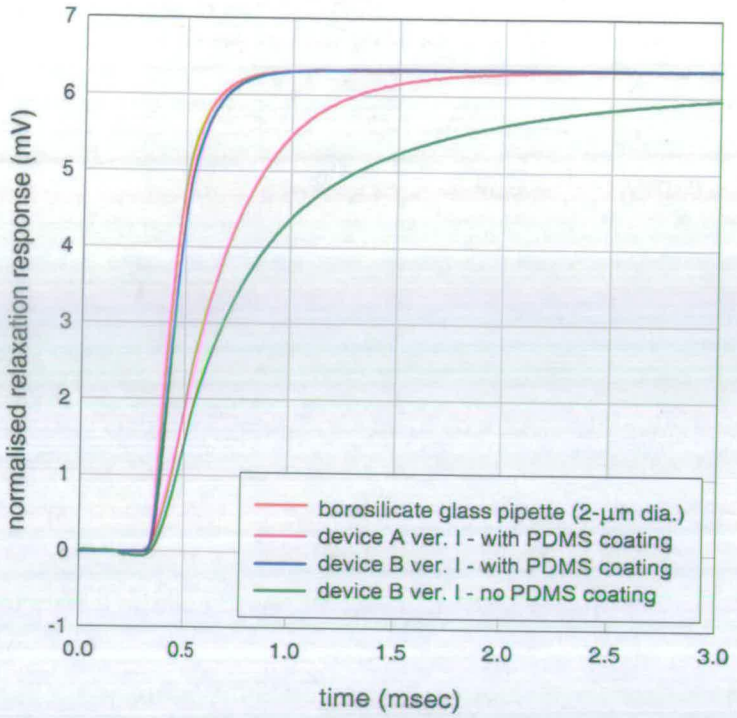

Figure 7.2.5c: The voltage relaxation responses of device I. The relaxation responses were normalised to compensate for differences in resistance. Device A (purple trace) includes the inferior Si_3N_4 insulating backside layer and the time response is lagging behind the pipette control (red trace). However, device B, with a SiO_2 insulating layer (blue trace) has a similar time response to the pipette. The time response of device B without the PDMS coating is severely limited from the large contact area of the patch solution (green trace).

7.2.6 Discussion

The devices and glass pipette are linear measuring instruments within the current range tested (±10 nA). All theoretical resistance and capacitive values were smaller than measured. Notably, the measured 40-pF capacitance of the pipette is higher than expected (≤10 pF is expected). It was assumed that other resistive and capacitive components exist in the testing equipment or the circuit that were unaccounted for, possibly from loose wire connections, leakage of the solution, and particle contamination of the aperture. The application of a backside PDMS coating was necessary to achieve a time response performance approaching that of conventional glass pipettes. Therefore, it was decided that a PDMS coating will be incorporated in patch device II. Also, the Si_3N_4/SiO_2 backside layer in device A was an inferior insulator to the single SiO_2 layer in device B.

In practice, the Si_3N_4 free-standing membrane was brittle and broke easily during attempts to manoeuvre neurons onto the aperture.[37] Also, the thin Si_3N_4 does not support theoretical minimum values of patch aperture lengths discussed in Chapter 2. Thus, further exploration of this device was abandoned for testing of a new prototype design. Finally, the PDMS base was shown to deform during suction. Air-bubble formation was speculated to be attributable to this deformation of the base.[38]

7.3 Patch Device II

7.3.1 Introduction

This design was an attempt to improve upon the poor performance and characteristics of device I. For scalability and MEA implementation for future prototypes, this single aperture design met the requirements for micron-scale internodal spacing. Due to the tight space requirements, wet etching was abandoned and high-aspect ratio deep silicon etching was used [106]. The new etch process allows unidirectional etching hundreds of microns into the bulk. This process was also used to fabricate a thicker membrane and longer aperture length.

7.3.2 Electrical theory and design

The design and electrical circuit is shown in Figure 7.3.2a and includes more capacitive components than did device I. However, the important consideration is that C_U, C_T and C_I are still in series, and the smallest of these values will greatly the overall capacitance of the circuit. Once again, it was imperative that the capacitance of the bottom insulator C_U be minimised. The C_S capacitance is still unavoidable, and C_U was reduced once again by the application of PDMS; C_T was bounded by the area of the cell-bath. $\leq$10 pF is an acceptable upper limit for capacitance.

[37] Thus, a more mechanically stable membrane was part of the next design process.
[38] Hence, the next design platform was based on a solid and non-deformable suction port and patch solution well.

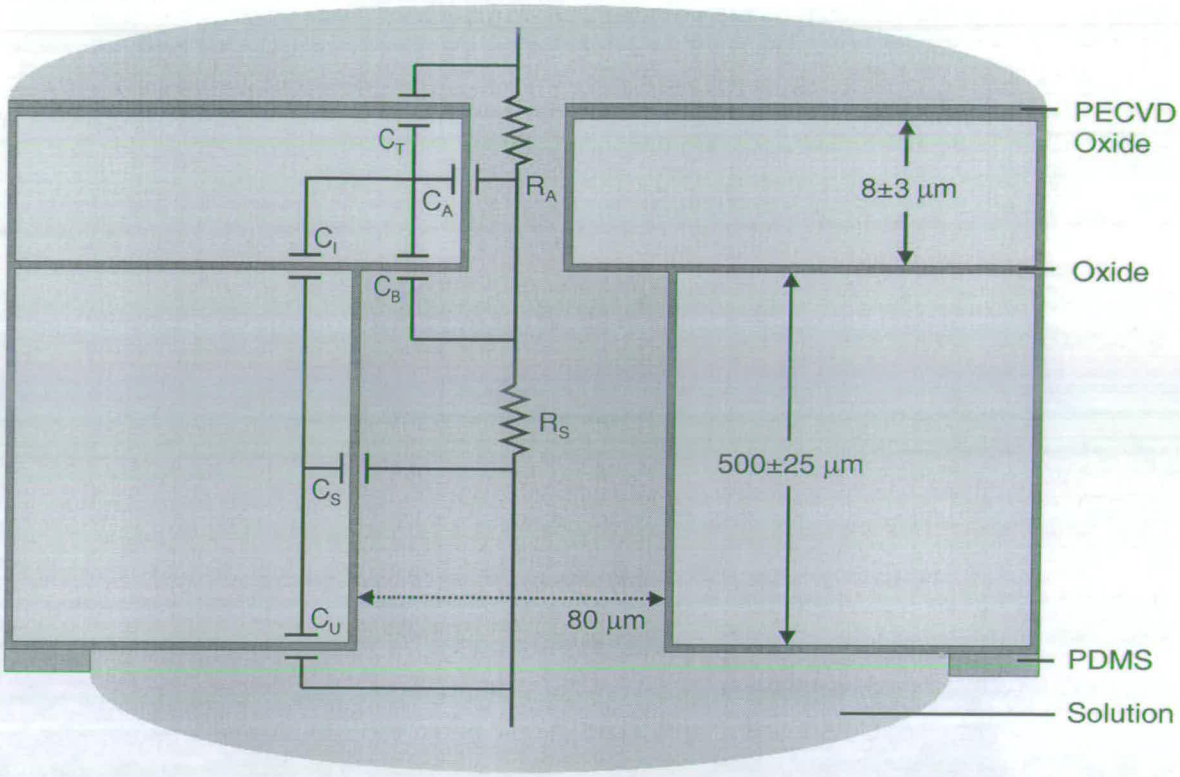

Figure 7.3.2a: Electrical circuit diagram illustrating the capacitive and resistive components in patch device II. The Figure is not drawn to scale.

From Section 7.2.2, the value of C_S was calculated from the Equation 7.2.2b by inserting the appropriate values for area and thickness:

$$C_S = (8.854\times10^{-12}\,F/m)\cdot(3.9)\cdot\frac{(4)\cdot(500\times10^{-6}\,m)\cdot(80\times10^{-6}\,m)}{(1\times10^{-6}\,m)} = 5.5\times10^{-12}\,F$$

This value of 5.5 pF is acceptable. Next, the diameter of the area in contact with the patch solution was estimated to be ≤1 mm by observation (see Fig. 7.3.4d). The value of C_U was calculated from the equation:

$$C_U = (8.854\times10^{-12}\,F/m)\cdot(3.9)\cdot\frac{\pi\cdot(0.5\times10^{-3}\,m)^2}{(1\times10^{-6}\,m)} = 2.7\times10^{-11}\,F = 27\,pF$$

This value of 27 pF is only slightly greater than 10 pF, but the value is still acceptable because the time response is R times C (the access resistance is considerably smaller than a conventional pipette with similar aperture diameter; see the calculations for R_S and R_A in the next paragraph).

The resistance of the device was calculated as the sum of the shank resistance R_s, and the aperture resistance R_A. These values were calculated as:

$$R_S = \frac{\rho \cdot L}{A_{conduction}} = \frac{(510 \times 10^3 \Omega \cdot \mu m) \cdot (500 \mu m)}{(80 \mu m)^2} = 40 k\Omega$$

$$R_A = \frac{\rho \cdot L}{A_{conduction}} = \frac{(510 \times 10^3 \Omega \cdot \mu m) \cdot (8 \pm 3 \mu m)}{\pi \cdot (1 \mu m)^2} = 1.3 \pm 0.49 M\Omega$$

Therefore, the shank resistance is negligible and R_A is acceptable for a 2-μm diameter opening (pipette resistances are typically between 2.5 and 6 MΩ). A graph of the influence on the length of the patch aperture and diameter on resistance R_A is shown in Figure 7.3.2b.

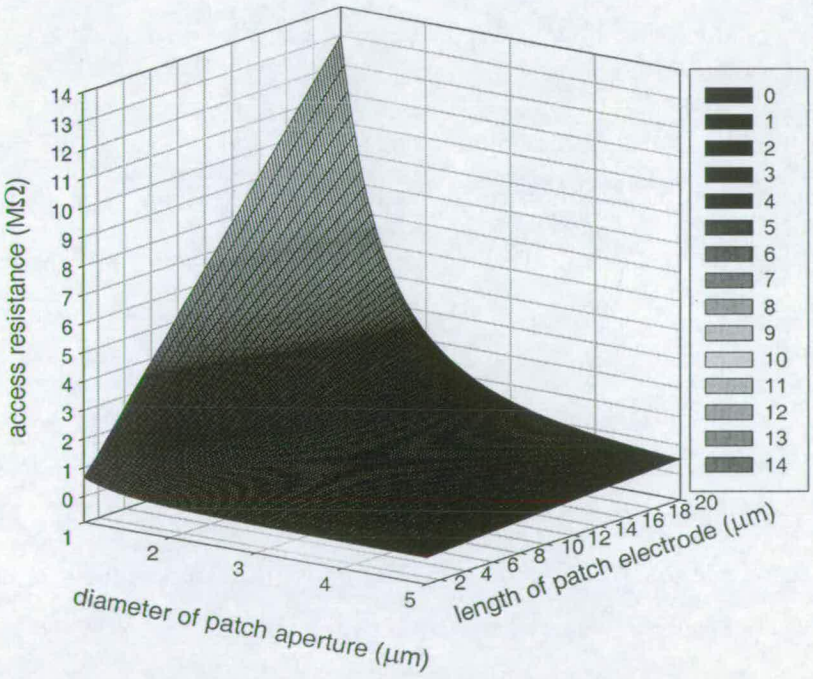

Figure 7.3.2b: Theoretical access resistance R_A vs. patch aperture length and diameter for device II.

7.3.3 Materials and Methods

Two BESOI (bonded and etched back silicon on insulator) 4" (100-mm) wafers were used, manufactured by Virginia Semiconductor Inc. These wafers consisted of the following characteristics: prime grade n-type (phosphorous doped) silicon of <100> orientation; polished silicon on both sides; a buried oxide (insulation) layer thickness of 1.3 μm; a handle wafer thickness of 500±25 μm; and a measured device layer thickness of 8±3 μm (15±0.5 μm was specified on the packaging). Before and after each process step, the wafers were routinely inspected, air blown and rinsed in distilled water. The fabrication process is below and shown in Figure 7.3.3e (see step 1).

1. The wafers were inspected to differentiate the top-side and back-side (both sides were polished);

2. The two device wafers and six additional dummy wafers were thermally wet oxidized at 1100°C for 150 min to grow a 1-μm oxide layer (Fig. 7.3.3e: step 2).

3. The wafers were subjected to HDMS vapour for 15 min to enhance the adhesion of photoresist to the surface. Then, the topside was coated with positive photoresist and hard-baked at 110°C, resulting in a uniform thickness of ~1.18 μm (Fig. 7.3.3e: step 3).

4. A 2.5-μm square cross feature was repeatedly exposed with a 10-μm pitch across an entire 4" thermally oxidized dummy wafer with a 5x reduction Optimetrix© stepper. The stepper configuration consisted of a range of exposures from 900 msec to 2900 msec in increments of 100 msec, and focus ranging from -9 μm to +11 μm in increments of 1 μm. This process formed a 21x21-feature FEM, shown in Figure 7.3.3a. The FEM was analysed in a SEM and two apertures were selected that featured a desired diameter and circularity.[39] Then, a 5" dark-

[39] The circularity was determined by observation only. From previous testing detailed in Chapter 5, the final aperture size was measured to be 0.5 μm less than the initial selected aperture diameter. Thus, for desired aperture diameters of ~1.5 μm and ~2.2 μm, two aperture sizes were selected with diameters of ~2.0 μm and ~2.7 μm, with corresponding exposure settings at 1300 msec and 2900 msec at focus settings at -3 μm and -2 μm respectively. To minimise any drift in the stepper settings, the aperture diameter selection from the FEM and final photoresist exposure on the product wafers were conducted on the same day.

field reticule (with a 2.5-μm cross feature) was aligned in X, Y and θ to the 4" device wafer and stepped at 7-mm pitch, yielding 109 devices (see Fig. 7.3.3f). In addition, a pair of global alignment marks (for subsequent processing requiring frontside and backside alignment) was printed on the frontside at an 80-mm pitch. The photoresist was processed on a Brewer Science, Inc. 8" track system (configured to 4"), first by hard baking at 110°C for 1 min, cooling for 15 sec, then developing (Fig. 7.3.3e: step 4).

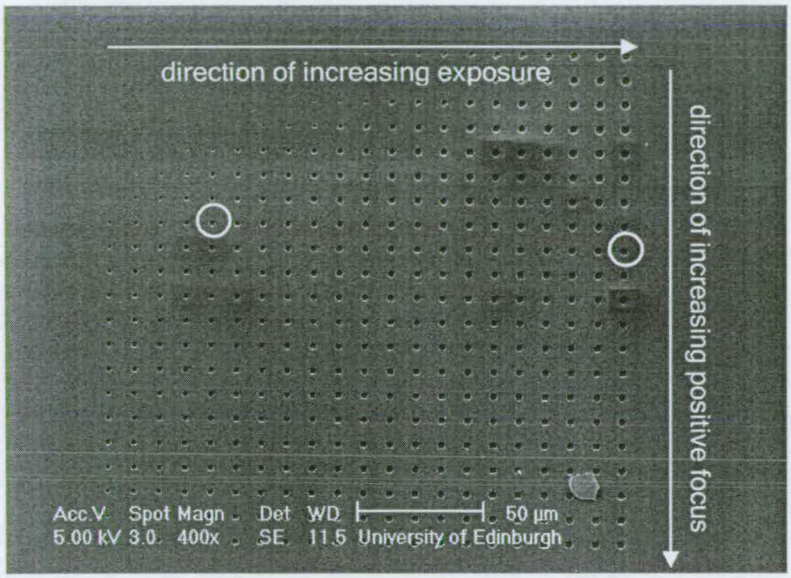

Figure 7.3.3a: A 21x21 Focus-Exposure-Matrix (FEM) of apertures etched in a 1-μm thermal oxide layer. Exposure is varied horizontally left to right from 900 msec to 2900 msec in increments of 100 msec. Focus is varied vertically top to bottom from -9 μm to +11 μm in increments of 1 μm (0 μm is in focus). The selected (circled) feature settings will be duplicated on the device wafers, with corresponding exposure settings at 1300 msec and 2900 msec at focus settings at -3 μm and -2 μm respectively. The absence of features in the top-right corner is due to insufficient light exposure of the positive photoresist from the synergistic effect of high defocusing and small exposure times. Darkened squares around apertures are interpreted as charge accumulation from high magnification SEM imaging over individual apertures.

5. After development, wafers were RIE etched to remove the frontside oxide (Fig. 7.3.3e: step 5).
6. Any remaining photoresist was removed by ashing. Next, the topside was re-coated in photoresist as described before. A MicroTec© Karl SUSS Mask Aligner MA8 system was used to print square boundary markings, or "streets,"

around the holes for observation and wafer breaking purposes (see Fig. 7.3.3f). The photoresist was exposed for 12 sec with proximal contact between the mask and device. After exposure, the wafers were developed, subjected to RIE and ashed as outlined previously (Fig. 7.3.3e: step 6).

7. At this stage, the frontside was ready for a deep-silicon etch process [107] in an STS© Multiplex inductively coupled plasma (ICP) etcher. The thermal oxide layer was used as the etch mask. Following the specified device layer thickness of ~15 μm, 24 etch-passivate cycles (20 sec/cycle) were initially performed (a total of 8 min) in order not to over-etch the aperture (Fig. 7.3.3e: step 7).[40]

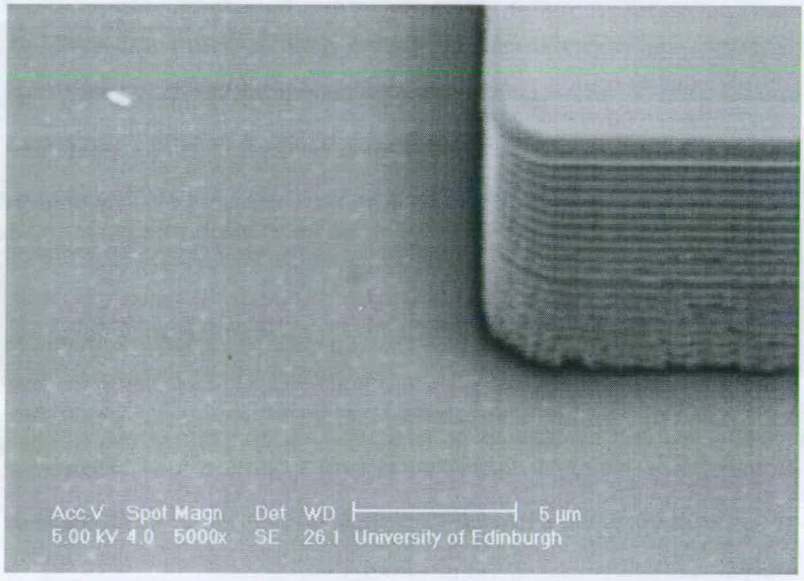

Figure 7.3.3b: SEM image at 45° of a street cross-section sidewall near the water edge after a 24-cycle deep silicon etch process. The length of the sidewall is ~8.9 μm (6.3 μm x 1.414). There exists 18 total etch grooves. Thus, the etch rate is approximately 0.58 μm/cycle, or ~1.74 μm/min given a 20 sec cycle time.

[40] An etch rate of ~1 μm/min was estimated from the machine logbook notes of similar etch parameters (see Fig. 7.4k). Verification that the silicon was completely etched was done by observing the number of ridges, or grooves, etched into the sidewalls of the device streets on a SEM (see Figure 7.3.3b). Each groove represents an etch/passivate cycle. The number of ridges was 18, and since 24 etch cycles were performed, it was deduced that the buried oxide layer was reached sooner than was anticipated. Immediately, the device thickness was measured on a Dektak™ 8000 profilometer, measuring approximately 11.0±1.0 μm at the centre and 8.0±1.0 μm near the edges. Thus, the etch rate under these conditions was ~0.58 μm/cycle, or 1.74 μm/min, higher than estimated. Furthermore, the buried oxide layer thickness was measured to be ~1.3 μm using a Nanospec™ AFT spectrophotometer.

8. For further processing of the backside, the frontside was coated with photoresist for protection. Next, the backside was coated with a thicker positive photoresist of type Shipley© HPR206 and spun at a speed of 2000 rpm, resulting in a uniform thickness of ~3.2 μm as measured from the NanoSpec™ spectrophotometer (Fig. 7.3.3e: step 8).

9. The Karl SUSS aligner was then used to provide frontside-to-backside alignment between the apertures and 80-μm square features by manual positioning of the global alignment marks. Exposure was performed at a longer duration of 40 sec to ensure full exposure of the thicker photoresist, again with proximal contact to the mask. The photoresist was developed as before, then hard-baked at 110°C for 1 min for maximum impermeability to RIE and deep-silicon etching (Fig. 7.3.3e: step 9).

10. Next, devices were subjected to RIE for 70 min for backside removal of the oxide layer (Fig. 7.3.3e: step 10).

11. Then, the wafers underwent extensive deep-silicon backside etching (under the same conditions as before) for six hours, upon reaching the sandwiched oxide stop layer (Fig. 7.3.3e: step 11). (The wafers were routinely inspected every 2 hours, and the depth was calculated using a Vickers© CSS microscope.) Inside the etched cavity, random dark spots, interpreted to be "grass," (un-etched silicon stalagmites from micro masking) were observed on a Reichert-Jung optical microscope in transmission mode. At this point, it was decided to re-etch the cavity for another 30 min and re-inspect. Upon re-inspection, a large percentage of the grass was removed from re-etching. Finally, it was decided to re-etch another 10 min, at which point most spots disappeared (notably around the aperture, see Fig. 7.3.3c).

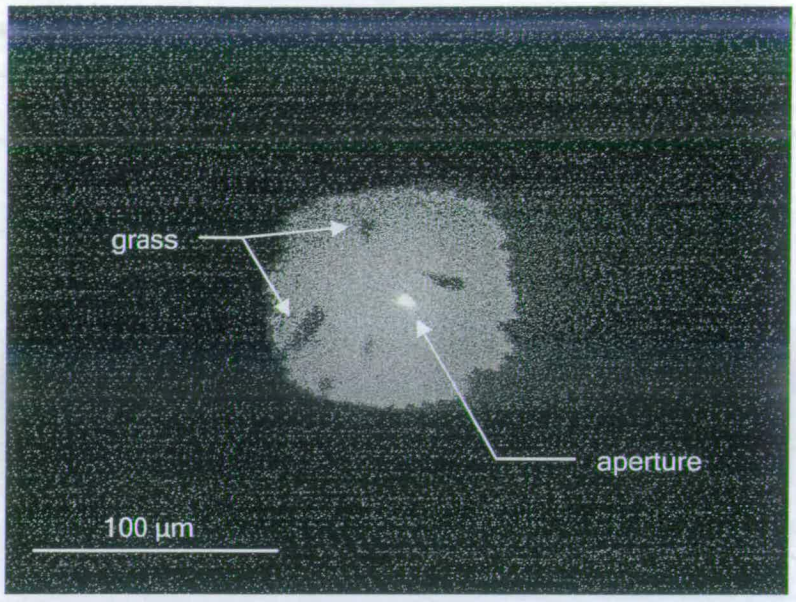

Figure 7.3.3c: Transmission light microscopy photograph of aperture and backside cavity. The white circle indicates the location of the aperture. The bright outline indicates where the backside cavity has been etched away (where orange light is transmitting through the silicon device layer). The dark spots, or "grass," inside the cavity indicate un-etched silicon fragments due to micro masking in the etch process. The blunt and jagged sidewalls of the cavity are due to slight non-uniformity of the deep silicon etch process 500 µm into the silicon handle layer. The diameter of the cavity is approximately 85 µm.

12. The wafers were ashed to remove any remaining photoresist. Then, they were dipped in a 48% HF, 0.01% Triton™ X-100 solution for 1 min to remove the exposed buried oxide layer and the thermal oxidation from the complete wafer. (The surfactant was added to the HF solution to promote maximum wetting into the aperture and cavity up to the buried oxide layer.[41] Next, the wafer featuring the 2.5-µm aperture diameter was subjected to an SF_6 plasma for 8 sec for optimum rounding of the aperture edges.[42] This wafer was then subjected to ultrasonic cleaning for 10 min. However, this process destroyed all of the structures by rupturing the freestanding device layer over the cavity. After abandoning the ultrasonic cleaning, the remaining wafer was thermally wet

[41] It was difficult to verify that the buried oxide has been removed using optical and electron microscopy.
[42] However, unnoticeable to the naked eye, the wafer was not cleaned and dried properly and micro masking pitted the surface, especially around the apertures. From this observation, it was decided not to subject the other wafer to this process to ensure maximum surface smoothness and risk starting over! Moreover, initial roundness tests were quite similar with and without SF6 treatment (although SF6 provides slightly more rounded cornering).

oxidised to grow a 1-μm oxide layer of thickness, then immediately stripped with the same HF/Triton™ solution for 2 min (Fig. 7.3.3e: step 12).

13. The wafer was agitated and flipped over, again to promote a complete etch of the exposed buried oxide layer (if not fully removed from the previous HF etch). Next, the wafer was thermally wet oxidised for a 1-μm growth of oxide (Fig. 7.3.3e: step 13).

14. A layer of PECVD oxide was deposited on the frontside from a STS© PECVD system. To obtain a 1-μm deposition thickness, oxide was deposited for 18.5 min (Fig. 7.3.3e: step 14).

15. As part of the post-process development, the wafer was quartered into four pieces to test the effects of different surface modifications. All breaking steps were done manually by diamond scribing and snapping. Extra care was taken to minimise the probability of silicon dust and fragments contaminating the apertures. For example, microscope slides were routinely cleaned in IPA and positioned over the wafer segments during these steps. In addition, fragments were air blown off the surface before removing the slides.

16. All surface modification steps were done in Tempress© furnace tubes (size #11) with a constant N_2 flow at 1000 sccm. For wafer segment no. 1 (upper-left corner), boron doping (from solid source boric oxide) and annealing was performed at a starting temperature of 900°C, ramped to 1000°C @ (5°C/min), held at constant temperature for 30 min, then ramped down to 900°C @ (5°C/min). For wafer segment no. 2 (upper-right corner), boron doping and annealing was performed at 800°C for 70 min. For wafer segment no. 3 (lower-right corner), annealing without boron deposition was performed at 1000°C. For wafer segment no. 4 (lower-right corner), the control group received no surface modifications. After surface modification, all wafer quarters were rinsed in distilled water three times for 5 min each and dried.

17. The wafers were again diamond scribed and snapped by hand between two microscope slides into 7-mm square chips.[43]

18. To reduce the capacitance of the device, the backside of each device was hand painted with PDMS. Using an ultra-fine paintbrush, an untouched circular area of 1-mm diameter was left uncoated around the cavity. This prevented the PDMS from creeping into the aperture during the time of curing (see Figure 7.3.3d).[44] The devices were placed face down in a thermoplastic container and cured in an oven for at least 2.5 hours at 80-85°C, after which the PDMS was probed with tweezers to verify curing was fulfilled.

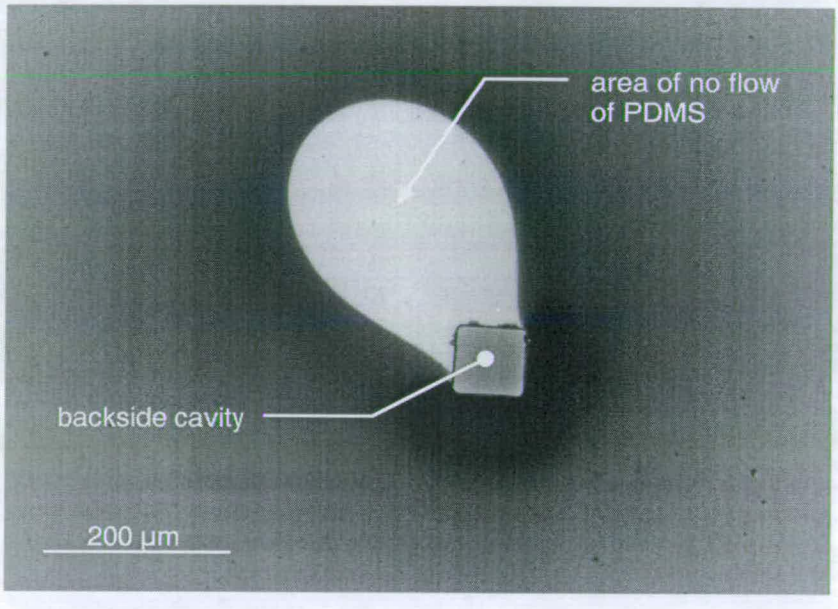

Figure 7.3.3d: Backside cavity with surrounding PDMS after curing. From observation, the PDMS has creped towards the centre and formed a lip around the cavity, but no flow into the cavity is observed or detected.

19. For the final post-processing step, device chips were fixed to the inset of a Perspex™ base frame (see Fig. 7.3.4) by introducing a drop of PDMS at each of the four edges of the device. From observation underneath, the PDMS creeps

[43] Care was taken to induce snapping down street guides; partial scribing at the edge of the wafer helped the snapping process substantially. Additional slides were placed elsewhere on the top of the wafer to reduce contamination from shrapnel and silicon dust.

[44] Later, it was discovered that some creeping occurred up to the cavity edge without flowing into the cavity.

across the edge of the device and formed a layer on the backside, stopping at the 3-mm hole in the frame. The creeping effect established physical (and electrical) isolation between the top and bottom of the frame to separate the patch solution from the extracellular solution. No PDMS crept to the topside of the device.

20. After curing, in order to remove any remaining silicon dust and fragments, frames were cycled with distilled water, IPA and warm/cool air in a Marangoni™ drier.

21. The individual frames were stored in dust-free single wafer handling containers until immediate use outside the cleanroom facility.

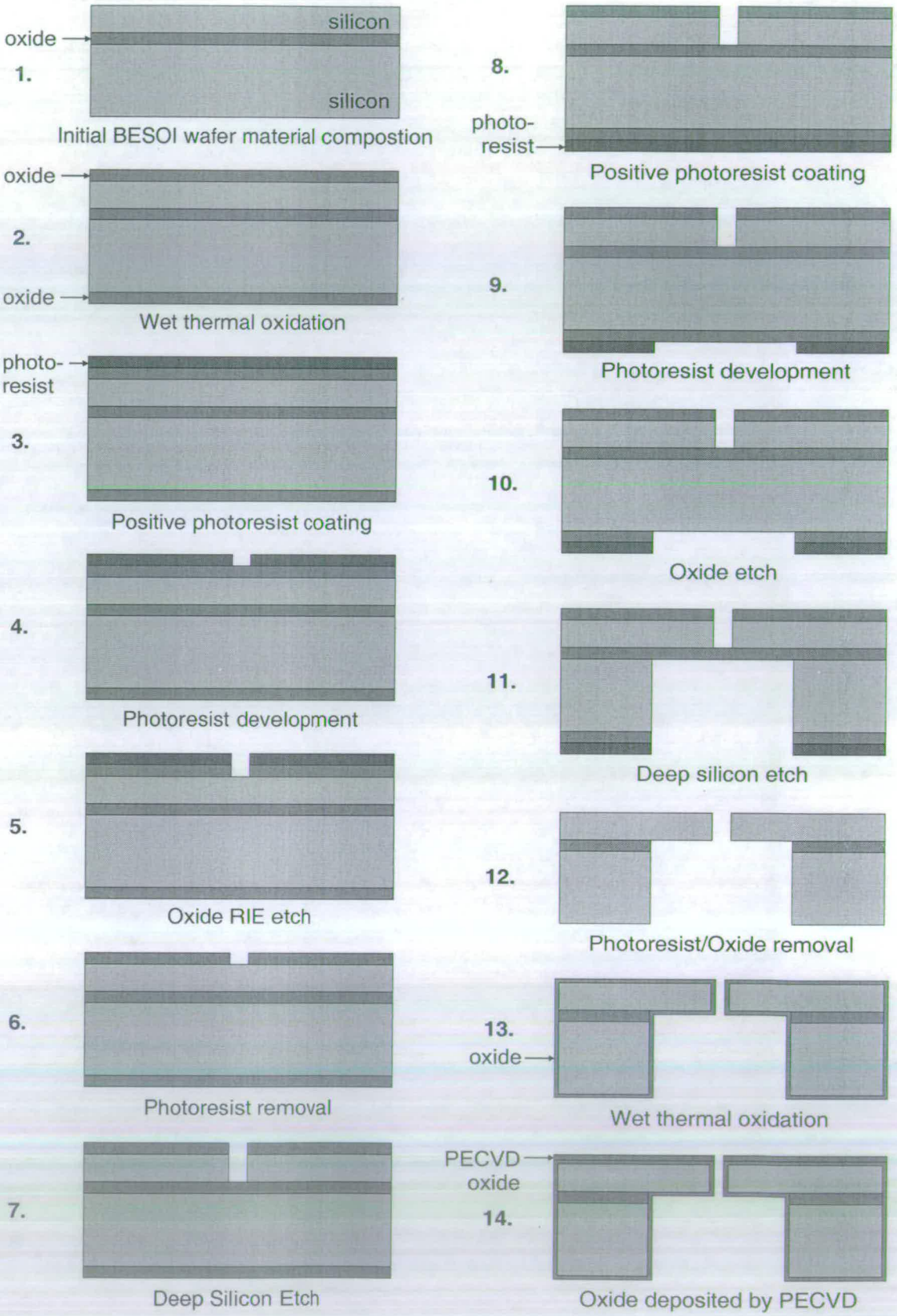

Figure 7.3.3e: Cross-section pictorial representation of the process steps for device II.

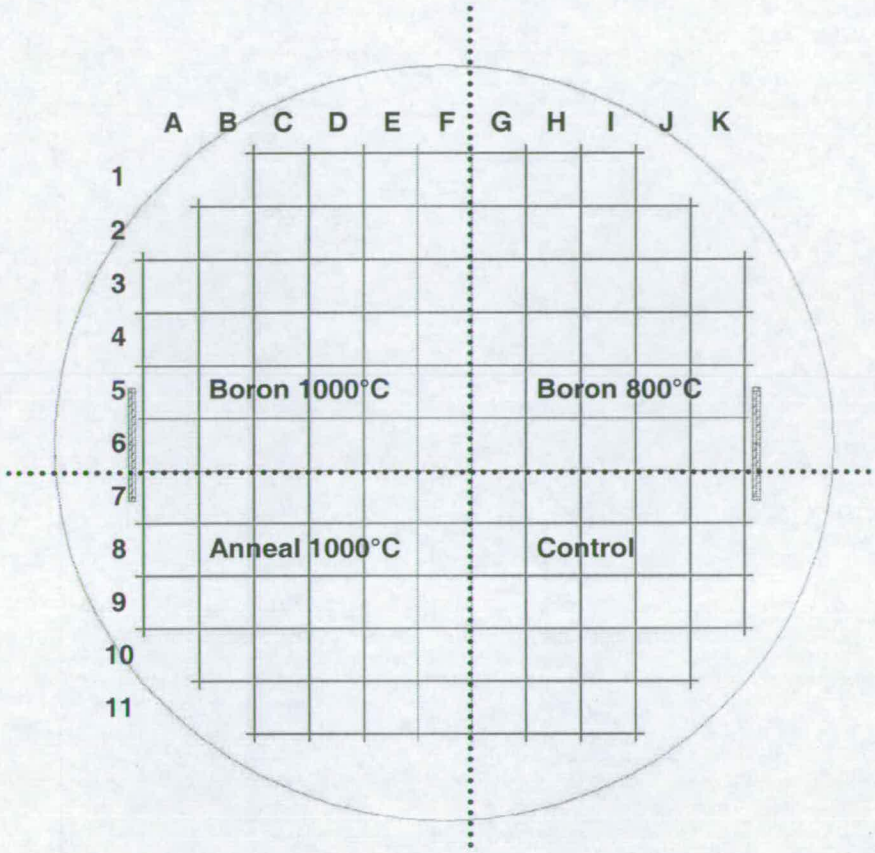

Figure 7.3.3f: Patch-clamp II mask layout on 4" wafer (7-mm square devices).

7.3.4 Platform II design and construction

The platform is an evolutionary step from the previous platform outlined in Section 7.2.4. To withstand pressure gradients during suction, an O-ring was inserted around the patch solution well to prevent the formation of air-bubbles. A transparent and solid Perspex™ base was designed to reduce air-bubble formation. A removable and re-useable Ag/AgCl pellet electrode was positioned to the side of the patch solution well. Platform II is shown in Figure 7.3.4.

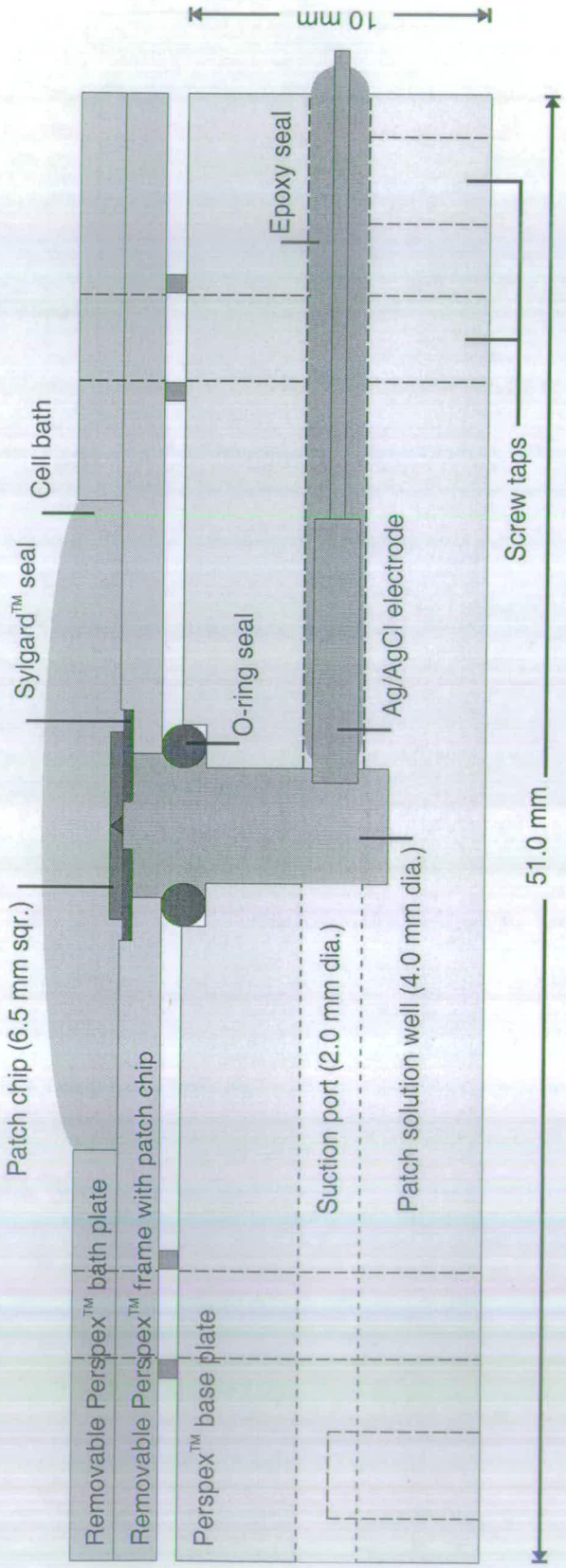

Figure 7.3.4: Cross-section diagram of device platform version II. The figure is drawn to a scale of <4:1>.

7.3.5 Cross-sectional analysis

Two devices were selected for focused-ion-beam (FIB) milling. One device was selected near the wafer edge and the other near the centre (B10 and F6 from Fig. 7.3.3f).[45] After milling, the cross-section of the device was examined by SEM imaging. The circular aperture, oxide layers, backside cavity and device layer were all clearly recognisable. The analysis helped verify that the expected physical geometry of the microstructure was achieved. The microstructure and respective components are shown in Figure 7.3.5.

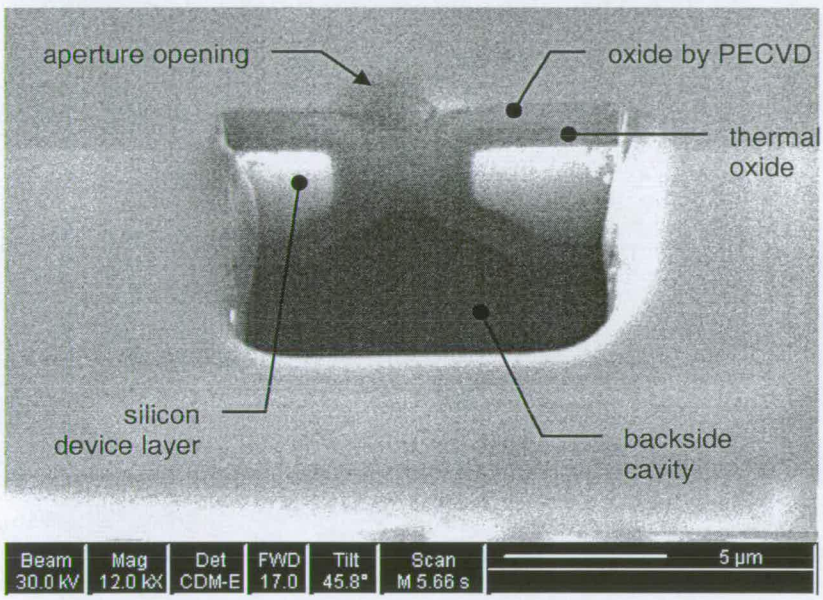

Figure 7.3.5: An embedded planar patch-clamp electrode in silicon (device B10). The feature was milled using a focused ion beam to view the cross-section at 45°. The V-groove visible on the bottom of the aperture is due to over etching of the aperture from frontside deep silicon etching. The aperture opening, as well as the thermal oxide layer (dark inside band) and PECVD oxide layer (outside band) are all clearly visible. The black empty space below the aperture is the backside cavity. The scale bar represents the horizontal distance of 5 µm, as shown. However, because of the tilt, the scale bar represents a vertical distance of $5 \cdot \cos(45°) = 3.54$ µm.

[45] It is important to note that, throughout the manufacturing of these devices, it was not possible to inspect the microstructure in cross-section.

7.3.6 Electrical Performance Measures

Filling the device with patch solution was not straightforward. The application of patch solution to the 80-μm backside cavity does not initiate self-filling due to surface tension. After repeated trials, it was discovered that filling the device first requires submerging the device completely in patch solution in a desiccator. Then, the chamber pressure needed to be lowered to ≤35 mTorr, past the point at which the solution boils violently. As the air escaped from the solution, the solution began to fill the cavity. During this process, the chamber was subjected to mechanical vibration to help to reduce the number of air-pockets. After 5 min, the desiccator was purged with air, once most air-bubbles disappeared. Finally, the device was removed and placed on the platform in the same process as in platform I. A base plate was screwed down and a seal was formed around the O-ring.

The experimental setup was described in Section 7.2.5. Three glass pipettes were used as a control, and a total of five devices were tested. Graphs of the current-voltage relationships and the distribution of time constants can be found in Figures 7.3.6a, 7.3.6b and 7.3.6c. In addition to these measurements, an attempt was made to perform an AC analysis to compare the pass-band of the devices to glass. The frequency response of a sinusoidal current input was measured over a range of 50 Hz to 10 kHz. The current amplitude was set at 4 nA, tested over a range of DC offsets of -2, 0, and +2 nA. By post-analysis of the input and output sinusoidal peaks in the software package pClamp 9.2, the phase offset and voltage amplitude were measured. (It was determined that the current DC offset had no effect on the response.) Noise levels were between 500-1000 μV_{pp}. This noise level made measuring the voltage amplitude difficult with the standard testing equipment and current input. As a control, a 3.4-MΩ metal-film type resistor was tested to study the frequency response of the testing equipment. The testing equipment, in conjunction with the device or pipette, determines the overall frequency response of the system. Bode plots of the phase offset and amplitude attenuation are shown in Figures 7.3.6e and 7.3.6f. The phase-offset was fit to a 5-parameter sigmoidal function given by the equation below:

$$y = y_0 + \frac{a}{\left[1 + e^{-\left(\frac{x - x_0}{b}\right)}\right]^c}$$

Next, the cut-off frequency $f_{C;fit}$ was calculated at the point where the phase-offset crossed 90° (as in a 2-pole low-pass filter). Then, the cut-off frequency f_C derived from *tau* was compared to $f_{C;fit}$. The time constant, resistance, capacitance and cut-off frequency (calculated from the time constant and resistance) are listed in Table 7.3.6.

Electrode	Parameters					
	τ (ms)	R (MΩ)	C (pF)	ω (rad/s)	f_C (Hz)	$f_{C;\,fit}$ (Hz)
dev. H4 *	0.413	2.53	163.2	2421	385	–
dev. H11	0.080	0.95	84.2	12500	1989	–
dev. G11	0.057	1.40	40.8	17544	2792	–
dev. I10	0.052	1.38	37.7	19231	3061	2749
dev. H6	0.093	1.48	62.7	10753	1711	1902
dev. G8	0.081	1.65	55.4	12346	1965	2076
mean	0.073	1.37	56.2	14475	2304	–
std. dev.	0.017	0.26	18.8	3685	587	–
pipette no. 1	0.043	4.14	10.5	23256	3701	4258
pipette no. 2	0.040	3.73	10.7	25000	3979	5038
pipette no. 3	0.037	3.63	10.9	27027	4301	5038
mean	0.040	3.83	10.7	25094	3994	–
std. dev.	0.003	0.27	0.2	1887	300	–

Table 7.3.6: Electrical parameters for device II and pipettes. The time constant, resistance, capacitance and cut-off frequency are included.

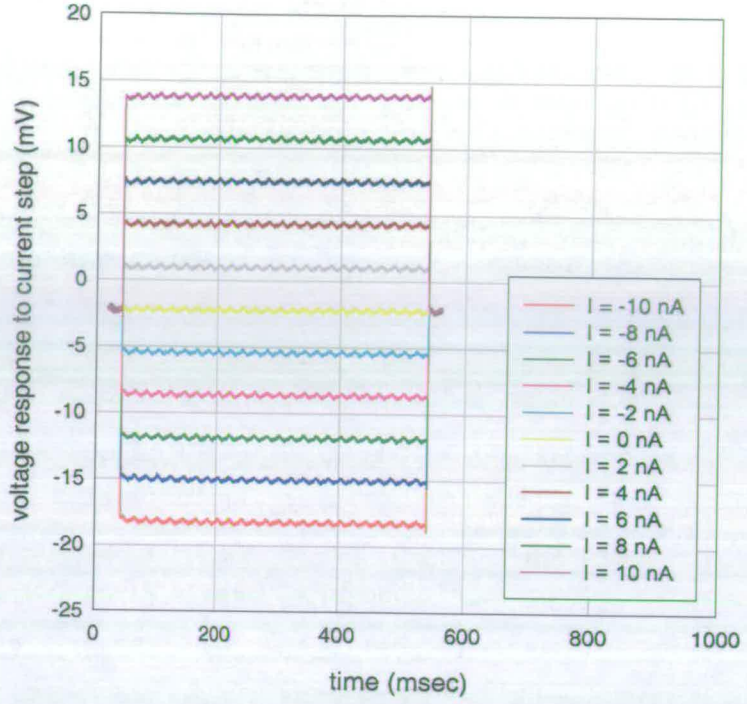

Figure 7.3.6a: Current-step response for device H6.

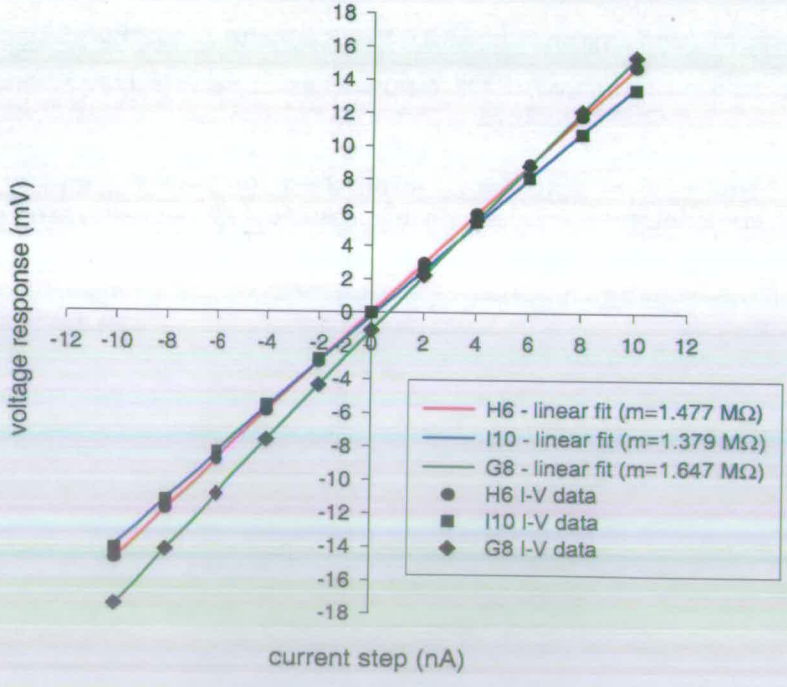

Figure 7.3.6b: I-V plots for devices G8, H6 and I10.

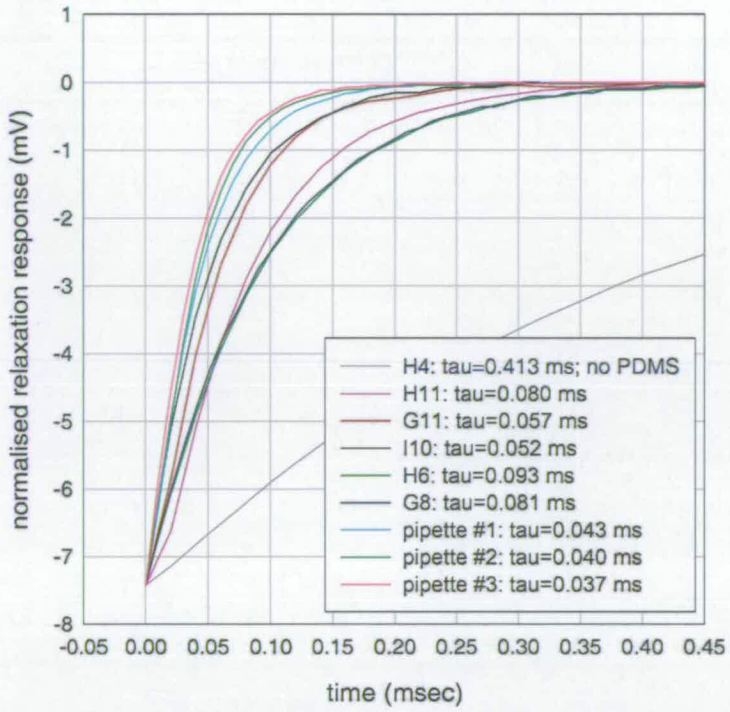

Figure 7.3.6c: Relaxation responses for patch chip version II compared with three conventional glass pipettes. The measurements were made with 150 mM potassium methyl-sulphate and 10 mM HEPES patch solution and the cell bath solution from Table 7.2.5b, with a 2-µm pipette aperture diameter.

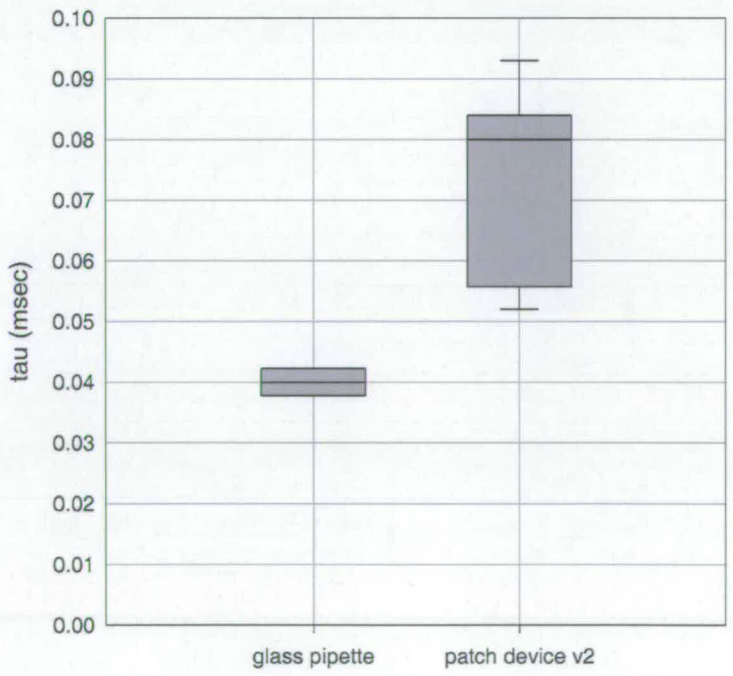

Fig 7.3.6d: Box-plot graph showing the range and distribution of time responses from three glass pipettes and six ver. II patch devices.

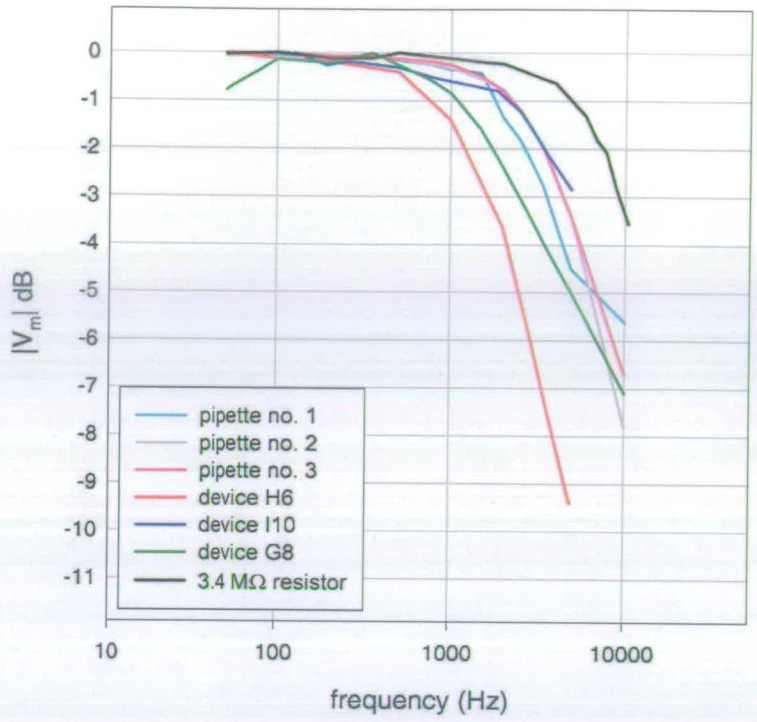

Figure 7.3.6e: Bode-plot of the amplitude attenuation in dB for device II, pipettes and 3.4-MΩ metal-film resistor.

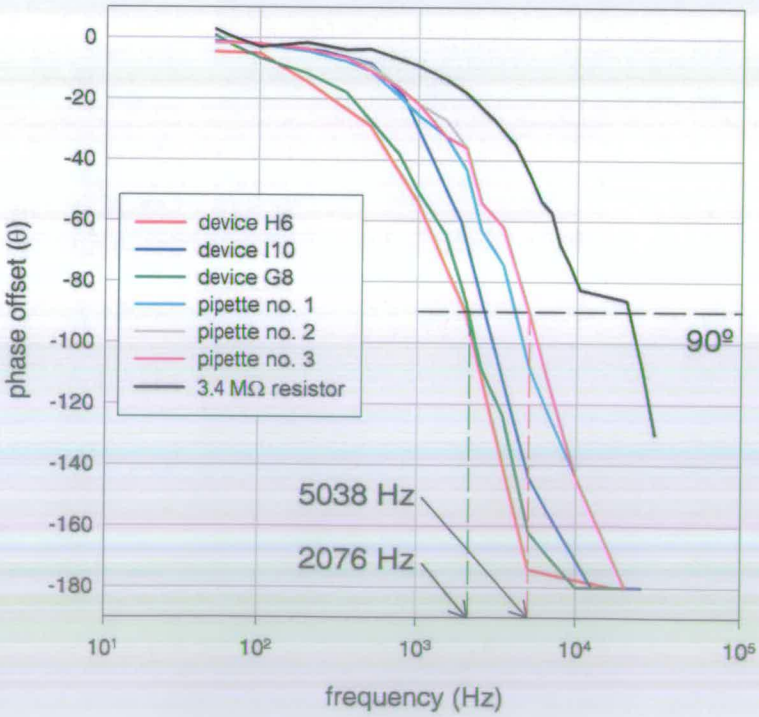

Figure 7.3.6f: Bode-plot of the phase offset for device II, the pipettes and 3.4-MΩ metal-film resistor. The pass-band width is smallest for the devices and larger for the pipette.

7.3.7 Surface roughness measurements

As discussed in Chapter 2, surface roughness may have a considerable impact on seal formation during patch-clamping. Thus, it was decided to study the roughness of ten devices of varying surface modification as described in Chapter 4. The mean roughness (R_a) was measured by averaging the values of four square areas of 100,000±15,000-nm^2 size selected in each corner of the AFM scan. The complete AFM scan size was approximately 4-μm square with the aperture positioned in the centre. Thus, roughness measurements were taken in close proximity to the aperture, as slight discrepancies and unwanted effects from the fabrication process are routinely evident from observations of the surface around the aperture, especially from etching processes. The mean roughness (and standard deviation) of 10 devices is listed in Table 7.3.7.

Device	Group	Mean Roughness (R_a in nm)	Std. Dev.
G7	control	2.649	0.577
J10	control	3.595	1.405
G5	800°C B^+	1.848	0.378
J2	800°C B^+	2.428	0.154
B3	1000°C B^+	5.781	5.771
B2	1000°C B^+	4.583	1.560
F6	1000°C B^+	3.125	1.051
F11	1000°C anneal	5.911	3.971
B10	1000°C anneal	3.231	0.761
E7	1000°C anneal	7.439	2.692

Table 7.3.7: Mean roughness R_a and std. dev. for 10 ver II devices.

7.3.8 Discussion – device II

The mechanical structure of device II is very stable (at the time of writing, no devices have been destroyed during attempts at patch-clamping in Section 7.4). The microfabrication yield of device II is given in the Table 7.3.8. Notably, 25% of the devices undergoing 1000°C boron deposition had defective apertures. Defects included notches and shards around the aperture walls. Otherwise, the yield for the other three groups was within an acceptable tolerance (≥96%).

Group	total devices	% yield	% defective
control	22	21/22 = 95%	1/22 = 4.5%
1000°C anneal	26	25/26 = 96%	1/26 = 3.8%
800°C boron dep.	27	26/27 = 96%	1/27 = 3.7%
1000°C boron dep.	32	24/32 = 75%	8/32 = 25%

Table 7.3.8: Microfabrication yield statistics for device II.

The mean roughness R_a values of the devices ranged from 1.8 to 7.5 nm. Due to the harsh environmental conditions of the processing, roughness values are typically larger than those measured from the pure material in Section 4. Interestingly, devices undergoing surface modifications at 1000°C show significantly larger values of R_a (Mann-Whitney U Rank Sum Test, P = 0.002). The increase in roughness was not observed from the same modifications of the pure materials in Section 4. It is speculated that the surface impurities from processing (as opposed to pure surface materials) may amplify the roughness after the same annealing procedure.

The electrical performance of this device approaches that of a pipette. First, the current-voltage relationship was linear in the range of ±10 nA. Second, the differences in distribution of the values of *tau* for the devices and pipettes are statistically significant (unpaired t-test, P = 0.021). The mean value of *tau* is 0.073 ms for the devices, compared to 0.040 ms for a conventional pipette. Also, the distribution of values of the cut-off frequency for the devices and pipettes are statistically significant (unpaired t-test, P = 0.002). The mean value for the glass pipettes is considerably larger at 3994 Hz, compared to 2304 Hz for the devices. However, for purposes of recording electrical activity of cortical neurons, this frequency is acceptable. For example, the maximum spiking rate of cortical pyramidal neurons of the guinea pig is >250 Hz [108].

7.4 Towards Highly Resistive Neuronal Recordings

7.4.1 Establishing the Neuron-electrode Junction

Several attempts at patch-clamping have been made with device II under a light transmission microscope using snail neurons. Such neurons are easily visualised when moving the cell in close proximity to the aperture and are easier to hold (by suction onto a >20 μm wide-mouth glass pipette aperture) and manoeuvre owing to their large soma.

First, clusters of ten or more neurons from various ganglions were positioned directly over the aperture. Suction was introduced and changes in light reflection were observed, suggesting that the applied suction created a pressure gradient at the aperture. However, visualisation of the process was impossible and seals were not obtained.

Second, coverglass of neuron cultures were positioned up-side down and placed directly over the device surface. The glass was moved across the device and the aperture resistance was continuously monitored. Visualisation of the neurons was possible with this configuration and suction was routinely applied when neurons were positioned over the aperture. However, no electrical signals or seals were found.

Thirdly, individual snail neurons were dissociated and prepared by the technique discussed in Chapter 3. Next, neurons were manoeuvred to the aperture by a wide-mouth glass pipette. Visualisation of the process was easily obtained; and suction was applied once a neuron was positioned appropriately. Seal resistances $\leq$ 600 MΩ were obtained; but no electrical signals were observed (see Figures 7.4a and 7.4b). It must be stressed that electrical signals were difficult to record from dissociated neurons in general; recordings from neurons still attached to the ganglion were typically observed. A CCD image of this process can be found in Figure 7.4c.

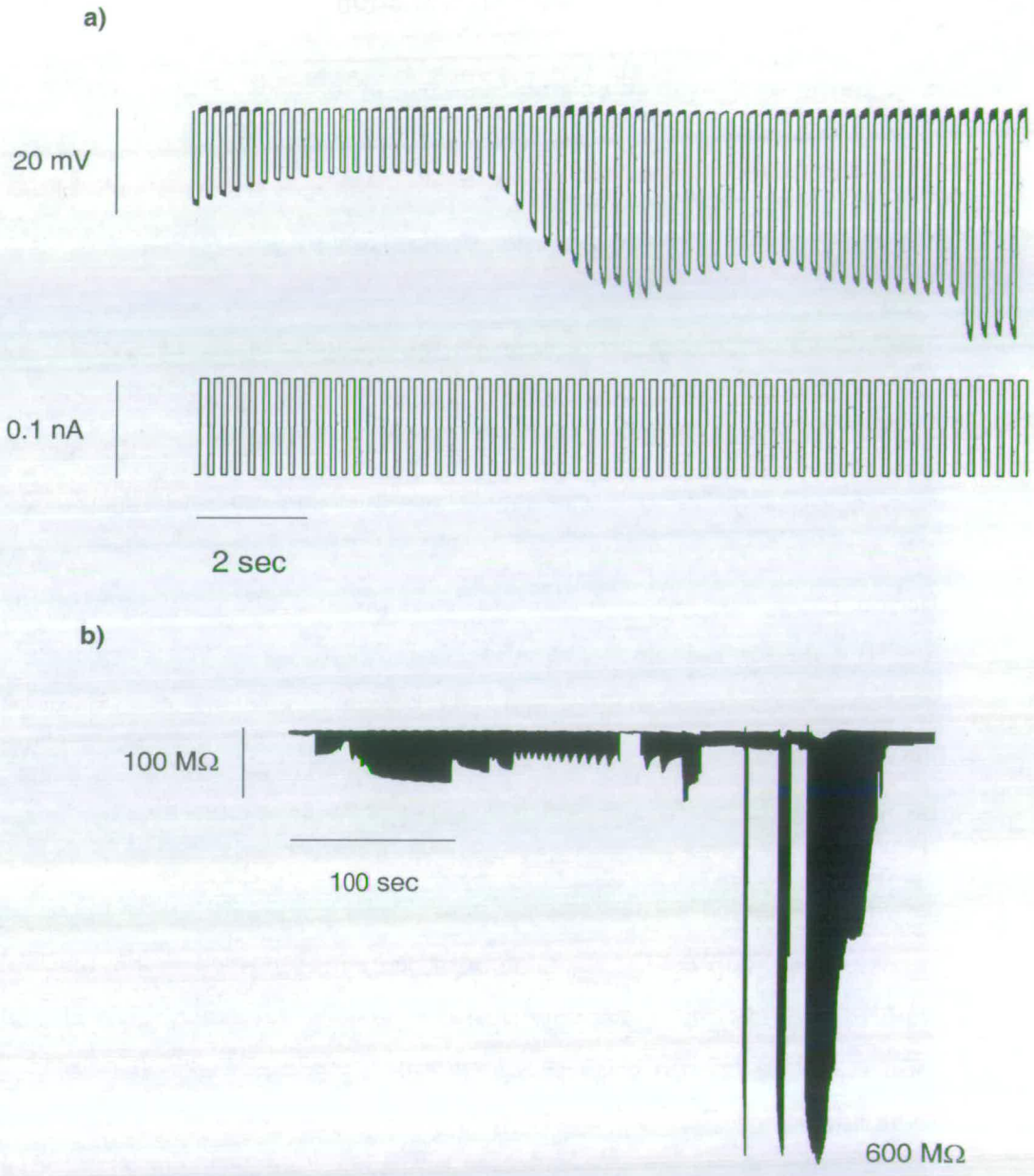

Figure 7.4a and 7.4b: Seal-resistance recordings. Maximum seal resistance recorded was 600 MΩ. Resistance was monitored by injection of 0.1 nA current steps with a period of 250 ms.

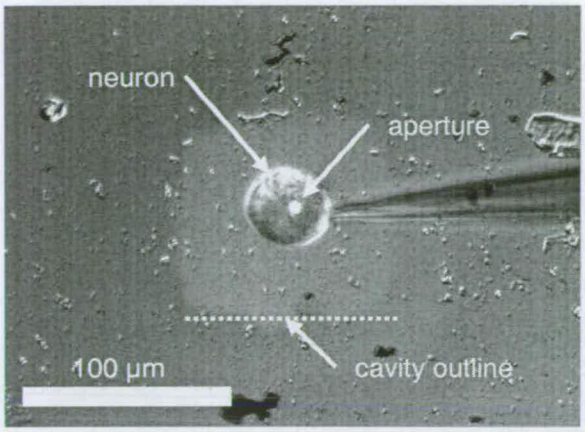

Figure 7.4c: The visualisation of the attempt to patch-clamp on a snail neuron with device II. Scale bar length is 100 µm. The soma diameter is approximately 60 µm. Transmission microscopy allows the backside cavity walls (85-µm square) to be dimly lit; the aperture is indicated by the bright light.

7.4.2 Discussion

The difficulty in achieving gigaohm seals or neuronal recordings with device II can be explained. First, a reasonable "baseline" in successfully patch-clamping on snail neurons with conventional glass pipettes has not yet been achieved. If patch recordings from conventional pipettes cannot be achieved reliably, it is impossible to comment on the quality of the planar device. We believe that the conditions of the cell membrane must be carefully controlled during the dissociation process. At the time of writing, attempts at achieving a baseline probability of patch-clamping using pipettes is still underway. Sub-gigaohm resistances may also be attributable to the large mean roughness value of the devices, which could allow current leakage between the patch aperture wall and cell membrane. Also, the physical act of positioning and performing suction described in this work may be inferior to other methods, including: (1) electrophoresis; (2) the use of an osmotic pump; and (3) the trapping of a cell from a suspension during suction. In fact, the current lack of proof to our theory as to how conventional patch-clamp seals are formed inhibits our study, as it is not clear precisely which characteristics of (say) a borosilicate glass pipette are most important.

7.5 Conclusion

The complete patch-clamp system (device, platform and recording equipment) outlined in this work suggests the possibility of recording from neurons. It remains unclear whether two or more neurons can be patched in a network from single planar microstructures. The patch-clamping of cortical neurons (as opposed to snail neurons) will be more difficult because of their small cell body. Mostly, there will be much difficulty in the future in aligning a group of neurons growing on a 2-D substrate to each aperture and forming a gigaohm seal, all at the same time. The feasibility of this task should be carefully investigated, given the extreme patience and tolerance of patch-clamping in general. Notably, the pipette must be positioned very carefully, and suction must be applied at the correct time on a viable neuron. Moreover, the question remains to be answered whether the use of individualised suction lines are necessary for multi-electrode patch-clamping. If the use of individualised suction lines is necessary, then a platform unit to accommodate this needs to be addressed. The answers to these questions are not easy given the variable conditions of biological tissue.

8 Conclusion

This study investigated the hypothesis that the important aspects of the patch-clamp technique can be miniaturised and scaled down to micron-size silicon-based microstructures. The work emulated many of the important characteristics that this electrophysiological method offers. The preliminary conclusions to this work were outlined at the end of each chapter. The overall conclusions to the hypothesis were drawn from these conclusions and are given below:

a) Healthy and viable cell cultures of primary rat cortical neurons can be grown on standard insulating materials for the study of network behaviour. The use of boron deposition was shown to enhance neuron survivability and reduce clumping. No strong correlations were made between viability and hydrophilicity and roughness of the surface. It remains the task to verify the electrical activity of these neuronal networks.

b) A minimum patch aperture length was obtained using theoretical models of gigaseal formation. The surface energy and atomic structure of the apertures fabricated in this study express similarities to borosilicate glass, an established material capable of gigaseal formation during patch-clamping.

c) Deposition techniques can ensure the cross-section radius of curvature of the aperture to be ≥ 0.5 μm. However, it was not possible to fabricate the aperture top-view to a high degree of circularity after thermal oxidation. An analysis of the profile texture to quantify the circularity error was useful. Large circularity error may reflect a truer probability of obtaining low seal resistance.

d) Patch-clamp electrodes can be fabricated into planar silicon microstructures with similar electrical performances of conventional borosilicate glass pipettes.

e) Electrophysiological recordings from *Lymnaea stagnalis* neurons have not been achieved with the current prototype and further experimentation should be explored. Patch-clamp recordings of non-neuronal cell types have been achieved with similar device microstructures reported in the current literature and currently used in industry for high-throughput ion-screening studies. Therefore, it remains unclear whether patch-clamp recordings from neurons can be achieved with planar microstructures.

f) The task remains to construct a multi-electrode array prototype with integrated Ag/AgCl electrodes. The miniaturisation of the electrode has yet to be achieved. It is unclear whether the living neural network can be cultured on the recording device without rendering the apertures unusable unless techniques are employed to keep the aperture surface clean (in practice, patch-clamp pipettes need to be clean for gigaseal formation to occur).

Therefore, the hypothesis is supported by points (a), (b), (c) and (d). However, until points (e) and (f) are achieved, the hypothesis is not upheld conclusively.

Bibliography

[1] Crick, F. and Koch, C., "A framework for consciousness," *Nature Neuroscience*, vol. 6, no. 2, pp. 119-126, 2003.

[2] Shepherd, G. M., *The Synaptic Organization of the Brain*, 3 ed. Oxford: Oxford University Press, 1990.

[3] Goddard, N. H., Hucka, M., Howell, F., Cornelis, H., Shankar, K., and Beeman, D., "Towards NeuroML: Model description methods for collaborative modelling in neuroscience," *Philosophical Transactions of the Royal Society of London Series B-Biological Sciences*, vol. 356, no. 1412, pp. 1209-1228, 2001.

[4] Arshavsky, Y., "Cellular and network properties in the functioning of the nervous system: from central pattern generators to cognition," *Brain Research Reviews*, vol. 41 pp. 229-267, 2003.

[5] Dudek, S. M. and Bear, M. F., "Bidirectional Long-Term Modification of Synaptic Effectiveness in the Adult and Immature Hippocampus," *Journal of Neuroscience*, vol. 13, no. 7, pp. 2910-2918, 1993.

[6] Gutnick, M. J., Connors, B. W., and Prince, D. A., "Mechanisms of Neocortical Epileptogenesis Invitro," *Journal of Neurophysiology*, vol. 48, no. 6, pp. 1321-1335, 1982.

[7] Roberts, P. D., "Computational consequences of temporally asymmetric learning rules: I. Differential Hebbian learning," *Journal of Computational Neuroscience*, vol. 7, no. 3, pp. 235-246, 1999.

[8] Song, S., Miller, K. D., and Abbott, L. F., "Competitive Hebbian learning through spike-timing-dependent synaptic plasticity," *Nature Neuroscience*, vol. 3, no. 9, pp. 919-926, 2000.

[9] Kirkwood, A. and Bear, M. F., "Hebbian Synapses in Visual-Cortex," *Journal of Neuroscience*, vol. 14, no. 3, pp. 1634-1645, 1994.

[10] Baker, P. F., Shaw, T. I., and Hodgkin, A. L., "Replacement of Axoplasm of Giant Nerve Fibres with Artificial Solutions," *Journal of Physiology-London*, vol. 164, no. 2, pp. 330-&, 1962.

[11] Hodgkin, A. L., Huxley, A. F., and Katz, B., "Ionic Currents Underlying Activity in the Giant Axon of the Squid," *Archives des Sciences Physiologiques*, vol. 3, no. 2, pp. 129-150, 1949.

[12] Hodgkin, A. L., Huxley, A. F., and Katz, B., "Measurement of Current-Voltage Relations in the Membrane of the Giant Axon of Loligo," *Journal of Physiology-London*, vol. 116, no. 4, pp. 424-448, 1952.

[13] Katz, B., *Nerve, Muscle, and Synapse* London: McGraw-Hill, 1966, pp. 1-193.

[14] Curtis, A. S. G., Breckenridge, L., Connolly, P., Dow, J. A. T., Wildinson, C. D. W., and Wilson, R., "Making Real Neural Nets - Design Criteria," *Medical & Biological Engineering & Computing*, vol. 30, no. 4, pp. CE33-CE36, 1992.

[15] Connolly, P., Clark, P., Curtis, A. S. G., Dow, J. A. T., and Wilkinson, C. D. W., "An Extracellular Microelectrode Array for Monitoring Electrogenic Cells in Culture," *Biosensors & Bioelectronics*, vol. 5, no. 3, pp. 223-234, 1990.

[16] Maher, M., Pine, J., Wright, J., and Tai, Y. C., "The neurochip: a new multielectrode device for stimulating and recording from cultured neurons," *Journal of Neuroscience Methods*, vol. 87 pp. 45-56, 1999.

[17] Jenkner, M. and Fromherz, P., "Bistability of membrane conductance in cell adhesion observed in a neuron transistor," *Physical Review Letters*, vol. 79, no. 23, pp. 4705-4708, 1997.

[18] Nakamura, W., Honma, S., Shirakawa, T., and Honma, K. I., "Clock mutation lengthens the circadian period without damping rhythms in individual SCN neurons," *Nature Neuroscience*, vol. 5, no. 5, pp. 399-400, May2002.

[19] DeMarse, T. B., Wagenaar, D. A., Blau, A. W., and Potter, S. M., "The Neurally Controlled Animat: Biological Brains Acting with Simulated Bodies," *Autonomous Robots*, vol. 11 pp. 305-310, 2001.

[20] Neher, E., "Molecular biology meets microelectronics," *Nature Biotechnology*, vol. 19 pp. 114, 2001.

[21] Fromherz, P., "Extracellular recording with transistors and the distribution of ionic conductances in a cell membrane," *European Biophysical Journal*, vol. 28 pp. 254-258, 1999.

[22] Fertig, N., Blick, R. H., and Behrends, J., "Whole Cell Patch Clamp Recording Performed on a Planar Glass Chip," *Biophysical Journal*, vol. 82 pp. 3056-3062, 2002.

[23] van Rossum, M., Turrigiano, G., and Nelson, S., "Fast Propagation of Firing Rates through Layered Networks of Noisy Neurons," *Journal of Neuroscience*, vol. 22, no. 5, pp. 1956-1966, Mar.2002.

[24] Fitzsimonds, R. M., Song, H. J., and Poo, M. M., "Propagation of activity-dependent synaptic depression in simple neural networks," *Nature*, vol. 388, no. 6641, pp. 439-448, 1997.

[25] Asmild, M., Korsgaard, M., and Willumson, N., "Upscaling and Automation of Electrophysiology: Toward High Throughput Screening in Ion Channel Drug Discovery," *Receptors and Channels*, vol. 9 pp. 49-58, 2003.

[26] Schnizler, K., Küster, M., Methfessel, M., and Fejtl, M., "The Roboocyte: Automated cDNA/mRNA Injection and Subsequent TEVC Recording on *Xenopus* Oocytes in 96-Well Microtiter Plates," *Receptors and Channels*, vol. 9 pp. 41-48, 2003.

[27] van Tol-Steye, H., Lodder, J. C., Planta, R. J., and van Heerikhuizen, H., "Convergence of multiple G-protein-coupled receptors onto a single type of potassium channel," *Brain Research*, vol. 777 pp. 119-130, 1997.

[28] van Soest, P. F. and Kits, K. S., "Conopressin affects excitability, firing, and action potential shape through stimulation of transient and persistent inward currents in mulluscan neurons," *Journal of Neurophysiology*, vol. 79, no. 4, pp. 1619-1632, 1998.

[29] van Soest, P. F., Lodder, J. C., and Kits, K. S., "Activation of protein kinase C by oxytocin-related conopressin underlies pacemaker current in Lymnaea central neurons," *Journal of Neurophysiology*, vol. 84, no. 5, pp. 2541-2551, 2000.

[30] Toselli, M. and Lux, H. D., "Gtp-Binding Proteins Mediate Acetylcholine Inhibition of Voltage Dependent Calcium Channels in Hippocampal-Neurons," *Pflugers Archiv-European Journal of Physiology*, vol. 413, no. 3, pp. 319-321, 1989.

[31] Neher, E. and Sakmann, B., "Single channel currents recorded from membrane of denervated frog muscle fibres," *Nature*, vol. 260 pp. 799-802, 1976.

[32] Sherman-Gold, R., *The Axon Guide for Electrophysiology & Biophysics Laboratory Techniques* Foster City, CA: Axon Instruments, Inc., 1993.

[33] Hille, B., *Ionic channels of excitable membranes*, 2nd ed. Sunderland, MA: Sinauer Associates Inc. Publishers, 1992.

[34] Sakmann, B. and Neher, E., *Single-Channel Recording*, 2nd ed. Plenium Press, 1995.

[35] Hamill, O., Marty, A., Neher, E., Sakmann, B., and Sigworth, F., "Improved Patch-Clamp Techniques for High-Resolution Current Recording from Cells and Cell-Free Membrane Patches," *Pflügers Archiv European Journal of Physiology*, vol. 391 pp. 85-100, 1981.

[36] Sokabe, M. and Sachs, F., "The Structure and Dynamics of Patch-clamped Membranes: A Study Using Differential Interference Contrast Light Microscopy," *The Journal of Cell Biology*, vol. 111 pp. 599-606, 1990.

[37] Cole, K. S., "Linear and Passive Cell Properties," *Membranes, Ions and Impulses: A Chapter of Classical Biophysics* University of California Press, 1968, pp. 5-113.

[38] Kandel, E. R., "Nerve Cells and Behavior," in Kandel, E. R. and Schwartz, J. H. (eds.) *Principles of Neural Science* 2 ed. New York: Elsevier Science Publishing Co., 1985, pp. 13-24.

[39] Fertig, N., Tilke, A., Blick, R. H., and Kotthaus, J. P., "Stable integration of isolated cell membrane patches in a nanomachined aperture," *Applied Physics Letters*, vol. 77, no. 8, pp. 1218-1220, Aug.2002.

[40] Schmidt, C., Mayer, M., and Vogel, H., "A Chip-Based Biosensor for the Functional Analysis of Single Ion Channels," *Angewandte Chemie*, vol. 39, no. 17, pp. 3137-3140, 2000.

[41] Fertig, N., Meyer, Ch., Blick, R. H., Trautmann, Ch., and Behrends, J., "Microstructured glass chip for ion-channel electrophysiology," *Physical Review E*, vol. 64 pp. 040901-1-040901-4, 2002.

[42] Fertig, N., Blick, R. H., and Behrends, J., "Whole Cell Patch Clamp Recording Performed on a Planar Glass Chip," *Biophysical Journal*, vol. 82 pp. 3056-3062, 2002.

[43] Zhou, X. B., Schlossmann, J., Hofmann, F., Ruth, P., and Korth, M., "Regulation of stably expressed and native BK channels from human myometrium by cGMP- and cAMP-dependent protein kinase," *European Journal of Physiology*, vol. 436, no. 5, pp. 725-734, 1998.

[44] Fertig, N., Klau, M., George, M., Blick, R. H., and Behrends, J., "Activity of single ion channel proteins detected with a planar microstructure," *Applied Physics Letters*, vol. 81, no. 25, pp. 4865-4867, Dec.2002.

[45] Klemic, K., Klemic, J., Reed, M., and Sigworth, F., "Micromolded PDMS planar electrode allows patch clamp electrical recordings from cells," *Biosensors and Bioelectronics*, vol. 17 pp. 597-604, Jan.2002.

[46] Gillmor, S. D., Larson, B. J., and Lagally, M. G. "Low-Contact-Angle Polydimethyl Siloxane (PDMS) Membranes for Fabricating Micro-Bioarrays." 1-6. 2002. University of Wisconsin-Madison.

[47] Sigworth, F. and Klemic, K. "Patch Clamp on a Chip." *Biophysical Journal* pp. 2831-2832, 2002.

[48] Matthews, B. and Judy, J., "Characterization of a Micromachined Planar Patch Clamp for Cellular Electrophysiology," *Proceedings of the 1st International IEEE EMBS Conference on Neural Engineering*, pp. 648-651, 2003.

[49] Corey, D. P. and Stevens, C. F., "Science and Technology of Patch-Recording Electrodes," *Single-Channel Recording* 1st ed. New York: Plenium Press, 1983, pp. 53-68.

[50] Sokabe, M., Sachs, F., and Jing, Z., "Quantitative video microscopy of patch clamped membranes stress, strain, capacitance, and strentch channel activation," *Biophysical Journal*, vol. 59 pp. 722-728, 1991.

[51] Sachs, F., "The Noise Produced by Patch Electrodes: A Model," *Biophysical Journal*, vol. 45 pp. 57a, 1984.

[52] Ruknudin, A., Song, M. J., and Sachs, F., "The Ultrastructure of Patch-clamped Membranes: A Study Using High Voltage Electron Microscopy," *The Journal of Cell Biology*, vol. 112, no. 1, pp. 125-134, 1991.

[53] Sakmann, B. and Neher, E., "Geometric Parameters of Pipettes and Membrane Patches," *Single-Channel Recording* 1st ed. New York: Plenum Press, 1983, pp. 37-51.

[54] Coleman, P. A. and Miller, R. F., "Measurement of Passive Membrane Parameters with Whole-Cell Recording from Neurons in the Intact Amphibian Retina," *Journal of Neurophysiology*, vol. 61, no. 1, pp. 218-230, 1989.

[55] Gil, Z., Priel, A., Moy, V. T., Magleby, K. L., and Silberberg, S. D., "Conditions affecting seal formation in patch-clamp recording," *Biophysical Journal*, vol. 80, no. 1, pp. 1858, 2001.

[56] Ogarev, V. A., Timonina, T. N., Arslanov, V. V., and Trapezni, A. A., "Spreading of Polydimethylsiloxane Drops on Solid Horizontal Surfaces," *Journal of Adhesion*, vol. 6, no. 4, pp. 337-355, 1974.

[57] Ausserre, D., Picard, A. M., and Leger, L., "Existence and Role of the Precursor Film in the Spreading of Polymer Liquids," *Physical Review Letters*, vol. 57, no. 21, pp. 2671-2674, 1986.

[58] Purves, R. D., "The Physics of Microelectrodes," *Microelectrode Methods for Intracellular Recording and Ionophoresis* 1981, pp. 26-38.

[59] Nir, S. and Bentz, J., "On the forces between phospholipid bilayers," *Journal of Colloid Interface Science*, vol. 65 pp. 399-412, 1978.

[60] Lyubartsev, A. P. and Laaksonen, A., "Concentration Effects in Aqueous NaCl Solutions. A Molecular Dynamics Simulation," *Journal of Physical Chemistry B*, vol. 100 pp. 16410-16418, 1996.

[61] Shelby, J. E., *Introduction to Glass Science and Technology* The Royal Society of Chemistry, 1997.

[62] Rae, J. and Levis, R., "Glass Technology for Patch Clamp Electrodes," *Methods in Enzymology*, vol. 207 pp. 66-92, 1992.

[63] Huettner, J. and Baughman, R., "Primary Culture of Identified Neurons from the Visual Cortex of Postnatal Rats," *Journal of Neuroscience*, vol. 6, no. 10, pp. 3044-3060, 1986.

[64] Brewer, G. J., "Isolation and culture of adult rat hippocampal neurons," *Journal of Neuroscience Methods*, vol. 71 pp. 143-155, 1997.

[65] Totterdell, S., Ingham, C. A., and Bolam, J. P., "Immunocytochemistry I: pre-embedding staining," in Bolam, J. P. (ed.) *Experimental neuroanatomy: a practical approach* 1 ed. Oxford: Oxford University Press, 1992, pp. 103-127.

[66] Withers, G. S. and Banker, G., "Characterizing and Studying Neuronal Cultures," in Goslin, K. and Banker, G. (eds.) *Culturing Nerve Cells* 2 ed. Cambridge: The MIT Press, 1998, pp. 113-151.

[67] Thomas, J. D., Lough, A. S., and Lodge, R. W., "Chemical Ecology of Biomphalaria-Glabrata (Say), Snail Host of Schistosoma-Mansoni Sambon - Search for Factors in Media Conditioned by Snails Which Inhibit Their Growth and Reproduction," *Journal of Applied Ecology*, vol. 12, no. 2, pp. 421-436, 1975.

[68] Soest, P. F. and Kits, K. S., "Conopressin affects excitability, firing, and action potential shape through stimulation of transient and persistent inward currents in mulluscan neurons," *Journal of Neurophysiology*, vol. 79, no. 4, pp. 1619-1632, 1998.

[69] Grove, A. S., *Physics and technology of semiconductor devices* New York: Wiley, 1967, pp. 1-366.

[70] Mayer, M., "Screening for Bioactive Compounds: Chip-based Functional Analysis of Single Ion Channels & Capillary Electrochromatography for Immunoaffinity Selection." Doctorate École Polytechnique Fédérale de Lausanne, 2000.

[71] Vogler, E., "Structure and reactivity of water at biomedical surfaces," *Advances in Colloid and Interface Science*, vol. 74 pp. 69-117, 1998.

[72] Johnson, R. E. Jr. and Dettre, R. H., "Wetting of Low-Energy Surfaces," in Berg, J. C. (ed.) *Wettability* New York: Marcel Dekker, 1993, pp. 1-73.

[73] Vogler, E., "Structure and reactivity of water at biomaterial surfaces," *Advances in Colloid and Interface Science*, vol. 74 pp. 69-117, 1998.

[74] Girifalco, L. A. and Good, R. J., "A theory for the estimation of surfface and interfacial energies, I. Derivation and application to interfacial tension," *Journal of Physical Chemistry B*, vol. 61 pp. 904-909, 1957.

[75] Fowkes, F. M., "Determination of interfacial tensions, contact angles, and dispersion forces by assuming additivity of intermolecular interactions at surfaces (letter)," *Journal of Physical Chemistry B*, vol. 66 pp. 382, 1962.

[76] Fowkes, F. M., "Additivity of intermolecular forces at interfaces, I. Determination of the contribution to surface and interfacial tensions of dispersion forces in various liquids," *Journal of Physical Chemistry B*, vol. 67 pp. 2538-2541, 1963.

[77] Lide, D. R., *CRC handbook of chemistry and physics : a ready-reference book of chemical and physical data*, 73rd ed. CRC Press, 1992.

[78] Good, R. J., Chaudhury, M. K., and van Oss, C. J., "Theory of adhesive forces across interfaces, I. Interfacial hydrogen bonds as acid-base phenomena and as factors enhancing adhesion," in Lee, L. (ed.) *Fundamentals of Adhesion* Plenum Press, 1991, pp. 153-172.

[79] Moita, A. S. H. and Moreira, A. L. N. Influence of Surface Properties on the Dynamic Behavior of Impacting Droplets. 2003. 9th International Conference on Liquid Atomization and Spray Systems.

[80] Meiron, T. S., Marmur, A., and Saguy, S., "Contact angle measurement on rough surfaces," *Journal of Colliod Interface Science*, vol. 274, no. 2, pp. 637-644, 2004.

[81] Higgins, D. and Banker, G., "Primary Dissociated Cell Cultures," in 2nd (ed.) *Culturing Nerve Cells* Cambridge: MIT Press, 1998, pp. 37-78.

[82] Padday, J. F., "Spreading, wetting, and contact angles," in Mittal, K. L. (ed.) *Contact Angle, Wettability and Adhesion* 1993, pp. 97-108.

[83] Adams, A. C., "Dielectric and Polysilicon Film Deposition," in Sze, S. M. (ed.) *VLSI Technology* McGraw-Hill, 1983, pp. 93-129.

[84] Bousse, L. and Mostarshed, S., "The Zeta-Potential of Silicon-Nitride Thin-Films," *Journal of Electroanalytical Chemistry*, vol. 302, no. 1-2, pp. 269-274, 1991.

[85] Chien, F. S., Chang, J. W., Lin, S. W., Chou, Y. C., Chen, T. T., and Gwo, S., "Nanometer-scale conversion of Si_3N_4 to SiO_x," *Applied Physics Letters*, vol. 76, no. 3, pp. 360-362, 2000.

[86] Parak, W. J., George, M., Kudera, R., Gaub, H. E., and Behrends, J. C., "Effects of semiconductor substrate and glia-free culture on the development of voltage-dependent currents in rat striatal neurones," *European Biophysics Journal with Biophysics Letters*, vol. 29, no. 8, pp. 607-620, 2001.

[87] Nicolau, D. V., Taguchi, T., Taniguchi, H., Tanigawa, H., and Yoshikawa, S., "Patterning neuronal and glia cells on light-assisted functionalised photoresists," *Biosensors & Bioelectronics*, vol. 14, no. 3, pp. 317-325, 1999.

[88] Guu, S. M. and Tsai, D. M., "Measurement of Roundness: a Nonlinear Approach," *Proc.Natl.Sci.Counc.ROC(A)*, vol. 23, no. 3, pp. 348-352, 1999.

[89] Chen, M. C., Tsai, D. M., and Tseng, H. Y., "A stochastic optimization approach for roundness measurements," *Pattern Recognition Letters*, vol. 20 pp. 707-719, 1999.

[90] Zhu, L. M., Ding, H., and Xiong, Y. L., "A steepest descent algorithm for circularity evaluation," *Computer-Aided Design*, vol. 35 pp. 255-265, 2003.

[91] Huang, J., "A new strategy for circularity problems," *Precision Engineering*, vol. 25 pp. 301-308, 2001.

[92] Sigworth, F. and Klemic, K. "Patch Clamp on a Chip." *Biophysical Journal* pp. 2831-2832, 2002.

[93] Casey, J., "Curvature of Curves," *Exploring Curvature* Vieweg, 1996, pp. 113-136.

[94] Henderson, D. W., "Extrinsic Curves," *Differential Geometry: a geometric introduction* New Jersey: Prentice-Hall, Inc., 1998, pp. 37-60.

[95] Coxeter, H. M. S., "Differential Geometry of Curves," *Introduction to Geometry* 2nd ed. John Wiley & Sons, Inc., 1969, pp. 307-327.

[96] Schmidt, C., Mayer, M., and Vogel, H., "A Chip-Based Biosensor for the Functional Analysis of Single Ion Channels," *Angewandte Chemie*, vol. 39, no. 17, pp. 3137-3140, 2000.

[97] Fertig, N., Tilke, A., Blick, R. H., and Kotthaus, J. P., "Stable integration of isolated cell membrane patches in a nanomachined aperture," *Applied Physics Letters*, vol. 77, no. 8, pp. 1218-1220, Aug.2002.

[98] Pandey, S. and White, M., "An Integrated Planar Patch-Clamp System," *International Symposium on Semiconductor Device Research*, pp. 170-173, 2003.

[99] Petersen, K. E., "Dynamic Micromechanics on Silicon - Techniques and Devices," *Ieee Transactions on Electron Devices*, vol. 25, no. 10, pp. 1241-1250, 1978.

[100] Nijdam, A. J., Gardeniers, J. G. E., Berenschot, J. W., van Veenendaal, E., van Suchtelen, J., and Elwenspoek, M., "Influence of the angle between etched (near) Si{111} surfaces and the substrate orientation on the underetch rate during anisotropic wet-chemical etching of silicon," *Journal of Micromechanics and Microengineering*, vol. 11, no. 5, pp. 499-503, 2001.

[101] Mayer, M., "Screening for Bioactive Compounds: Chip-based Functional Analysis of Single Ion Channels & Capillary Electrochromatography for Immunoaffinity Selection." Doctorate École Polytechnique Fédérale de Lausanne, 2000.

[102] Armani, D., Liu, C., and Aluru, N. Re-configurable Fluid Circuits by PDMS Elastomer Micromachining. 222-227. 1999. Micro Electro Mechanical Systems, 1999. MEMS '99. Twelfth IEEE International Conference on.

[103] Fujii, T., "PDMS-based microfluidic devices for biomedical applications," *Microelectronic Engineering*, vol. 61-2 pp. 907-914, 2002.

[104] Thiebaud, P., Lauer, L., Knoll, W., and Offenhausser, A., "PDMS device for patterned application of microfluids to neuronal cells arranged by microcontact printing," *Biosensors & Bioelectronics*, vol. 17, no. 1-2, pp. 87-93, 2002.

[105] Cousin, M. A. and Nicholls, D. G., "Synaptic vesicle recycling in cultured cerebellar granule cells: Role of vesicular acidification and refilling," *Journal of Neurochemistry*, vol. 69, no. 5, pp. 1927-1935, 1997.

[106] Hynes, A. M., Ashraf, H., Bhardwaj, J. K., Hopkins, J., Johnston, I., and Shepherd, J. N., "Recent advances in silicon etching for MEMS using the ASE (TM) process," *Sensors and Actuators A-Physical*, vol. 74, no. 1-3, pp. 13-17, 1999.

[107] Raul, S., Dauksher, W., Clemens, B., and Smith, K., "Model for a multiple-step deep Si etch process," *Journal of Vacuum Science and Technology A*, vol. 20, no. 4, pp. 1177-1190, 2002.

[108] Mccormick, D. A. and Prince, D. A., "Two Types of Muscarinic Response to Acetylcholine in Mammalian Cortical-Neurons," *Proceedings of the National Academy of Sciences of the United States of America*, vol. 82, no. 18, pp. 6344-6348, 1985.

Appendix

A.1 Scripts

A.1.1 Polar-coordinate conversion

```
{
    Find_Outline_Polar script
    Brad Dworak
    26/5/04
}

var int, cmx, cmy : integer; xoutline, youtline, anglearray,
distarray : Array; b : real;

procedure findoutline(x, y : integer);
begin
      { Data extraction of image outline }
      xoutline[int] := x;
      youtline[int] := y;

      { Find another pixel if x and y value is same as previous }
      IF ( int > 1 ) THEN
            IF (( xoutline[int] = xoutline[int-1] ) AND (
youtline[int] = youtline[int-1] )) THEN int := int - 1;
      int := int + 1;
end;

procedure polarconversion;
var count : integer;
begin

      { Calculate radius and angle }
      FOR count := 1 TO ( int-1 ) DO
      BEGIN

            { Distance calculation }
            distarray[count] := sqrt( sqr( xoutline[count] - cmx ) +
sqr( youtline[count] - cmy ) );

            { Manually enter angle in case x-pos is 0 }
            IF ( xoutline[count] - cmx ) = 0 THEN
                  IF ( youtline[count] < cmy ) THEN
anglearray[count] := pi / 2
                  ELSE anglearray[count] := 3 * pi / 2

            { Angle calculation }
            ELSE anglearray[count] := arctan( ( youtline[count] -
cmy ) / ( xoutline[count] - cmx ) );

            { Convert radians to degrees }
            anglearray[count] := ( anglearray[count] / pi ) * 180;

            { Conver to base-360 with 0 degrees starting at Q1 ccw }
            IF ( xoutline[count] > cmx ) AND ( youtline[count] > cmy
) THEN anglearray[count] := 360 - anglearray[count] ELSE {q4}
```

```
51              IF ( xoutline[count] > cmx ) AND ( youtline[count] <=
52  cmy ) THEN anglearray[count] := anglearray[count] * -1 ELSE {q1}
53              IF ( xoutline[count] < cmx ) THEN
54              anglearray[count] := 180 - anglearray[count];
55          END;
56  end;
57
58  procedure viewresults;
59  var count : integer;
60  begin
61          { View results in window }
62          FOR count := 1 TO ( int-2 ) DO
63          BEGIN
64
65          AddResults('x\ty\tTheta\tr\tXOrigin\tYOrigin\tThetaSmooth\tRSm
66  ooth\tDer1Smooth', xoutline[count], '\t', youtline[count], '\t',
67  anglearray[count], '\t', distarray[count], '\t', cmx, '\t', cmy );
68          END;
69  end;
70
71  macro 'FindOutline';
72  var a : integer;
73  begin
74          { Initialise variables }
75          FOR a := 1 TO 5000 DO
76          BEGIN
77                  xoutline[a] := 0;
78                  youtline[a] := 0;
79          END;
80          int := 1;
81          b := 1;
82          cmx := 0;
83          cmy := 0;
84
85          { Find aperture }
86          GetUserRoi('Outline the area to search', false);
87          GetUserThresholds('', 150, 150);
88          FindObjects;
89          cmx := GetNumber('Enter x-origin', 0);
90          cmy := GetNumber('Enter y-origin', 0);
91          ObjectToRoi( 1 );
92          ShowResults( true );
93          DiscardResults;
94          Trace(findoutline, false);
95          polarconversion;
96          viewresults;
97  end;
```

A.1.2 Find Outline

```
1  {
2      FindOutline script
3      Brad Dworak
4      26/5/04
5  }
6
7  var c, int : integer; distarray, anglearray, xoutline, youtline :
8  Array; b : real;
9
```

```
10  procedure findoutline(x, y : integer);
11  begin
12        { Data extraction of image outline }
13        xoutline[int] := x;
14        youtline[int] := y;
15
16        { Find another pixel if x and y value is same as previous }
17        IF ( int > 1 ) THEN
18              IF (( xoutline[int] = xoutline[int-1] ) AND (
19  youtline[int] = youtline[int-1] )) THEN int := int - 1;
20        int := int + 1;
21  end;
22
23  procedure findproperties;
24  var count : integer; area, cmx, cmy : real;
25  begin
26        { Initialise variables }
27        area := 0;
28        cmx := 0;
29        cmy := 0;
30
31        { Calculate Area }
32        FOR count := 1 TO ( int-1 ) DO
33        BEGIN
34              area := area + ( ( xoutline[count] * youtline[count+1] )
35  - ( xoutline[count+1] * youtline[count] ) );
36        END;
37        area := abs( area );
38        area := area / 2;
39
40        { Calculate x-pos centroid }
41        FOR count := 1 TO ( int-1 ) DO
42        BEGIN
43              cmx := cmx + ( ( xoutline[count] + xoutline[count+1] ) *
44  ( ( xoutline[count] * youtline[count+1] ) - ( xoutline[count+1] *
45  youtline[count] ) ) );
46        END;
47        cmx := abs( cmx );
48        cmx := cmx / ( 6 * area );
49
50        { Calculate y-pos centroid }
51        FOR count := 1 TO ( int-1 ) DO
52        BEGIN
53              cmy := cmy + ( ( youtline[count] + youtline[count+1] ) *
54  ( ( xoutline[count] * youtline[count+1] ) - ( xoutline[count+1] *
55  youtline[count] ) ) );
56        END;
57        cmy := abs( cmy );
58        cmy := cmy / ( 6 * area );
59
60        { Calculate radius and angle }
61        FOR count := 1 TO ( int-1 ) DO
62        BEGIN
63
64              { Distance calculation }
65              distarray[count] := sqrt( sqr( xoutline[count] - cmx ) +
66  sqr( youtline[count] - cmy ) );
67
68              { Manually enter angle in case x-pos is 0 }
```

```
69              IF ( xoutline[count] - cmx ) = 0 THEN
70                    IF ( youtline[count] < cmy ) THEN
71  anglearray[count] := pi / 2
72                    ELSE anglearray[count] := 3 * pi / 2
73
74              { Angle calculation }
75              ELSE anglearray[count] := arctan( ( youtline[count] -
76  cmy ) / ( xoutline[count] - cmx ) );
77
78              { Convert radians to degrees }
79              anglearray[count] := ( anglearray[count] / pi ) * 180;
80
81              { Conver to base-360 with 0 degrees starting at Q1 ccw }
82              IF ( xoutline[count] > cmx ) AND ( youtline[count] > cmy
83  ) THEN anglearray[count] := 360 - anglearray[count] ELSE {q4}
84              IF ( xoutline[count] > cmx ) AND ( youtline[count] <=
85  cmy ) THEN anglearray[count] := anglearray[count] * -1 ELSE {q1}
86              IF ( xoutline[count] < cmx ) THEN
87              anglearray[count] := 180 - anglearray[count];
88        END;
89
90        { View results in window }
91        FOR count := 1 TO ( int-2 ) DO
92        BEGIN
93
94        AddResults('Area\tx\ty\tcmx\tcmy\tAngle\tDist\tSmoothData',
95  area, '\t', xoutline[count], '\t', youtline[count], '\t', cmx, '\t',
96  cmy, '\t', anglearray[count], '\t', distarray[count] );
97        END;
98  end;
99
100 macro 'FindOutline';
101 var a : integer;
102 begin
103       { Initialise variables }
104       FOR a := 1 TO 5000 DO
105       BEGIN
106             xoutline[a] := 0;
107             youtline[a] := 0;
108       END;
109       int := 1;
110       b := 1;
111       c := 0;
112
113       { Find aperture }
114       GetUserRoi('Outline the area to search', false);
115       GetUserThresholds('', 0, 150);
116       FindObjects;
117       { a := GetNumber('Enter object number', 0); }
118       { b := GetNumber('Enter radius times factor', 0); }
119       ObjectToRoi( 1 );
120       ShowResults;
121       Trace(findoutline, false);
122       findproperties;
123 end;
```

A.1.3 Circularity

```
1
2   {
3   {
4       Circularity script
5       Brad Dworak
6       26/5/04
7   }
8
9   var int, count : integer; d1array, d2array, ysmooth : Array; b, max,
10  tfactor : real;
11  strdata : string;
12
13  procedure extractsmooth;
14  begin
15        max := 0;
16        FOR count := 1 TO int DO
17        BEGIN
18              strdata := GetResults('SmoothData', count );
19              ysmooth[count] := StringToNum( strdata );
20              IF ysmooth[count] > max THEN max := ysmooth[count];
21        END;
22        FOR count := 1 TO int DO
23        BEGIN
24              ysmooth[count] := ysmooth[count] * ( tfactor / max );
25        END;
26  end;
27
28  procedure findproperties;
29  var d1ave, d2ave : real;
30  begin
31        { Initialise variables }
32        d1ave := 0;
33        d2ave := 0;
34
35        b := int; { quasi convert integer to real }
36
37        { Calculate RMS value of 1st derivative }
38        FOR count := 1 TO ( int-1 ) DO
39        BEGIN
40              { Derivative calculation = change in radius }
41              d1array[count] := ysmooth[count+1] - ysmooth[count];
42
43              { Add square to average variable }
44              d1ave := d1ave + sqr( d1array[count] );
45        END;
46        { RMS value is square root of average of squares }
47        d1ave := sqrt( d1ave / ( b - 1 ) );
48
49        { Calculate 2nd derivative }
50        FOR count := 1 TO ( int-2 ) DO
51        BEGIN
52              { Derivative calculation = change in 1st derivative }
53              d2array[count] := d1array[count+1] - d1array[count];
54
55              { Add square to average variable }
56              d2ave := d2ave + sqr( d2array[count] );
```

```
57          END;
58          { RMS value is square root of average of squares }
59          d2ave := sqrt( d2ave / ( b - 2 ) );
60
61          { View results in window }
62          FOR count := 1 TO int DO
63          BEGIN
64                AddResults('SmoothData\tDer1\tDer2\tRMSDer1\tRMSDer2',
65    ysmooth[count], '\t', d1array[count], '\t', d2array[count], '\t',
66    d1ave, '\t', d2ave );
67          END;
68    end;
69
70    macro 'Circularity';
71    var a : integer;
72    begin
73          FOR a := 1 TO 105 DO
74          BEGIN
75                ysmooth[a] := 0;
76                d1array[a] := 0;
77                d2array[a] := 0;
78          END;
79          int := 101;
80          ShowResults;
81          tfactor := GetNumber('Enter maximum radius per set', 100.000,
82    3);
83          extractsmooth;
84          DiscardResults;
85          findproperties;
86    end;
```

A.2 Aperture Family Images

Step	Process for aperture $A_{thermal}$	SEM images at 0° and 45° AOI
		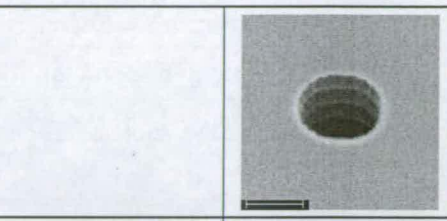
1.	RIE oxide etch	
2.	deep silicon etch (8-µm depth)	
3.	oxide strip (complete HF etch)	
		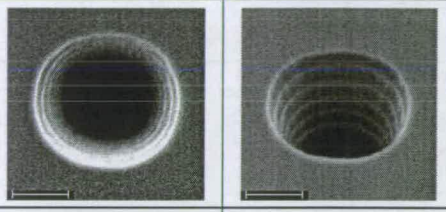
4.	SF_6 etch (20 sec)	
		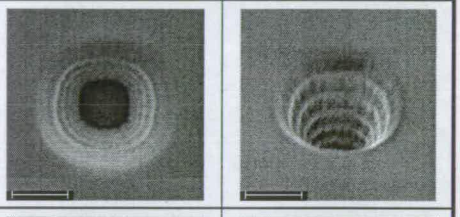
5.	wet thermal oxidation (1.1 µm)	
		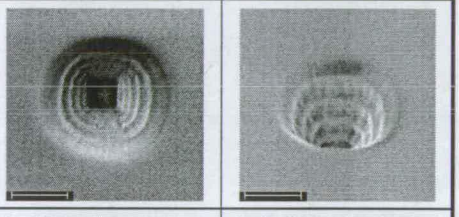
6.	wet thermal oxidation (1.6 µm total)	
		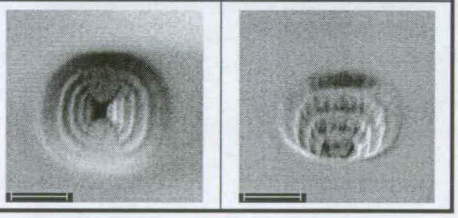
7.	wet thermal oxidation (1.9 µm total)	

Table A.2.1: Processing steps and associated SEM images for aperture $A_{thermal}$.

Step	Process for aperture A_{pecvd}	SEM images at 0° and 45° AOI
		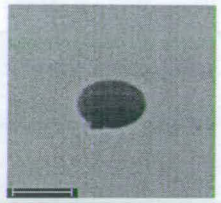
1.	RIE oxide etch	
2.	deep silicon etch (8-µm depth)	
3.	oxide strip (complete HF etch)	
		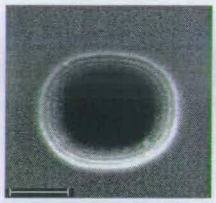 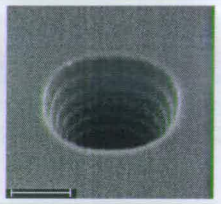
4.	SF_6 etch (20 sec)	
		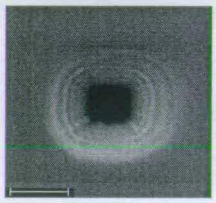 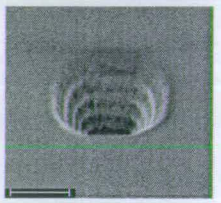
5.	wet thermal oxidation (1.1 µm)	
		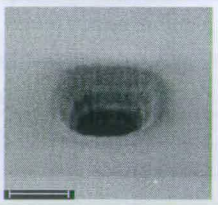
6.	PECVD oxide deposition (0.5 µm total)	
		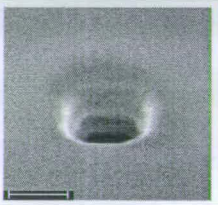
7.	PECVD oxide deposition (1.0 µm total)	

Table A.2.2: Processing steps and associated SEM images for aperture A_{pecvd}.

Step	Process for aperture $B_{thermal}$	SEM images at 0° and 45° AOI
		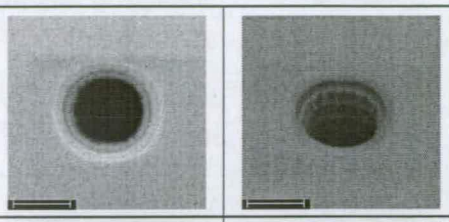
1.	RIE oxide etch	
2.	deep silicon etch (8-µm depth)	
3.	partial HF etch (180 sec)	
		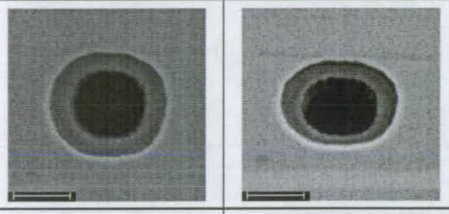
4.	partial HF etch (90 sec)	
		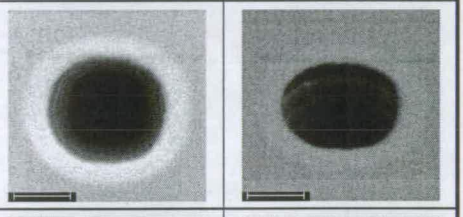
5.	SF_6 etch (20 sec)	
		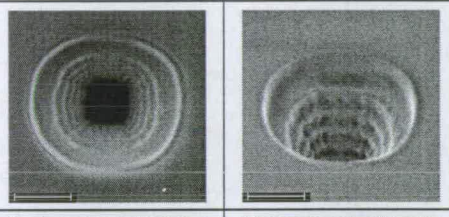
6.	oxide strip (complete HF etch)	
7.	wet thermal oxidation (1.1 µm)	
		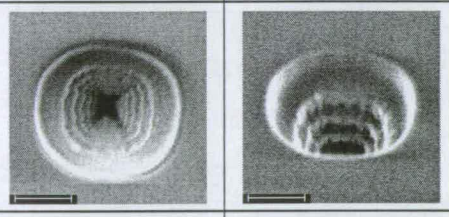
8.	wet thermal oxidation (1.6 µm total)	
		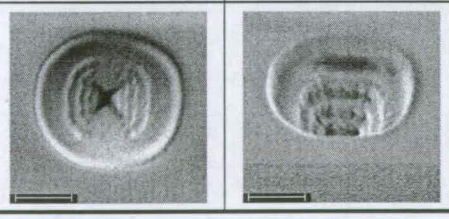
9.	wet thermal oxidation (1.9 µm total)	

Table A.2.3: Processing steps and associated SEM images for aperture $B_{thermal}$.

Step	Process for aperture B_{pecvd}	SEM images at 0° and 45° AOI
		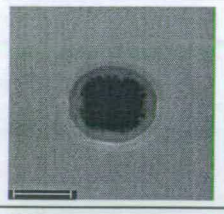 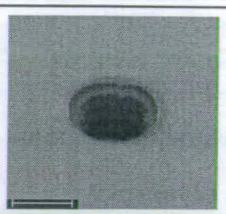
1.	RIE oxide etch	
2.	deep silicon etch (8-µm depth)	
3.	partial HF etch (3.0 min)	
		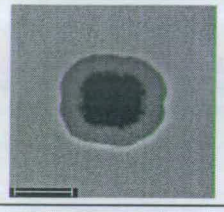 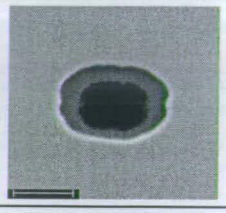
4.	partial HF etch (1.5 min)	
		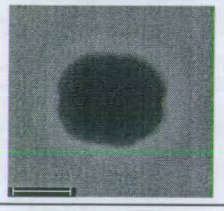 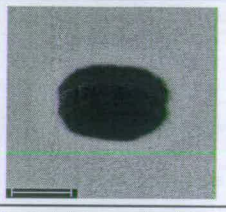
5.	SF_6 etch (20 sec)	
		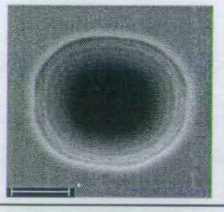 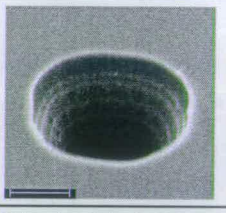
6.	oxide strip (complete HF etch)	
7.	wet thermal oxidation (1.1 µm)	
		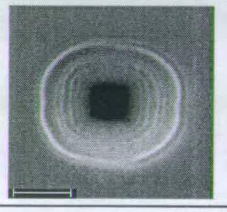 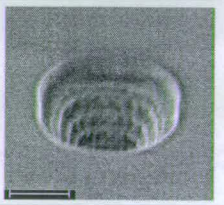
8.	PECVD oxide deposition (1.6 µm total)	
		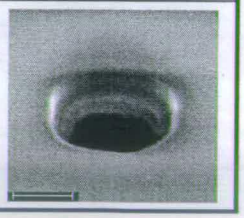
9.	PECVD oxide deposition (1.9 µm total)	

Table A.2.4: Processing steps and associated SEM images for aperture B_{pecvd}.

Step	Process for aperture $C_{1,thermal}$	SEM images at 0° and 45° AOI
		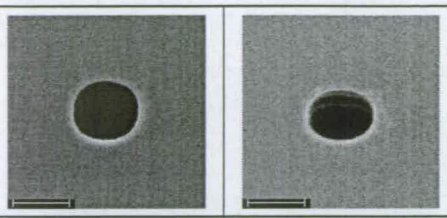
1.	RIE oxide etch	
2.	deep silicon etch (8-µm depth)	
3.	oxide strip (complete HF etch)	
		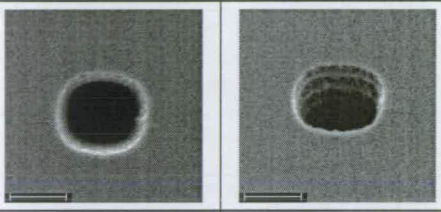
3.	SF_6 etch (10 sec)	
		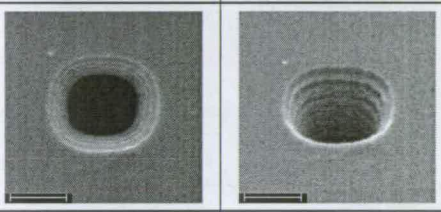
4.	SF_6 etch (10 sec; 20 sec total)	
		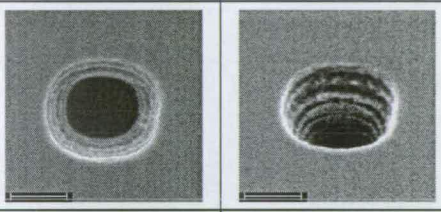
5.	SF_6 etch (10 sec; 30 sec total)	
		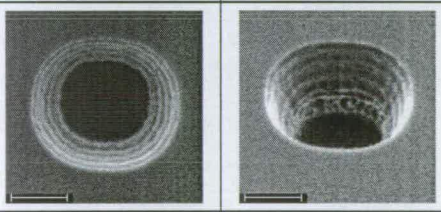
6.	SF_6 etch (10 sec; 50 sec total)	
		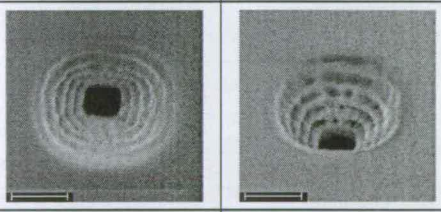
7.	wet thermal oxidation (1.1 µm)	
		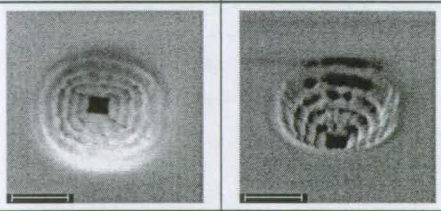
8.	wet thermal oxidation (1.6 µm total)	
		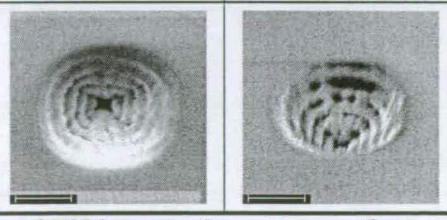
9.	wet thermal oxidation (1.9 µm total)	

Table A.2.5: Processing steps and associated SEM images for aperture $C_{1,thermal}$.

Step	Process for aperture $C_{2,thermal}$	SEM images at 0° and 45° AOI
		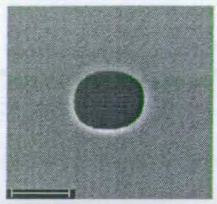 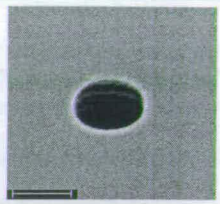
1.	RIE oxide etch	
2.	deep silicon etch (8-µm depth)	
3.	oxide strip (complete HF etch)	
		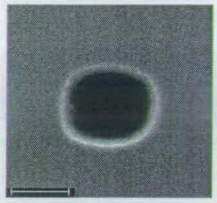 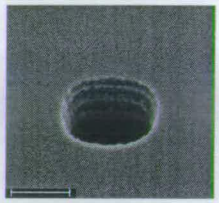
4.	SF_6 etch (10 sec)	
		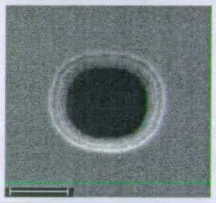 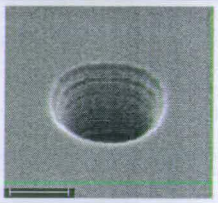
5.	SF_6 etch (10 sec; 20 sec total)	
		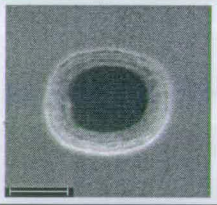 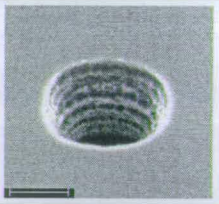
6.	SF_6 etch (10 sec; 30 sec total)	
		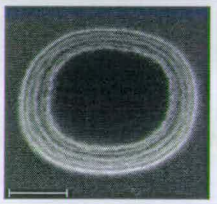 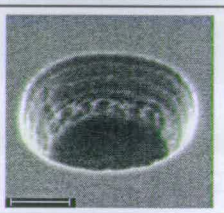
7.	SF_6 etch (10 sec; 50 sec total)	
		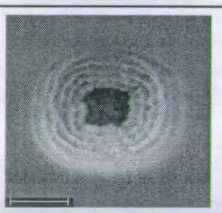 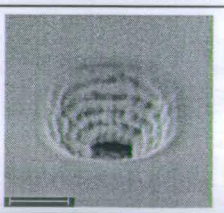
8.	wet thermal oxidation (1.1 µm)	
		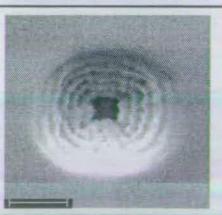 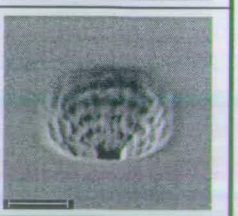
9.	PECVD oxide deposition (0.5 µm total)	
		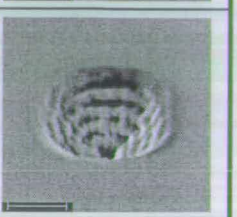
10.	PECVD oxide deposition (1.0 µm total)	

Table A.2.6: Processing steps and associated SEM images for aperture $C_{2,thermal}$.

Step	Process for aperture $C_{1,pecvd}$	SEM images for 0° and 45° AOI
		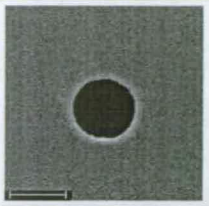
1.	RIE oxide etch	
2.	deep silicon etch (8-µm depth)	
3.	oxide strip (complete HF etch)	
		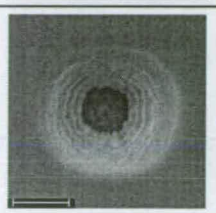 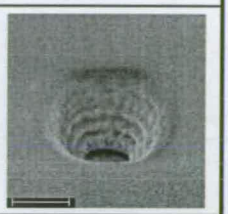
4-7.	SF_6 etch (50 sec total);	
8.	wet thermal oxidation (1.1 µm)	
		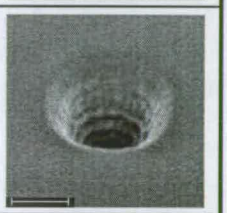
9.	PECVD oxide deposition (0.5 µm)	
		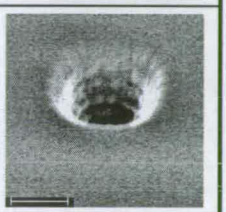
10.	PECVD oxide deposition (1.0 µm total)	

Table A.2.7: Processing steps and associated SEM images for aperture $C_{1,pecvd}$.

Step	Process for aperture $C_{2,pecvd}$	SEM images for 0° and 45° AOI	
		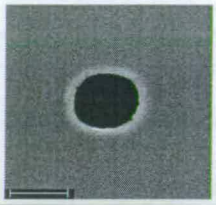	
1.	RIE oxide etch		
2.	deep silicon etch (8-µm depth)		
3.	oxide strip (complete HF etch)		
		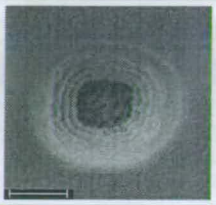	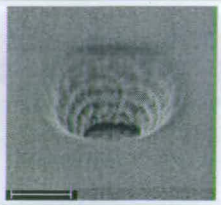
4-7.	SF_6 etch (50 sec total);		
8.	wet thermal oxidation (1.1 µm)		
9.	PECVD oxide deposition (0.5 µm)		
			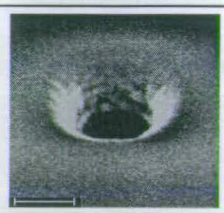
10.	PECVD oxide deposition (1.0 µm total)		

Table A.2.8: Processing steps and associated SEM images for aperture $C_{2,pecvd}$.

Step	Process for aperture $D_{1,thermal}$	SEM images at 0° and 45° AOI
		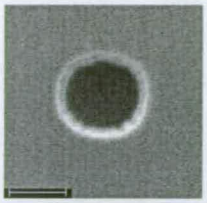
1.	RIE oxide etch	
2.	deep silicon etch (4-µm depth)	
3.	oxide strip (complete HF etch)	
		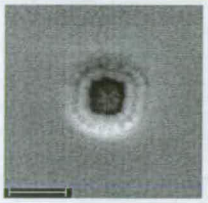 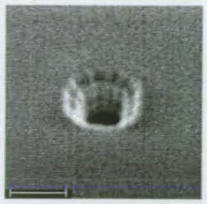
4.	SF_6 (8 sec)	
5.	wet thermal oxidation (1.1 µm)	
		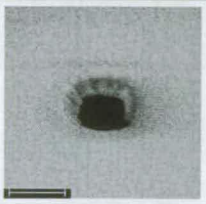
6.	PECVD oxide deposition (0.5 µm)	
		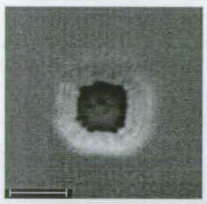 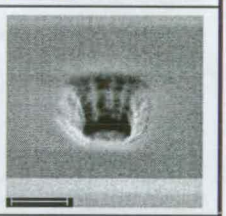
7.	partial HF etch for 1.0 min	
		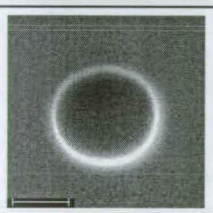 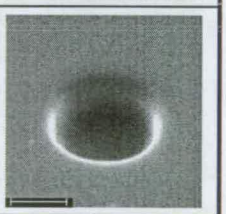
8.	oxide strip (complete HF etch)	
		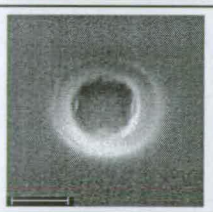 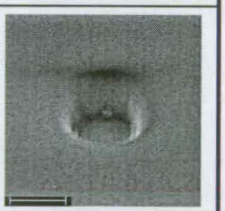
9.	wet thermal oxidation (1.1 µm)	
		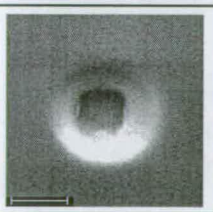 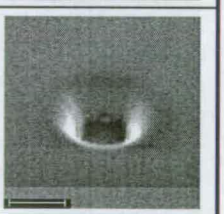
10.	wet thermal oxidation (1.6 µm total)	
		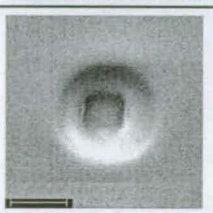
11.	wet thermal oxidation (1.9 µm total)	

Table A.2.9: Processing steps and associated SEM images for aperture $D_{1,thermal}$.

Step	Process for aperture $D_{2,thermal}$	SEM images at 0° and 45° AOI
		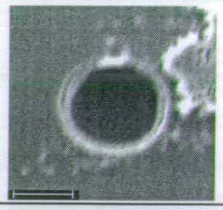
1.	RIE oxide etch	
2.	deep silicon etch (4-µm depth)	
3.	oxide strip (complete HF etch)	
		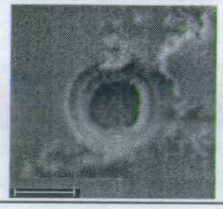
4.	SF_6 (8 sec)	
5.	wet thermal oxidation (1.1 µm)	
		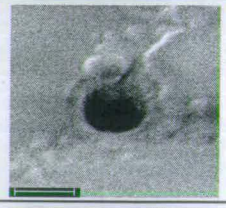
6.	PECVD oxide deposition (0.5 µm)	
		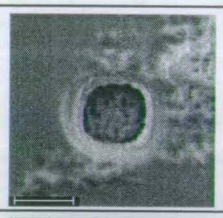 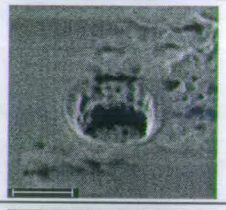
7.	partial HF etch for 1.0 min	
		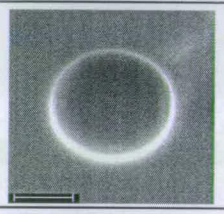 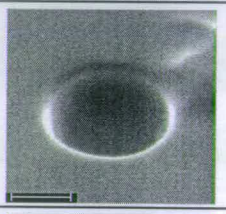
8.	oxide strip (complete HF etch)	
		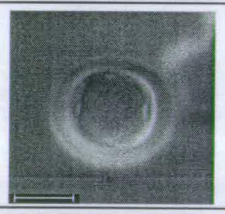
9.	wet thermal oxidation (1.1 µm)	
		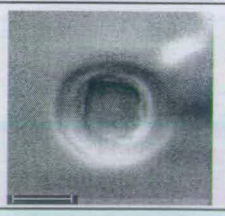
10.	wet thermal oxidation (1.6 µm total)	
		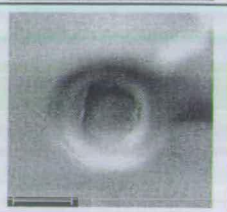 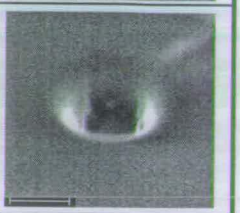
11.	wet thermal oxidation (1.9 µm total)	

Table A.2.10: Processing steps and associated SEM images for aperture $D_{2,thermal}$.

Step	Process for aperture $D_{1,pecvd}$	SEM images at 0° and 45° AOI	
1-2.	RIE oxide etch; deep silicon etch (4 μm)	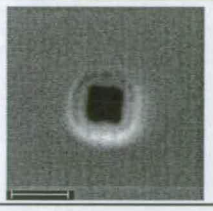	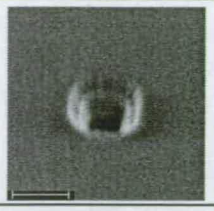
3.	oxide strip (complete HF etch)		
4.	SF_6 (8 sec)		
5.	wet thermal oxidation (1.1 μm)		
			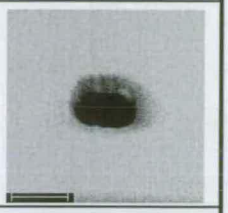
6.	PECVD oxide deposition (0.5 μm)		
		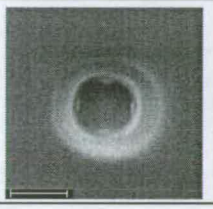	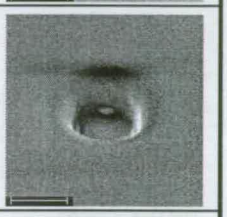
7.	partial HF etch (1.0 min)		
8.	oxide strip (complete HF etch)		
9.	wet thermal oxidation (1.1 μm)		
			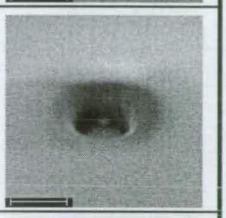
10.	PECVD oxide deposition (1.6 μm total)		
			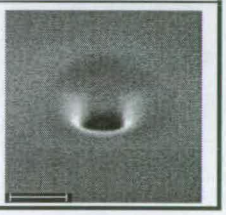
11.	PECVD oxide deposition (1.9 μm total)		

Table A.2.11: Processing steps and associated SEM images for aperture $D_{1,pecvd}$.

Step	Process for aperture $D_{2,pecvd}$	SEM images at 0° and 45° AOI
1-2.	RIE oxide etch; deep silicon etch (4 µm)	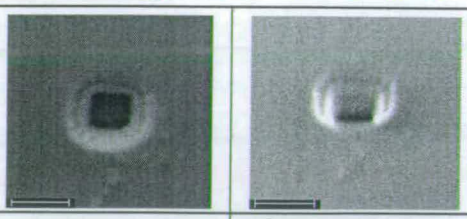
3.	oxide strip (complete HF etch)	
4.	SF_6 (8 sec)	
5.	wet thermal oxidation (1.1 µm)	
6.	PECVD oxide deposition (0.5 µm)	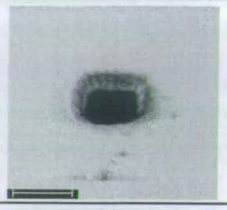
7.	partial HF etch (1.0 min)	
8.	oxide strip (complete HF etch)	
9.	wet thermal oxidation (1.1 µm)	
10.	PECVD oxide deposition (1.6 µm total)	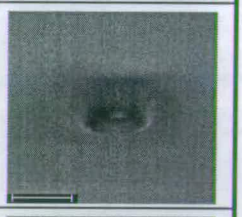
11.	PECVD oxide deposition (1.9 µm total)	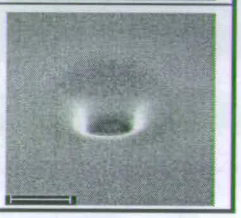

Table A.2.12: Processing steps and associated SEM images for aperture $D_{2,pecvd}$.

Step	Process for aperture $E_{1,thermal}$	SEM images at 0° and 45° AOI
		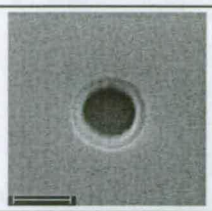
1.	RIE oxide etch	
2.	deep silicon etch (4-µm depth)	
		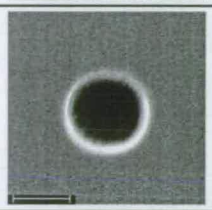
3.	oxide strip (complete HF etch)	
		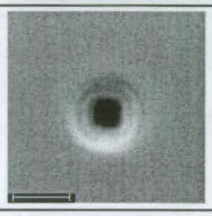 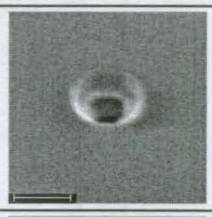
4.	wet thermal oxidation (1.1 µm)	
		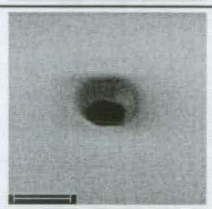
5.	PECVD oxide deposition (0.5 µm)	
		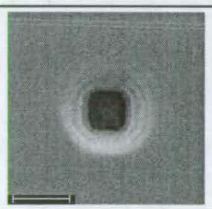 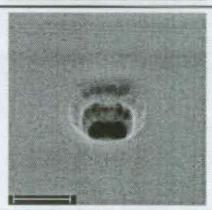
6.	partial HF etch for 1.0 min	

Table A.2.13a: Processing steps and associated SEM images for aperture $E_{1,thermal}$.

Step	Process for aperture $E_{1,thermal}$ (cont.)	SEM images at 0° and 45° AOI
		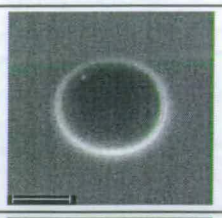
7.	oxide strip (complete HF etch)	
		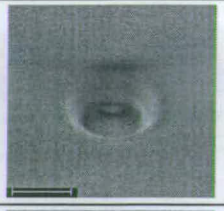
8.	wet thermal oxidation (1.1 µm)	
		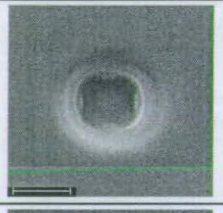 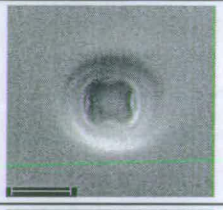
9.	wet thermal oxidation (1.6 µm total)	
		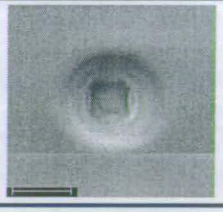
10.	wet thermal oxidation (1.9 µm total)	

Table A.2.13b: Processing steps and associated SEM images for aperture $E_{1,thermal}$.

Step	Process for aperture $E_{2,thermal}$	SEM images at 0° and 45° AOI
		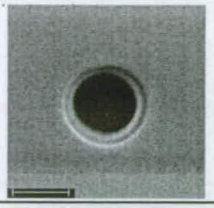
1.	RIE oxide etch	
2.	deep silicon etch (4-µm depth)	
		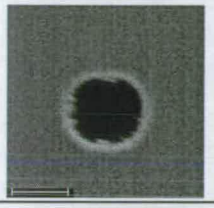 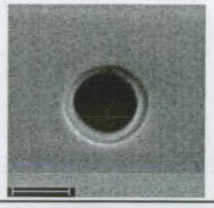
3.	oxide strip (complete HF etch)	
		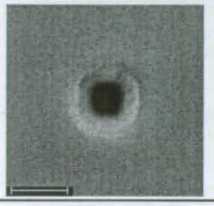 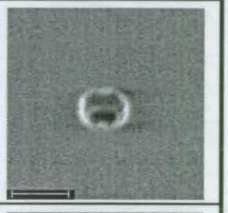
4.	wet thermal oxidation (1.1 µm)	
		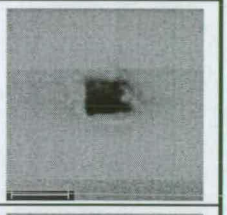
5.	PECVD oxide deposition (0.5 µm)	
		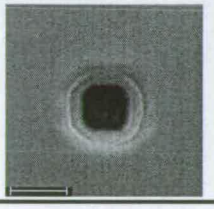 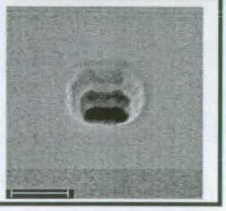
6.	partial HF etch (1.0 min)	

Table A.2.14a: Processing steps and associated SEM images for aperture $E_{2,thermal}$.

Step	Process for aperture $E_{1,thermal}$ (cont.)	SEM images at 0° and 45° AOI
		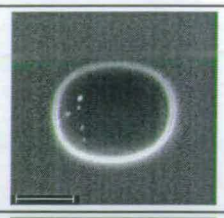
7.	oxide strip (complete HF etch)	
		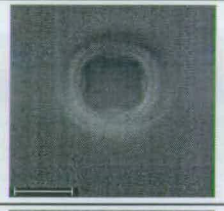 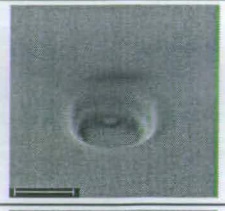
8.	wet thermal oxidation (1.1 µm)	
		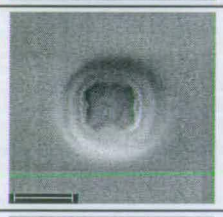 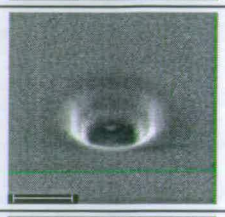
9.	wet thermal oxidation (1.6 µm total)	
		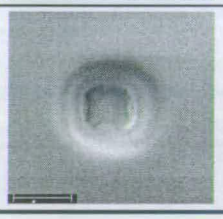 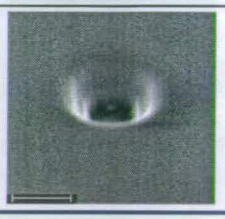
10.	wet thermal oxidation (1.9 µm total)	

Table A.2.14b: Processing steps and associated SEM images for aperture $E_{2,thermal}$.

Step	Process for aperture $E_{1,pecvd}$	SEM images at 0° and 45° AOI	
		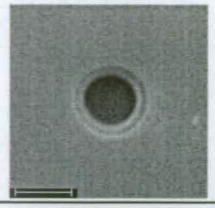	
1.	RIE oxide etch		
		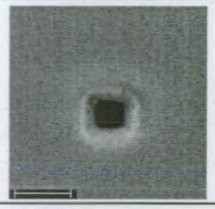	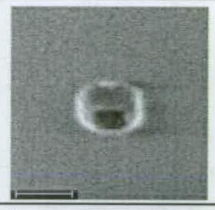
2.	deep silicon etch (4-µm depth)		
3.	oxide strip (complete HF etch)		
4.	wet thermal oxidation (1.1 µm)		
5.	PECVD oxide deposition (0.5 µm)	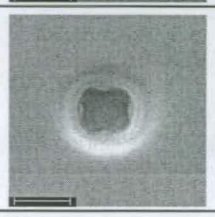	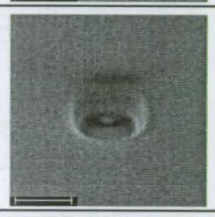
6.	partial HF etch (1.0 min)		
7.	oxide strip (complete HF etch)		
8.	wet thermal oxidation (1.1 µm)		
			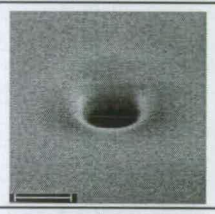
9.	PECVD oxide deposition (0.5 µm)		
			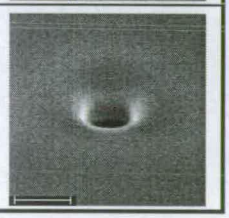
10.	PECVD oxide deposition (1.0 µm total)		

Table A.2.15: Processing steps and associated SEM images for aperture $E_{1,pecvd}$.

Step	Process for aperture $E_{2,pecvd}$	SEM images at 0° and 45° AOI	
		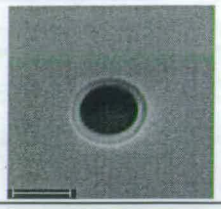	
1.	RIE oxide etch		
		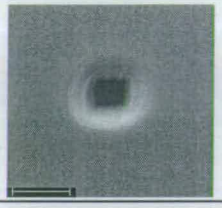	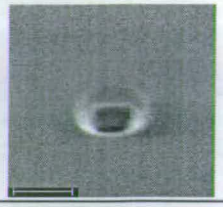
2.	deep silicon etch (4-µm depth)		
3.	oxide strip (complete HF etch)		
4.	wet thermal oxidation (1.1 µm)		
5.	PECVD oxide deposition (0.5 µm)	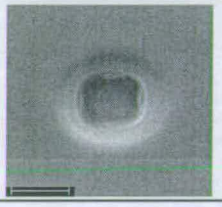	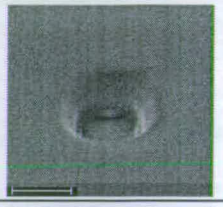
6.	partial HF etch (1.0 min)		
7.	oxide strip (complete HF etch)		
8.	wet thermal oxidation (1.1 µm)		
			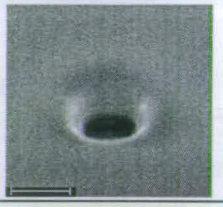
9.	PECVD oxide deposition (0.5 µm)		
			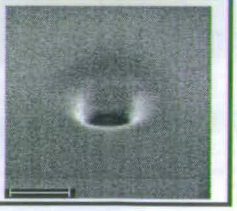
10..	PECVD oxide deposition (1.0 µm total)		

Table A.2.16 Processing steps and associated SEM images for aperture $E_{2,pecvd}$.

A.3 Process parameters

Parameter	Value
Temperature	1100°C
H_2 flow	3 sccm
O_2 flow	1.7 sccm

Table A.3.1: Thermal oxidation parameters

Parameter	Value
Type	Positive
Model	Shipley© SPR2Fx1.3
RPM	5200
Typical thickness	1.18 µm

Table A.3.2: Photoresist parameters for thin coating (1.18 µm)

Parameter	Value
Type	Positive
Model	Shipley© SPR2Fx1.3
RPM	3300
Typical thickness	1.4 µm

Table A.3.3: Photoresist parameters for medium coating (1.4 µm)

Parameter	Value
Type	Positive
Model	Shipley© HPR206
RPM	2000
Typical thickness	3.2 µm

Table A.3.4: Photoresist parameters for thick coating (3.2 µm)

Parameter	Value
Machine Type	Electrotech©
Power	330 watts
Pressure	668 mTorr
O_2 flow percentage	41.5%

Table A.3.5: Ashing parameters

Parameter	Value
Machine Type	Tempress© furnace
Method	LPVCD
NH_3 flow	12.0 sccm
SiH_2Cl_2 flow	48.0 sccm
Pressure	168 mTorr
Temperature	805°C
Deposition rate	500 Å/min

Table A.3.6: Si_3N_4 deposition parameters

Parameter	Value
Type	Shipley© MF-319
Duration	60 sec
Rinse liquid	De-ionised water
No. of cycles	2

Table A.3.7: Development parameters

Parameter	Value
CF_4 flow	60 sccm
H_2 flow	10 sccm
Pressure	~55 mTorr
Power	750 watts
Etch rate	~15 nm/min

Table A.3.8: Reactive ion etching parameters

Parameter	Value
Machine Type	STS© PECVD system
Method	PECVD
N_2 flow	392 sccm
N_2O flow	1420 sccm
SiH_4 flow	10 sccm
Temperature	300°C
Power	30 watts @ 13.56 MHz
Deposition rate	~540 Å/min

Table A.3.9: SiO_2 deposition parameters

Parameter	Value
Method	Solid source boric oxide
Temperature	Variable from 800-1000°C
N_2 flow	1.0 sccm

Table A.3.10: Boron deposition parameters

Parameter	Etch cycle	Passivation cycle
Coil power	600 watts	600 watts
Platen power	12 watts	0 watts
On-time	12 sec	8 sec
SF_6 flow	130 sccm	0 sccm
O_2 flow	13 sccm	0 sccm
C_4F_8 flow	0s ccm	85 sccm
RF frequency	13.56 MHz	13.56 MHz
Pressure	25 mTorr	25 mTorr
Etch rate	1.74 µm/min	

Table A.3.11: Deep Silicon Etch Parameters for Inductively-Coupled-Plasma Configuration.